Dissertation

submitted to the
Combined Faculties for the Natural Sciences and for Mathematics
of the Ruperto-Carola University of Heidelberg, Germany
for the degree of
Doctor of Natural Sciences

put forward by

Dipl.-Phys. Tilman Hüneke

born in Potsdam, Germany

Oral examination: December 14th, 2016

The scaling method applied to HALO measurements:

Inferring absolute trace gas concentrations from airborne limb spectroscopy under all sky conditions

Referees:

Prof. Dr. Klaus Pfeilsticker

Prof. Dr. Thomas Wagner

Abstract

The novel HALO mini-DOAS instrument was developed for measurements of UV/vis/near-IR spectra of scattered skylight in limb and nadir geometry aboard the new research aircraft HALO. The absorptions of a suite of trace gases (O_3, O_4, NO_2, CH_2O, BrO, OClO, and others) are identified in the measured spectra using the DOAS-technique. Previously employed methods to infer absolute concentrations from DOAS measurements rely on a priori knowledge of aerosols and cloud cover. The recently developed scaling method promises to enable the retrieval of target gas concentrations under all sky conditions. Effective light path lengths are estimated by employing a scaling gas, whose concentration at flight level is known, in conjunction with modelled profile shapes, radiative transfer calculations, and using the measured absorptions of the targeted species relative to those of the scaling gas. The present thesis describes the development and characterises the measurement properties of the HALO mini-DOAS instrument. For the first time, random and systematic errors of the scaling method are thoroughly investigated. It is argued that random errors are 10 – 20% for most measurement conditions and that the scaling method is practically unperturbed by changing cloud cover if applied appropriately. It is however shown that biases may occur if the assumed profile shapes are significantly different from actual profile shapes. Retrieved mixing ratios of BrO and NO_2 from measurements obtained during the science mission TACTS/ESMVal in August/September 2012 indicate that (a) no enhanced tropospheric BrO was detected in the mid-troposphere (3.5 – 9 km altitude) near the Antarctic continent (65° S) in spring (Sept. 13, 2012), (b) LMS and bottom polar vortex [BrO] agree with previous measurements, (c) other oxidants beside O_3 influence NO oxidation in the UT/LS where [N_2O] < 310 ppb, and (d) the same finding was confirmed for very low-NO_x conditions, although the latter measurements are uncertain.

Zusammenfassung

Das Instrument “HALO mini-DOAS” wurde für die flugzeuggetragene Messung von atmosphärischen Spurengasen mit Hilfe von Absorptionsspektroskopie im UV, sichtbaren und nah-infraroten Spektralbereich entwickelt. Es ermöglicht die Detektion einer Reihe von Spurengasen (O_3, O_4, NO_2, CH_2O, BrO, OClO u.v.m.) in Limb- und Nadirgeometrie mit der DOAS-Methode. Bisherige Ansätze, um aus DOAS-Messungen absolute Spurenstoffkonzentrationen zu berechnen, sind von Annahmen über Aerosol- und Wolkenvorkommen abhängig. Die in unserer Arbeitsgruppe neu entwickelte Skalierungsmethode umgeht diese Schwierigkeiten, indem mit einem Skalierungsgas, dessen Konzentration in Flughöhe bekannt ist, mit Strahlungstransport- und Chemietransportmodellrechnungen sowie mit den gemessenen Absorptionen von Skalierungs- und zu messendem Spurengas effektive Lichtwege abgeschätzt werden. Diese Arbeit beschreibt die Entwicklung und charakterisiert die Eigenschaften des “HALO mini-DOAS”-Instruments. Des Weiteren werden zum ersten Mal zufällige und systematische Unsicherheiten der Skalierungsmethode ausführlich untersucht. Es wird gezeigt, dass die Messunsicherheit meist bei 10 – 20% liegt und dass die Skalierungmethode von Änderungen der Bewölkung praktisch unabhängig ist, wenn sie richtig angewandt wird. Andererseits kann es zu systematischen Fehlern kommen, wenn die vom Modell vorhergesagten Spurengasprofile sich deutlich von den tatsächlichen unterscheiden. Messungen von BrO und NO_2 während der Messkampagne TACTS/ESMVal im August/September 2012 deuten darauf hin, dass (a) keine erhöhten BrO-Konzentrationen in der Troposphäre (3,5 – 9 km Höhe) in der Nähe des antarktischen Kontinents (65° S) im Frühling (13.09.2012) gemessen wurden und (b) BrO-Konzentrationen in der LMS und am Bodes des polaren Vortex’ mit früheren Messungen übereinstimmen sowie (c) andere Oxidantien neben O_3 die NO-Oxidation in der UTLS in Luftmassen mit [N_2O] < 310 ppb beeinflussen und (d) dass dasselbe für Messungen unter extrem NO_x-armen Bedingungen beobachtet wurde, wobei letztere Messergebnisse unsicher sind.

Contents

Chapter 1

Introduction

The chemical properties of the atmosphere are of interest for academic reasons and because of their direct influence on human life through e.g. local or regional air pollution, the destruction of the stratospheric ozone layer, and anthropogenically induced climate change (Kampa and Castanas, 2008; WMO, 2014; Stocker et al., 2013). Knowledge about chemical processes, radiation, dynamics, as well as interactions between them, are fundamental in understanding these observations. While ground-based measurements provide data with high spatial and temporal resolution but limited spatial coverage, satellites are suited to observe the atmosphere on a global scale. The need to observe complicated chemical and physical processes in the troposphere, stratosphere, and in particular in their transition regions, motivates airborne measurements with in-situ and remote sensing instruments.

As part of the initiative of the German science community to deploy the novel research aircraft DLR-HALO[1] (Krautstrunk and Giez, 2012), a novel instrument (hereafter called HALO mini-DOAS instrument) for the detection of UV/visible and near-IR absorbing species in scattered skylight was developed. The HALO mini-DOAS instrument allows for the observation of a suite of atmospheric trace gases, e.g. O_3, NO_2, CH_2O, BrO, OClO, and others. The main advantage of UV/visible absorption spectroscopy is its ability to measure trace gases at remote locations without interference, while the long light paths of up to several 100 km in limb geometry enable very low detection limits. Near-infrared channels were added in order to derive information on the phase, optical density, and phase function of clouds and their particles. In conjunction with other instruments assembled aboard the aircraft, the HALO mini-DOAS instrument provides the possibility to study a wide range of subjects of interest. Among other objectives these include ozone destruction by catalytic processes involving halogen oxides, the oxidation of volatile organic compounds (VOCs), air pollution and its impact on the budget of nitrogen oxides, questions regarding stratosphere-troposphere exchange (STE), as well as properties of clouds of low optical depths (e.g. subvisible and visible cirrus and mixed-phase clouds) and their influence on radiative transfer (chapter 2).

[1] Deutsches Zentrum für Luft- und Raumfahrt – High Altitude, LOng range research aircraft, www.halo.dlr.de

The instrument design and assembly was documented by the author's and subsequent diploma, bachelor, and master theses prior to this publication (Raecke, 2010; Hüneke, 2011; Kenntner, 2013; Schulte, 2013; Reichert, 2014; Weimar, 2014; Bounin, 2015). In the years 2012 – 2016 the instrument has participated in 7 science missions, which comprised more than 80 sorties of the aircraft of typically 8 hours duration (Table 4.1). More than 10^6 spectra of scattered light were recorded. Instrument performance and improvements made after campaign deployments are documented in the present thesis.

Spectroscopic measurements of scattered skylight from airborne platforms have been carried out since the 1990s. The detected absorptions are conventionally converted into absolute concentrations using inversion by optimal estimation (e.g. Rodgers, 2000; Bruns et al., 2004). This method has the disadvantage of strongly relying on a priori information about the optical state of the atmosphere, i.e. the presence of clouds and aerosols. It also presupposes that the same optical state of the atmosphere is sampled by all measurements involved. This precludes the evaluation of many measurements, since most airborne research is carried out in environments with scattered, and changing, cloud patterns. Therefore, until recently, the retrieval of absolute concentrations from scattered skylight absorption in limb geometry was limited to few and selected flight sections, mostly under clear-sky conditions.

The present thesis focuses on the development and characterisation of a novel retrieval method, the so-called scaling method, which enables the retrieval of trace gas concentrations under all sky conditions. Thereby, the scaling method promises to greatly extend the usefulness of airborne limb spectroscopy. Effective light path lengths are estimated by employing a scaling gas, whose concentration at flight level is known, in conjunction with modelled profile shapes, radiative transfer calculations, and using the measured absorptions of the targeted species relative to those of the scaling gas. The scaling method was applied in a number of studies in the recent past (Raecke, 2013; Großmann, 2014; Werner, 2015; Stutz et al., 2016; Werner et al., 2016; Aderhold, 2016). The present thesis shows for the first time a detailed analysis of random and systematic errors and draws generalised conclusions on the applicability and sensitivity of the method. The strengths and weaknesses of the scaling method are further illustrated by sample results from measurements of two exemplary research flights of the TACTS/ESMVal science mission in August/September 2012.

Chapter 2 elaborates on the scientific questions which motivate the measurements carried out by the HALO mini-DOAS instrument, and gives a brief review of the history of airborne limb-viewing scattered skylight measurements and retrievals. Instrument development, characteristics, and performance are detailed in chapter 3. Chapter 4 describes the particular research flights which are investigated in the present thesis, followed by a description of data processing, spectral retrieval, and simulations in chapter 5. The scaling method and its uncertainties are discussed in chapter 6. The following chapter 7 presents sample results and the work is summarised in chapter 8.

Chapter 2

Background

The following sections illustrate the scientific questions relevant to the HALO mini-DOAS instrument measurements (sect. 2.1) and the hitherto development of the measurement technique of airborne scattered light spectroscopy in the UV/visible wavelength range (sect. 2.2, cf. Platt and Stutz, 2008; Wendisch and Brenguier, 2013). The fundamentals of atmospheric chemistry and physics are omitted here, since the available literature provides plentiful information, e.g. Goody and Yung (1995); Finlayson-Pitts and Pitts (2000); Wallace and Hobbs (2006); Brasseur and Solomon (2006); Roedel and Wagner (2011); Wendisch and Yang (2012); Seinfeld and Pandis (2016).

2.1 Scientific objectives

Measurements undertaken with the HALO mini-DOAS instrument contribute to address a range of scientific objectives (Curtius et al., 2012). The science missions where the HALO mini-DOAS instrument has participated are listed in Table 4.1 on page 42. Main research objectives to which the HALO mini-DOAS instrument measurements may contribute comprise atmospheric oxidation mechanisms, stratospheric ozone depletion and tropospheric ozone production, stratosphere-troposphere exchange (STE), and atmospheric radiative transfer. These research topics are further described in the following sections.

2.1.1 Oxidation mechanisms

Oxidation is the process by which pollutants are removed from the atmosphere, mostly by catalytic cycles involving hydroxyl radicals (HO_x = OH + HO_2) and nitrogen oxides (NO_x = NO + NO_2). NO_x sustaines oxidation through the production of ozone (O_3) and replenishment of OH. Hence, nitrogen oxides are among the most important molecules in atmospheric chemistry. Oxidation of carbon monoxide (CO) and methane (CH_4) dominates in the pristine troposphere. Oxidation of volatile organic compounds (VOCs) is important near their sources due to their much shorter lifetimes

(Wennberg et al., 1998; Jaeglé et al., 2001; Rohrer and Berresheim, 2006; Schumann and Huntrieser, 2007; Nicely et al., 2016). NO_x and VOCs are emitted by natural (soils, biosphere, lightning) as well as anthropogenic (fossil fuel and biomass burning) sources (Finlayson-Pitts and Pitts, 2000). They are removed from the atmosphere by the deposition of reaction products (e.g. HNO_3, N_2O_5, cf. Lelieveld et al., 2008).

Oxidation processes can be monitored by measurements of the HALO mini-DOAS instrument and complimentary instrumentation through the detection of several key species:

- NO_2: The lifetime of NO_x is limited to a few hours near the surface (Beirle et al., 2011) but increases to several days at higher altitudes due to lower temperatures (Seinfeld and Pandis, 2016). It can also be transported to remote regions by reservoir species such as PAN, which thermally decomposes again at lower altitudes releasing NO_x into the remote troposphere (Huntrieser et al., 2005; Fischer et al., 2014). While NO_x mixing ratios of several ten ppb are common close to strong sources, e.g. urban areas (Chate et al., 2014), NO_x mixing ratios rarely exceed 200 ppt in remote environments. In the stratosphere, NO_x mixing ratios increase with altitude due to the NO production from the decay of N_2O. The largest NO_2 mixing ratios of approximately 8 ppb are found at 30 – 35 km altitude at nighttime (Seinfeld and Pandis, 2016). While there are extensive ground-based NO_2 measurements, representative altitude profiles of NO_2 in the remote free troposphere (FT) are sparce. Gomez et al. (2014); Gil-Ojeda et al. (2015); Schreier et al. (2016) show an approach to derive FT profiles from ground-based MAX-DOAS measurements at high altitude mountain sites. Gil-Ojeda et al. (2015) derive $[NO_2] = 20 \pm 20$ ppt during winter and 40 ± 20 ppt during summer for the pristine subtropics in the northern hemisphere. However, such measurements are necessarily constrained to few geographical locations. Others (e.g. Bradshaw et al., 2000; Velders et al., 2001; Kühl et al., 2008; Choi et al., 2014) obtain global NO_2 mixing ratios in the FT from satellite measurements, which are however averaged over large vertical and horizontal distances. Measurements giving more detailed profile information are sparce due to the large effort involved in airborne measurements. Vertical column amounts were measured and compared with model predictions starting in the 1990s (e.g. Glatthor et al., 1998). More recently, airborne NO_2 profile measurements were reported by e.g. Kritten et al. (2010); Volkamer et al. (2015), who sampled air at polar and tropical latitudes, respectively. Airborne science missions investigating NO_x chemistry in the UT/LS such as the SPURT campaign (Hegglin et al., 2006) have so far lacked independent NO_2 measurements. Together with in-situ measurements of O_3, NO, the photolysis frequency J_{NO_2}, and the temperature-dependent coefficient k_{O3+NO} the so-called Leighton ratio

$$\Phi = \frac{J_{NO_2} \cdot [NO_2]}{k_{O3+NO} \cdot [O_3] \cdot [NO]} \tag{2.1}$$

can be used as a proxy of atmospheric oxidation capacity (Leighton, 1961). Leighton ratios significantly greater than unity indicate that peroxy radicals (PO_2), halogen monoxides, nitrate radicals, or some unidentified species convert NO to NO_2 in excess of the reaction between NO and O_3 (e.g. Davis et al., 1993; Carpenter et al., 1998; Griffin et al., 2007). Air masses with Leighton ratios $\Phi > 1$ were encountered during several HALO science missions (influenced by

e.g. biomass burning, combustion, aged megacity plumes, or aircraft emissions). Potential explanations will be addressed in forthcoming studies. For example, as part of the OMO mission (Table 4.1), emissions from South-East Asia, lifted into the free troposphere by the Asian summer monsoon, were detected above the eastern Mediterranean. Measurements by the HALO mini-DOAS instrument indicate elevated concentrations of NO_2 in these air masses (Aderhold, 2016).

- CH_2O (formaldehyde) is a key intermediary in the oxidation chain of hydrocarbons and thus an indicator for the degradation of CH_4 and NMHC (non-methane hydrocarbons)(e.g. Frost et al., 2002; Stavrakou et al., 2009; Heue et al., 2014; De Smedt et al., 2015). During the Acridicon mission, distinct CH_2O concentration profiles in convective air masses over the Amazonian rain forest were detected in pristine and polluted air by the HALO mini-DOAS instrument (Wendisch et al., 2016).

- $C_2H_2O_2$ (glyoxal) is an intermediary in the oxidation chain of many VOCs, such as isoprene (Volkamer et al., 2005; Wittrock et al., 2006; Sinreich et al., 2007), and an indicator of secondary organic aerosol (SOA) formation (Sinreich et al., 2007; Fu et al., 2008; Vrekoussis et al., 2009). There are many unresolved questions about the abundance and sources of glyoxyl in the troposphere (e.g. Mahajan et al., 2014).

- HONO (nitrous acid) is a product of the oxidation of NO with OH, influencing the OH budget and thus oxidation capacity. HONO is rapidly photolysed under daylight conditions but some studies indicate that not all sources are properly understood (Li et al., 2014; Ye et al., 2016; Neuman et al., 2016).

- BrO, IO: The influence of halogens on tropospheric ozone photochemistry is uncertain because of the limited knowledge of halogen oxide concentrations and distributions in the troposphere (Fitzenberger et al., 2000; Roozendael et al., 2002; Platt and Hönninger, 2003; von Glasow et al., 2004; Volkamer et al., 2015; Werner et al., 2016). Some measurements point to a global tropospheric background of up to 1 ppt BrO (e.g. Sinnhuber et al., 2005; Prados-Roman et al., 2011; Theys et al., 2011; Chen et al., 2016) which would have consequences for O_3 and OH chemistry and the oxidation of mercury (Schmidt et al., 2016). Of particular interest are so-called ozone depletion events (ODEs) during Arctic and Antarctic spring, when bromine radicals emitted from sea-ice surfaces lead to a complete depletion of ozone in the lower troposphere, persisting for days and extending over several 100 km (Evans et al., 2003; Salawitch et al., 2010). Iodine radical concentrations may also be elevated in polar spring (Schönhardt et al., 2012).

Oxidation mechanisms were addressed during HALO science missions TACTS/ESMVal, OMO, and Acridicon.

2.1.2 Halogen oxides and stratospheric ozone depletion

Halogen oxides are major drivers of stratospheric ozone depletion, particularly in the polar stratosphere during winter and spring (Solomon, 1999; Douglass et al., 2014; WMO, 2014). Halogenated very short lived substances (VSLS) are also an important source of stratospheric halogens, in particular in the upper troposphere / lower stratosphere (UT/LS) (Butz et al., 2009; Brinckmann et al., 2012; Hossaini et al., 2015; Werner et al., 2016; Hossaini et al., 2016). Major pathways for transporting ozone destroying substances and in particular brominated VSLS into the UT/LS and the extratropical tropopause layer (ExTL) are thought to be the Western Pacific during the convective season, the Asian Monsoon, as well as the quasi isentropic transport across the subtropical jet (Levine et al., 2008; Fueglistaler et al., 2009; Aschmann et al., 2009, 2011; Aschmann and Sinnhuber, 2013; Liang et al., 2014; Orbe et al., 2015).

The short atmospheric lifetime of halogenated VSLS result in their significant potential for affecting extratropical UT/LS ozone and thus radiative forcing (sect. 2.1.4). Recent chemical transport model (CTM) simulations indicate that ozone loss from VSLS had a radiative effect nearly half of that from long-lived halocarbons in 2011 and since pre-industrial times has contributed a total of about -0.02 Wm^{-2} to global radiative forcing (Hossaini et al., 2015). However, these calculations did not consider the effect of inorganic bromine directly transported into the lowermost stratosphere on ozone concentrations. Evidence for the latter contribution to stratospheric bromine mostly came through simultaneous balloon-borne and airborne measurements of total organic and inorganic species in the stratosphere (Pfeilsticker et al., 2000; Dorf et al., 2008; Laube et al., 2008; Brinckmann et al., 2012; Sala et al., 2014; WMO, 2014) and more recently by measurements of the inorganic bromine budget in the tropical tropopause layer (TTL, Fueglistaler et al., 2009) over the eastern Pacific (Werner et al., 2016). While the former studies indicated a range of 0 — 5 ppt (WMO, 2014) for the inorganic bromine mostly entrained from the tropical troposphere into the stratosphere, the latter most recent study could establish a smaller range (2.63 $\pm$ 1.04 ppt) (Werner et al., 2016). However, it is still unclear how transport processes contribute to the inorganic bromine budget either by direct injection of inorganic bromine species from the troposphere or by injection of brominated VSLS.

A contribution of iodine to stratospheric ozone depletion was predicted in the 1990s (Solomon et al., 1994) and mixing ratios of 0.1 to 0.2 ppt of total reactive iodine were later measured in the lower stratosphere (Bösch et al., 2003; Butz et al., 2009). More recent publications argue that ozone depletion by iodine radicals may be underestimated in the stratosphere (Saiz-Lopez et al., 2015) as well as in the troposphere (Dix et al., 2013).

Examining stratospheric ozone depletion was the main focus of the Polstracc mission in winter 2015/16, including in particular testing the reaction ClO + BrO (Canty et al., 2005; Frieler et al., 2006; Butz et al., 2007). To that end, measurements of BrO and OClO by the HALO mini-DOAS instrument play an important part.

2.1.3 Stratosphere - troposphere exchange

The tropopause is a physical barrier for the exchange of air masses between troposphere and stratosphere due to the reversal of the atmospheric temperature profile. Nevertheless, several transition layers and transport processes across the tropopause have been identified (Holton et al., 1995; Fueglistaler et al., 2009; Birner and Bönisch, 2011). The extratropical UT/LS, polewards of the subtropical jets, is composed of air transported downwards by the Brewer-Dobson-Circulation (Bönisch et al., 2011) from the deeper stratosphere, as well as younger air of tropospheric origin (Gettelman et al., 2011). Lower tropospheric air is often lifted to higher altitudes by planetary waves and large scale meteorological systems (e.g. the high pressure system at the western side of the Asian monsoon, see Vogel et al., 2014, 2015; Orbe et al., 2015; Müller et al., 2016). Subsequent transport pathways into the extratropical lowermost stratosphere include isentropic transport above the subtropical jets and in-mixing of higher latitude upper tropospheric air by Rossby wave breaking (Randel et al., 1993; Riese et al., 2002; Vogel et al., 2011). Both processes, their magnitude, seasonality, and signatures of chemical composition are subjects of current research (Riese et al., 2014). Transport processes are often studied through tracer-tracer correlations (e.g. Jurkat et al., 2014; Vogel et al., 2015), such as the relative abundances of "stratospheric tracers" ($O_3, NO_x, ...$) and "tropospheric tracers" ($N_2O, CO, CH_4, ...$), and measurements by the HALO mini-DOAS instrument can complement the in-situ measured tracers.

In the tropics, moist and hot air ascends through the TTL, the "gate" to the stratosphere (Fueglistaler et al., 2009). Airborne measurements with similar instruments like the HALO mini-DOAS instrument have been carried out in the western Pacific at lower altitudes (2-12 km, Sala et al., 2014) and higher altitudes (14-19 km, Werner et al., 2016) than those typical of HALO research flights (11-15 km). The HALO mini-DOAS instrument can close the observational gap with respect to e.g. the photochemistry and budget of NO_x and NO_y ($= NO_x + HONO, HNO_3, N_2O_5, HO_2NO_2, ClONO_2$) (Ziereis et al., 2000; Huntrieser et al., 2002; Ott et al., 2007), and bromine compounds (Werner et al., 2016).

Stratosphere-troposphere exchange (STE) was one focus of the TACTS/ESMVal mission but relevant air masses were also sampled during OMO, Acridicon, and Polstracc.

2.1.4 Radiative transfer

Composition changes in the UT/LS region significantly influence surface climate (Solomon et al., 2010; Riese et al., 2012). Small changes in the amounts of greenhouse gases like water vapour (H_2O) and ozone, which exhibit strong gradients across the tropopause, as well as properties of aerosols and (subvisible) cirrus clouds change the radiative balance and influence each other (Gettelman et al., 2004).

In addition to monitoring UT/LS chemistry, limb sounding in the near-infrared can provide information on (sub-visible) cirrus cloud abundance and properties. Cirrus clouds are influenced by water vapour transport from the troposphere into the lowermost stratosphere (LMS) and in turn strongly influence the radiation budget of the UT/LS (Stocker et al., 2013; Riese et al., 2014). Their influence on the Earth's total radiation budget depends on their microphysical properties such as ice crystal number, size and shape (Zhang et al., 1999; Wendisch et al., 2005, 2007), which is not well understood to date. Sub-visible cirrus (SVC), which are optically very thin (optical depth $\tau < 0.03$), are of particular interest. They are difficult to observe but probably extend over large areas (Davis et al., 2010).

Measurements in limb are better suited than nadir geometry to investigate cirrus clouds of low optical depth because of longer light path lengths through the cloud layers (Spang et al., 2012). Measurements by the HALO mini-DOAS instrument during the ML-CIRRUS and Acridicon missions show promising comparability of retrieved cloud parameters with the absolute calibrated measurements of nadir radiances by Wolf et al. (2016).

2.2 History of airborne UV/vis skylight measurements

Based on the pioneering work of Noxon (1975) and later Noxon et al. (1979) to exploit ground-based spectroscopic observations of the zenith scattered skylight to monitor stratospheric NO_2 (and later O_3, BrO and OClO), UV/visible absorption spectroscopy was later als0 deployed on research aircraft, e.g. the NASA DC-8 during Airborne Arctic Stratospheric Expedition (AASE) in 1989 (e.g., Wahner et al. (1990a), Schiller et al. (1990), and Wahner et al. (1990b)) and later on the German Transall (Brandtjen et al., 1994; Pfeilsticker and Platt, 1994; Pfeilsticker et al., 1997a, 1999). The instruments were however limited to one line of sight and lacked proper attitude control. McElroy et al. (1999) were the first to exploit aircraft-borne nadir scattered skylight measurements to study plumes of BrO in the lower troposphere during arctic spring. Wagner et al. (2001a) developed an aircraft-borne multi-axis DOAS instrument with a fixed, limited set of elevation angles for the purpose of satellite validation and reported tropospheric NO_2 measurements, retrieving boundary layer column amounts by making use of the wavelength dependency of radiative transfer due to Rayleigh scattering (Wang et al., 2005, 2006). Later measurements by Bruns et al. (2006) over Europe and on major air traffic corridors by Dix et al. (2009) within the CARIBIC[1] project were used to gain information on the distribution and photochemistry of pollutants and their products within the troposphere (Heue et al.,

[1] http://www.caribic-atmospheric.com/

2014). Melamed et al. (2003), Merlaud et al. (2011), Merlaud et al. (2012), and Berg et al. (2012) used DOAS instruments on very light aircraft, allowing measurements inside or just above the boundary layer. Meanwhile more versatile DOAS-based 2-D imaging Nadir techniques have become available to monitor the ground for sources and sinks of UV/visible/and near-IR absorbing radicals, pollutants and their products and green-house gases (Heue et al., 2008; Gerilowski et al., 2011; General et al., 2014; Schönhardt et al., 2015). ol Airborne UV/vis measurements in limb geometry began with the balloon-borne study of Weidner et al. (2005), which aimed at studies of the photochemistry, budgets, and trends of the NO_x and BrO_x families in the stratosphere (Dorf et al., 2006b; Kritten et al., 2010; Kreycy et al., 2013; Kritten et al., 2014). The airborne limb measurements of scattered skylight continued with the aircraft studies of Prados-Roman et al. (2011) from aboard the DLR Falcon, and more recently from the American High-performance Instrumented Airborne Platform for Environmental Research (GV HIAPER) aircraft (Baidar et al., 2013; Volkamer et al., 2015), the NSF/NCAR C-130 (Gratz et al., 2015; Ye et al., 2016), the NASA Global Hawk (Stutz et al., 2016; Werner et al., 2016), and those reported here from the German GV aircraft HALO (Wendisch et al., 2016; Voigt et al., 2016).

Common between all these airborne UV/vis limb measurements is the need for a stable observation geometry (or pointing) of the desired line of sight (required are a few tenth of a degree). Therefore all modern airborne UV/Vis spectrometers collect skylight with actively controlled telescopes to compensate for the movements (i.e. the roll and pitch angle) of the airborne measurement platform. Ideally the attitude data to control the telescope's pointing are provided by the inertial navigation system (INS) of the aircraft or by custom built stabilizing systems (e.g. Baidar et al., 2013).

Potentially the largest problem that must be addressed for UV/vis limb measurements is the inherent inversion problem of assigning the correct trace gas concentrations to the right altitudes in the atmosphere (Rodgers, 2000). Bruns et al. (2004) published a concise treatment of the optimal estimation profile retrieval for measurements obtained from several telescope elevation angles (EAs) relative to the limb from an airborne platform. They later expanded the method by including several different wavelength ranges at each EA (Bruns et al., 2006). The retrieval method was further developed for balloon-borne measurements in the stratosphere by Kritten et al. (2010) who used a time-dependent inversion scheme. However, this is only possible if the change of the light path distribution with time is known sufficiently well.

Unfortunately, under conditions of heavy aerosol loading and/or a cloudy atmosphere, light paths (or light path distributions) are not well defined due to multiple scattering of collected skylight and the a priori unknown spatial distribution of the scatterers. Sample light paths are illustrated in Figure 2.1, underscoring the complexity of light path estimates under these conditions. The inversion problem becomes almost intractable when the radiative transfer forward model is not constrained by additional means, including parameters like aircraft and telescope attitude, celestial, and atmospheric data (i.e. the aerosol and cloud distribution taken from in-situ aerosol measurements, lidar or radar observations, model predictions, et cetera). Thus, most retrievals of UV/visible limb measurements from fast-moving aircraft platforms have until recently been limited to few selected flight sections with clear sky conditions (e.g. Dix et al., 2009; Prados-Roman et al., 2011; Volkamer et al., 2015).

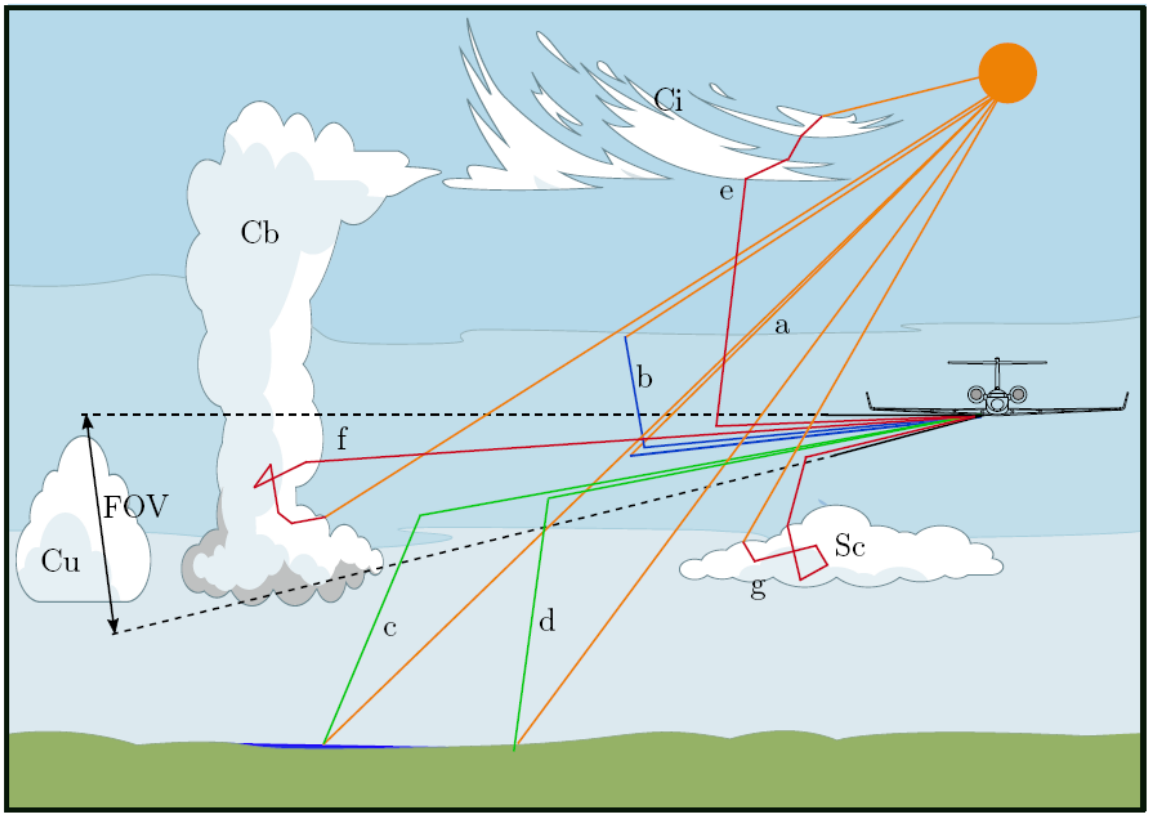

Figure 2.1: Sample light paths and processes contributing to airborne DOAS measurements in limb geometry for a range of typical atmospheric conditions. Single scattering on gas molecules or on aerosol occurs in case of light path a. Radiation along the light path b is scattered multiple times before reaching the telescope. Reflection at a land and a water surface happen for light path c and d respectively before they are scattered into the telescope. Light path e traverses a Ci cloud. The length of the light path f is enhanced in a large Cb cloud or an extended cloud layer. Sc clouds may shield gaseous constituents in the boundary layer from being observed by an airborne instrument above the Sc clouds (light path g). Adopted from Knecht (2015).

The employed retrieval strategies often rely on constraining the radiative transfer from simultaneous measurements of the absorption bands of the O_2 collisional complex (O_4) or relative radiances, or a combination of both. This method comes with a number of problems when the optical state of the atmosphere changes fast during or between measurements. In order to render the interpretation of airborne UV/vis limb measurements more feasible for all skies, in particular for measurements from fast-moving platforms in partly clouded skies, we recently developed the so-called scaling method (Raecke, 2013; Großmann, 2014; Knecht, 2015; Aderhold, 2016; Werner, 2015; Stutz et al., 2016; Werner et al., 2016). The scaling method makes use of the concentration of a scaling gas, either in-situ measured (e.g. O_3) or calculated (e.g. O_4), which is used together with simultaneous remote sensing of the scaling gas and the targeted gases. The in-situ measured concentration and the remotely observed absorption of the scaling gas are used to infer an effective light path length. However, the relative profile shapes of target and scaling gas need to be taken into account, because radiative transfer (RT) simulations show their importance for estimating effective light path lengths (Knecht, 2015). One draw-back of the scaling method is the resulting (moderate) sensitivity towards the relative profiles shapes (but not absolute concentrations) of the involved gases. The sensitivity can best be dealt with by using a scaling gas with a similar profile shape to that of the target gas. The relative profile shapes of both gases are then often obtained from either in-situ measurements performed during dives of the aerial vehicle and/or from chemical transport models (CTMs, e.g. CLaMS, EMAC, SLIMCAT, ChemCam). The latter is very convenient since the measurements are often used together with the other complementary measurements performed on board the research aircraft to validate the predictions of the respective CTMs.

Previous studies (Raecke, 2013; Großmann, 2014; Werner, 2015; Aderhold, 2016; Stutz et al., 2016; Werner et al., 2016) used either O_3 or O_4 as the scaling gas and estimated the uncertainty of the inferred trace gas concentrations by carrying out large numbers of sensitivity studies for individual measurements. The present thesis outlines a more generalised approach. Random and systematic errors are distiguished and generalised expressions for all contributions to the random error are derived. Thus, the uncertainty of an inferred trace gas concentration is calculated without the need for individual sensitivity studies. Furthermore, systematic errors are examined by comparing model-predicted and measured trace gas concentrations and conclusions regarding the potential bias of inferred trace gas concentrations are drawn. Additionally, the influence of low altitude cloud layers on O_3 and O_4 scaling is compared and the applicability of O_3 and O_4 scaling is examined. Thus, the present thesis constitutes a major contribution to the development and application of the novel scaling method with the aim to retrieve trace gas concentrations from airborne UV/vis limb spectroscopy measurements under all sky conditions.

Chapter 3

Instrument

The HALO mini-DOAS instrument (from here on shortly called HALO mini-DOAS instrument) and its technical features and modifications have previously been described by Raecke (2010), Hüneke (2011), Kenntner (2013), Schulte (2013), Reichert (2014), Weimar (2014), and Bounin (2015). Therefore, only a brief overview of major features of the HALO mini-DOAS instrument is given in this chapter. Section 3.1 describes the design and section 3.2 discusses major instrument properties.

3.1 Instrument design

Section 3.1.1 gives an overview of the HALO mini-DOAS instrument purpose and general design, and section 3.1.5 lists the major upgrades and modifications made within the timeframe of the present thesis. Optical and electronical features are described in sections 3.1.2 and 3.1.3, respectively, and section 3.1.4 explains the software applications developed for calibration, measurement and command and control of the HALO mini-DOAS instrument.

3.1.1 Overview

The purpose of the HALO mini-DOAS instrument is to collect and analyse atmospheric straylight in the UV, visible and near-IR wavelength ranges in two viewing geometries, nadir and limb. In order to clearly identify each of the six channels, the convention has been adopted to use odd numbers for the nadir channels (UV1, VIS3, NIR5) and even numbers for the limb channels (UV2, VIS4, NIR6). The skylight is collected by a separate telescope for each channel and guided to separate grating spectrometers, where its spectral irradiance[1] is recorded. This data is stored as spectra on a flash drive. The spectra are later analysed using the Differential Optical Absorption Spectrscopy (DOAS, Platt and Stutz, 2008) technique (sect. 5.2). The HALO mini-DOAS instrument is mounted in the

[1] By definition, the telescopes "integrate" over a certain solid angle and thus an *irradiance* is recorded by the detector. Nevertheless, when considering normalised values the term *radiance* is used out of convention.

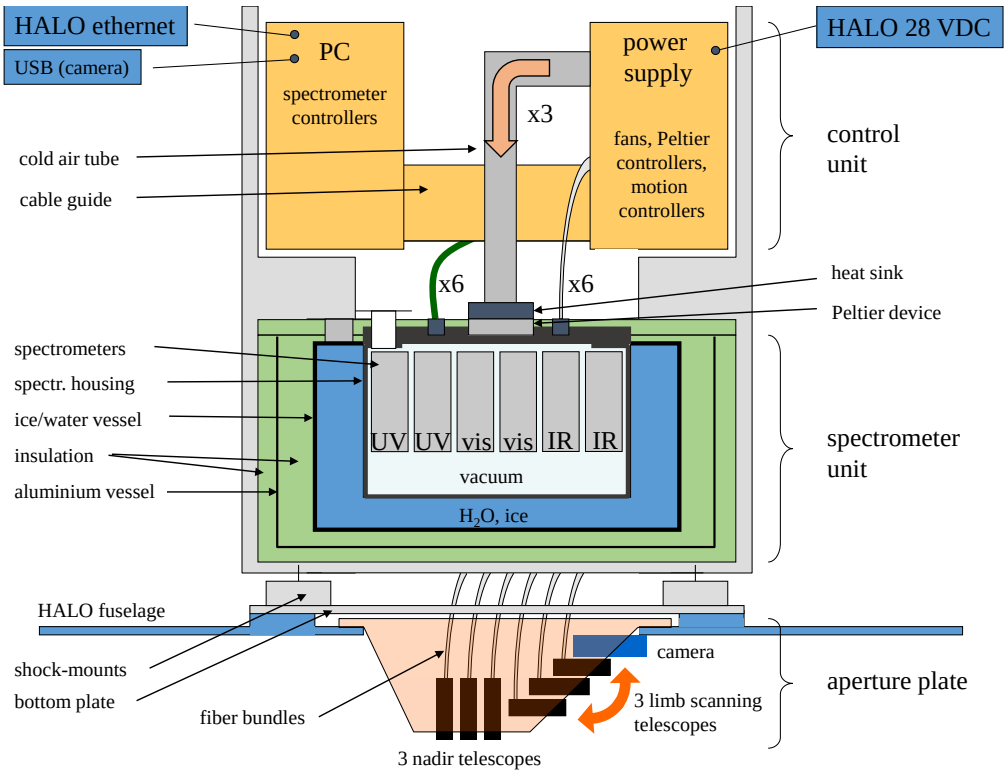

Figure 3.1: Sketch of the HALO mini-DOAS instrumentwith the control unit (top, yellow), spectrometer unit (center, green and blue), and aperture plate (bottom, orange).

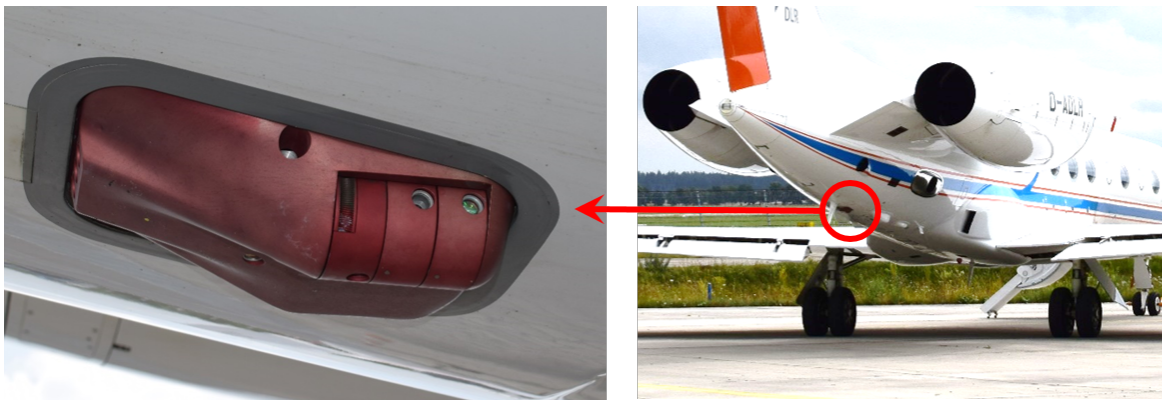

Figure 3.2: Image of the aperture plate mounted in the aircraft fuselage. The limb telescopes are pointing in starboard direction, perpendicular to the aircraft's main axis.

so-called position 21 of the aircraft fuselage, which is located in the unpressurised boiler room of the HALO aircraft (Figure 3.2). An image of the rack mounted in the boiler room is shown in Figure A.1. The boiler room houses parts of the cabin air conditioning as well as hydraulics, avionics and other vital appliances. The HALO mini-DOAS instrument is designed in such a way that changing ambient temperatures and pressures should exert a mininal influence on its optical characteristics. The instrument has a total operating weight of 58 kg, including 7 kg ice/water. The principle components of the HALO mini-DOAS instrument are shown in Figure 3.1 and consist of three main parts:

1. The **control unit** containing an industrial computer (Bressner AA BT-6831, 1.6 GHz CPU, 1 GB RAM) for storage of the measurement data (16 GB industrial flash drive) and communication with the on-board network and operator; motion controllers (Faulhaber MCBL 3006S) to control the motors (Faulhaber DC 2057S024B) in the aperture plate; a controller (Supercool) for the Peltier elements; and a DC/DC power supply (150 W) for all components. Additionally, fans in the control unit ventilate the heat sinks of the Peltier elements with ambient air.

2. The **spectrometer unit** accomodates a well-insulated ice-water vessel, surrounding an evacuated aluminum container which houses the six spectrometers (Figure A.4). The spectrometers are mounted onto the housing lid. Each is fed via vacuum tight fibre bundles with the collected skylight and via wire connectors (LEMO) with power and control signals. Additionally, the spectrometer lid is cooled by six Peltier elements (PEs).

3. The **aperture plate** houses three nadir telescopes, three limb telescopes and a camera to monitor the sky in limb direction. The angle of the limb telescopes are controlled individually by three step-motion motors (Figures A.2 and A.3).

3.1.2 Optics

The atmospheric straylight is collected by six telescopes. The collimating lenses of the telescopes have a diameter of 12 mm and a focal length of 30 mm, and each lense is selected in order to achieve maximum transmittance in the respectively targeted wavelength range. The solid angle from which the atmospheric light is sampled is called the field of view (FOV), and is further characterised in section 3.2.5. The light collected by the telescopes' lenses passes through optical filters to minimise spectrometer straylight from outside of the targeted wavelength band (out-of-band straylight, section 3.2.2). It is coupled into 1.5 m long fibre bundles, where the glass fibres at each end are aligned in a row of seven (UV/vis) or two (near-IR) fibres, respectively. The row of fibres at the spectrometer end illuminate the entrance slit of the spectrometers. The spectrometers are arranged in a Czerny-Turner type configuration, and their imaging is characterised by the so-called slit function (section 3.2.4). The properties of the optical components are summarised in Table 3.1.

Table 3.1: Specifications of the HALO mini-DOAS instrument optics and detector electronics.

Parameter	**UV**	**VIS**	**NIR**	**Notes**
Lens type	UV-AR	VIS 0°	NIR II	Edmund Optics
Lens focal length	30 mm			
Lens diameter	12 mm			
Filter type	BG3	GG400	RG1000	Schott
Fibre type	UVVIS AS200/210		VISIR AS400/480	LEONI / Fibertech
No. of fibres per bundle	7		2	
Fibre diameter	200 μm		400 μm	
Fibre bundle width	1652 μm		884 μm	
Field of view	3.15°x 0.38°		1.68°x 0.76°	Hüneke (2011) and sect. 3.2.5
Fibre bundle length	1.5 m			
Fibre bundle NA	0.22			
Spectrometer type	ctf-60			OMT
Wavelength range	310 - 440 nm	416 - 640 nm	1095 - 1680 nm	Section 3.2.3
Spectr. focal length	60 mm			
Spectr. f/#	f/4			
Slit width	100 μm			
Slit height	1500 μm		500 μm	
Grating constant	2100 / mm	1300 / mm	300 / mm	
Blend insert	Yes		No	Hüneke (2011)
Detector type	Si-CCD		InGaAs-PDA	
Detector model	S10141-1107S		G9204-512	Hamamatsu
No. of channels	2048		512	
No. of pixels	2048 x 124		512	
Pixel area	12 x 12 μm^2		25 x 500 μm^2	
Channel area	12 x 1464 μm^2		25 x 500 μm^2	
Active sensor area	24.576 x 1.464 mm^2		12.8 x 0.5 mm^2	
Full Well Capacity	2 x 10^5 e^-		1.87 x 10^8 e^-	
A/D converter	16 bit			
Quantum efficiency	0.6	0.85	0.8	typical values

3.1.3 Electronics

The design and set-up of the major components is illustrated in Figure 3.3. The instrument is supplied by the aircraft with 28 VDC (direct current). This is converted and stabilised to 24 VDC by the main DC/DC, which supplies the Peltier element (PE) controllers and the computer. It is further converted to 12 VDC to supply the spectrometer controllers. The PE current is supplied by the PE controller, which can be accessed from the computer. The computer constantly receives attitude data via the aircraft's BAHAMAS system and the telescopes are actively controlled to compensate for the aircraft's roll angle (see sections 3.1.4 and 3.2.6). The total power consumption of the instrument is 100-200 W, depending on the power consumption of the Peltier elements. The detector properties are summarised in Table 3.1.

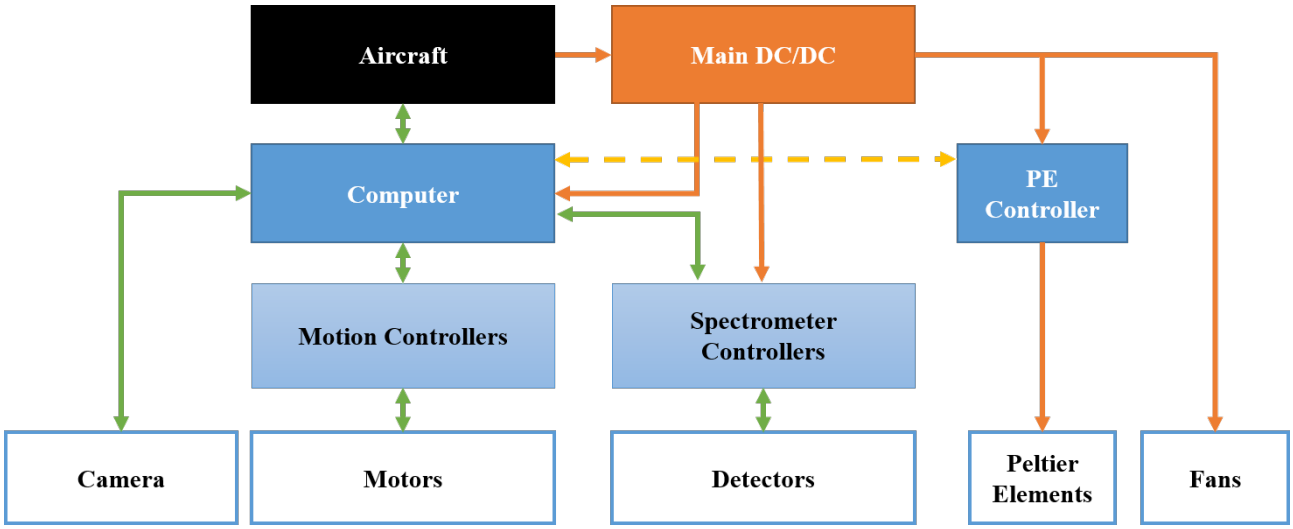

Figure 3.3: Sketch of the instrument's major electronic components. Red: Power supply, Green: Command and control, Yellow: Access possible if needed.

3.1.4 Software

The instrument is controlled by four main software tools custom-made on a LabView platform. In addition, several tools are provided by producers of industrial components (e.g. Supercool, Faulhaber, KHS electronics).

3.1.4.1 Calibration

The calibration software is designed for laboratory measurements as well as calibration measurements during field deployments. Starting the software does not automatically load any scripts or activate any parts of the instrument. It is sub-divided into three parts (Figure A.5) - a main screen at the top showing recorded spectra, a comments section at the left to save notes during the measurements and several panels in the lower part of the screen. These contain the following functionalities:

1. **Manual Command** allows to manually set the exposure time and number of readouts for each detector and start a single or sequential readout.

2. **Offset and DC** supports calibration measurements of offset and dark current for several or all detectors simultaneously, in order to enable quick calibration measurements during a science mission, i.e. during the flight preparation procedures.

3. **FOV** starts a script that automatically scans through a given set of elevation angles and reads out the maximum intensity recorded in the channel range selected in the top screen. This feature can be used to

   - record a field of view (FOV) of a given telescope (section 3.2.5), or
   - determine the horizontal viewing direction when the aperture plate is installed aboard the aircraft (section 3.2.6).

4. **Noise** activates measurements to determine the relative and absolute noise of measured spectra of each detector (section 3.2.8).

5. **Cooling** enables the temperature read-out and control of the six detector internal Peltier elements.

6. **Motors** enable the manual control of the three limb scanning motors. The motors can either be commanded to move to a certain position, or to move into a certain direction.

3.1.4.2 Measurement

The measurement software is designed for data acquisition during measurement flights. When started, it automatically imports a measurement script (or configuration file) and initilises variables according to the given parameters. A typical measurement script is shown in appendix A.2. The control parameters less obvious to understand are explained in Table A.1. An overview of all routines in the software is given in Table 3.2. The routines are running simultaneously and access a common set of global variables.

The **Motors** routine reads the currently targeted elevation angle and moves the motor towards the target angle. If the target angle is reached (within the tolerance given in the script), the routine sets a variable such that the **Spect** routine starts to add up readouts in order to record a spectrum. When a complete spectrum is recorded, either because the maximum number of readouts or the maximum integration time is reached, then the targeted elevation angle is set to the next preset angle (if scanning is enabled) and the process starts again. The targeted elevation angles are the result of the elevation angles set in the measurement script, constantly corrected for the roll angle of the aircraft by the **QDS** routine. Therefore the elevation angle is also constantly corrected during spectrum integration, which is very important given typical integration times of 30 s and typical aircraft roll rates of 0.2 degree/s (Figure A.8).

Table 3.2: Independently running routines of the measurement software.

Routine	**Purpose**	**Frequency**
Spect	Detector control and readout	Depending on exposure times
Motors	Motor control and command	10 Hz
QDS	Readout of BAHAMAS quicklook data stream	10 Hz
Sender	Send status data to operator and *Planet* system	1 Hz
Receiver	Receive commands from operator	1 Hz
Logfile	Write logfile with status (housekeeping) data	1 Hz

The most time consuming process of all routines is the communication with the detector electronics, because the driver software can only communicate with one of the six detectors at any given time. Therefore, the **Spect** routine anticipates from the exposure times, when the data from a certain detector will be available. Thus detectors with low exposure times are polled more often than detectors with high exposure times, and the driver usage is minimised. After each readout, the spectrum is further checked for saturation. If the saturation level (maximum irradiance in the spectrum) is above or below the range targeted in the script, the exposure time is changed accordingly, and from the following readouts a number of so-called "dummy scans" is discarded. The latter is necessary in order to prevent the recording of spectra while the detector-internal clocking signal is being reset. If the spectrum is oversaturated, the spectrum is also discarded.

After startup, the **QDS** routine sets up the communication with the HALO quicklook data stream, which is an UPD stream sent from BAHAMAS over the on-board ethernet. The process involves three steps:

1. Listening at the UDP InfoPort for a string that contains the address and port of the InfoServer.
2. Reading the XML-File from the InfoServer and interprete it. The XML-File contains the format, port numbers and channel IDs of the data in the QDS.
3. Opening UDP connections for the relevant ports identified from the XML-File, and start to receive and interprete the QDS data.

The **Sender** routine sends status data via UDP from global variables to the Operator-IP given in the script. It also sends data to the *Planet* system installed on board the aircraft, which provides a downlink via satellite communication. Thereby, basic housekeeping data like spectrometer temperatures and exposure times can be observed in real time from operators on the ground, who can advise the cabin operator during the flight via chat massages.

3.1.4.3 Operator interface

In typical science mission modifications 10-20 scientific instruments are accomodated on board the HALO aircraft, which are operated by 4-6 operators. It is therefore necessary to design an operator

interface that is easy to understand and gives a quick overview over the most critical parameters during data acquisition. The current operator interface (Figure A.6) enables the operator to control the following parameters:

- detector data acquisition, exposure times and temperatures,
- motor positions and roll angle correction,
- QDS stream functionality,
- and measurement software routine functionality.

The operator interface also enables the operator to enable or disable the scanning of elevation angles and the roll correction, or to move all telescopes into nadir position for comparison with other nadir looking instruments.

3.1.4.4 Camera

The camera software reads images from the camera mounted into the aperture plate and saves them on the computer flash drive with a time stamp for later reference. The typical image recording frequency is 1 Hz.

3.1.5 Instrument modifications and upgrades

Based on the operational experience gained during the first science missions, the HALO mini-DOAS instrument has been subsequently upgraded several times to improve its operational and optical stability:

- In **Oktober / November 2012**, after the TACTS/ESMVal science mission, the thermal insulation was improved by employing va-Q-vip panels (section 3.2.7), adding insulating buffers to the mounts that fix the spectrometer unit in the rack and to the mounts of the spectrometers inside the spectrometer unit.
- In **June / July 2013**, the LEMO data connectors on the lid of the spectrometer housing were exchanged to improve their stability and Peltier elements and heat sinks were installed to reverse the flow of heat from the outside into the spectrometer unit. Fans were installed into the control unit to improve the airflow through the heat sinks. Further improvements were made inside the spectrometer unit to lower the heat resistance between the spectrometers and the ice/water vessel.
- In **February 2014**, after the Narval science mission, a shielding was added on top of the rack in order to avoid radiative heating by aircraft appliances above the HALO mini-DOAS instrument.

The insulating foam was replaced by a type more robust and durable under ambient pressure changes.

- In **June 2015**, before the OMO-Asia science mission, the coupling of the fibre bundles into the spectrometers was improved, in order to increase the temperature stability of the slit function (sect. 3.2.4 and Bounin (2015)).

3.2 Characterisation and performance

DOAS measurements required a stable and thoroughly charaterized instrument (Platt and Stutz, 2008). This includes offset and dark-current (sect. 3.2.1), instrument straylight (3.2.2), channel to wavelength mapping (sect. 3.2.3), slit function (sect. 3.2.4), field of view (sect. 3.2.5), pointing (sect. 3.2.6), temperature stability (sect. 3.2.7), and noise characteristics (sect. 3.2.8).

3.2.1 Offset and DC

The spectra are recorded by CCD (UV/visible) and PDA (near-IR) detectors, where offset and dark current have to be considered. The offset is an electronic signal (e.g. an analogue voltage or current) which is added to the photon induced signal of each pixel for every exposure, because the AD-converter can not convert a negative input. The dark current is caused by thermally excited electrons which pass the semiconductor band gap due to Boltzmann statistics. Offset and dark current of the detectors as a function of temperature were previously studied by Raecke (2010), Hüneke (2011), and Schulte (2013). Most recently, Bounin (2015) measured the temperature dependency of the dark current for all channels of all detectors and suggested a temperature dependent dark current correction for all measured spectra. However, tests showed that this does not significantly change the resulting slant columns or the signal to noise ratio of the DOAS fit (see section 5.2; Dominique Loerks, pers. comm.).

3.2.2 Instrument straylight

Straylight within spectrometers can occur due to e.g. reflection of optical elements and reflection of unused diffraction orders or unused portions of the spectrum onto the detector (Pribram and Penchina, 1968; Pierson and Goldstein, 1989). The spectrometers originally delivered by OMT had a significant problem with spectrometer straylight, because there were no screens inside the spectrometers. As a result, the 0th and 2nd scattering orders were reflected onto the detector by surfaces inside the spectrometer housing (*in-band straylight*) and near-infrared light was also detected (*out-of-band straylight*). Accordingly, custom made screens were developed for each spectrometer, as described in Hüneke (2011). A significant reduction of straylight was achieved. Tests in the laboratory using a

halogen lamp showed a reduction of spectrometer straylight from around 10% without screens to between 0.5% and 4% in the UV and <0.1% in the VIS spectrometers. In the case of analysing scattered sun light, the irradiance of near-infrared light relative to the UV/VIS is much lower than in the case of a halogen lamp. Therefore it can be expected that the amount of out-of-band straylight decreases and hence the spectrometer straylight in recorded atmospheric spectra is likely much smaller than in lab measurements.

3.2.3 Channel to wavelength mapping

With changing temperatures, the channel to wavelength mapping of any real spectrometer changes due to thermally induced distortion of the spectrometer housing. This thermally-induced distortion is particularly important for spectrometers of small f numbers. It should however not change the imaging properties, if the spectrum is not undersampled (compare section 3.2.4). Because of the potential impact of a changing wavelength mapping on the measurement result, several approaches were compared by Weimar (2014):

- All measurements were calibrated with a single calibration polynomial obtained from a calibration lamp spectrum recorded before or after the measurement flight. A 2nd degree polynomial was fitted to the known wavelength of the lamp emission lines to obtain the channel to wavelength mapping.
- An improved lamp calibration, where the temperature dependency of the channel to wavelength mapping is measured in the laboratory and then applied to field measurement spectra according to their temperature.
- A calibration algorithm, which derives the wavelength information from a least squares fit of each measurement spectrum to a literature Fraunhofer spectrum (Platt and Stutz, 2008).

Weimar (2014) found the simple lamp calibration to be sufficient for the DOAS evaluation, because spectral shifts between the package of the trace gas reference spectra and the measured spectra are allowed in the evaluation process (sect. 5.2). The other approaches do not significantly improve the retrieval result or the residual. Typical channel to wavelength calibration coefficients and the resulting wavelength ranges for a cooled instrument are given in Table 3.3.

3.2.4 Slit function and resolution

The *slit function*, more accurately termed *point spread function* (Schnierle, 2014), defines the imaging property of a spectrometer. It is the response of an imaging system to a point source. It is often wavelength dependent and, because of thermally induced distortion of the spectrometer casing and entrance slit T-dependent. Since the natural widths of emission lines of gases like Hg, Ne, Kr are of the order of pm, they can be considered a point source in wavelength space (e.g. Sansonetti et al.,

Table 3.3: Typical detector channel to wavelength calibration coefficients and resulting wavelength ranges recorded by each of the detectors. Here, $\lambda = A + B \cdot ch + C \cdot ch^2$ and the channel ch is 0 ... 2044 for the CCDs and 0 ... 511 for the PDAs, respectively.

Detector	**A** (nm)	**B** (nm/ch)	**C** (nm/ch^2)	**Spectral range [nm]**
UV1	310.20	0.0776	7E-6	310.2 - 439.4
UV2	310.66	0.0773	7E-6	310.7 - 439.2
VIS3	416.33	0.1307	1E-5	416.3 - 639.4
VIS4	417.28	0.1295	1E-5	417.3 - 639.6
NIR5	1095.32	1.1475	-9E-6	1095.3 - 1679.4
NIR6	1088.1521	1.2202	-6E-8	1088.2 - 1711.7

Table 3.4: Spectral resolutions of spectrometers UV2 and VIS4 in a cooled instrument. UV2: 405 nm Hg line. VIS4: 587 nm Kr line. The UV2 spectrometer was not operational during Acridicon. The science missions are listed in Table 4.1.

Mission	**UV2**		**VIS4**	
	FWHM [nm]	FWHM [ch]	FWHM [nm]	FWHM [ch]
TACTS/ESMVal	0.48	6.3	0.75	5.8
Narval	0.48	6.2	1.50	11.6
ML-Cirrus	0.73	9.4	1.42	11.0
Acridicon	n.a.	n.a.	1.46	11.3
OMO	0.47	6.1	1.09	8.4

1996). Figure 3.5 shows the image of the 587 nm Kr line recorded by the VIS4 spectrometer in several HALO science missions. Evidently, the slit function is very sensible to how the fibre bundle is mounted to the spectrometer entrance slit. As a measure of wavelength resolution, the FWHMs of the VIS4 and UV2 spectrometers for different science missions are given in Table 3.4. The widths are generally larger than 5 channels, thus the lines are all well sampled (cf. Roscoe et al., 1996; Chance et al., 2005).

The slit function of the UV1 spectrometer and its temperature dependency were thoroughly investigated by Bounin (2015) for two different configurations (Acridicon and OMO). Due to a new fibre bundle mounting, the resolution and its temperature dependency were significantly improved in June 2015 (fig. 3.4). Over a temperature range of nearly 20 K, the spectral shift was reduced by one order of magnitude. The spectral resolution was improved by 30% and its temperature dependency by 80%. This also significantly reduced the temperature dependency of the DOAS fit result and the residual (Bounin, 2015). The width of the slit function is most sensitive at low temperatures, with a sensitivity of 0.005 nm/K (0.04 channels/K). Depending on flight conditions, spectrometer temperatures change during the flight by amounts of 0.1 K for stable flights and up to several K for instable flights (section 3.2.7).

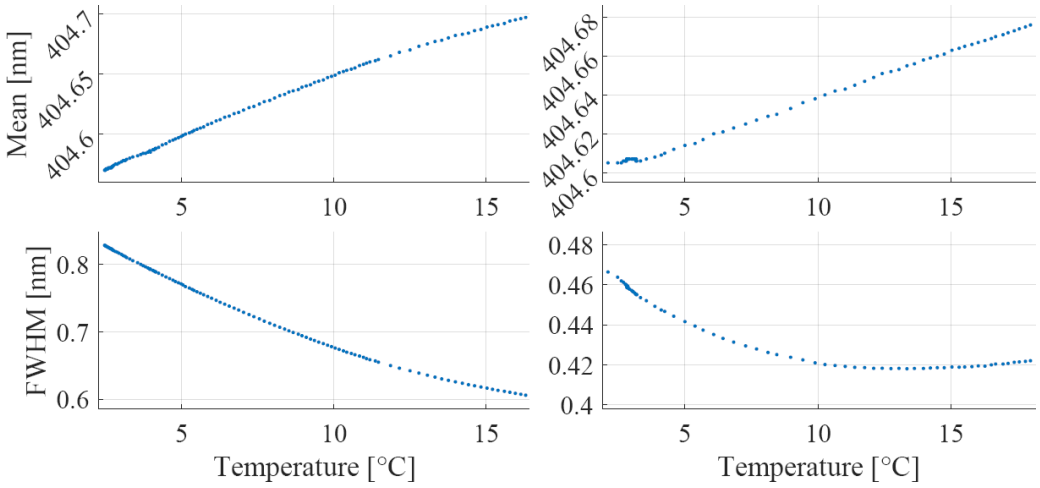

Figure 3.4: Temperature dependency of the center wavelength position and full width at half maximum (FWHM) of the 405 nm Hg emission line measured by the UV1 spectrometer before (left panels) and after (right panels) the modifications in June 2015. Adopted from Bounin (2015).

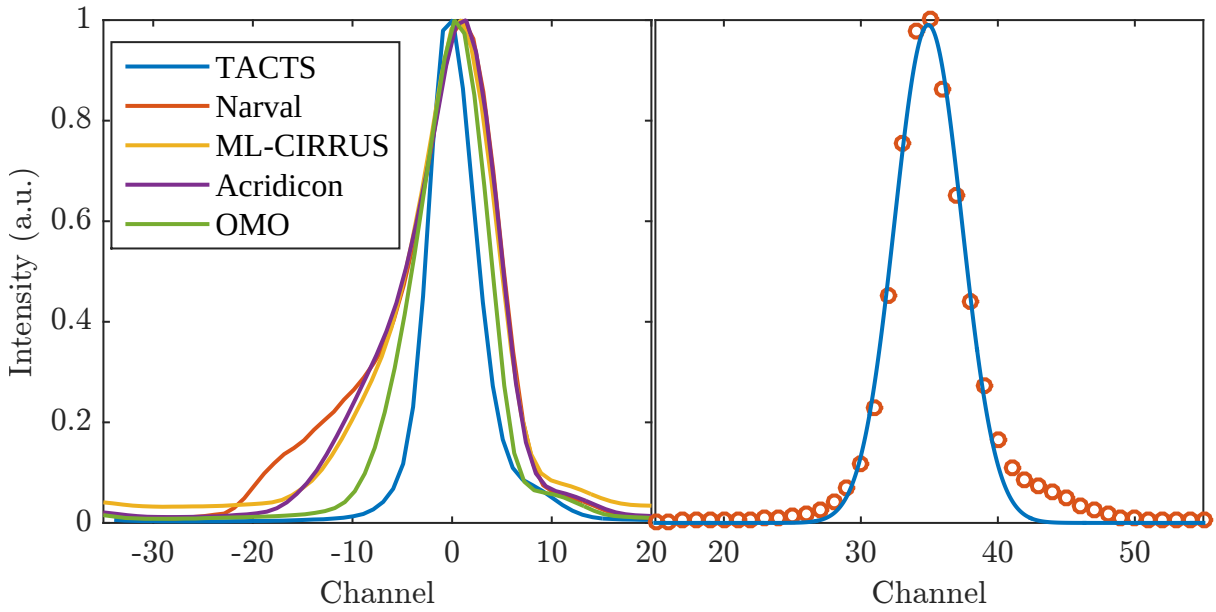

Figure 3.5: Slit function of the 587 nm Kr line (VIS4 spectrometer). Left: Slit functions for different science missions. Right: TACTS slit function (red circles: measurements) with Gaussian fit (blue line).

3.2.5 Field of view

The field of view (FOV) describes the solid angle in the sky where incoming radiation is collected by the telescope. The FOV has to be known in order to correctly simulate the radiative transfer, i.e. the Box-AMFs (sect. 5.3.2). The individual glass fibres of the fibre bundles are aligned in a row next to each other. Therefore, the FOV has to be measured in two dimensions, one along the row of fibres *(horizontal FOV)* and one perpendicular *(vertical FOV)*.

3.2.5.1 Vertical FOV

The total vertical FOV in limb viewing geometry is subject to three effects:

1. The optical FOV_{opt} of the telescopes.
2. The gear play Δ of the telescope control.
3. The pointing precision σ, i.e. the delay between aircraft movement and movement of the telescopes.

Table 3.1 gives the theoretical FOV_{opt} calculated from the telescope properties (Hüneke, 2011). The FOV_{opt} is highly sensible to how well the fibre bundle entrance is mounted in the focal point of the lens. Since the fibre bundles and telescopes are disconnected between science missions for maintenance, the FOV_{opt} has to be determined for each measurement science mission. When scanning with the telescope over a distant emission line point source (fig. 3.6), the FOV_{opt} is measured by recording the emission peak maximum intensity with respect to the telescope elevation angle. The calibration measurement directly after the TACTS/ESMVal science mission is shown in Figure 3.7a. A Gaussian fit gives a FWHM of 0.41°. When the scan is carried out in the opposite direction, a reproducible shift Δ between the intensity maxima can be determined due to the gear play between motor and telescope. In the case of the TACTS/ESMVal science mission the shift is Δ=0.05°(fig. 3.7b). Figure 3.7c shows the same measurements carried out for the ML-Cirrus science mission.

As the aircraft cruises during the recording of a spectrum, an additional effect influencing the field of view of the telescope results from the delay between the aircraft's roll angle and the correction of the telescope's elevation angle (Knapp, 2016). The aircraft roll rate is typically 0.2 degree/s (Figure A.8), such that a roll angle correction frequency of 10 Hz (sect. 3.1.4.2) should be sufficient with respect to the optical FOV, the other pointing errors (sect. 3.2.6), and the need for a resonable inversion of the measurements (width of the averaging kernel, sect. 5.5.1). Figure 3.8 shows the arbitrarily sampled difference between the target angle and the actual telescope angle. The lag time of the telescope position with respect to the measurement instrument receiving the attitude data in this case resulted in a pointing error of $\sigma = 0.18°$, which is a typical value for all telescopes for measurements during the TACTS/ESMVal and ML-Cirrus science missions.

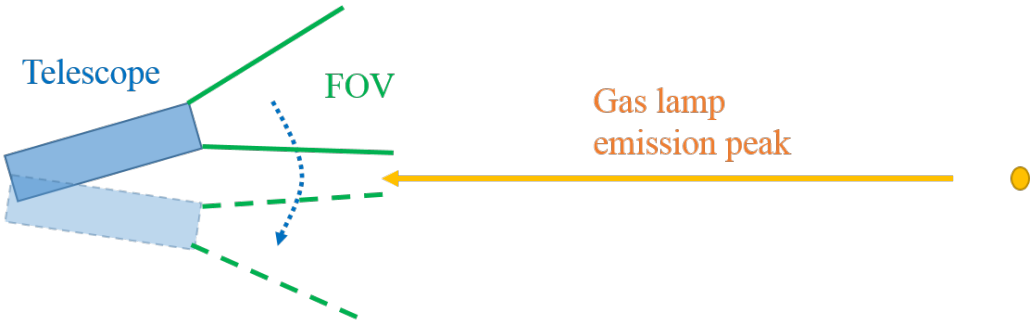

Figure 3.6: Sketch of a field of view measurement.

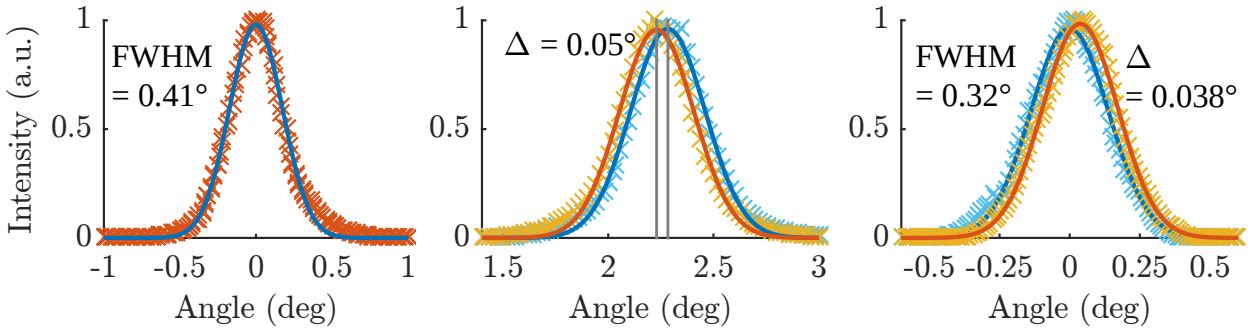

(a) TACTS FOV$_{opt}$ (b) TACTS Δ value (c) ML-Cirrus FOV and Δ

Figure 3.7: Monitoring of the FOV$_{opt}$ and gear play Δ of the VIS4 detector telescope for the science mission TACTS/ESMVal and ML-Cirrus.

In case of the TACTS/ESMVal science mission, the total FOV of the VIS4 detector telescope was 0.41°+ 0.05°+ 0.18°= 0.64°. For the ML-Cirrus science mission, it was 0.32°+ 0.04°+ 0.18°= 0.54°.

3.2.5.2 Horizontal FOV

Figure 3.9 shows near field measurements of the FOV in the horizontal. The FOVs of the individual glass fibres may be merged at larger distances. Knowing the horizontal FOV is necessary for RTM simulations, but is also crucial in order to determine the light throughput of the fibre bundles. Here, the VIS3 fibre bundle is intact with 7 fibres showing near maximum light throughput. However, the VIS4 fibre bundle is damaged with a light throughput below 60% in three of the fibres.

3.2.6 Pointing accuracy

After mounting the aperture plate into the aircraft fuselage, the elevation angle relative to the aircraft has to be calibrated. Similar to the FOV measurement a line point source is placed in 15 m distance (fig. 3.6). The telescope elevation angle θ_{Cal} with the largest emissivity is determined with the calibration software (section 3.1.4). θ_{Cal} is then corrected for by the roll angle $\theta_{R,Cal}$ of the aircraft at the time of the calibration measurement to derive the angle offset $\theta_O = \theta_{Cal} + \theta_{R,Cal}$. The angle

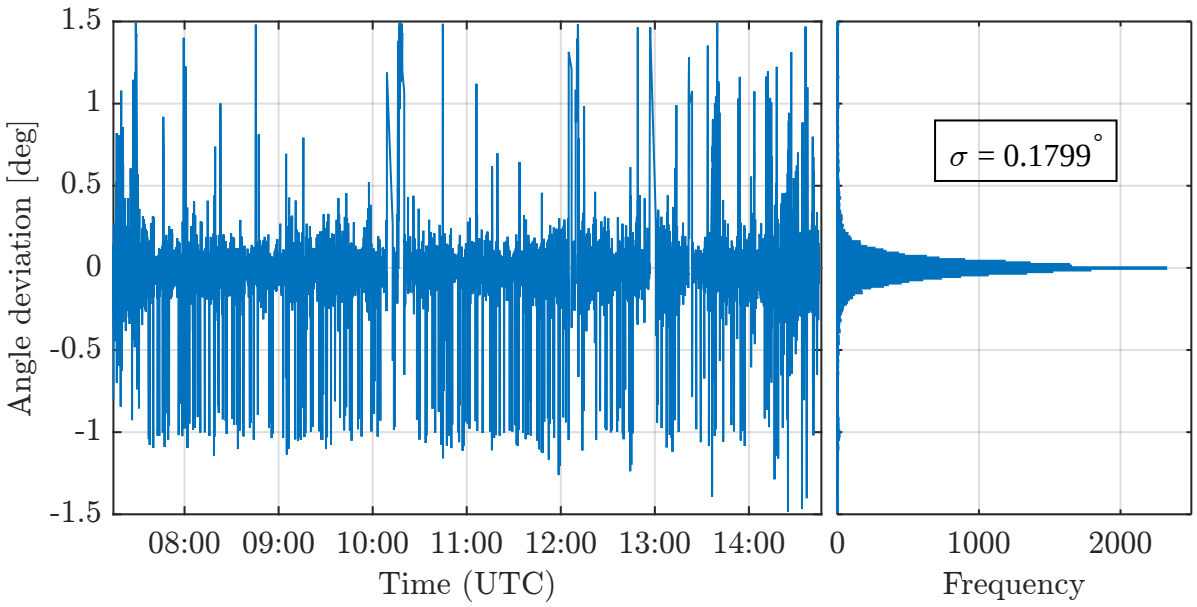

Figure 3.8: Disalignment of aircraft roll angle and UV2 telescope elevation angle during the science flight on 30. August 2012. Left panel: Difference of the targeted and actual telescope elevation angle sampled arbitrarily at 1 Hz over the course of a measurement flight. Right panel: Corresponding frequency occurance histogram of the same data. The relatively frequent occurrence of values around -1° is due to the selection of a subsequent elevation angle not yet reached by the telescope (compare section 3.1.4.2).

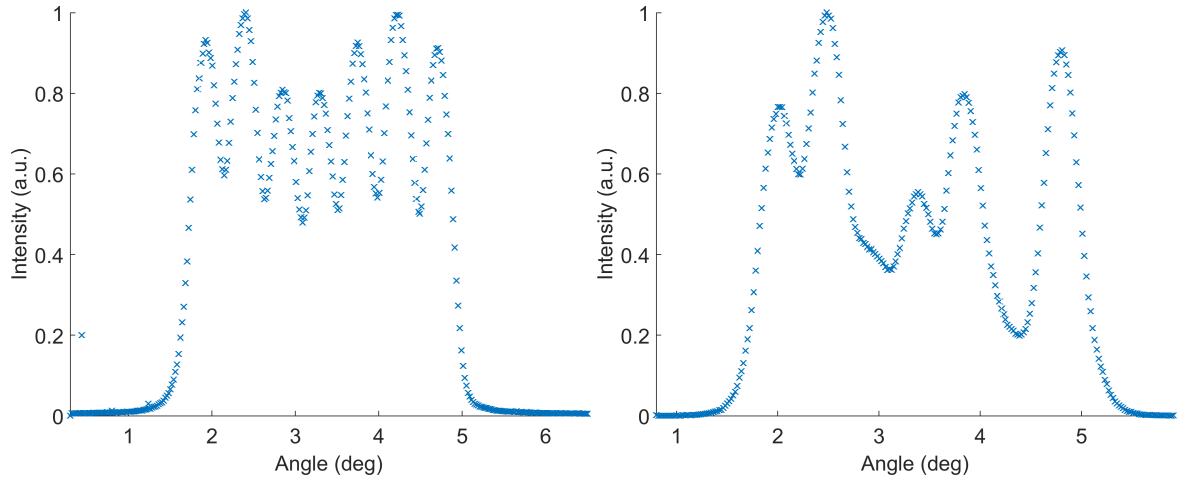

(a) VIS3 (b) VIS4

Figure 3.9: Horizontal field of view at ≈ 1.5 m distance from the telescope measured after the TACTS/ESMVal science mission.

offset θ_O is then used as a parameter in the measurement software to derive the telescope elevation angle relative to the aircraft $\theta_{EA,AC} = \theta_{EA,Hor} - \theta_R + \theta_O$ from the targeted elevation angle relative to the horizon $\theta_{EA,Hor}$ and the roll angle of the aircraft θ_R, which is continuously received at 10 Hz from the BAHAMAS system during each science flight.

The uncertainty of $\theta_{EA,AC}$ is given by the following contributions:

1. When the aircraft is grounded, the aircraft roll angle given by the aircraft attitude data has a standard deviation of 0.2° , estimated from the BAHAMAS data stream.

2. Under the assumption of a 2 cm uncertainty in the height of the lamp relative to the aperture plate (1 cm at either side) and for a distance of 15 m, the angle uncertainty is 0.076° .

Accordingly, the total systematic error in telescope alignment is $\Delta EA < 0.3°$.

The in-flight pointing and FOV can be tested by observing the maximum of the relative radiance as a function of wavelength. Figure 3.10 shows measurements and simulations of relative radiances of two limb scans over a set of elevation angles (EAs) in steps of 0.25°. Even though the simulations are carried out using a climatological background aerosol profile, the shape of the measured relative radiances closely follows the simulations for each wavelength. The derivatives of the relative radiances increase (decrease) above (below) the maxima, indicating different aerosol OD profiles of model and measurement. For some observations the maxima appear to be shifted by 0.25° at most.

3.2.7 Temperature stability

The aircraft's boiler room into which the HALO mini-DOAS instrument is mounted is subject to ambient pressures and temperatures. The latter is influenced by ambient air temperature and heat released by the aircraft's air conditioning system and the APU (auxiliary power unit). The observed temperatures in the boiler room close to the HALO mini-DOAS instrument typically range from -20 °C to +40 °C (Kenntner, 2013) which is challenging to be compensated in an optical instrument. Changing temperatures may alter the imaging properties of the spectrometers, thereby increasing measurement noise and detection limits for the targeted species. In order to keep the spectrometers at near constant temperatures, the time constant $\tau = C/Q$ for the thermal adjustment to ambient conditions is increased by (a) immersing the spectrometer housing into an ice/water vessel with high heat capacity C (see below), and (b) layers of insulation material with low thermal conductivity in order to decrease the heat flow Q. The instrument is insulated by a combination of insulation materials (Table 3.5) with a total thickness of 2-3 cm on all sides. The materials have very low heat conductivity and do not change their form or loose their insulating properties under the influence of water or changing ambient pressure. To understand the heat flow and identify heat bridges, thorough investigations were carried out and the HALO mini-DOAS instrument was modified (sect. 3.1.5) according to recommendations made by Kenntner (2013).

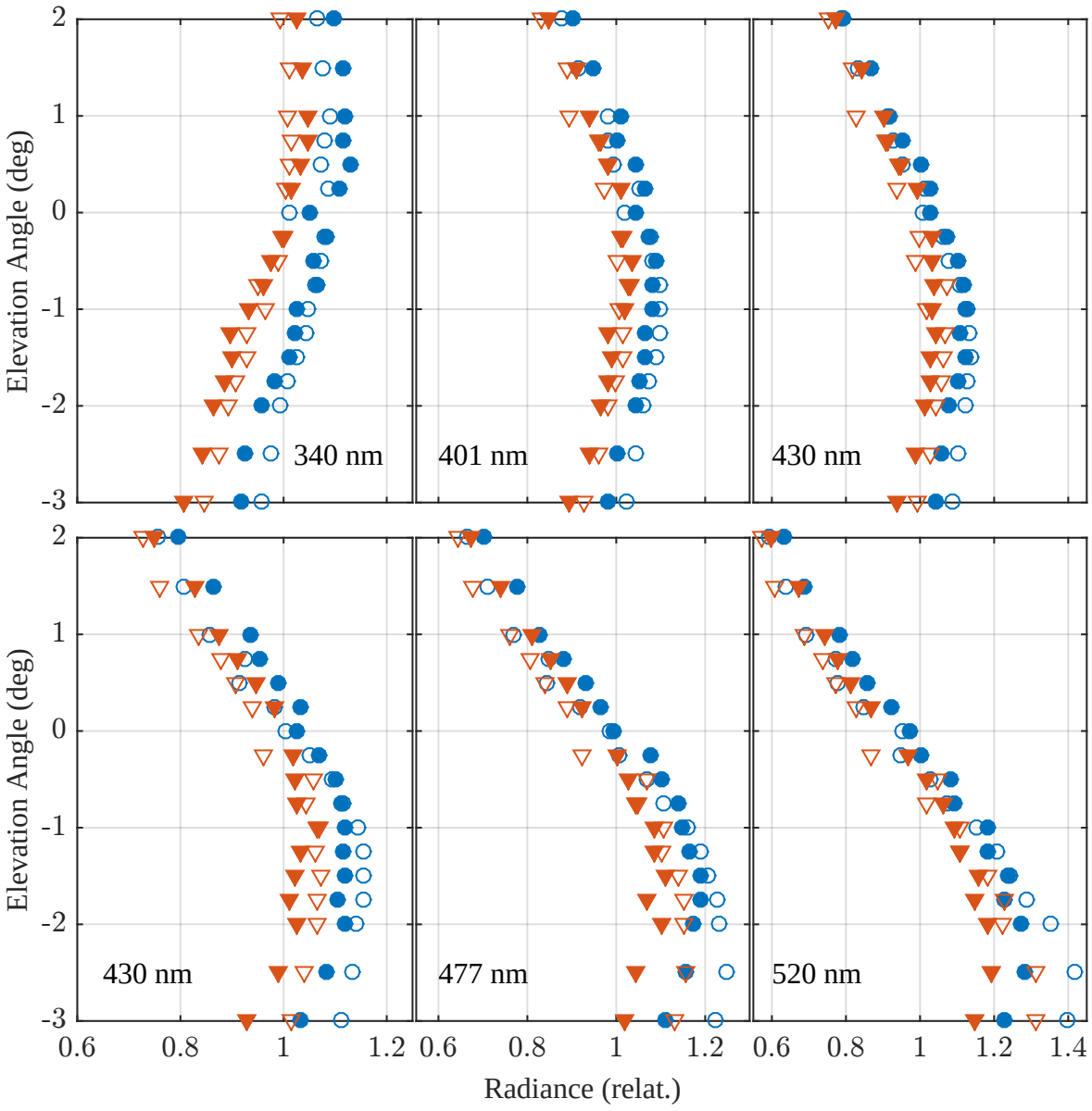

Figure 3.10: Comparison of modelled (filled symbols) and measured (unfilled symbols) relative radiances for a set of elevation angles between +2° and -3° , recorded with the telescopes of UV2 (upper panels) and VIS4 (lower panels). Blue and red symbols indicate two subsequently recorded limb scans. Models and measurements are normalised to the mean of the respective dataset. The simulations employ the radiative transfer model (RTM) McArtim (sect. 5.3) and climatological background aerosol profiles from satellite measurements (Calipso, SageII). The measurements were carried out during the Polstracc science mission on February 26, 2016, at 13.7 km altitude, SZA 80° ... 82° , SRAA 67° ... 69° , at 70°N, 47°W.

Table 3.5: Insulation materials used for the HALO mini-DOAS instrument.

Insulation material	**Type**	**Heat conductivity** $\left[\frac{\mathrm{W}}{\mathrm{mK}}\right]$	**Producer**
PVDF-Foam	Zotek F semi-rigid	0.037	Wulfmeyer
Evacuated plate	va-Q-vip B	0.008	va-Q-tec

The ice/water vessel has a volume of 7 l, of which around 4 l can be ice, which corresponds to a heat of melt of 4 kg $\cdot$ 333 kJ/kg $\approx$ 1300 kJ. If the instrument is warm (20 °C), then around 20 kg $\cdot$ 20 K $\cdot$ 1 kJ/(kg K) = 400 kJ are needed to cool the instrument to 0 °C, with 900 kJ remaining for measurements during the science flight. In the first science missions, especially in the case of high ground ambient temperatures in the tropics, the available heat of sublimation was not sufficient. Improvements of the insulation and colder ambient temperatures lead to temperature variations of $\Delta T < 1$ K over several hours. Figure 3.11 shows spectrometer temperatures of some exemplary science flights. While e.g. the flight from Barbados (red) started at 7 °C and exhibited strong temperature changes, the flight from Iceland (yellow) showed much lower and more constant temperatures. This indicates a strong dependence on ambient temperatures during flight preparation, i.e. if more heat of melt is needed to cool down the instrument this decreases the available amount during the flight. Temperature stability was however improved by different measures (sect. 3.1.5), such that the temperatures stayed constant e.g. during the OMO science flight with take-off in the Maldives (Figure 3.11, green line).

Future improvements are planned, such as (a) decreasing the number of electronic connectors on the lid from 12 to 6, and (b) extending the plugs for the connectors with stainless steel tubes with low heat conductivity in order to raise them above the insulation, which will further improve the temperature stability.

3.2.8 Noise and theoretical detection limits

This section considers the statistical noise of the instrument and the photoelectrons related to an ideal measurement process. Field measurements exhibit additional noise contributions (section 5.2.3) and further uncertainties have to be taken into account when trace gas mixing ratios are retrieved from the measurements (section 6.3).

A number of factors contribute to the noise of the output of a CCD detector, including the photoelectron shot noise, dark-current noise, preamplifier and readout noise, and analog-to-digital converter noise (Ferlemann et al., 2000). The photoelectron shot noise follows Poisson statistics and can thus be estimated as the square root of the number of photons N_{ph} incident on the detector. N_{ph} can in turn be calculated from detector properties:

$$\delta_{ph} = \sqrt{N_{ph}} \tag{3.1}$$

$$N_{ph} = \frac{N_{ro} \cdot S \cdot FWC_{channel}}{QE} \tag{3.2}$$

N_{ro} is the number of detector readouts, S is the saturation, $FWC_{channel}$ is the full well capacity of

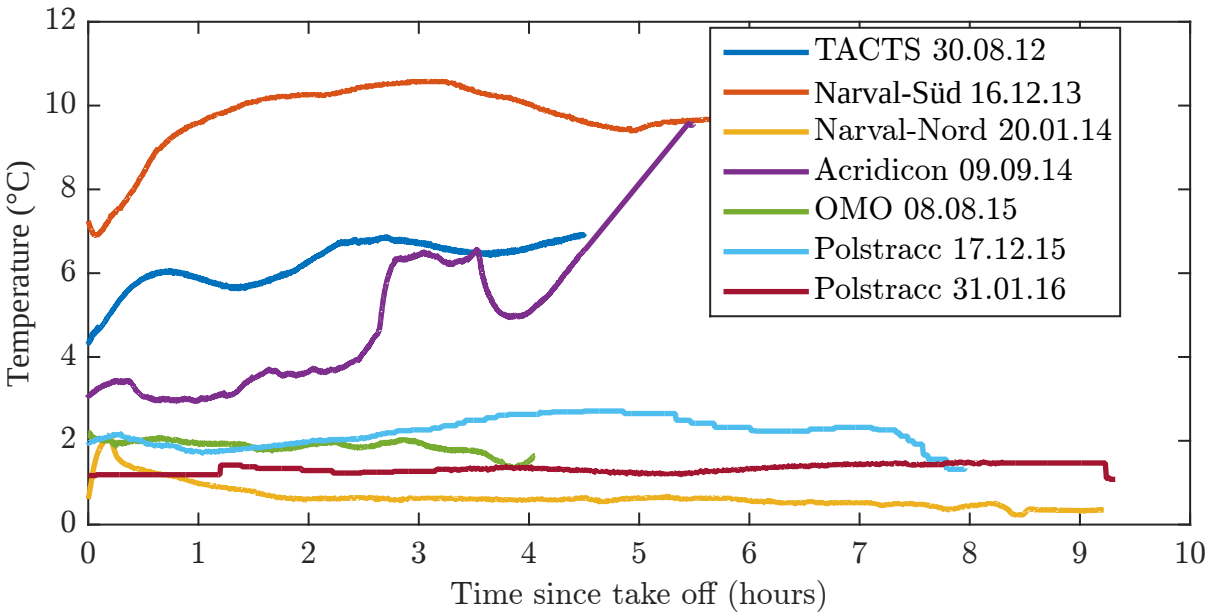

Figure 3.11: Spectrometer temperatures recorded during selected measurement flights. TACTS 30.08.12 and Polstracc 17.12.15 took off from Oberpfaffenhofen (Germany), Narval-Süd 16.12.13 from Barbados, Narval-Nord 20.01.14 from Iceland, Acridicon 09.09.14 from Manaus (Brasil), OMO 08.08.15 from Gan (Maldives), and Polstracc 31.01.16 from Kiruna (Sweden).

the detector channel and *QE* is the quantum efficiency (compare Table 3.1). Detailed information on the other noise contributions are not given by the manufacturers of the detector and the readout electronics. However, the sum of all contributions can be measured and two components can be distinguished: One component proportional to the exposure time (hereafter called "dark-current noise") and one component proportional to the number of readouts (hereafter called "statistical readout noise"). These components were investigated by Schulte (2013) from standard deviations of offset and dark current measurements. She found typical values of 20 digital units (∼60 electrons) statistical readout noise per readout and 60 digital units (∼180 electrons) dark-current noise per second for the CCD detectors of the UV/visible channels. Using these measurements, one can calculate the theoretical noise level for any number of readouts or any exposure time (Figure 3.12). Photoelectron shot noise dominates the other components for saturations > 5%. A large number of readouts and a high saturation decreases the noise level, as expected from eq. 3.1. The calculations are validated by ratioing two subsequently recorded spectra of a halogen lamp. The standard deviation and the peak-to-peak deviation of a 200-pixel wide subset of the ratio is shown as green symbols in Figure 3.12.

However, one aspect is omitted in this consideration: When collecting more and more light, at a certain point all statistical noise is so small that only systematic readout noise remains in the residual, which can not be lowered further by collecting more photons. This does not appear in Figure 3.12 due to the low number of readouts, but is shown by e.g. General et al. (2014) in their Figure 10 using similar detectors to the ones of the HALO mini-DOAS instrument. Such large numbers of readouts (>10^4) are not employed in HALO mini-DOAS instrument field measurements, since this would imply a too long overall integration time for the recorded spectrum. Long integrations times decrease the spatial resolution of the measurements due to the high aircraft velocity of ≈ 200 m/s up to the point where the interpretation of the measurements becomes impossible, e.g. 10^4 readouts

$\times$ 0.3 s $\times$ 200 m/s = 600 km. Levels of purely systematic noise are therefore not reached during air-borne measurements of the HALO mini-DOAS instrument. At typical measurement conditions of 60% saturation, 300 ms exposure time and 100 readouts, the theoretical noise level is $\delta = 3 \times 10^{-4}$ relative to the signal.

Stutz and Platt (1996) find that the theoretical limit D_{theo} for the detection of a trace gas can be approximated by

$$D_{\text{theo}} \approx \delta \times \frac{6}{\sqrt{n-1}} \tag{3.3}$$

for a given random noise level δ and a number of pixels n. This detection limit can be converted to column densities D_{column} and mixing ratios D_{MR}:

$$D_{\text{MR}} = \frac{D_{\text{column}}}{\text{TND} \cdot l} = \frac{D_{\text{theo}}}{\sigma_{TG} \cdot \text{TND} \cdot l} \tag{3.4}$$

$$D_{\text{column}} = \frac{D_{\text{theo}}}{\sigma_{TG}} \tag{3.5}$$

$$\text{TND} = \frac{p}{T \cdot k_b} \times 10^{-6} \tag{3.6}$$

Here, σ_{TG} is the respective trace gas absorption cross section, TND is the total number density of air in molecules/cm^3 and $k_b = 1.38 \times 10^{-23}$ Nm/K the Boltzmann constant. Representative conditions of a HALO research flight at 12 km altitude are e.g. a light path length of 100 km, 200 hPa ambient pressure p and 220 K ambient temperature T. Table 3.6 lists the resulting detection limits for a number of trace gases detectable by the HALO mini-DOAS instrument.

These detection limits are theoretical limits, since they assume purely random noise in the spectrum. This assumption is not realistic for field measurements, where residual structures from atmospheric and instrumental effects are common and one would expect much higher detection limits (Platt and Stutz, 2008). An account of detection limits for straylight spectra from field measurements is given in section 5.2.3 in the context of the DOAS retrieval.

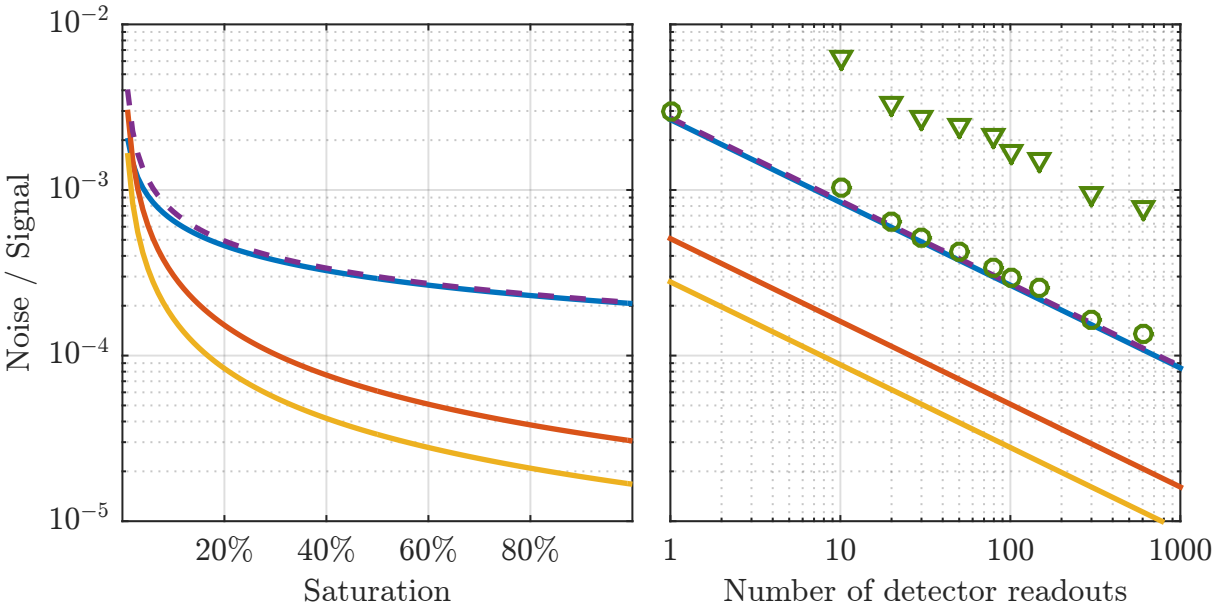

Figure 3.12: Noise relative to the signal for the CCDs of the HALO mini-DOAS instrument as a function of saturation (left, with 300 ms exposure time and 100 readouts) and as a function of the number of readouts (right, with 300 ms exposure time and 60% saturation). Statistical readout noise (red) and dark-current noise (orange) are calculated from noise level measurements by Schulte (2013), photoelectron shot noise (blue) is calculated from detector quantum efficiency and full well depth (see text). The broken line shows the sum of all statistical noise contributions. Green symbols denote laboratory measurements of a 200-pixel wide subset of a halogen lamp spectrum (circles: standard deviation, triangles: peak-to-peak). Note that the level of systematic readout noise is not reached.

Table 3.6: Theoretical trace gas detection limits D in limb viewing geometry calculated according to equations 3.3-3.4. The trace gas cross sections are listed in Table 5.1. The number of pixels $n = 100$ is assumed as an approximation in the cases of $C_2H_2O_2$, IO, and SO_2.

Gas	**Wavelength**	**Cross section**	**n**	D_{column}	D_{MR}
	nm	cm^2	#	molec./cm^2	ppt
O_3	500	1×10^{-21}	385	9.2×10^{16}	140
	331	5.5×10^{-21}	346	1.8×10^{16}	27
NO_2	435	3×10^{-19}	508	2.7×10^{14}	0.4
HONO	354	4.5×10^{-19}	449	1.9×10^{14}	0.3
HCHO	325	7.6×10^{-20}	436	1.1×10^{15}	1.7
$C_2H_2O_2$	455	5×10^{-19}	100	3.6×10^{14}	0.5
OClO	344	8×10^{-18}	372	1.2×10^{13}	0.02
BrO	338	1.1×10^{-17}	269	1.0×10^{13}	0.02
IO	427	3×10^{-17}	100	6×10^{12}	0.01
SO_2	318	9×10^{-20}	100	2.0×10^{15}	3
O_4	477	6.6×10^{-46} $\text{cm}^5/\text{molec.}^2$	231	1.8×10^{41} molec.$^2/\text{cm}^5$	0.9%

Chapter 4

Measurements

Table 4.1 lists all science missions where the HALO mini-DOAS instrument has participated. The data analysed furtheron in the present thesis was recorded during the TACTS/ESMVal mission in 2012. This chapter presents the concept of TACTS/ESMVal, and details two research flights and the instruments whose measurements are used in the following.

4.1 TACTS/ESMVal

The goal of the combined TACTS (Transport and Composition in the upper troposphere / lowermost stratosphere) and ESMVal[1] (Earth System Model Validation) mission was the mapping of large scale trace gas distributions in the UT/LS region, and the investigation of mixing processes between the upper troposphere and the lower stratosphere. The measurements of TACTS were intiated by scientific knowledge obtained during previous science missions STREAM and SPURT (Engel et al., 2006; Hegglin et al., 2006). Compared to the previous missions, which used a Learjet 35A, the new mission provided new measurements with ceiling altitudes of up to 15 km. A larger set of measurement instruments than before was assembled (sect. 4.2). TACTS was centered on the UT/LS above Europe, with some flights conducted south to Cape Verde islands and north into polar latitudes (Figure 4.1a). ESMVal was set up as a meridional survey in order to obtain observations of trace gas distributions in the free troposphere and lower stratosphere from 80° N to 65° S (Figure 4.1b). One particular objective was the validation of the global ECHAM/MESSy Atmospheric Chemistry (EMAC) model.

TACTS/ESMVal was the first science mission where the HALO mini-DOAS instrument was deployed. The HALO mini-DOAS instrument was fully operational throughout the mission, resulting in only very few flight sections without measurements being recorded. Measurements conducted by other instruments during the TACTS/ESMVal science mission are presented in the following publications:

[1] http://www.pa.op.dlr.de/ESMVal/

Table 4.1: Science mission deployments of the HALO mini-DOAS instrument from 2012 to 2016.

Date	Name		Flights	Hours	References
Aug.-Sept. 2012	TACTS	Transport and Composition in the UT/LS	6	54	see text
	ESMVal	Earth System Model Validation	7	58	see text
Dec.-Jan. 2013/14	NARVAL	Next Generation Remote Sensing for Validation Studies	15	120	Klepp et al. (2014)
Mar.-Apr. 2014	ML-Cirrus	Mid-Latitude Cirrus	16	77	Voigt et al. (2016); Wolf et al. (2016)
Aug.-Oct. 2014	Acridicon	Aerosol, Cloud, Precipitation, and Radiation Interactions and Dynamics of Convective Cloud Systems	14	96	Wendisch et al. (2016)
July-Aug. 2015	OMO	Oxidation Mechanism Observations	20	116	Aderhold (2016)
Dec.-Mar. 2015/16	Polstracc	Polar Stratosphere in a Changing Climate	18	156	

- Jurkat et al. (2014) use tracer-tracer correlations of O_3, CO, HCl, and HNO_3 to estimate the stratospheric content of air masses in the extratropical UT/LS.

- Vogel et al. (2014) use backward trajectory calculations and find a novel, fast transport way, which carried air from the Southeast Asia/West Pacific boundary layer to the lowermost stratosphere over northern Europe was within approximately 5 weeks.

- Riese et al. (2014), Ungermann et al. (2015), and Kaufmann et al. (2015) use measurements from the TACTS/ESMVal mission to illustrate the scientific goals, data processing, and the retrieval of three-dimensional structures for the GLORA instrument.

- Rolf et al. (2015) show the detection of strongly dehydrated air by the GLORIA instrument during science flight ANT (sect. 4.1.2) down to 7 km altitude and attribute the transport into the troposphere to Rossby wave breaking.

- Müller et al. (2016) investigate correlations of O_3, CO, and N_2O during science flight ML (sect. 4.1.1), showing that tropospheric air from the monsoon circulation affects the change in chemical composition of the extratropical UT/LS at potential temperatures above 380 K.

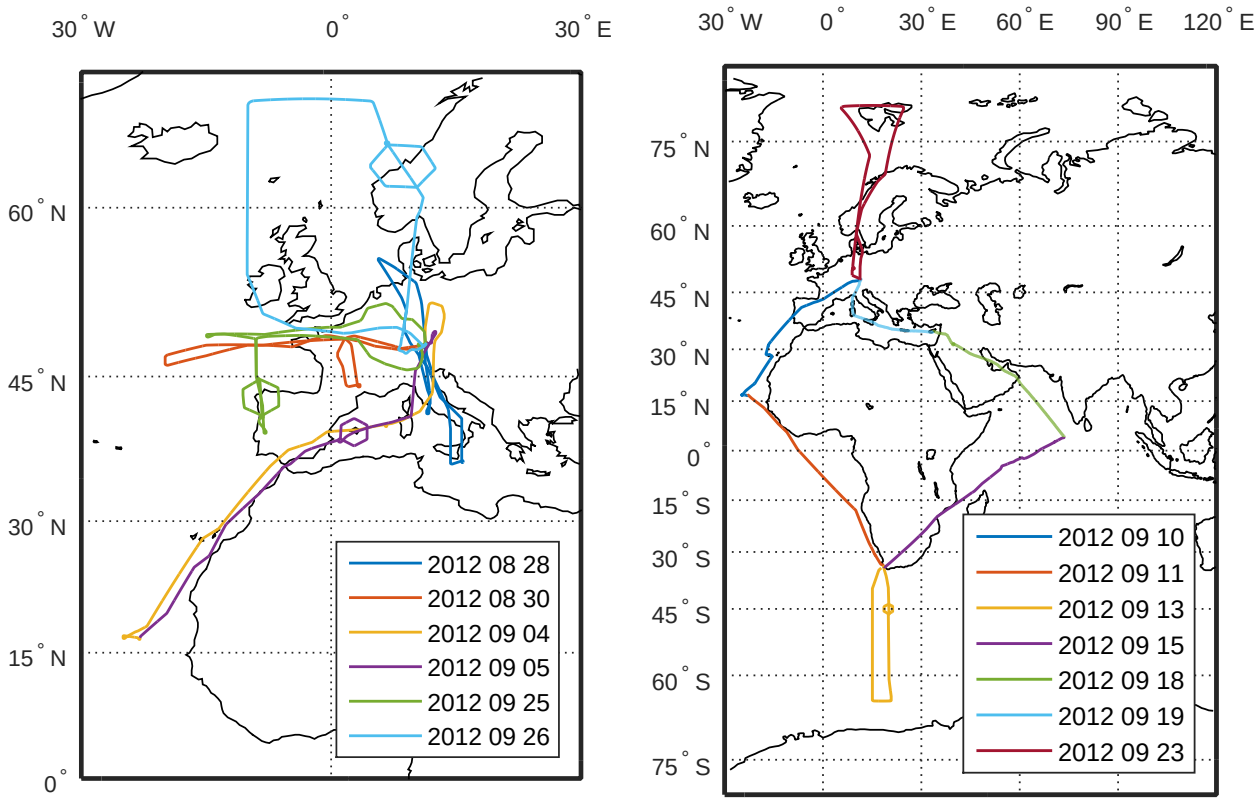

(a) TACTS (b) ESMVal

Figure 4.1: Maps of science flight trajectories of the TACTS/ESMVal mission.

4.1.1 Flight ML: TACTS science flight on August 30, 2012

The flight was performed over mid-latitude western Europe and the eastern Atlantic with take-off and landing in Oberpfaffenhofen (Munich). It is hereafter referred to as science flight "ML". As described by Müller et al. (2016), a trough of stratospheric air was crossed several times at flight altitudes between 11.5 and 15 km, i.e. 220 and 130 hPa pressure level, respectively. Air masses with potential temperatures up to 405 K were sampled, and potential vorticity (PV) values above 12 pvu were reached (Figure 4.2). Hence, these air masses are located well above the dynamical tropopause, which is commonly defined by PV values from 1 to 4 pvu in the extratropics (Randel et al., 2007).

4.1.2 Flight ANT: ESMVal science flight on September 13, 2012

The flight was performed over the Antarctic Ocean, with take-off and landing in Cape Town (South Africa). It is hereafter referred to as science flight "ANT". After a first flight section near the subtropical tropopause, stratospheric air of the polar winter vortex was reached south of ≈ 48° S (Figure 4.3). The flight continued until 65° S, then turned eastwards. At 20° E, the aircraft turned northwards, with a subsequent dive down to ≈ 3.5 km altitude into the polar troposphere. When the aircraft left the polar vortex again, a hexagon-shaped flight pattern was carried out for tomographic measurements with GLORIA. In order to facilitate a structured discussion, the science flight is subdevided into five flight sections, which also coincide with changes in flight altitude (Figure 4.4):

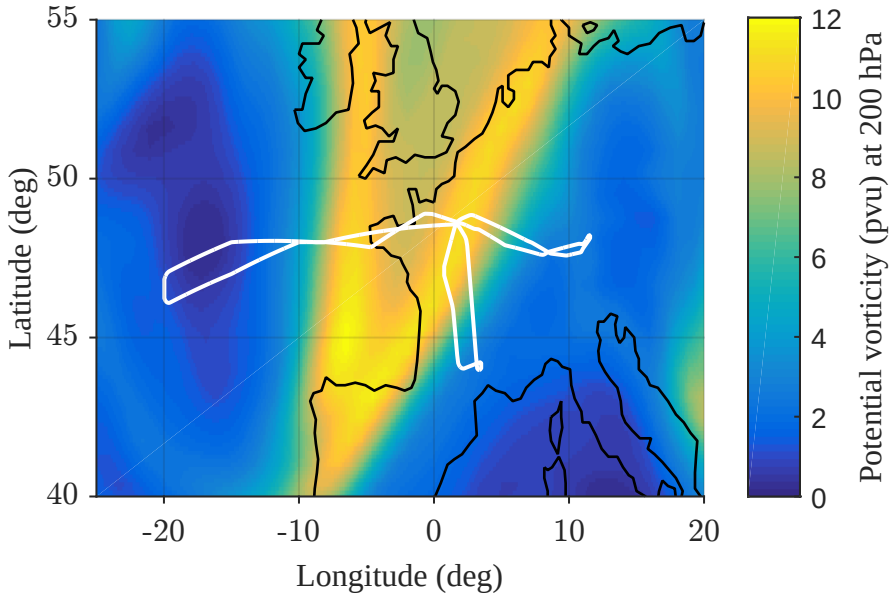

Figure 4.2: Potential vorticity (PV) at 200 hPa (≈ 11.8 km altitude) from ECMWF ERA-Interim reanalysis data (Dee et al., 2011) at 12:00 UTC (corlour coded) and trajectory of science flight ML (white line).

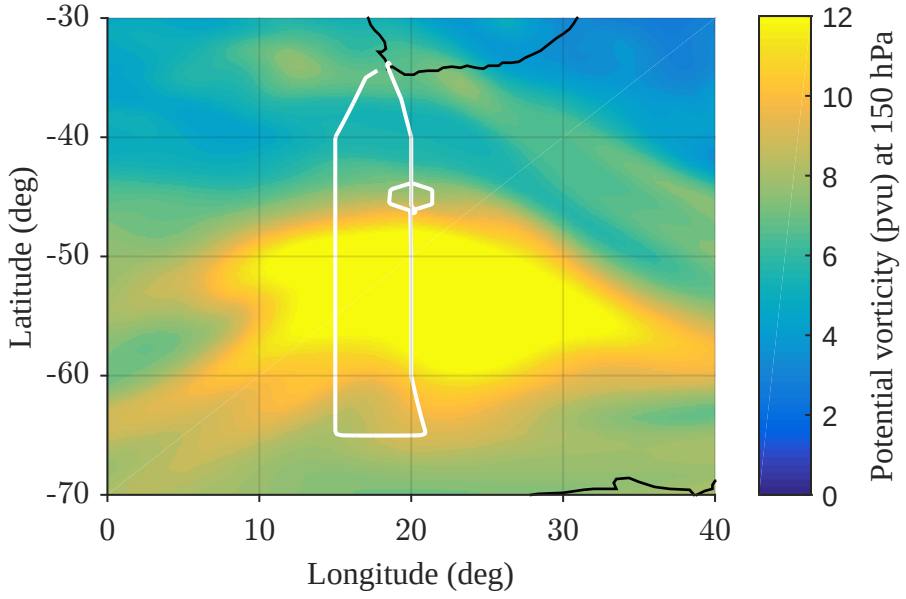

Figure 4.3: Absolute potential vorticity (PV) at 150 hPa (≈ 13.6 km altitude) from ECMWF ERA-Interim reanalysis data (Dee et al., 2011) at 12:00 UTC (colour coded) and trajectory of science flight ANT (white line).

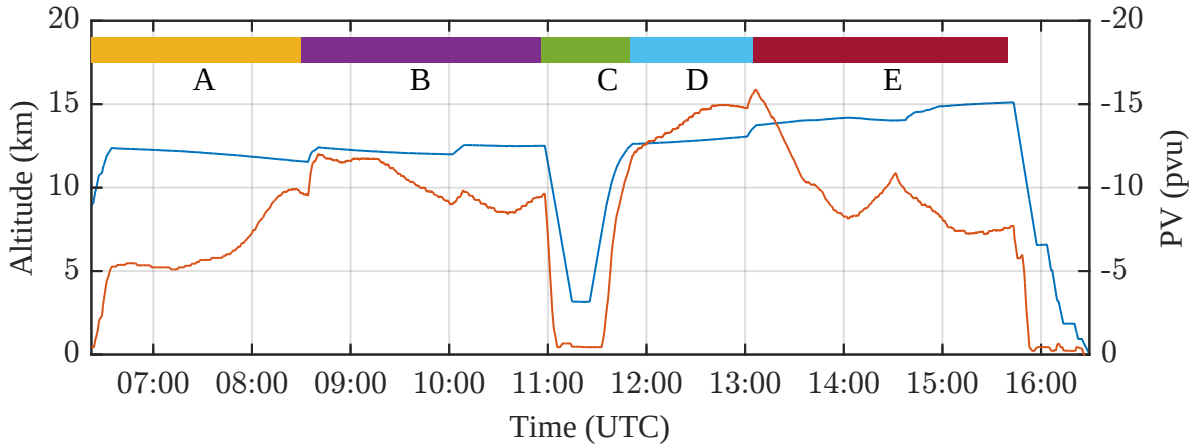

Figure 4.4: Timeseries of flight altitude (blue) and Potential vorticity (PV, red) from ECMWF ERA-Interim reanalysis data (Dee et al., 2011) during science flight ANT. The flight sections marked with coloured bars are described in the text.

- Flight section **A**: From take-off until 08:30 UTC, approximately 49° S. The airmasses probed during this flight section can be described as subtropical lowermost stratospheric air. Potential vorticity (PV) is often above PV = 4 pvu, the commonly defined dynamical tropopause, but below PV = 10 pvu.
- Flight section **B**: The lowermost edge of the polar vortex was probed from the end of flight section A until the beginning of the dive at 10:56 UTC. The aircraft is heading south for the first part of the flight section, but is heading east after approx. 10:35 UTC. The predicted PV is around 10 pvu. The chemical composition is much different to flight section A, which is shown in chapter 7.
- Flight section **C**: Polar tropospheric air was probed during the dive from 10:56 – 11:50 UTC, heading North. Accordingly, tropospheric PV was encountered.
- Flight section **D**: The polar stratosphere was probed again from the end of the dive until 13:05 UTC (49° S). Very high PV $\approx$ 15 pvu was encountered in this flight section, probably due to the descent of stratospheric air from higher altitudes (Rolf et al., 2015).
- Flight section **E**: The extratropical lowermost stratosphere was probed again from 13:05 UTC until the descent towards Cape Town began at 15:40 UTC, with PV mostly below 10 pvu.

4.2 Other instruments

Table 4.2 lists all instruments deployed during the TACTS/ESMVal science mission aboard the DLR HALO. The measurements of three of the instruments are lateron used for the scaling method and for comparison purposes:

- FAIRO is a light-weight (14.5 kg) and accurate 2-sensor device for measuring O_3. It combines two techniques, i.e. (a) a UV photometer that measures the light absorption of O_3 at a wavelength of λ = 250 - 260 nm emitted by an UV-LED and (b) a chemiluminescence detector that monitors the chemiluminescence generated by O_3 on the surface of an organic dye adsorbed on dry silica gel. Both techniques are simultaneously applied in order to combine the high measurement accuracy of UV photometry with the high measurement frequency of chemiluminescence detection. The UV photometer shows a 1-σ precision of 0.08 ppb at a measurement frequency of 0.25 Hz (and a pressure of 1 bar) and an accuracy of 1.5% (determined by the uncertainty of the O_3 cross section). The chemiluminescence detector shows a precision of 0.05 ppb at a measurement frequency of 12.5 Hz (Zahn et al., 2012). In post-processing the chemiluminescence detector data is calibrated using the UV photometer data. FAIRO was first deployed on HALO during the TACTS/ESMVal campaign (July to September 2012); its performance was excellent during all 13 flights (A. Zahn, pers. comm.).

- NO and NO_y measurements on board HALO were performed using a two-channel chemiluminescence detector (AENEAS - Atmospheric nitrogen oxide measurement system) in combination with a catalytic conversion technique (Ziereis et al., 2000; Stratmann et al., 2016). A commercial two-channel chemiluminescence detector (ECO PHYSICS, Switzerland) was modified for use on board of research aircraft. The chemiluminescence technique is widely used for the detection of atmospheric NO and relies on the emission of light in the near infrared following the reaction of NO with O_3 (e.g. Drummond et al., 1985). Heated gold tubes in combination with CO or H_2 as reducing agent are frequently used to convert all species of the odd nitrogen family (NO_2, HNO_2, HNO_3, HO_2NO_2, N_2O_5, PAN, ...) into NO (e.g. Bollinger et al., 1983; Fahey et al., 1985) that is subsequently detected by chemiluminescence. The conversion efficiency of the gold converter is quantified using gas phase titration of NO and O_3 before and after each flight with a conversion efficiency of typically more than 98%. The statistical detection limit is 7 pmol/mol for the NO measurements and 8 pmol/mol for the NO_y measurements for an integration time of 1 s. The overall uncertainty for the NO and NO_y measurements is 8% (6.5%) for volume mixing ratios of 0.5 nmol/mol (1 nmol/mol) (H. Ziereis, pers. comm.).

- The TRIHOP instrument is a three channel Quantum Cascade Laser Infrared Absorption spectrometer capable of the subsequent measurement of CO, CO_2, CH_4, and N_2O (Schiller et al., 2008; Müller et al., 2016). The instrument applies Quantum Cascade Laser Absorption Spectroscopy (QCLAS) in the mid-infrared with a multipass absorption cell (type White), which is kept at a constant pressure of P = 30 hPa and has a path length of 64 m and a volume of 2.7 L. During TACTS/ESMVal the instrument is in-situ calibrated approx. every 30 min during the flights against a secondary standard of compressed ambient air. The mixing ratios of

Table 4.2: Instruments deployed during the TACTS/ESMVal mission, besides the HALO mini-DOAS instrument.

Species	**Instrument**	**Reference**
N_2O, CO, CO_2, CH_4	TRIHOP	Schiller et al. (2008)
O_3	FAIRO	Zahn et al. (2012)
H_2O	FISH	Zöger et al. (1999)
H_2O	HAI	Buchholz et al. (2014)
$H_2{}^{16}O$, $H_2{}^{18}O$, HDO	ISOWAT	Dyroff et al. (2010)
HCl, HNO_3, $ClONO_2$, SO_2	AIMS	Kaufmann et al. (2016); Jurkat et al. (2016a)
SF_6, CFC_{12}, Halons, VSLS	GhOST-MS	Sala et al. (2014)
PAN, $ClNO_2$, SO_2, HCN, HNO_2	PAN-MS	Speidel et al. (2007)
NO, NO_y	AENEAS	Ziereis et al. (2000)
N_2O, CH_4, H_2O, HDO, SF_6, CFCs, O_3	GLORIA	Riese et al. (2014); Ungermann et al. (2015); Kaufmann et al. (2015)
Isotopologues	MIRAH	
Meteorology, Avionics	BAHAMAS	

the secondary standard are determined before and after the campaign in the laboratory against National Oceanic and Atmospheric Administration (NOAA) standards. Therefore, the in-flight calibrations allow to identify and correct slow instrumental drifts in the post-flight data evaluation. The integration time for each species is 1.5 s at a duty cycle of 8 s, which finally limits the temporal resolution of the measurements. During TACTS/ESMVal TRIHOP CO, (N_2O) data achieved a 2-σ precision of 1.0 (1.1) ppbv and stability of the instrument of 1.5 (2.2) ppbv, respectively, before applying the post flight data correction. The total uncertainty relative to the working standard of 1.8 (2.5) ppbv can be regarded as an upper limit (P. Hoor, pers. comm.).

- AIMS is a chemical ionisation mass spectrometer, using an electrical discharge source and in-flight calibration (Jurkat et al., 2016a). It is suited for the measurement of e.g. HCl, HNO_3. $ClONO_2$, SO_2, and HONO (Jurkat et al., 2014, 2016b), but can also be operated in a water vapour mode (Kaufmann et al., 2016). The residence time in the heated inlet (40° C) is below 0.1 s, minimising thermal decomposition of the measured species. The accuracy of $ClONO_2$, HCl, and HNO_3 measurements are of the order of 15 – 25%, and the time resolution is 1 s with a precision of 10 – 15% (Jurkat et al., 2016b).

Chapter 5

Auxiliary methods

In order to apply the scaling method, slant column densities (SCDs) need to be derived from the measurements. This chapter first describes the postprocessing of the recorded data in section 5.1. The spectral retrieval with the DOAS method and its application within the present thesis is explained in section 5.2. For the interpretation of the retrieved quantities, the *differential* slant column densities (SCDs), the concept of Air Mass Factors and their calculation by means of radiative transfer modelling are introduced in section 5.3. Section 5.4 describes the chemical transport models (CTMs) which are used for a priori information for the concentration retrieval. In section 5.5 the so-called Fraunhofer reference SCD is determined, which is necessary in order to derive the SCDs.

5.1 Postprocessing of recorded data

The measured spectra (with typically 100 readouts each) of each spectrometer as well as a log file with housekeeping data are saved on a flash drive during a science flight. In order to prepare the recorded spectra for the spectral retrieval, they have to be corrected for offset voltage, dark-current and a possible time stamp offset. Furtheron, a channel to wavelength mapping is applied. Eventually, they may be further added up sequentially in order to reduce the retrieval noise and thereby the detection limits (section 5.2.3).

5.1.1 Correction of offset voltage, dark-current, time stamp

As described in section 3.2.1 and Hüneke (2011), the effects of offset and dark-current are corrected for, depending on the added number of detector readouts and the exposure time, respectively.

Another important aspect of the recorded data which has to be corrected is the time stamp of each spectrum. To this end, the time stamp of the aircraft's BAHAMAS data stream is recorded alongside the time stamp of the instrument's PC in a log file. The clocks should be synchronised prior to each flight. Otherwise, the difference between both clocks can range between several seconds and several

ten seconds. The additional time shift accumulated during the flight is on the order of 1 second, which is short compared to the relevant integration times of the recorded spectra (∼30 s). The corrected spectrum time stamps are therefore accurate within 1 s at most, which is sufficient for the calculation of the celestial geometry for radiative transfer modelling (sect. 5.3).

5.1.2 Wavelength calibration

The channel to wavelength mapping is carried out with a gas discharge tube emission line spectrum of HgNe and/or Kr recorded prior or after each measurement flight as described in section 3.2.3. This calibration is then applied identically to all spectra recorded during the corresponding measurement flight. Although a temperature change of the spectrometers results in a wavelength shift and squeeze (sect. 3.2.7), this small remaining distortion is easily compensated by the fitting algorithm (sect. 5.2.2). The file used for the wavelength calibration is also used later to fit a Gaussian to one of the emission lines in order to retrieve the slit function (sect. 3.2.4), which is necessary to convolute literature reference cross sections (Table 5.1) for use in the DOAS fit procedure (sect. 5.2).

5.1.3 Spatial resolution

As described in section 3.2.8, the noise level of the recorded spectra strongly depends on the number of photons, i.e. the number of added detector readouts. When measuring on a fast moving aircraft platform, the desire for low noise (i.e. low detection limits) competes with the spatial resolution of the measurements:

- The spatial resolution has to be high enough to identify atmospheric features on a scale that corresponds to the sampled area, i.e. the area sampled by the FOV (sect. 3.2.5). Radiative transfer simulations show that the bulk of the signal recorded by the telescopes is sampled from an area extending typically 20 km perpendicular to the line of sight (i.e. in flight direction of the HALO aircraft) (Raecke, 2013).
- The noise of the reacorded spectra has to be low enough to detect the targeted trace gases with sufficient precision. During different measurement campaigns, typical exposure times (for each detector readout) for the UV and visible detectors ranged between 100 ms and a few seconds, depending on viewing geometry, atmospheric conditions, and solar zenith angle (SZA). Accumulation of readouts also varied, from recording every single readout during altitude changes (ascents/descents) to adding (i.e. integrating) 20, 100 or more readouts during flight legs at constant altitudes. While a detection of the relatively strong absorbers O_3, O_4, and NO_2 is generally possible with 20 added readouts, the detection of e.g. BrO, OClO, and HCHO sometimes makes further accumulation necessary.

In the case of the TACTS/ESMVal mission, spectra with 100 readouts each were used for the retrieval of O_3, O_4, and NO_2, and 500 readouts for the retrieval of BrO. At 200 m/s approximate aircraft speed

and a typical exposure time of 300 ms this leads to 6 km and 30 km spatial resolution, respectively.

During take-offs, landing approaches and dives, 20 added readouts result in a time resolution of around 10 s. Such short integration times favor the altitude resolution of the measurements, useful for quantifying the Mie extinction and profiles of major absorbers (sect. 5.5.3).

5.2 Spectral retrieval (DOAS)

***D**ifferential **O**ptical **A**bsorption **S**pectroscopy* is a widely used technique in atmospheric research for the detection of numerous trace gases, such as ozone, NO_2, NO_3 (at night), formaldehyde, glyoxal, halogen radicals (BrO, OClO, IO), water vapour etc. (Platt et al., 1979; Platt and Stutz, 2008, and many others). It's fundamentals are discussed in section 5.2.1, followed by a summary of the fit settings used for DOAS retrievals in this thesis in section 5.2.2. Section 5.2.3 finally examines retrieval uncertainties.

5.2.1 DOAS Formalism

Solar and infrared radiation experiences a wavelength dependent attenuation of its radiance I when travelling through the atmosphere, i.e. $\mathrm{d}I(\lambda) = -I(\lambda)\,\mathrm{d}\tau$. The *optical density* τ can be written as a product of *absorption coefficient* σ_i and *absorber density* ρ_i of a trace gas i, and a differential path length $\mathrm{d}s$. Integrating the relation over the whole path length L of light travelling through an absorbing medium from an emitter to a detector gives the *Lambert-Beer Law*:

$$I(\lambda,L) = I_0(\lambda)\cdot\exp\left(-\int_0^L \sum_i^n \sigma_i(\lambda)\cdot\rho_i(s)\,\mathrm{d}s\right) \tag{5.1}$$

If the absorption cross sections $\sigma_i(\lambda)$ are assumed to be constant along the light path, they can be separated from the integral, which becomes the *slant column density* (SCD or S), defined as the integrated concentration ρ of a trace gas i along a light path of length L:

$$\mathrm{SCD} = S_i(\lambda) = \int_0^{L(\lambda)} \rho_i(s)\,\mathrm{d}s \tag{5.2}$$

The measurement I is compared with a so called Fraunhofer reference spectrum I_0, named after the Fraunhofer lines contained in spectra emitted and absorbed from the sun's photosphere. Ideally, it does not contain any absorption of the targeted trace gases. However, in passive DOAS applications (i.e. I_0 is measured from scattered light without using an artificial light source) the Fraunhofer reference spectrum already contains absorptions of trace gases located overhead the measurement site. Therefore the SCD is called *differential* Slant Column Density (dSCD, ΔSCD or ΔS), referring to the differential absorption between the measurement I and the reference I_0. In order to account for additional effects, equation 5.1 must be expanded to include the Ring effect $R(\lambda)$ (Grainger and Ring, 1962; Lampel et al., 2015), Rayleigh scattering ε_R and Mie scattering ε_M (Wendisch and Yang, 2012),

and a separation of broadband (σ_i^b) and narrowband, or differential, characteristics (σ_i^d) of the trace gas cross sections σ_i:

$$I(\lambda,L) = I_0(\lambda)\cdot\exp\left(-R(\lambda)-\sum_i \sigma_i^d(\lambda)\cdot S_i(\lambda)\right)\cdot \exp\left[-L\cdot\left(\sum_i(\sigma_i^b(\lambda)\cdot\rho_i)+\varepsilon_R(\lambda)+\varepsilon_M(\lambda)\right)\right] \tag{5.3}$$

The first exponent now contains all narrowband components and the second exponent contains all broadband components. Solving equation 5.3 for $\ln(I/I_0)$ yields the *optical density* τ:

$$\begin{aligned}\tau &= \ln\left(\frac{I(\lambda)}{I_0(\lambda)}\right)\\ &= -R(\lambda)-\sum_i \sigma_i^d(\lambda)\cdot S_i(\lambda)-\sum_k b_k\lambda^k\end{aligned} \tag{5.4}$$

$\sum b_k\lambda^k$ is a polynomial to account for the second exponent of equation 5.3, which includes all broad band features. Due to noise of the measurement (section 3.2.8), potentially unaccounted effects, or approximations made (see below) the modelled optical density can in practice never perfectly match the measured optical density. Therefore, a least squares fit ("DOAS fit") is applied to find the minimum of the following cost function (dependencies omitted for readability):

$$\chi^2 = \left[\ln\left(\frac{I_0}{I}\right)-R-\sum_i \sigma_i^d\cdot S_i-\sum_k b_k\lambda^k\right]^2 \tag{5.5}$$

The unexplained remainder of the spectrum after minimisation (by varying the parameters S_i and b_k) is called the fit residual δ. Ideally, the residual is only composed of random noise. In order to detect a trace gas, its optical density needs to be larger than the residual. This measure can be used to estimate the detection limit for a particular species (section 3.2.8). Several absorbers can be measured simultaneously even if their absorption features are superimposed (Figure 5.1).

This is the standard DOAS approach, and equation 5.4 is called the *standard DOAS equation*. Rozanov and Rozanov (2010) point out that the following main assumptions need to be satisfied in the considered wavelength interval in order for the equation to be applicable:

1. The absorption cross section σ_i of the retrieved species has to contain a component rapidly varying with wavelength (σ_i^d), which can not be approximated by a low-order polynomial.

2. The wavelength dependence of the broadband parts (σ_i^b) as well as other scattering and extinction processes (ε_R, ε_M) can be approximated by a low-order polynomial.

3. The slant column S is independent of the wavelength.

4. Linearity of the optical density with respect to variations in the amounts and cross sections of absorbers and scatterers in the atmosphere.

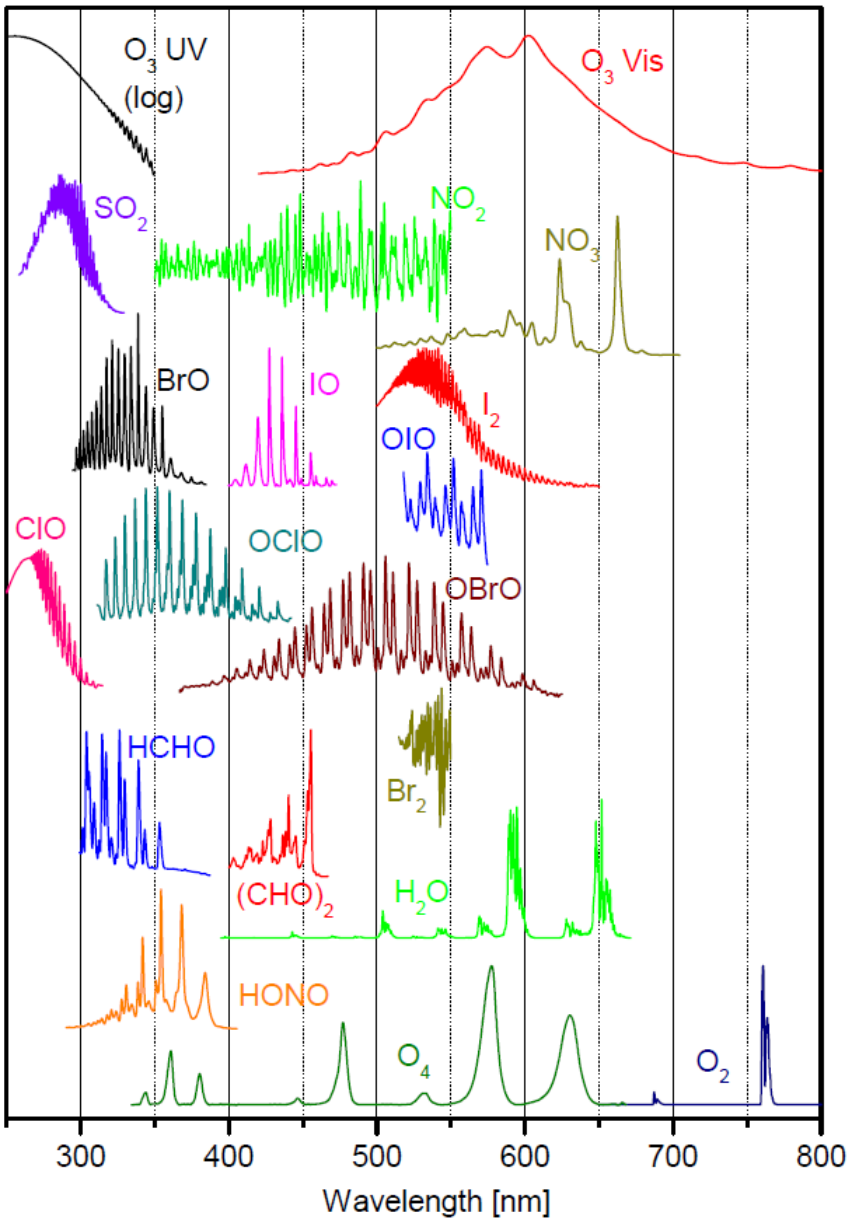

Figure 5.1: UV/Vis absorption cross sections of atmospheric trace gases relevant in atmospheric DOAS applications. Adopted from Platt and Stutz (2008).

Assumptions 1 and 2 are empirically satisfied by the choice of reference cross sections and DOAS polynomials (see below, Table 5.2). Assumption 3 may sound peculiar, because the column density of molecules in a particular light path should be independent of wavelength anyway. However, light path distributions change with wavelength, in particular if strong wavelength-dependent absorption is present (Platt et al., 1997; Pfeilsticker et al., 1998b; Puķīte et al., 2010; Puķīte and Wagner, 2016). When the light path changes, the sampled layers of the atmosphere and therefore also the integrated sum of trace gas molecules along the light path change. Wavelength ranges are therefore selected in way that avoids these circumstances, i.e. avoiding wavelengths below 335 nm (if possible) because of strong O_3 absorption, and minimising the width of analysed wavelength ranges. The wavelength-dependent light path distributions are again addressed in sections 5.3.2 and 6.1.1 in the context of radiative transfer modelling and the scaling method, respectively.

Considering assumption 4 it has to be noted that any spectrum recorded by the instrument is a stray-light spectrum that is convoluted with the instrument function H:

$$I^*(\lambda) = I(\lambda) * H = \int I(\lambda - \lambda') \cdot H(\lambda') \mathrm{d}\lambda' \tag{5.6}$$

In reality, trace gases absorb atmospheric light at "high resolution" (eq. 5.3) and the resulting spectrum is subsequently recorded by the instrument, i.e. processes by the instrument function. In the DOAS fit, convoluted cross sections are used to estimate the trace gas absorption. This exchange of the exponential (eq. 5.3) and the convolution (eq. 5.6) is an approximation applicable only in the case of weak absorptions (as is the case here), i.e. $\tau \approx 10^{-3} ... 10^{-2} < 0.1$.

5.2.2 Retrieval settings

Table 5.1 lists the trace gas absorption cross sections and Table 5.2 summarises the DOAS fit scenarios as they are set up in the scope of this thesis. The term *fit scenario* is used to refer to the complete set of parameters which is used in a DOAS spectral retrieval. A shift and squeeze of the channel wavelength mapping of the trace gas cross sections, as a group, relative to the measured spectra, is allowed. This compensates for changes in the channel to wavelength mapping (Stutz and Platt, 1996), e.g. due to temperature instabilities of the instrument (sect. 3.2.7). The following paragraphs explain the respective parameters of the fit scenario:

Fit windows The criteria for the selection of the wavelength ranges (fitting windows) are:

- A significant, rapidly with wavelength varying cross section of the targeted trace gas is available.
- Stable spectral retrieval resulting in low residuals.
- The wavelength range of the spectral retrieval of the scaling and target gas used in the scaling method (sect. 6.1) should be similar and overlap.

In the case of the visible wavelength range, all radiative transfer calculations are carried out at 477 nm, which is the central wavelength of an O_4 absorption band. Accordingly, the DOAS retrieval of O_3 and NO_2 is carried out in close wavelength ranges (Table 5.2). Retrieval interval mapping (Vogel et al., 2013) was intensively investigated for the spectral data collected by the HALO mini-DOAS instrument by Kenntner (2013). The technique exploits shifting the fitting windows systematically to determine the behaviour of key parameters such as the dSCD, the fit error, the residual, and shift and squeeze of the channel wavelength mapping. This supports better understanding of the behaviour of the spectral retrieval and the selection of adequate fitting windows.

Reference cross sections The reference cross sections listed in Table 5.1 are convoluted with the instrument slit function (sect. 3.2.4), which is retrieved from the wavelength calibration file (sect. 5.1.2). Absorption cross sections in the UV/vis wavelength range usually have a weak temperature dependence. Weighted mean temperatures of the trace gases observed by the HALO mini-DOAS instrument are typically in the range of 220-230 K (Figure B.4), and only change in particularly extreme conditions such as during dives (Figure 5.5). If an absorber exhibits significant absorption at strongly different temperature regimes, e.g. boundary layer and stratospheric ozone, it is accounted for by including two orthogonalised absorption cross sections of different temperatures (Platt et al., 1997). Often allowing for two reference cross sections for strong absorbers, such as O_3, improves the residual for the detection of an underlying target gas, e.g. BrO.

Solar I_0 effect The high resolution trace gas cross sections available in the literature are convolved with the appropriate instrument slit function (sect. 3.2.4). The convolution is carried out by considering the so-called Solar I_0 effect (Johnston, 1996; Wagner et al., 2001b; Aliwell et al., 2002; Platt and Stutz, 2008). This effect arises because of the interaction of the highly structured incident sun light with the trace gas cross sections. Dividing the measured spectrum (eq. 5.6) by the Fraunhofer spectrum (eq. 5.4) does not fully remove the Fraunhofer structures, because convolution and exponential can not be exchanged.

Instrument straylight The instrument straylight (sect. 3.2.2) is accounted for by a so-called 'Offset' polynomial I_{Ofs}. When considering a straylight term in a taylor series expansion of eq. 5.4, the straylight can be approximated by an additive polynomial $I_{\mathrm{Ofs}}(\lambda) \propto 1/I_0$ (Platt and Stutz, 2008, chapter 8.7.2).

Table 5.1: Trace gas absorptions cross sections used for the DOAS retrieval and their uncertainty according to the cited publications.

No.	Absorber	Temp.	Reference	Uncert.
1	O_4	293 K	Thalman and Volkamer (2013)	4%
2	O_3	223 K	Gorshelev et al. (2014); Serdyuchenko et al. (2014)	3%
3	O_3	293 K	Gorshelev et al. (2014); Serdyuchenko et al. (2014)	3%
4	NO_2	223 K	Bogumil et al. (2003)	3.4%
5	NO_2	293 K	Bogumil et al. (2003)	3.4%
6	H_2O	273 K	Rothman et al. (2009)	
7	HCHO	293 K	Chance and Orphal (2011)	5%
8	HONO	298 K	Stutz et al. (2000)	5%
9	BrO	223 K	Fleischmann et al. (2004)	10%
10	OClO	213 K	Kromminga et al. (2003)	5%

Ring effect When comparing measurements of direct and scattered sun light, Grainger and Ring (1962) discovered a *filling in* of Fraunhofer lines, which was thereafter termed *Ring effect*. It was shown that rotational Raman scattering (RRS) at molecules is the main reason for the Ring effect (Kattawar et al., 1981; Fish and Jones, 1995; Sioris and Evans, 1999), and further investigations have quantified its influence on Fraunhofer lines and trace gas absorptions (Bussemer, 1993; Chance and Spurr, 1997; Langford et al., 2007; Wagner et al., 2009a). The influence of vibrational Raman scattering (VRS) on DOAS measurements was recently analysed by Lampel et al. (2015), but its strength is of the order of 10^{-4}, which is below the noise level of the measurements discussed here. Because the amplitude and wavelength dependency are in the range of trace gas absorptions targeted by DOAS instruments, RRS has to be considered in the evaluation of DOAS measurements (Solomon et al., 1987; Vountas et al., 1998). The strength of the Ring effect strongly depends on the scattering angle and on the presence of aerosols and clouds. Because Mie scattering on cloud particles is an elastic process, the presence of clouds leads to a decrease of the Ring effect for optically thin clouds. On the other hand, multiple scattering inside optically thick clouds can strongly enhance the light path and thus increase the Ring effect (Wagner et al., 2014). With the help of radiative transfer models, the Ring effect is also used to retrieve information on radiative transfer properties of aerosols and clouds (Joiner and Bhartia, 1995; De Beek et al., 2001; Wagner et al., 2009b, 2014).

For retrievals in the scope of the present thesis, the Ring effect is considered via a simple Ring spectrum calculated from the Faunhofer reference spectrum (Bussemer, 1993) and an additional Ring spectrum, calculated from the former by multiplication with λ^4 and orthogonalised to the original Ring spectrum, as suggested by Wagner et al. (2009a).

Table 5.2: Fit scenarios (retrieval settings) employed for the DOAS retrieval of data recorded by the HALO mini-DOAS instrument with parameters as described in the text. The absorbers are listed in Table 5.1.

Target gas	λ (nm)	Fitted absorbers	Add. Param.	Polyn.
O_4	350 – 370	1, 2, 3, 5, 7, 9	I_{Ofs}, R, $R \cdot \lambda^4$	2
	460 – 490	1, 2, 4, 6	I_{Ofs}, R, $R \cdot \lambda^4$	2
O_3	335 – 362	1, 2, 4, 7, 9	I_{Ofs}, R, $R \cdot \lambda^4$	2
	450 – 500	1, 2, 4, 6	I_{Ofs}, R, $R \cdot \lambda^4$	2
NO_2	424 – 490	1, 2, 4, 6	I_{Ofs}, R, $R \cdot \lambda^4$	2
H_2O	490 – 520	1, 2, 5, 6	I_{Ofs}, R, $R \cdot \lambda^4$	2
HCHO	323 – 357	1, 2, 3, 5, 7, 8, 9	I_{Ofs}, R, $R \cdot \lambda^4$	2
HONO	337 – 372	1, 2, 3, 4, 7, 8, 9	I_{Ofs}, R, $R \cdot \lambda^4$	2
BrO	342 – 363	1, 2, 3, 4, 7, 9	I_{Ofs}, R, $R \cdot \lambda^4$	2
OClO	353 – 392	1, 2, 3, 4, 10	I_{Ofs}, R, $R \cdot \lambda^4$	2

Polynomial A multiplicative polynomial is applied to account for scattering processes with low wavelength dependency (sect. 5.2.1). Sensitivity tests with polynomials of orders from 1 to 5 are carried out, and a polynomial of order 2 is found to be sufficient for the fitting process. Higher orders increase the degrees of freedom of the cost function (eq. 5.5) and in this way can increase the instability of the retrieval.

Figure 5.2 shows examples of the detection of O_3, O_4, NO_2, HCHO, BrO and OClO in spectra collected during different HALO science missions. Figure 5.4 shows a comparison of O_3 dSCDs inferred from limb spectra at EA=0° with in-situ measured volume mixing ratios of O_3 from a flight section of science flight ANT. The flight altitude was 12-14 km, with a dive down to below 4 km altitude between 11:00 and 12:00. The correspondence of in-situ and remotely sensed O_3 provides a motivation for the scaling method, detailed in chapter 6.

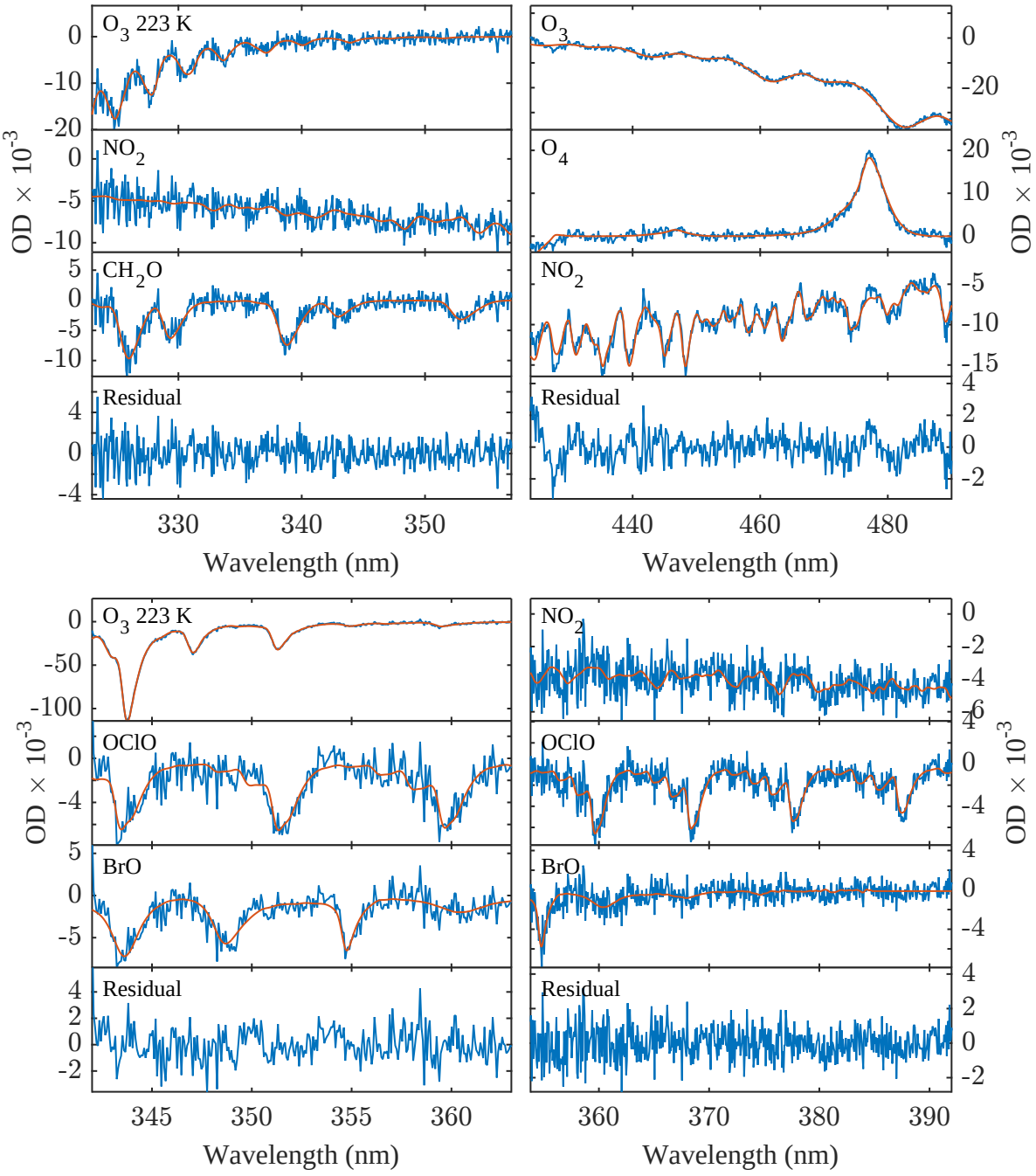

Figure 5.2: Sample DOAS fit results demonstrating the detection of a range of trace gases. Top left: HCHO fit scenario; spectrum from Acridicon science flight on Sept. 16, 2014. Top right: NO_2 fit scenario in the visible wavelength range; spectrum from science flight ANT. Bottom left: BrO fit scenario; spectrum from Polstracc science flight on January 31, 2016. Bottom right: OClO fit scenario, spectrum from Polstracc science flight on January 31, 2016.

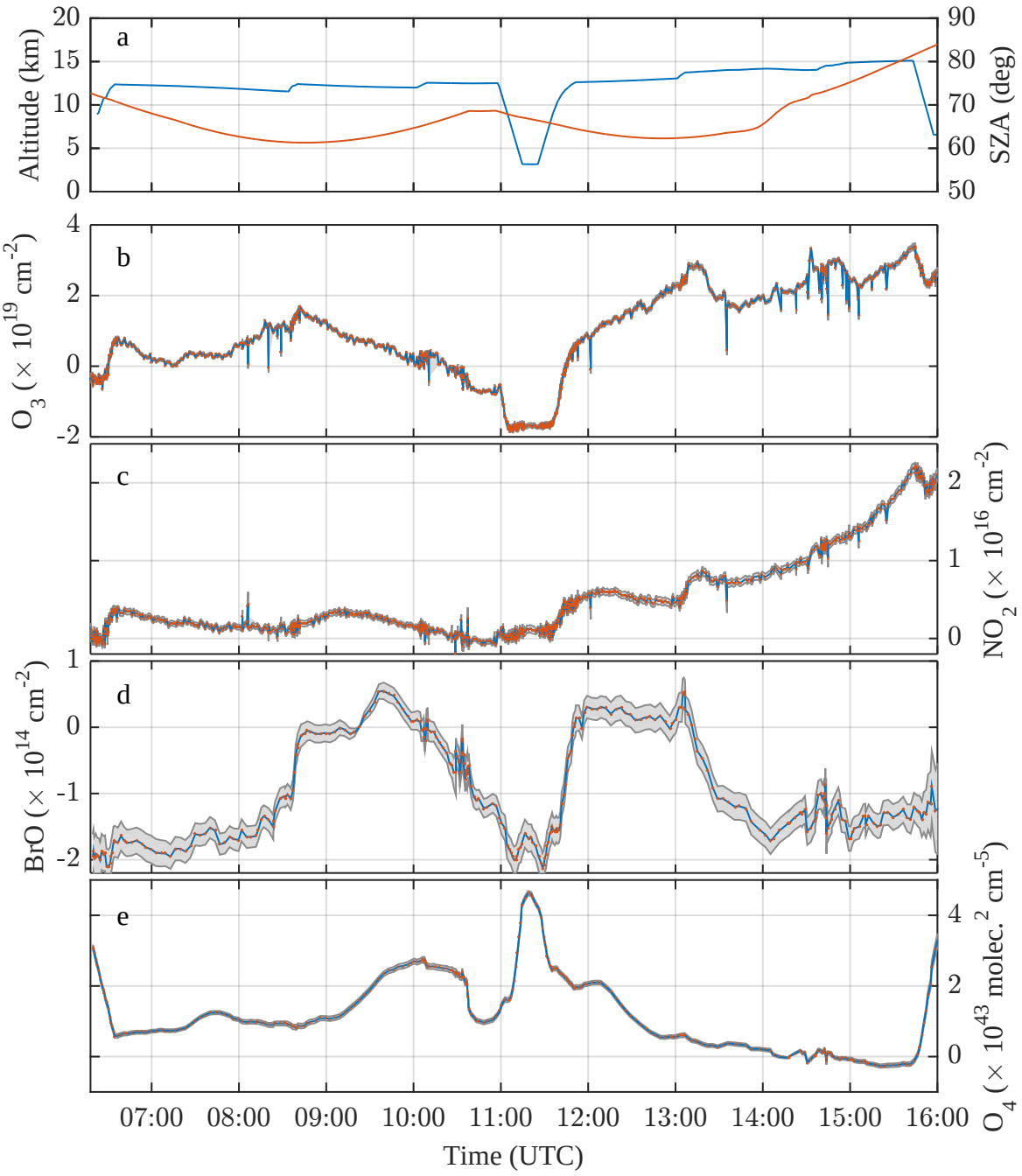

Figure 5.3: Retrieved dSCDs for science flight ANT. Panel (a) shows flight altitude and SZA during the measurement. Panels (b) and (c) show retrieved dSCDs of O_3 and NO_2, respectively, from the VIS4 channel. Panels (d) and (e) show retrieved dSCDs of BrO and O_4, respectively, from the UV2 channel. Both channels observe in limb geometry, and only the measurements at EA=0° are shown here. The measurements of the UV2 channel are smoothed to five-point running averages in order to reduce measurement noise. Red dots indicate the individual measurements, grey shaded areas show the DOAS fit error.

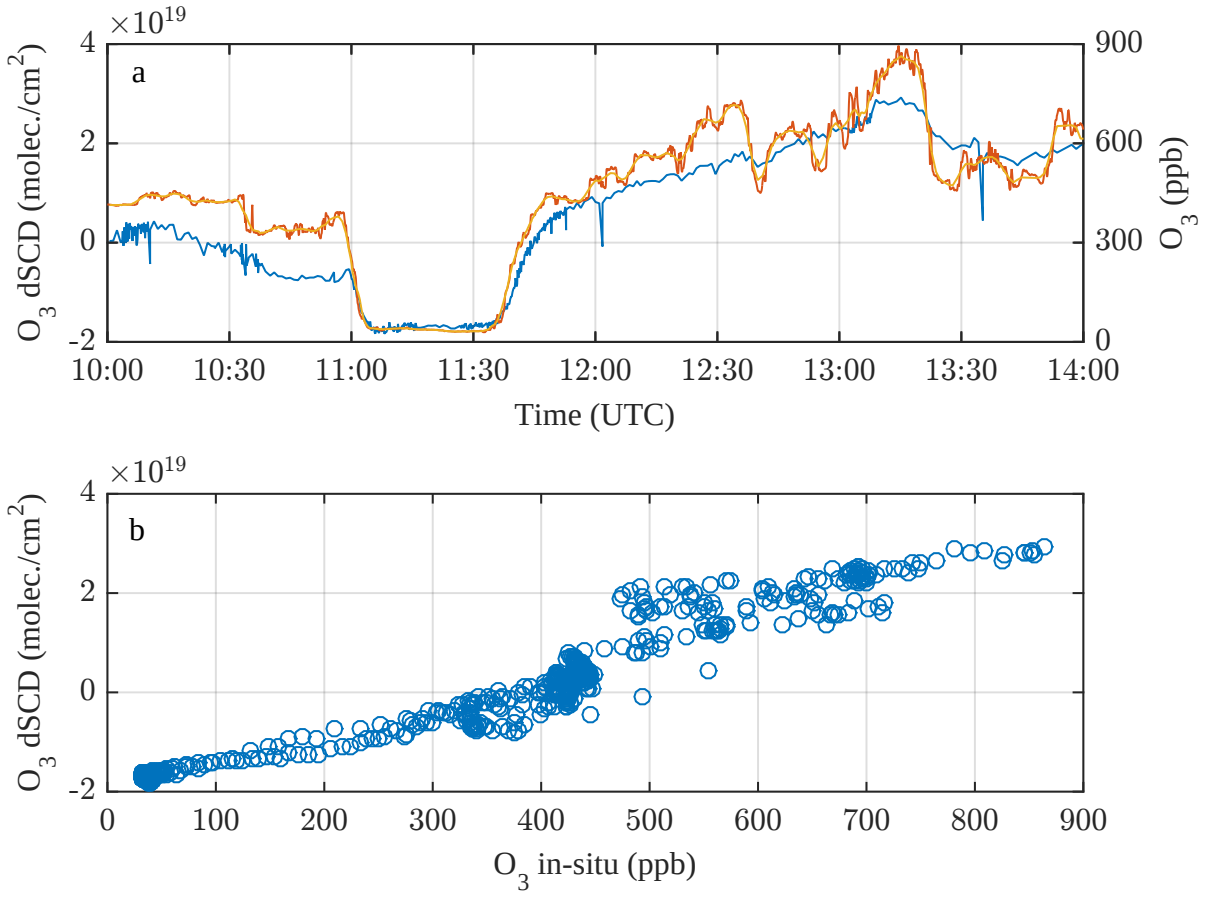

Figure 5.4: Top panel: Comparison of Fairo in-situ measured O_3 (red line), 5 min running averaged (orange line) and remotely sensed O_3 (blue line) versus flight time for a segment of science flight ANT. The aircraft carried out a descent from 12 km to below 4 km altitude at around 11:00 UTC, and a ascent to 13 km at around 11:40 UTC. Bottom panel: Correlation of in-situ measured 5-min running average O_3 and remotely sensed dSCD-O_3 for segment shown in top panel.

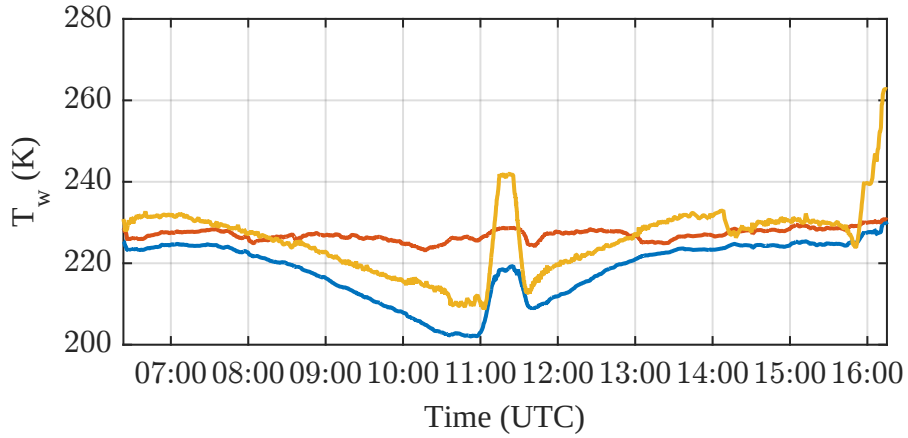

Figure 5.5: Weighted mean temperature T_w for the absorption of O_3 (blue), NO_2 (red), and O_4 (yellow) during science flight ANT. T_w is calculated by multiplying the BoxAMFs (sect. 5.3.2) with the trace gas profiles provided by the chemical transport model (sect. 5.4) to retrieve so-called contribution profiles (sect. 6.1), i.e. a measure for the amount of trace gas absorption at a certain altitude. Using the altitude temperature profiles provided by the CTM, the weighted mean temperature T_w of the observed trace gas absorption is retrieved.

5.2.3 Retrieval uncertainty

The uncertainty of the DOAS retrieval is estimated from three measures:

1. A retrieval uncertainty Δ_{Stutz} based on the retrieval residual is derived by multiplying the detection limit D_{theo} (equation 3.3) from Stutz and Platt (1996) by a factor of 4 as suggested by (Platt and Stutz, 2008, sect. 8.5).

$$\Delta_{\text{Stutz}} = 4 \times \delta \cdot \frac{6}{\sqrt{n-1}} \cdot \frac{1}{\sigma_{TG}} \tag{5.7}$$

2. A retrieval uncertainty Δ_{LSQ} is derived from the error Δ_{fit} of the fit coefficient given by the DOAS least squares fit by multiplying the fit error with a factor of 4 (Hausmann et al., 1999).

$$\Delta_{\text{LSQ}} = 4 \times \Delta_{\text{fit}} \cdot \frac{1}{\sigma_{TG}} \tag{5.8}$$

3. A more empirical retrieval uncertainty Δ_{empir} is estimated from the standard deviation of the dSCDs from fitting the spectra recorded during a science flight against two different Fraunhofer reference spectra. Figure 5.6 illustrates this exercise for NO_2 for science flight ML.

Typical residuals are of the order of $\delta \approx 1.2 \times 10^{-3}$ in the case of UV/visible spectra containing 100 readouts each. The residual decreases to $\delta \approx 6 \times 10^{-4}$ if a sequence of five spectra is added up. The columns are converted to mixing ratios through division by TND $\cdot l$ using the same assumptions as in sect. 3.2.8. Table 5.3 lists the resulting detection limits for trace gases detected in field measurements. All three measures give comparable detection limits within a factor of 2-3. The actual detection limit for measurements of a particular science flight or flight section depends on several factors, e.g. (a) the temperature stability of the instrument, (b) light path lengths depending on local meteorological conditions and SZA, and (c) stability of the measurement geometry, as well as radiative transfer effects not accounted for in the DOAS fit.

Table 5.3: Detection limits according to DOAS retrieval uncertainties estimated by three different measures (see text). O_3 and NO_2 uncertainties are estimated for science flight ANT. HCHO uncertainties are estimated for the Acridicon flight on September 16, 2014. BrO and OClO uncertainties are estimated for the Polstracc flight on January 31, 2016 (Dominique Loerks, pers. comm.).

Target gas	Δ_{Stutz} molec./cm^2	ppt	Δ_{LSQ} molec./cm^2	ppt	Δ_{empir} molec./cm^2	ppt
O_3 (vis.)	1.5×10^{18}	2234	2.4×10^{18}	3650	4×10^{18}	6075
NO_2	4.3×10^{15}	6.5	2×10^{15}	3.1	2×10^{15}	3.1
HCHO	1.8×10^{16}	28.6	1.6×10^{16}	24.3	7×10^{15}	10.7
BrO	7.6×10^{13}	0.12	1.6×10^{14}	0.25	2×10^{13}	0.04
OClO	7.5×10^{13}	0.12	8×10^{13}	0.13	3×10^{13}	0.05

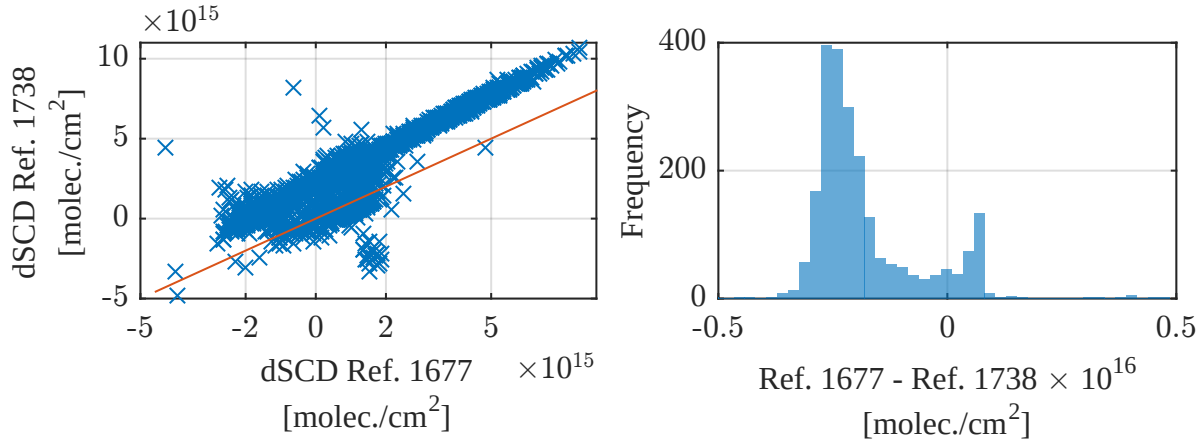

Figure 5.6: Comparison of the spectral retrieval of NO_2 using two different Fraunhofer reference spectra from science flight ML. Left panel: The strong correlation illustrates the stability of the spectral retrieval. Right panel: The dSCDs shown in the left panel are substracted from one another. The retrieval uncertainty Δ_{empir} is the standard deviation of the resulting frequency distribution.

5.3 Radiative transfer modelling

Knowledge of the light path distribution is necessary in order to calculate trace gas mixing ratios from slant column densities. Of particular interest is the contribution of the different atmospheric layers to the total absorpiton (dSCD). In order to obtain this information, the the radiative transfer equation (RTE, e.g. Wendisch and Yang (2012)) has to be solved. While no exact analytical solution has been found yet (Marshak and Davis, 2005), there are several approaches for simplifying and approximating the RTE. Prevalent methods to solve the RTE for the purpose of atmospheric remote sensing are *Discrete Ordinate* and *Monte Carlo* methods. Discrete ordinate methods divide each parameter into a limited set of grid points or cells, and thereby reduce the necessary computational effort. At the same time, these methods introduce errors by limiting e.g. the possible scattering angles. The other popular approach, the Monte Carlo method, is used in this thesis and explained in the following subsection. Subsequently, the concept of Air Mass Factors (AMFs) is presented, which are the main quantities derived from the radiative transfer model (RTM) and used to calculate trace gas mixing ratios with the scaling method (chapter 6).

5.3.1 The Monte Carlo method

As the name suggests, Monte Carlo methods are based on statistical modelling of scattering properties. The RT model of choice for the present thesis is McArtim (Deutschmann, 2008; Deutschmann et al., 2011; Deutschmann, 2014). McArtim solves the RT for a fully spherical and refractive atmosphere using the so-called backward Monte Carlo technique in combination with ray tracing. The modelled photons are emitted at the telescope, with the initial trajectory weighted by the telescope's FOV. Scattering events along the photon's path are then modelled by successive order of scattering, whereby for each absorption and scattering event the probability is calculated that the photon origi-

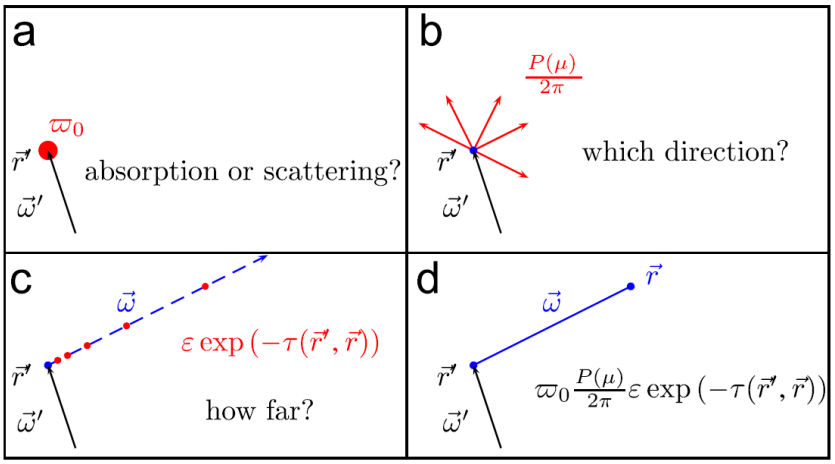

Figure 5.7: Schematic depiction of the random sampling of a) the single scattering albedo ω_0 for a photon travelling along path $\vec{\omega}'$ and arriving at $\vec{r}'$, b) the scatter angle, depending on phase function $P(\mu)$, c) the free light path in new direction $\vec{\omega}$, with the extinction coefficient ε and the optical density τ between $\vec{r}'$ and $\vec{r}$. Panel d) shows all multiplied probabilities which characterize one scattering event. Adopted from Deutschmann et al. (2011).

nated from the sun (Figure 5.7). Backward RT modelling favors the computational effort, because a photon light path in this direction is more likely to happen than vice versa. Because of the so-called *principal of reciprocity*, the solution of the time-reversed RTE, or *adjoint* RTE, is the same as for the regular RTE (Deutschmann et al., 2011). The accuracy of Monte Carlo models depends on the number of photons considered, while McArtim also applies variance reduction techniques (Deutschmann, 2014). With 10,000 photons, as applied in the scope of this thesis, the SCDs and radiances are simulated with an uncertainty of $\approx 1\%$, and the Air Mass Factors (see next section) with an uncertainty of $\approx 3.5\%$.

Table 5.4: Overview of the different variables and parameters required for the model atmosphere in McArtim.

Variable name	**Description**	**Unit**	**Value/source**
SZA	Angle between the position of the Sun and the zenith	°	BAHAMAS
SAA	Azimuth angle of the Sun with respect to the North	°	BAHAMAS
North azimuth	Azimuth viewing direction of the telescope (= viewing direction) towards the north pole meridian; north azimuth = heading direction of the aircraft	°	BAHAMAS
SRAA	Sun relative azimuth angle: angle between the azimuth angle of the Sun and the azimuth viewing direction of the telescope; SRAA = SAA - north azimuth	°	BAHAMAS
Elevation angle α	Angle between the horizon and the line of sight of the telescope	°	instrument records
Colatitude	90° - latitude	°	BAHAMAS
Longitude		°	BAHAMAS
Altitude	Altitude of the HALO aircraft	km	BAHAMAS
Ground albedo	Ground albedo of sea / land	-	sea: 0.15 land: 0.3
SSA	Singe scattering albedo	-	clouds: 0.999 aerosol: 0.97
ε (extinction)	Vertical extinction profile of aerosol or cloud particles	km^{-1}	SAGEII, Calipso
g	Asymmetry parameter of the Henyey-Greenstein parametrisation of the phase function	-	clouds: 0.75 aerosol: 0.72
Air data	Vertical profiles of temperature and pressure of the air	hPa, K	CLaMS, EMAC
Strong absorbers	Concentration profiles of trace gases with high optical depth in the atmosphere (e.g. O_3, O_4, NO_2) that influence the light path	$molec/cm^3$	CLaMS, EMAC
FOV	Field of view of the telescopes	°	sect. 3.2.5
λ	Wavelength (compare sect. 5.3.2)	nm	477 nm (vis), 340 nm (UV)

5.3.2 Air Mass Factors

Air Mass Factors (*AMF* or *A*) depend on the wavelength λ, the viewing geometry Ω (telescope elevation angle (EA), SZA, SRAA, FOV (sect. 3.2.5)) and the optical state ε (e.g. presence of clouds, aerosol optical depth (AOD), strong absorbers like water vapor, etc.) of the atmosphere. The concept was first introduced for ground based zenith-sky measurements, in order to enable the conversion of slant column amounts S to vertical column amounts V of a measured trace gas, e.g. stratospheric ozone (Solomon et al., 1987; Perliski and Solomon, 1993). They are defined as the enhancement factor

$$A(\lambda,\Omega,\varepsilon) = \frac{S(\lambda,\Omega,\varepsilon)}{V}. \tag{5.9}$$

The primary output of the RTM simulations are so-called Box Air Mass Factors (*BoxAMFs* or *B*), of which examples are shown in the left panels of Figure A.18. They are the Air Mass Factors of a box, in our case an atmospheric layer, j, of the atmosphere with height h_j. The slant column density S_i of a gas i can then be written as the layerwise sum of the product of the BoxAMFs B_j and the trace gas columns $\rho_{ij} \cdot h_j$ in the respective layers j:

$$S_i = \sum_j B_j(\lambda,\Omega,\varepsilon) \cdot \rho_{ij} \cdot h_j. \tag{5.10}$$

In general, there are two caveats: First, Marquard et al. (2000) show that these relations only strictly hold if the optical density is a linear function of the absorption coefficient $k_i = \sigma_i \cdot \rho_i$ (compare sect. 5.2.1). Effects of nonlinearity, i.e. multiple scattering and its wavelength dependence, are discussed in e.g. Rozanov and Rozanov (2010); Puķīte et al. (2010). This is insignificant in the case of weak absorption discussed here ($\tau \approx 10^{-3}$). Second, the AMFs are in general wavelength dependent (Platt et al., 1997). The wavelength-dependence is weak in the visible wavelength range, but increases at lower wavelengths in the UV due to strong O_3 absorption. Hence, it is desirable to use short wavelength intervals and avoid strong O_3 absorption for DOAS retrievals of individual trace gases. The treatment of unequal BoxAMFs for the scaling and target gas of the scaling method is discussed in section 6.1.1.

The RTM McArtim calculates BoxAMFs B_j of a layer j of the height h_j as derivatives of the radiance I_* with respect to the absorption coefficient k_{ij} of trace gas i in layer j:

$$B_j \cdot h_j = -\frac{\mathrm{d}\ln I_*}{\mathrm{d}k_{ij}} = \frac{\left\langle \sum_n^N w_n l_j^n \right\rangle}{\left\langle \sum_n^N w_n \right\rangle} \tag{5.11}$$

On the right hand side of equation 5.11, the sums comprise N photon trajectories n, where w_n is a weight, or probability, of a trajectory n, and l_j^n is the path length of trajectory n in layer j (Deutschmann et al., 2011). This can be interpreted as the *intensity weighted photon path length* through layer j, or as the *sensitivity* of a measurement of atmospheric radiation towards trace gas absorption in the atmospheric layer j (Deutschmann, 2014, sect. 6.2.2).

5.4 Chemical transport models

The CTMs provide curtains of atmospheric properties along the flight trajectory of the aircraft. The use reanalysed meteorological data from the ERA-interim dataset by ECMWF. The accuracy of this data can be assessed by comparing in-situ measured temperature and pressure with model data (Figure A.9). Typical accuracies of modelled meteorological parameters are $\Delta T < 1$ K and $\Delta p < 10$ hPa for temperature and pressure, respectively.

5.4.1 CLaMS

The simulation by the Chemical Lagrangian Model of the Stratosphere (CLaMS) was used in the present thesis for interpertation and comparison. CLaMS is a Lagrangian chemistry transport model (CTM) system developed at Forschungszentrum Jülich, Germany. The specific model setup is described in detail by Vogel et al. (2014). It is driven by horizontal winds from ERA-Interim reanalysis (Dee et al., 2011) provided by the European Centre for Medium-Range Weather Forecasts (ECMWF). The horizontal resolution of CLaMS is 100 km and the simulation period ranges from May 2012 until October 2012. It is initialized using satellite data from AURA-MLS and ACE-FTS as well as tracer-tracer-correlations. For further details of the model run, see Vogel et al. (2014) and references therein. Due to its Lagrangian construction, the model is particularly good at representing tracer gradients (e.g. the extratropical tropopause or the polar vortex edge). It should be noted that this simulation is not primarily suited to reproduce the lower tropospheric photochemistry in detail. Therefore the employed chemistry setup does only contain reactions of importance within the stratosphere (Grooß et al., 2014) and it does neither contain sources of higher carbon compounds (e.g. VOCs and NMHCs) nor any interactions of the chemical compounds with clouds. Thus model results of short-lived species between the ground level and the free troposphere probaly are not reliable (J.-U. Grooß, pers. comm.).

5.4.2 EMAC

The ECHAM/MESSy Atmospheric Chemistry (EMAC)[1] model is a numerical chemistry and climate simulation system that includes sub-models describing processes in the troposphere and middle atmosphere and their interaction with oceans, land and human influences (Jöckel et al., 2010). It uses the second version of the Modular Earth Submodel System (MESSy2) to link multi-institutional computer codes. The core atmospheric model is the 5th generation European Centre Hamburg general circulation model (ECHAM5, Roeckner et al., 2006). For the present study the EMAC (ECHAM5 version 5.3.02, MESSy version 2.51) is applied in the T42L90MA-resolution, i.e. with a spherical truncation of T42 (corresponding to a quadratic Gaussian grid of approx. 2.8 by 2.8 degrees in latitude and longitude) with 90 vertical hybrid pressure levels up to 0.01 hPa (P. Joeckel, pers. comm.).

The activated modules for the simulations used in the present thesis are Air-Sea exchange (AIRSEA),

[1] http://www.messy-interface.org/

CH_4 module (simplified chem.) (CH_4), CLOUD Optical Properties (CLOUDOPT), CONTRAIL, CONVECTion module, new ConVective tracer TRANSport (CVTRANS), 222Rn (DRADON), Dry DEPosition (DDEP), Gravity Waves (GWAVE), correction of H_2O + feedback (H2O), J Values (JVAL), lightning NO_x (LNOX), MECCA (AERO), ONline EMISsions (ONEMIS), QBO nudging (QBO), Radiation (RAD), Passive Tracers (PTRAC), Orbits (ORBIT), Sampling in 4 dimensions S4D, SATellite SIMulatorS (SATSIM), SCAVenging (SCAV), Selectable Column OUTput (SCOUT), aerosol SEDImentation (SEDI), Sample along ORBIT (SORBIT), Surf Lake Icetemp Sicetemp (SURFACE), Tracer Budget (TBUDGET), Tracer NUDG(E)ing (TNUDGE), Tracer Release EXPeriment (TREXP), TROPOPause (TROPOP), Values on horizontal ISO-surfaces (VISO) (S. Matthes, pers. comm.).

5.5 Determination of the Fraunhofer reference SCD

The retrieved dSCD from the spectral retrieval described in equation 5.5 is the *differential* slant column density (dSCD) with respect to the Fraunhofer reference spectrum. In order to calculate the total SCD, the absorption already present in the Fraunhofer reference spectrum has to be determined. This is called the Fraunhofer reference SCD (SCD_{Ref}):

$$SCD = dSCD + SCD_{Ref} \tag{5.12}$$

In many DOAS applications, either a zenith sky spectrum or a direct sun light spectrum is used as Fraunhofer reference, and SCD_{Ref} is calculated by geometrical approximations. This relatively simple approach is not applicable for measurements with the HALO mini-DOAS instrument , because every atmospheric spectrum recorded during a flight is a scattered light spectrum with potentially very complicated light path distributions (compare Figure 2.1). SCD_{Ref} can however be calculated with the radiative transfer model (sect. 5.3), if the optical state of the atmosphere, i.e. the Mie extinction profile and the profiles of the considered species, is sufficiently well known. The following subsection describes the method of optimal estimation, by which the optical state of the atmosphere is retrieved (sect. 5.5.1). This is carried out for three sample flight sections, and the Fraunhofer reference SCDs of the other flights of the TACTS/ESMVal campaigns are retrieved by either comparing their reference spectra with the references of the sample flight sections or by simulations assuming similar aerosol profiles (sect. 5.5.3). Section 5.5.2 discusses the limitations of the method of optimal estimation to retrieve mixing ratios for full flights in the given measurement geometry, and motivates the novel approach to derive trace gas abundances described in chapter 6.

5.5.1 Inversion by optimal estimation - Formalism

Inversion by optimal estimation is an established approach for the interpretation of ground-based, air-borne, and space-borne DOAS measurements. Rodgers (2000) describes the concept of inversion by optimal estimation for the retrieval of atmospheric properties from remote sensing instruments. Bruns et al. (2004) show the conceptual adaptation to limb viewing DOAS instruments on aircraft

platforms. The formalism is replicated here in abbreviated form in the same formulation as in sect. 7.1 of Werner (2015).

A set of measurements y can be approximated by a forward model $F(x,b)$, with the vertical profile x and forward model parameters b:

$$y \approx F(x,b) + \varepsilon \tag{5.13}$$

ε is the sum of the measurement and model errors. In our case, y is the vector of measured slant column densities and x is the vertical Mie extinction profile. However, the problem is often mathematically ill-posed because of a lack of information content in y to fully represent x. In order to constrain the problem, a priori information $x_a + \varepsilon_a$ is introduced. After the measurement, one seeks a value $\hat{x}$ that is the best compromise of measurement information and a priori information. Assuming Gaussian error propagations, the probabilities for x and y given x are:

$$P(x) = \frac{1}{S_a(\sqrt{2\pi})^n} \exp\left[-\tfrac{1}{2}(x-x_a)^T S_a^{-1}(x-x_a)\right] \tag{5.14}$$

$$P(y|x) = \frac{1}{S_\varepsilon(\sqrt{2\pi})^{mn}} \exp\left[-\tfrac{1}{2}(F(x)-y)^T S_\varepsilon^{-1}(F(x)-y)\right] \tag{5.15}$$

S_ε and S_a are the measurement and a priori error covariance matrices, where the square errors are the diagonal elements. Applying Bayes' theorem one obtains

$$P(x|y) \sim \exp(-\left[(F(x)-y)^T S_\varepsilon^{-1}(F(x)-y) + (x-x_a)^T S_a^{-1}(x-x_a)\right]). \tag{5.16}$$

The maximum value for $P(x|y)$ is the same as the minimum value of the cost function

$$\chi^2(x) = \left[(F(x)-y)^T S_\varepsilon^{-1}(F(x)-y) + (x-x_a)^T S_a^{-1}(x-x_a)\right]. \tag{5.17}$$

The optimal state $\hat{x}$ is the solution to

$$\nabla_x \chi^2(x) = 0. \tag{5.18}$$

Depending on the nature of the forward model the solution $\hat{x}$ can be found directly in the linear case or iteratively for the non-linear case.

Linear case In the linear case the forward model can be described by

$$F(x) = Kx \rightarrow \nabla_x F(x) = K, \tag{5.19}$$

where K is the so-called Kernel matrix or weighting function matrix, containing the partial derivatives $K_{ij} = \partial F_i(x)/\partial x_j$. These weighting functions describe the dependence of the slant column densities on the vertical profile for each measurement. In other words, they give the change of the slant column densities due to variations of the trace gas concentration by a certain amount at a certain altitude. Combining equations 5.18 and 5.19 yields:

$$\hat{x} = (K^T S_\varepsilon^{-1} K + S_a^{-1})^{-1}(K^T S_\varepsilon^{-1} y + S_a^{-1} x_a) \tag{5.20}$$

Non-linear case In the non-linear case, which is applied in the retrievals in sect. 5.5.3, χ^2 has to be minimised by numerical methods. This is done iteratively, and the most basic method is the *Gauss-Newton* method. In this method, the gradient of the χ^2-landscape

$$\nabla_x \chi^2(x) =: g(x) \tag{5.21}$$

is followed iteratively, such that

$$x_{i+1} = x_i - [\nabla_x g(x_i)]^{-1} g(x_i) \tag{5.22}$$

with the Hessian elements

$$H_{GN} := \nabla_x g(x). \tag{5.23}$$

In cases of very strong non-linearity however, there are cases when the Gauss-Newton algorithm does not converge. Levenberg (Levenberg, 1944) and Marquardt (Marquardt, 1963) suggested to modify the Hessian elements of the Gauss-Newton method and to use:

$$H_{LM} = H_{GN} + \gamma S_a^{-1} \tag{5.24}$$

The Levenberg-Marquardt algorithm thus combines the Gauss-Newton method with the so-called *steepest descent*, which is slow but more stable in strongly non-linear cases. Therefore, γ should be increased in strongly non-linear and decreased in less non-linear cases in order to allow for the faster Gauss-Newton method (Rodgers, 2000, chapter 5.7).

5.5.2 Limitations of optimal estimation

In principal, inversion by optimal estimation (OEI) could be applied to all sections of a measurement flight and, as mentioned above, has been used often in similar cases. However, the retrieval from measurements aboard fast moving aircraft platforms poses major challenges to this method. Bruns et al. (2004) study the sensitivity of the retrieval towards tropospheric trace gas profiles using simultaneous DOAS measurements of a fixed set of EAs. They assume a clear sky atmosphere, which occurs very rarely in the Earth atmosphere. This is the reason why only few flight sections are applicable to OEI. Because the optical state of the atmosphere (e.g. the Mie extinction profile) determines the light path distribution, three limitations arise for inversion by optimal estimation:

1. Spatially and temporally changing atmospheric conditions demand too much a priori information.

2. Constraints for Mie extinction by e.g. O_4 absorption or relative radiances are strongly modulated by the optical state of the atmosphere outside of the directly sampled area.

3. Cloud patterns are changing rapidly at low altitudes. A constant optical state of the atmosphere can therefore not be assumed during the time when a set of measurements at different EAs is carried out subsequently.

The first limitation is obvious if one considers the scales of time and space involved in the measurement. For example, an ascent or descent of the aircraft typically covers distances of 50-200 km. If one considers an average Mie extinction profile, the result can be unrealistic, depending on the change in cloud cover. If one approaches the problem with a changing Mie extinction profile, a priori information for every altitude at each point in time (i.e. measurement) is necessary. Because a priori knowledge of such high spatial resolution and accuracy is not available, the result will heavily rely on assumptions regarding the optical state of the atmosphere. The alternative approach to the ascent/descent is the use of a set of EAs. However, the HALO mini-DOAS instrument records EAs successively. If the integration time per spectrum is 30 s, the recording of a set of 10 EAs takes 5 minutes, in which the aircraft (velocity 200 m/s) covers a distance of 60 km. Again, the change in cloud cover from one spectrum to the other and the assumption of an average Mie extinction profile can alter the results in uncontrollable ways.

The second limitation comes into play if one attempts to retrieve the Mie extinction profile from O_4 measurements of a set of EAs. O_4 is a collisional complex and is also referred to as tetraoxygen or $(O_2)_2$ to point out that it is not a bound molecule. Collision induced absorption that excites $O_2 + O_2$ to the singlet states $^1\Sigma_g$ and $^1\Delta_g$ occurs from the UV to the visible wavelength range (Perner and Platt, 1980; Greenblatt et al., 1990). It was first predicted by Lewis (1924). The lifetime and rate coefficient of $O_2 + O_2$ are however unknown, and therefore it is not possible to measure the absolute absorption cross section σ_{O_4}. Its product with the equilibrium constant K_{eq} is detected instead:

$$\alpha_{O_4} = \frac{\varepsilon(T)}{[O_2]^2} = K_{eq} \cdot \sigma_{O_4} \tag{5.25}$$

$[O_2] = 0.2094 \cdot p/(k_B \cdot T)$ is the oxygen number density, and ε the absorption per unit length. Due to its proportionality with $[O_2]^2$, O_4 decreases exponentially with altitude with a scale height of ≈ 4 km (Figure B.9 on page 180, right panel). O_4 contributes to the atmospheres energy balance (Pfeilsticker et al., 1997b) and is an important parameter for DOAS measurements. Since its relative profile is well known, it is convenient to use O_4 to retrieve information on e.g. multiple scattering, clouds, and light path lengths from atmospheric stray light measurements (Erle et al., 1995; Wagner et al., 1998; Pfeilsticker et al., 1998a; wag).

However, shortcomings of using O_4 in airborne measurements at high altitudes are apparent if one calculates the product of the O_4 profile and the BoxAMFs (sect. 5.3.2). The result is called the *contribution* profile C and is defined below in eq. 6.4. The contribution profile visualizes the contribution of each altitude layer to the total O_4-OD detected in the measured spectra. Figure 5.8 shows the O_4 contribution profile (here multiplied by the O_4 absorption cross section) for a measurement at 17 km altitude for a clear sky atmosphere (panel a) and the cases of two cloud covers (panels b and c) of different OD just above the planetary boundary layer (PBL) (i.e. like marine stratocumulus clouds, mSc). Even for EAs around 0°, and in a clear sky atmosphere (panel a), the OD of O_4 is strongly influenced by "upwelling" photons, i.e. light beeing backscattered from the lower parts of the atmosphere (e.g. Oikarinen, 2002). Cloud cover at low altitudes (panels b and c) strongly increases the O_4-OD due to the increased albedo. The O_4-OD is then dominated by upwelling photons. A small change in cloud cover thus results in a strongly changing O_4-OD at all EAs, which makes it

impossible to constrain a retrieval of the Mie extinction profile on the O_4-ODs (compare also figures 5 and 7 in Stutz et al. (2016)). Therefore, the scattering properties of the troposphere - even of those parts which are not being directly sampled by the telescope's field of view (FOV) - may mimic the presence, or lack of, aerosols and cloud particles at flight altitude. Thus if a significant fraction of the targeted gas is located off the telescope's field of view, assigning proper amounts of the measured gas to the correct locations in the atmosphere becomes ambiguous, or impossible. In consequence until the recent past, the retrievals of UV/vis limb measurements had been restricted to clear or almost clear sky observations (Baidar et al., 2013; Volkamer et al., 2015).

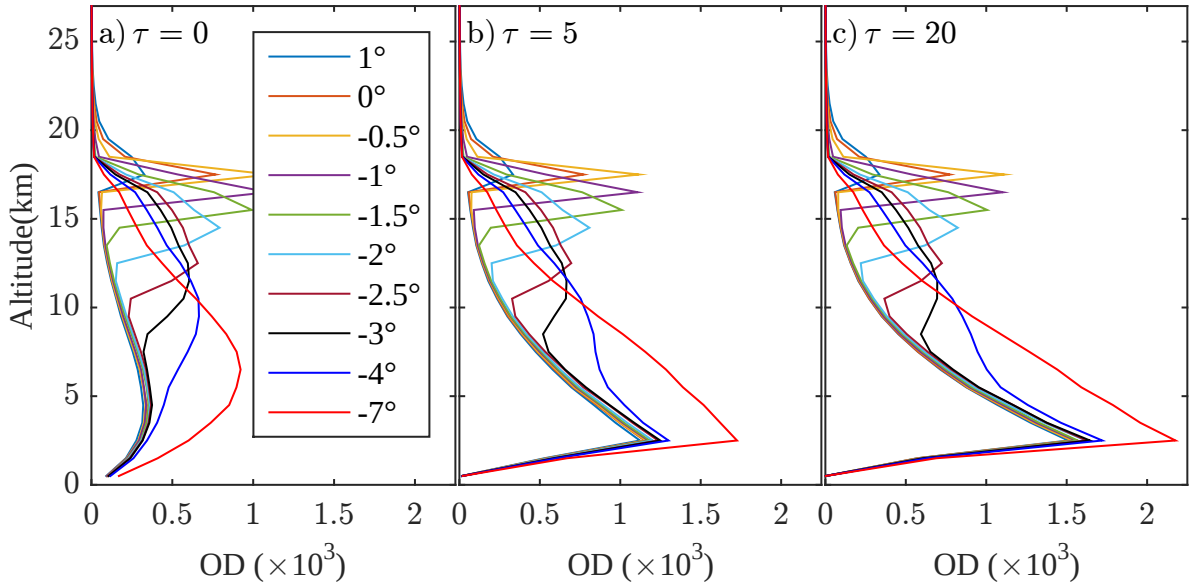

Figure 5.8: Altitude profiles of the O_4 optical density (OD) at 360 nm. Simulated for a set of elevation angles (see legend) for a measurement altitude of 17 km. The optical density τ of the cloud layer at 1-2 km altitude is 0 (panel a), 5 (panel b) and 20 (panel c), respectively. Adapted from Stutz et al. (2016). Note that the OD (eq. 5.4) is the product of the contribution C (eq. 6.4) and the absorption cross section σ.

5.5.3 Fraunhofer reference SCDs of the TACTS/ESMVal mission

Inversion by optimal estimation can not be used efficiently to retrieve the state of the atmosphere for all flight sections, as is examined in section 5.5.2. Three flight sections are selected due to their proximity to the reference spectra of the respective flights and their relative absence of clouds (see camera images in appendix A.3). The latter renders the retrieval of Mie extinction profiles relatively more reliable:

1. A horizontal flight track above the tropical Atlantic ocean, west of Africa, on the 11. September 2012. At a constant flight altitude, scans with elevation angles between +1°and -5°provide altitude dependent information.

2. The take-off from Cape Town and ascent over South Africa on 15. September 2012.

Table 5.5: Selected flight sections for Mie extinction profile retrievals.

Section No.	Date	Time [UTC]	Altitude [km]	Spec. No.	Ref. No.
1	09/11/2012	11:55 – 12:20	12.5	943 – 1080	998
2	09/15/2012	6:28 – 6:50	5.1 – 12.5	1 – 115	115
3	09/18/2012	11:54 – 12:18	13.1 – 1.3	2064 – 2173	2066

3. The landing approach towards Cyprus on 18. September 2012. The descent started above the coast of Lebanon and continued above the Mediterranean until touchdown on Cyprus.

The meteorological conditions are indicated by the images taken by the aircraft camera (appendix A.3 from page 158) and the specifics of the flight sections are summarised in Table 5.5. The SCD_{Ref} calculated by McArtim using the retrieved Mie extinction profiles are summarised in Table 5.6.

For flight section 1, two Mie extinction retrievals are carried out: One based on the differential O_4 optical density, and one based on relative logarithmic radiances. The measurements are averaged for each elevation angle over the 23 scanning sequences carried out during the flight section. The a priori aerosol profile is compiled from climatological "cloudless" SAGEII[2] and Calipso[3] data. The aircraft position at the time of the reference spectrum was 0.5°S, 7.0°E, the selected SAGEII data is from 5°S (summer 2004), and the selected Calipso data is from 0°E, 10°S (September 2011). However, the climatological nature of the a priori (averages over several months and/or several degree latitude and longitude) imply a large a priori uncertainty of 80%. Since the altitude resolution ranges between 2 and 4 km (Bruns et al., 2004, Figure 2), a retrieval grid of 3 km appears to be appropriate. The retrievals results are shown in figures A.10 and A.11. The relatively small set of 6 different elevation angles does not give good profile information for the full altitude range: The averaging kernels directly above and below flight altitude are near 1, but all other values are smaller than 0.5 or much smaller. The retrieved aerosol profiles are similar over a large altitude range, with extinctions of around 0.01 km^{-1} near 10 km and near 5 km altitude, and a minimum in extinction in between. The retrieval results strongly disagree at the lowest and highest altitudes, i.e. at the "edges" of the retrieval grid. Both these disagreements and the low averaging kernels at altitudes below 10 km reduce confidence in the retrieved aerosol extinction profile.

In order to retrieve aerosol profiles with much higher altitude resolution, two other flight sections are analysed. Flight section 2 covers a take-off from Cape Town and the subsequent ascent over South Africa. All measurements were recorded wkth EA = 0° at altitudes between 5 and 12.5 km (Table 5.5). The resulting profile retrieval is shown in Figure A.13. The averaging kernels above 5 km are between 0.6 and 1, but drop sharply below 5 km. Flight section 2 took place over land (Figure A.14) and the ground albedo was accordingly set to 0.3 in the RT simulation. The retrieved extinction profile shows an extinction of around 0.006 km^{-1} above 9 km altitude and lower values of

[2]NASA Langley Research Center Atmospheric Science Data Center. https://eosweb.larc.nasa.gov/project/sage2/sage2_v7_table

[3]NASA Langley Research Center Atmospheric Science Data Center. https://eosweb.larc.nasa.gov/project/calipso/cal_lid_l3_apro_cloudfree-standard-V3-00

around 0.003 km^{-1} below. Below 4 km altitude the Mie extinction decreases further, albeit with high uncertainties. However since no other measurements are available which probed the atmosphere near the ground, the inferred Mie extinction can not be validated.

Flight section 3 (Figure A.15) is a landing approach towards Cyprus, most of which took place over sea. At the beginning and in the end several minutes over Lebanon and Cyprus are over land. This flight section spans the largest altitude range, from above 13 km to below 2 km. For most altitudes, the averaging kernels are between 0.4 and 0.8, i.e. most of the information is inferred from the measurements. The retrieved extinction profile shows an overall increase from the highest altitude towards the ground, with maximum extinctions near the ground of >0.06 km^{-1}. However, the shape of the O_4 OD measurements in the last part of the descent can not be fully reproduced: The measured ODs drop sharply just below 4 km altitude. This coincides with the approach to the island of Cyprus, which strongly alters the ground albedo. The change in ground albedo during the measurement is therefore a major caveat on the results of this retrieval, especially at altitudes below 4 km.

Most of the uncertainty for inferring the O_3 and NO_2 SCD_{Ref} is not due to the cloud cover below the aircraft, but due to changing aerosol optical depth (AOD) at flight altitude and uncertainty of the overhead trace gas column. Both parameters are altered in sensitivity tests to determine the uncertainty of SCD_{Ref}. AOD profiles from climatological satellite data and retrieved from OEI are both employed. The overhead trace gas columns are provided by the CTM CLaMS up to an altitude of ≈ 28 km. They are further extrapolated up to 60 km assuming an exponential decrease of the concentration with a scale height of 8 km, i.e. assuming constant mixing ratios. Constant O_3 mixing ratios are a good approximation (Brasseur and Solomon, 2006), while variations due to seasons and the solar cycle can be up to a few percent (Ball et al., 2016), but are smaller than 10%. The column above 28 km amounts to ≈ 20% of the total O_3 column.

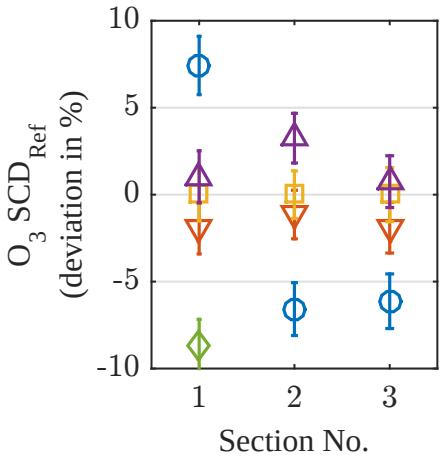

Figure 5.9: Comparison of O_3 SCD_{Ref} retrieved for the flight sections listed in Table 5.5. The standard case (yellow squares) assumes aerosol optical depth (AOD) profiles retrieved from O_4 inversion. Red triangles: Overhead column reduced by 10%. Violet triangles: Overhead column increased by 10%. Blue circles: Assuming climatological AOD profile. Green diamond: AOD profile retrieved from relative radiances. Error bars show RT model uncertainty.

Figure 5.9 shows the deviation of simulated ozone SCD_{Ref}, relative to standard cases. The respective AOD profile retrieved by optimal estimation and a scale height of 8 km above 28 km altitude are applied in the standard cases. The other cases use either the climatological AOD profile (see above) or a scale height of 7.2 (8.8) km, which decreases (increases) the overhead column above 28 km altitude by 10%, i.e. decreases (increases) the total O_3 column by ≈2%. The AOD profile retrieved based on relative radiances is included in the case of flight section 1. Overall, the SCD_{Ref} does not change by more than 10% compared with the standard cases. A similar result is obtained for NO_2.

Two strategies are applied to retrieve the SCD_{Ref} for the remaining research flights (compare Table 5.6):

- Cross flight spectral fitting (CF): The spectral retrieval for all measurements of the targeted research flight against a Fraunhofer reference spectrum of one of the flight sections for which the SCD_{Ref} is known. The SCD_{Ref} of the reference spectrum of the targeted research flight is then the sum of the known SCD_{Ref} and the offset OS = dSCD(Ref_{known}) - dSCD($Ref_{unknown}$). This is shown in Figure 5.10 for O_3 for the ESMVal research flight on 19.09.2012. The uncertainty is then estimated from the scatter of the difference and ranges from 5% to 20%.
- Simulation (Sim.): If the CF procedure does not yield usable results, i.e. the residual is too large due to diverging imaging properties of the spectrometer from one flight to the other, then the camera images recorded at the time of the reference spectrum are used to approximate the meteorological conditions. The SCD_{Ref} is then simulated with the RTM, using the CLAMS trace gas curtain and climatological background aerosols (Calipso, SageII). As mentioned above, the uncertainty is estimated by varying the aerosol optical density at flight altitude and the overhead column above 30 km. This results in estimated SCD_{Ref} uncertainties of 10% for the flight sections of Table 5.5 and 15-20% for all other cases.

In order to retrieve [BrO] via O_3 scaling for science flight ANT (chapter 7), SCD_{Ref} are also simulated at 340 nm for both gases using trace gas concentration profiles from CTMs CLaMS and EMAC and assuming climatological background aerosols (see above). The retrieved SCD_{Ref} are 2.4×10^{14} molec/cm^2 (EMAC) and 2.0×10^{14} molec/cm^2 (CLaMS) for BrO, and 5.5×10^{19} molec $\cdot$ /cm^2 (EMAC) and 5.6×10^{19} molec $\cdot$ /cm^2 (CLaMS) for O_3.

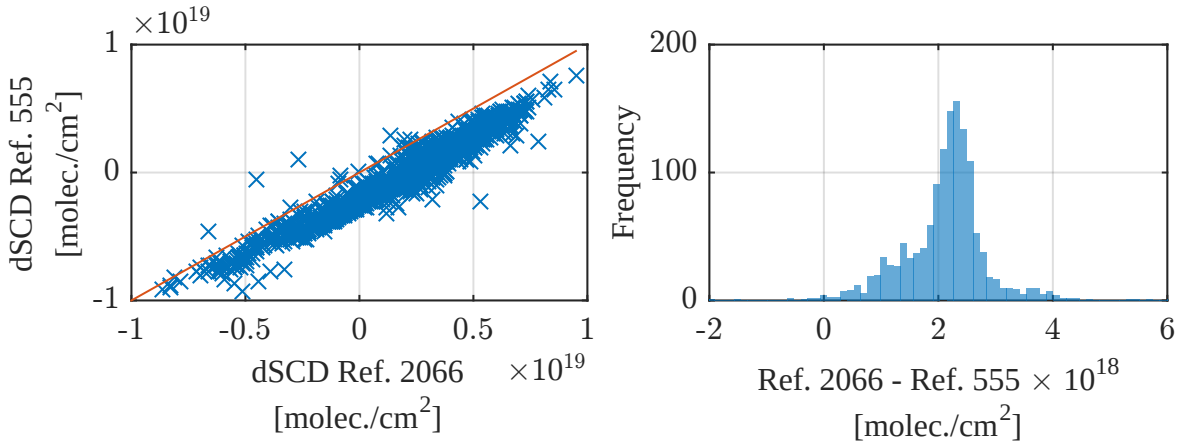

Figure 5.10: Cross flight spectral fitting of O_3 slant column densities for the HALO science flight on 19. September 2012. Left panel: Blue crosses: Scatterplot of dSCDs [molec./cm^2] with respect to reference spectrum 555 of 19. September 2012 against the dSCDs [molec./cm^2] with respect to the reference spectrum 2066 of flight section 3 (18. September 2012, Table 5.5). Red line: 1:1 line. Right panel: Histogram of the differences of the data points from the left panel with mean: 2.11×10^{18} molec./cm^2 and σ : 7.83×10^{17} molec./cm^2.

Table 5.6: Retrieved Fraunhofer reference SCDs (SCD_{Ref}) of O_3 and NO_2 for spectra recorded by the VIS4 channel during flights of the TACTS/ESMVal science mission. The unit of the SCD_{Ref} is molecules/cm^2. The methods are explained in the text.

Campaign	Date	Spec. No.	Method	O_3	NO_2
ESMVal	10.09.	1004	Sim.	2.31×10^{19}	6.57×10^{15}
	11.09.	998	Inv.	1.20×10^{19}	3.42×10^{15}
	13.09.	1505	CF	2.55×10^{19}	3.71×10^{15}
	15.09.	115	Inv.	3.77×10^{19}	7.98×10^{15}
	18.09.	2066	Inv.	1.80×10^{19}	6.94×10^{15}
	19.09.	555	CF	2.02×10^{19}	5.21×10^{15}
	23.09.	1001	CF	2.86×10^{19}	5.51×10^{15}
TACTS	28.08.	1804	Sim.	2.71×10^{19}	1.22×10^{16}
	30.08.	1738	Sim.	2.47×10^{19}	7.75×10^{15}
	04.09.	2003	Sim.	1.83×10^{19}	5.30×10^{15}
	05.09.	1204	Sim.	3.87×10^{19}	1.02×10^{16}
	25.09.	2003	Sim.	3.37×10^{19}	8.21×10^{15}
	26.09.	1542	CF	5.09×10^{19}	1.11×10^{16}

Chapter 6

Trace gas concentration retrieval using the scaling method

A novel method to retrieve trace gas mixing ratios from slant column densities has been developed in our working group (Raecke, 2013; Großmann, 2014; Knecht, 2015; Werner, 2015; Werner et al., 2016; Stutz et al., 2016; Aderhold, 2016; Knapp, 2016) in order to overcome the limitations of the inversion method mentioned in section 5.5.2. The knowledge about the light path distribution is gained by comparing the SCDs of a so-called *scaling-gas* with its in-situ measured concentration at flight altitude. This effective light path distribution is subsequently used to scale the SCDs of the targeted trace gas. Hence, the method is called the *scaling method*. The method was employed by Raecke (2013) and Werner (2015) for measurements aboard the NASA Global Hawk aircraft at high altitudes (14 to 19 km) above the tropical pacific using ozone as the scaling gas (Stutz et al., 2016; Werner et al., 2016). It was also employed by Großmann (2014) for measurements aboard the DLR Falcon aircraft at lower altitudes (planetary boundary layer to 12 km) using O_4 as the scaling gas.

6.1 Formalism

The scaling method aims to infer the target gas concentration $[X]$ using a scaling gas with concentration $[P]$. The concentration of trace gas X in layer i is denoted $[X]_i$. The corresponding SCDs measured by the HALO mini-DOAS instrument instrument are S_X and S_P, and can be expressed similar to equation 5.10:

$$\begin{aligned} S_X &= \sum_i [X]_i \cdot B_{X_i} \cdot h_i \\ S_P &= \sum_i [P]_i \cdot B_{P_i} \cdot h_i \end{aligned} \tag{6.1}$$

Equation 6.1 is solved for the trace gas concentration in the layer of interest j:

$$[X]_j = \frac{S_X - \sum\limits_{i \neq j} [X]_i \cdot B_{X,i} \cdot h_i}{B_{X,j} \cdot h_j} \tag{6.2}$$

and the ratio of this equation and the same formula for $[P]_j$ yields

$$\frac{[X]_j}{[P]_j} = \frac{B_{P,j}}{B_{X,j}} \cdot \left(\frac{S_X - \sum_{i \neq j} [X]_i \cdot B_{X,i} \cdot h_i}{S_P - \sum_{i \neq j} [P]_i \cdot B_{P,i} \cdot h_i} \right). \tag{6.3}$$

If both gases are evaluated in the same wavelength range (compare sections 5.2.2 and 5.3.2) for the same spectrum, i.e. same viewing geometry, it follows that $B_{X,i} = B_{P,i} = B_i$. In the following, the so-called α factors are defined:

$$\begin{aligned} \alpha_X &:= \frac{S_X - \sum_{i \neq j} [X]_i \cdot B_{X_i} \cdot h_i}{S_X} = \frac{B_j \cdot [X]_j \cdot h_j}{\sum_i B_i \cdot [X]_i \cdot h_j} = \frac{C_{X,j}}{\sum_i C_{X,i}} = \frac{C_{X,j}}{S_X} \\ \alpha_P &:= \frac{S_P - \sum_{i \neq j} [P]_i \cdot B_{P_i} \cdot h_i}{S_P} = \frac{B_j \cdot [P]_j \cdot h_j}{\sum_i B_i \cdot [P]_i \cdot h_j} = \frac{C_{P,j}}{\sum_i C_{P,i}} = \frac{C_{P,j}}{S_P} \end{aligned} \tag{6.4}$$

$C_{X,i}$ is called the *contribution* and describes the contribution of layer i to the total slant column density S_X of trace gas X. Accordingly, the slant column density is the sum of all contributions. The final equation for the scaling method now follows from equations 6.3 - 6.4:

$$[X] = \frac{\alpha_X}{\alpha_P} \cdot \frac{S_X}{S_P} \cdot [P] \equiv \alpha_R \cdot S_R \cdot [P] \tag{6.5}$$

The subscript R on the right hand side denotes the ratios of α and SCD, respectively. The α factors describe the relative contribution of a layer of interest to the total slant column density, which is obvious on the right hand side of equation 6.4. Typical α factors are $\alpha_{NO_2} \approx 0.05$ in the troposphere (Figure 6.1), $\alpha_{O_3} \approx 0.3$ in the lowermost stratosphere at 13 km altitude (Figure B.5), and $\alpha_{BrO} \approx 0.6$ at 17 km (Werner et al., 2016, Figure 11). When applying the method to limb measurements, the layer of interest can be defined as the altitude range directly sampled by the FOV of the telescopes. Raecke (2013) calculated the scattering events contributing to the NASA Global Hawk limb DOAS measurements in a 3D atmosphere. He found almost all scattering events to occur within a maximum distance of 180-210 km, and most events even much closer at a distance of $\approx$ 20 km. At HALO ambient pressures, most scattering events can be expected to occur within $\approx$ 100 km. A FOV of 0.64° (sect. 3.2.5) in limb geometry results in an altitude range of 1.1 km sampled by the telescope, i.e. 550 m above and below flight altitude. When this altitude range is enlarged or shrunk, even by several hundred meters, there is no significant difference to the ratio of α factors in equation 6.5 (Bodo Werner, personal communication). Therefore, this approximate altitude range is adequate for the evaluation of measurements on the targeted spatial scales. Perpendicular to the line of sight, the simulations by Raecke (2013) show that scattering events from $\pm$20 km horizontally along the flight path contribute to the measured irradiance. With an aircraft speed of 200 m/s, this equates to 100 s travelling time of the aircraft. The in-situ measured concentration of the scaling gas is therefore averaged for each recorded spectrum from 100 s before start of spectrum integration to 100 s after end of spectrum integration.

Figure 6.1 shows all steps involved in the retrieval of trace gas concentrations using the scaling method. For exemplifying purposes the retrieval of NO_2 concentrations via O_3 scaling, applied to the measurements of science flight ANT, is discussed in the following. Panels a and b show the CLaMS modelled trace gas curtains along the flight trajectory of O_3 and NO_2, respectivley. The

curtains are multiplied by the BoxAMFs calculated by the RTM McArtim (panel c) to obtain the contribution profiles (not shown). The ratio of the resulting α factors, α_R (panel d), is multiplied with the ratio of the trace gas SCDs (panel e) and the O_3 mixing ratio (panel f, blue) to retrieve the NO_2 mixing ratio (panel f, red). The uncertainties given by the grey shaded areas are derived in section 6.2 and summarised in section 6.3.

The choice of the scaling gas determines the robustness and the sensitivity of the method (sect. 6.4.3). The profile shapes of NO_2 und O_3 are quite similar (Figure 6.2), so that it seems obvious to retrieve $[NO_2]$ via O_3 scaling. The highest concentration of both trace gases occurs above the aircraft, i.e. in the stratosphere, while in the unpolluted troposphere the concentration is comparably low. Conversely O_4 is quadratically proportional to air pressure (equation 5.25) and its "concentration" is largest near the ground (Figure 6.2).

6.1.1 Wavelength dependency

Because of the strong wavelength dependence of Rayleigh scattering cross section ($\propto \lambda^{-4}$), BoxAMFs and inferred α factors are expected to be strongly wavelength-dependent quantities (Platt et al., 1997). Commonly BoxAMFs are calculated using the center wavelength of the respective fitting window. Figure A.18 shows (in the upper panels) a comparison of BoxAMFs calculated at 477 nm - the center of the O_4 fitting window - and at 457 nm - the center of the NO_2 fitting window. The lower panels show a comparison with 427 nm - the lower end of the NO_2 fitting window. While there is a strong bias of up to 20% (457 nm) and 50% (427 nm) at lower altitudes for downward looking elevation angles, the measurements at EA=0° used for the scaling method are within 5% (457 nm) and 10% (427 nm) of deviation from the 477 nm case. The wavelength dependency is much stronger in the UV wavelength range, due to the stronger wavelength dependency of Rayleigh scattering cross section and stronger O_3 absorption at shorter wavelengths (Figure 5.1). The wavelength dependency is accounted for by calculating α_X and α_P from BoxAMFs of the respective wavelength ranges. Additionally, equation 6.5 is extended according to equation 6.3 because the BoxAMFs in the measurement altitude layer j no longer cancel each other out:

$$[X]_j = \frac{B_{P,j}}{B_{X,j}} \cdot \frac{\alpha_{X,j}}{\alpha_{P,j}} \cdot \frac{S_X}{S_P} \cdot [P]_j \tag{6.6}$$

6.1.2 O_4 scaling

O_4 as a measure of light path distributions is introduced above (sect. 5.5.2) together with its shortcomings for airborne measurements at high altitudes when constraining an inversion by optimal estimation. It is nevertheless expedient to use O_4 as a scaling gas at lower altitudes and in particular for trace gases with similar concentration profile shapes, i.e. high concentrations near the surface and strongly decreasing concentrations with increasing altitude (Figure 6.2). This was pioneered for a range of trace gases by Großmann (2014) and applied to HALO mini-DOAS instrument measurements of CH_2O over the Amazon rain forest (Wendisch et al., 2016).

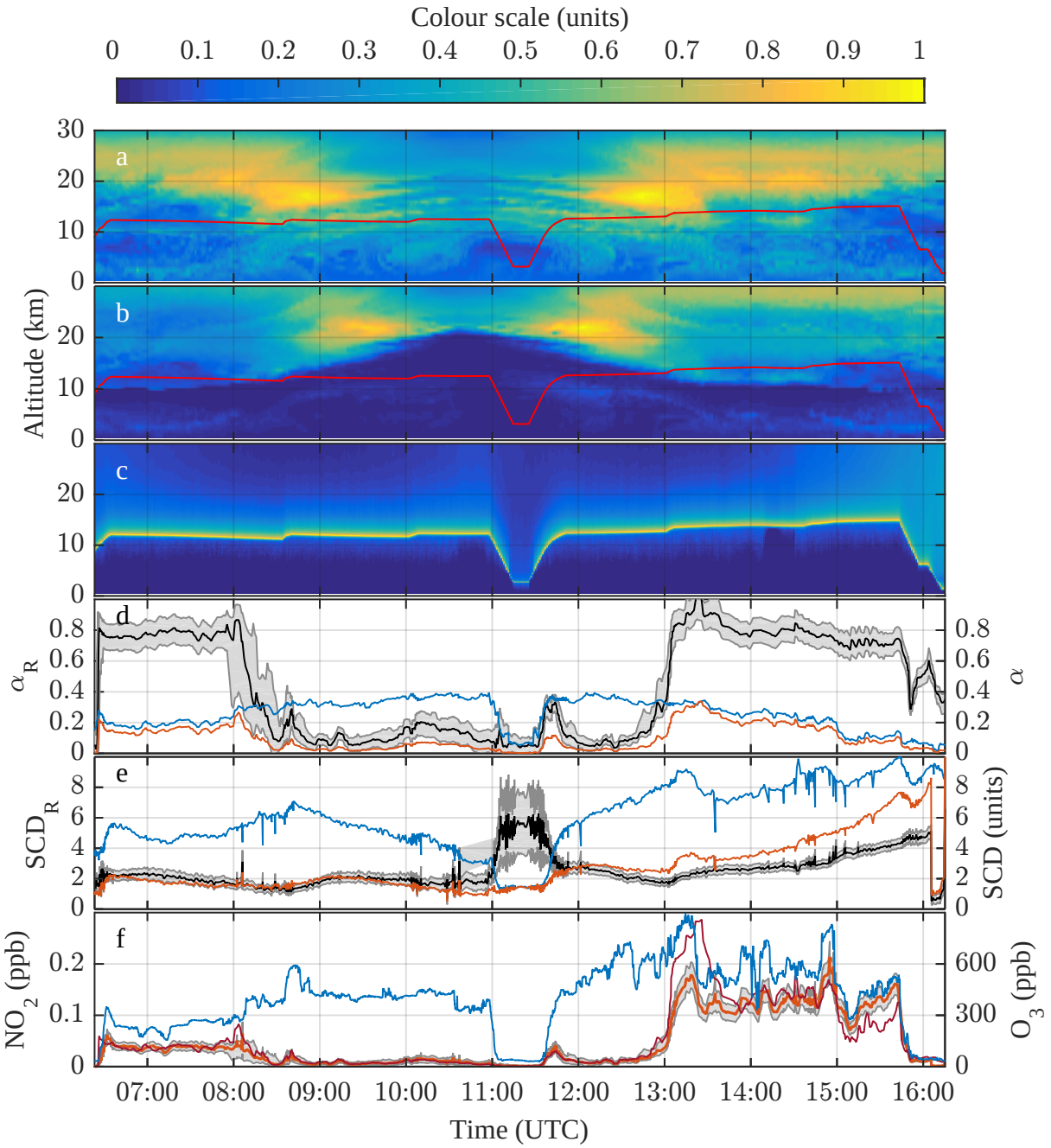

Figure 6.1: Illustration of NO_2 mixing ratio retrieval for science flight ANT. Panel a: CLaMS curtain of O_3 concentration (colour scale $\times\ 7.9 \cdot 10^{12}$ cm^{-3}) and aircraft altitude (red line). Panel b: CLaMS curtain of NO_2 concentrations (colour scale $\times\ 2.9 \cdot 10^{9}$ cm^{-3}) and flight altitude (red line). Panel c: BoxAMFs calculated by the RTM McArtim (colour scale $\times \log(217)$). Panel d: α factors for O_3 (blue) and NO_2 (red) as well as α_R (black line) with its uncertainty range (grey shaded area). Panel e: SCDs from DOAS evaluation of the recorded spectra for O_3 (blue) and NO_2 (red) as well as their ratio (black line) with its uncertainty range (grey shaded area). SCDs are normalised to the maximum value recorded. Panel f: Retrieved NO_2 mixing ratio (red line) with its uncertainty range (grey shaded area) and in-situ measured O_3 (blue line), which was used as scaling gas. The dark red line denotes the NO_2 mixing ratio predicted by the CLaMS model.

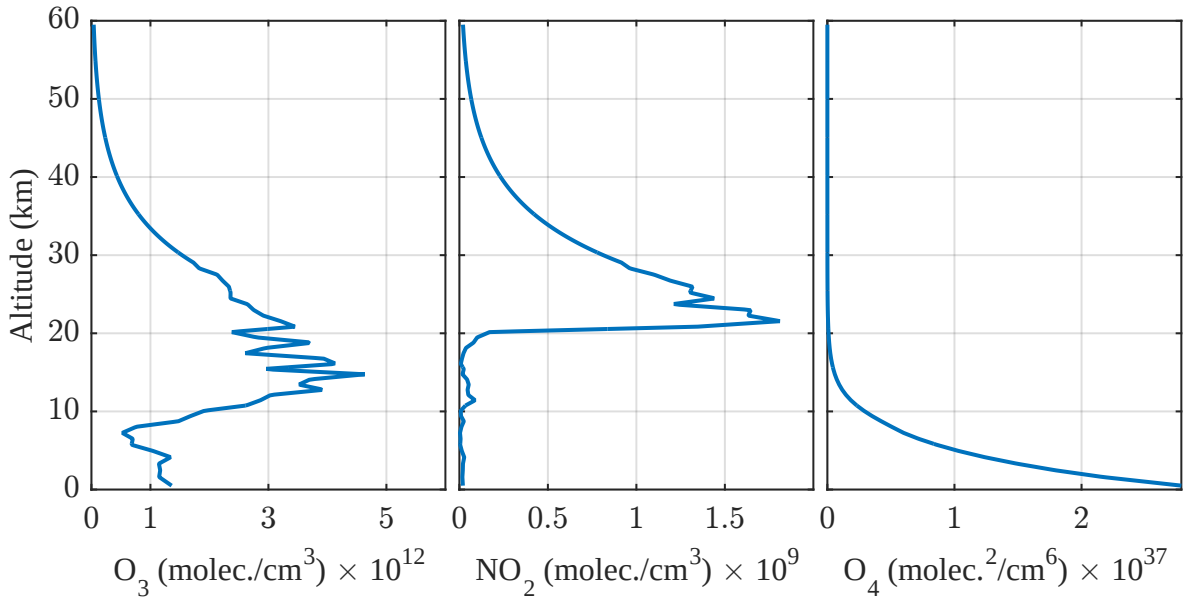

Figure 6.2: Concentration profiles for trace gases O_3, NO_2, and O_4 as predicted by CLaMS for science flight ANT at 07:45 UTC, 45° S, 15° E. Northern hemisphere mid-latitude profiles are shown in Figure B.9.

The unit of the O_4 absorption "cross section" α_{O_4} (equation 5.25) is [$cm^5 \cdot$ $molecule^{-2}$] and the O_4 "concentration" is given in [$molecule^2 \cdot cm^{-6}$]. For the purpose of inferring mixing ratios with the scaling method (equation 6.5) the O_4 "mixing ratio" O_4^{MR} can be written as:

$$O_4^{MR} = \frac{[O_2]^2}{\mathrm{TND}} = \frac{0.21^2 \cdot \mathrm{TND}^2}{\mathrm{TND}} = 0.21 \cdot [O_2] \tag{6.7}$$

where $\mathrm{TND} = p/(k_B \cdot T)$ is the total number density of air. The unit of O_4^{MR} is [cm^{-3}], which is cancelled out in O_4 scaling because of the SCD-ratio of the target gas X and the scaling gas O_4:

$$S_R = \frac{S_X}{S_{O_4}} \equiv \frac{[\mathrm{molec.} \cdot \mathrm{cm}^{-2}]}{[\mathrm{molec.}^2 \cdot \mathrm{cm}^{-5}]} = [\mathrm{cm}^3 \cdot \mathrm{molec.}^{-1}] \tag{6.8}$$

A comparison of O_3 scaling and O_4 scaling for the measurements considered in the present thesis is presented in section 6.4.3.

6.2 Random error contributions

The statistical error budget for the trace gas concentration $[X]_j$ for a measurement j retrieved according to eq. 6.5 is

$$\Delta[X]_j = \left[\left(\frac{\Delta\alpha_{R,j}}{\alpha_{R,j}} \right)^2 + \left(\frac{\Delta S_{X,j}}{S_{X,j}} \right)^2 + \left(\frac{\Delta S_{P,j}}{S_{P,j}} \right)^2 + \left(\frac{\Delta[P]_j}{[P]_j} \right)^2 \right]^{0.5} \cdot [X]_j. \tag{6.9}$$

Three factors contributing to $\Delta\alpha_{R,j}$ are investigated in this section: (a) The occurrence of random Mie extinction (i.e. cloud fields) during the measurement (sect. 6.2.1), (b) small scale variability of the target and scaling gas concentrations at flight level (sect. 6.2.2), and (c) uncertainty as to which parts of the vertical trace gas profiles are sampled during measurements (sect. 6.2.3). The error contributions are summarised including the other factors in section 6.3.

6.2.1 Sensitivity to Mie extinction and trace gas profile shapes

Knecht (2015) investigated the influence of Mie extinction on the ratio α_R in equation 6.5. In his study the RTM McArtim (sect. 5.3.1) was used to randomly sample viewing geometries in a 3D atmosphere with complex cloud patterns (Figure A.17). Figure 6.3 shows the resulting α_R for the target gas HCHO and scaling gas O_4 as column distributions for each altitude layer with thickness of 500 m. The α_R are displayed for two solar zenith angles (red and blue distributions). The red and blue lines and the grey shaded area indicate the medians and the variation for the clear sky case, respectively. The ratio of the concentration profiles is calculated from the profiles shown in the inset. The results of the study support the following conclusions:

1. α_R mainly depends on the relative profile shapes of the involved atmospheric constituents.
2. A changed Mie extinction profile (e.g. complex cloud pattern) does not significantly change α_R or its variability, which is around 5-10%, compared to a clear sky scenario. I.e. α_R is largely independent of the presence of clouds. This is however not entirely true for extreme cases, e.g. the retrieval of stratospheric trace gases through O_4 scaling. In such a case, a low altitude cloud layer can alter the O_4 absorption very differently from how it alters the absorption of the stratospheric trace gas. This behaviour is detailed in section 6.4.3. It is therefore desireable to use a scaling gas with a profile shape similar to the target gas.
3. Changing SZAs have little effect on α_R. The maximum effect at ground level is $\approx$ 10% and decreases with increasing altitude.

The most significant sensitivity of the α factor is with respect to the profile shape of the scaling and target gas. The most significant precondition for the accurate assessment of the α factors is therefore knowledge of the profile shapes. The most simple though inaccurate approach would be to assume profile shapes for both gases. The present study however makes use of the information available from CTMs (sect. 5.4). This approach offers the advantage that the scaling method can be thoroughly validated.

6.2.2 Small scale variability

Small scale dynamical effects are not resolved by CTMs. When comparing modelled and measured trace gas mixing ratios a certain amount of uncertainty is evident, even during flight sections with overall agreement between measurements and models. Figure A.24 shows the scatter of O_3 clustering in several peaks with width of $\approx$40 ppb. Similarly, a scatter of $\approx$0.01 ppb NO_2 can be estimated from Figure A.25. The effect of a deviation of the trace gas concentration at flight altitude on the α factor is calculated in the following. The assumed α without deviation is calculated as in equation 6.4. However, the true α^* is enhanced by the additional contribution x at flight altitude, i.e. in the telescopes' FOV:

$$\alpha^*(\alpha,x) = \frac{C_{FOV}(1+x)}{S+C_{FOV}\cdot x} = \ldots = \frac{\alpha(1+x)}{1+\alpha x} \tag{6.10}$$

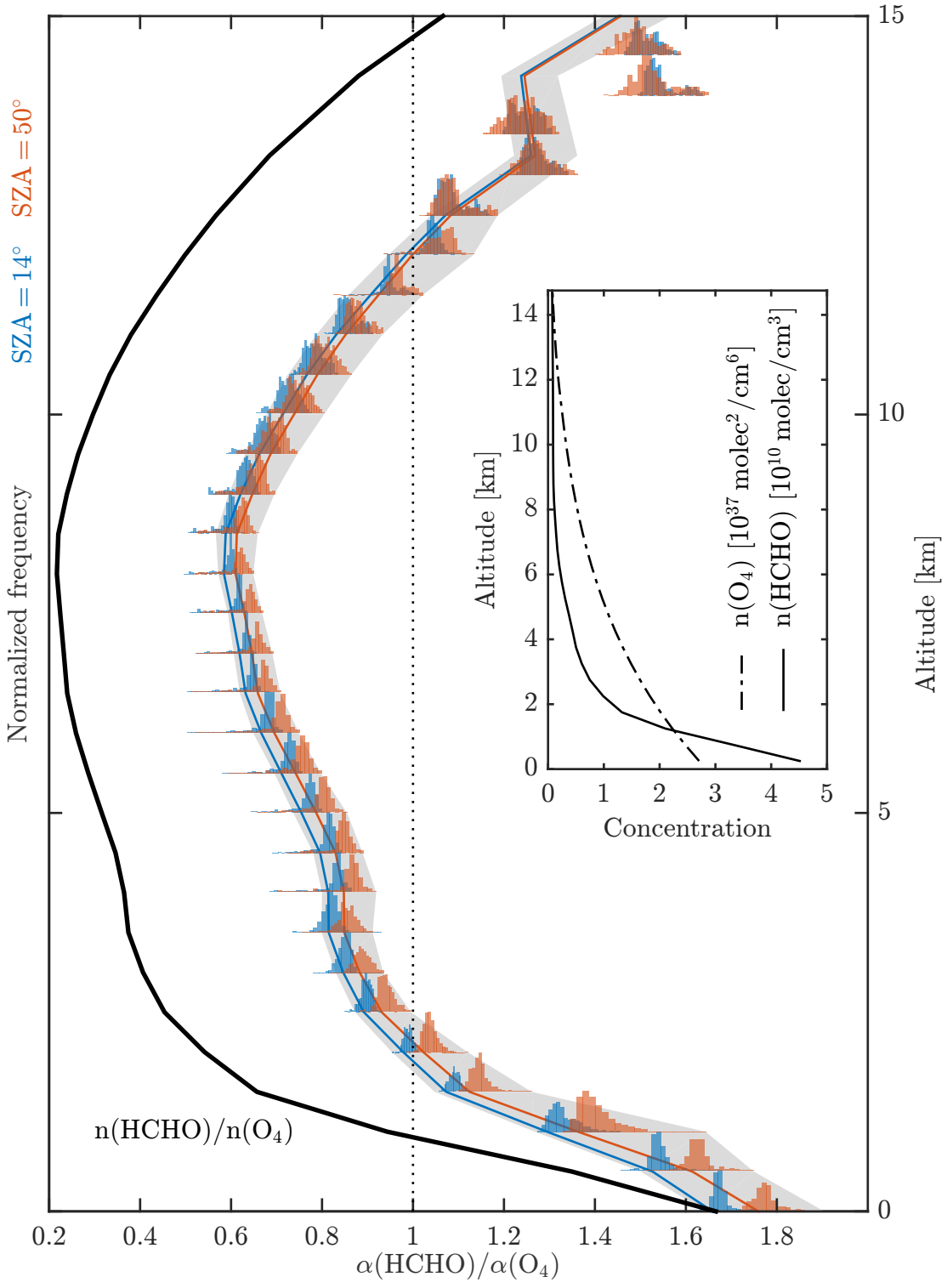

Figure 6.3: Distributions of $\alpha_R = \alpha(HCHO)/\alpha(O_4)$ for arbitrarily sampled viewing geometries in an atmosphere with complex cloud patterns (column distributions) and a clear sky scenario (median indicated by lines and variation by grey shaded area). Pictured are two SZAs: 14°(blue), and 50°(red). The inset shows the profile shapes of the atmospheric constituents, the black line in the large panel shows their ratio. The cloud scenario is pictured in Figure A.17. Adopted from Knecht (2015).

Figure 6.4 shows this function in the left panel. As an example, if the original α is 0.5, and the concentration at flight altitude is in fact 40% higher than in the model, it follows that $\alpha^* = 0.6$. As expected, the true α^* is larger than the assumed α, because of the additional contribution at flight altitude. The difference

$$\alpha_d(\alpha, \pm x) = |\alpha^*(\alpha, \pm x) - \alpha| \tag{6.11}$$

is then the uncertainty of α, with the lower boundary calculated from $\alpha_d(\alpha, -x)$ and the upper boundary calculated from $\alpha_d(\alpha, +x)$. Figures 6.5 and B.7 show the calculated uncertainty in α_R for

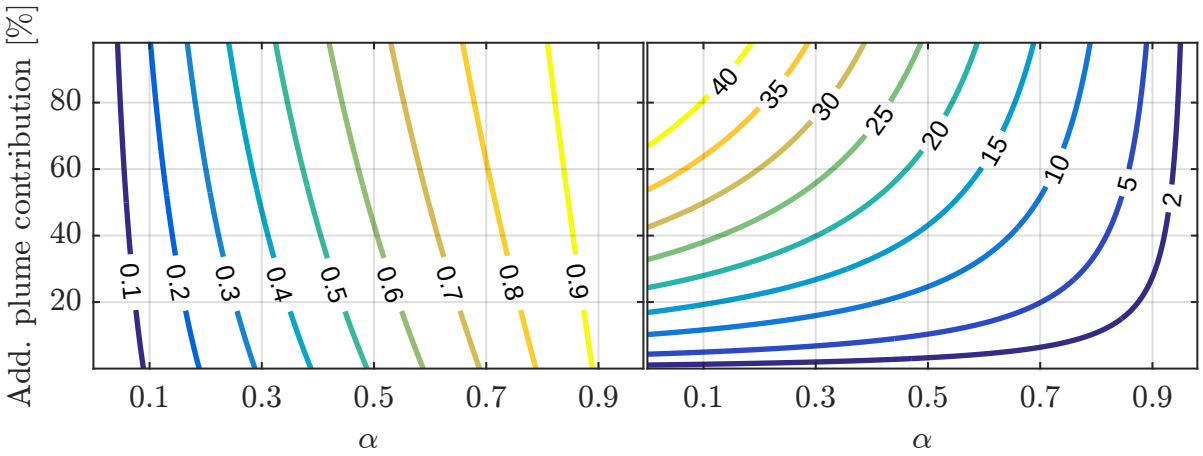

Figure 6.4: Left: α^* (coloured contour lines) as a function of α and the additional contribution x, compare eq. 6.10. Right: Underestimation of α in % in case of a trace gas plume, compare eq. 6.15.

science flights ANT and ML, respectively. Typical values are between 0 and 0.05 α_R.

6.2.3 Vertical profile sampling uncertainty

The uncertainty regarding which part of the trace gas profile is actually sampled by the telescope is motivated by two factors. First, CTM trace gas profiles are linearly interpolated to the RTM atmosphere altitude grid in order to simulate the radiative transfer. This is an approximation within the boundaries of the previous and next CTM profile grid point. CTMs are calculated with a vertical resolution of approximately 500 m at typical measurement altitudes of the HALO research aircraft (sect. 5.4.1). Secondly, the telescope's pointing accuracy is $\Delta EA < 0.3°$(sect. 3.2.6). In an assumed sampling distance of 100 km, this translates to a vertical misalignment of $\approx$ 500 m. Therefore, an inspection of the sensitivity of α_R regarding a 500 m altitude shift of the trace gas profiles appears appropriate. A sensitivity of α_R can be expected if the measurement is performed in strong vertical gradients of the target and scaling gas. In order to investigate this sensitivity, the target and scaling gas are shifted simultaneously by 500 m and α_R is calculated for an *upwards* shifted and a *downwards* shifted case as well as for the unmodified case. Of the resulting range of α_R, the maximum is chosen as the upper confidence interval, and the minimum is chosen as the lower confidence interval for each measurement. The resulting $\Delta\alpha_R$ is shown in figures 6.5 and B.7 for science flights ANT and ML, respectively. Typical $\Delta\alpha_R$ are between 0 and 0.05, and up to 0.5 in cases of very strong vertical gradients, as they may occur at the edge of the polar vortex (Figure 6.5, 08:00 – 09:00 UTC).

6.3 Budget of random errors

Recalling equation 6.9, the statistical error budget for the trace gas concentration $[X]_j$ for a measurement j retrieved according to eq. 6.5 is

$$\Delta[X]_j = \left[\left(\frac{\Delta\alpha_{R,j}}{\alpha_{R,j}} \right)^2 + \left(\frac{\Delta S_{X,j}}{S_{X,j}} \right)^2 + \left(\frac{\Delta S_{P,j}}{S_{P,j}} \right)^2 + \left(\frac{\Delta[P]_j}{[P]_j} \right)^2 \right]^{0.5} \cdot [X]_j. \tag{6.12}$$

The contributions to $\Delta\alpha_{R,j}$ are examined above in sections 6.2.1, 6.2.2, and 6.2.3. Figure 6.5 shows the Gaussian propagated error contributions for science flight ANT. The $\Delta\alpha_R$ is largest when vertical gradients of trace gas concentrations are strongest, e.g. at the stratosphere/troposphere transition (08:00 – 09:00 UTC). In the real atmosphere these cases are rare. Typical $\Delta\alpha_R$ are between 0.05 and 0.1, as demonstrated for science flight ML (Figure B.7, p. 178).

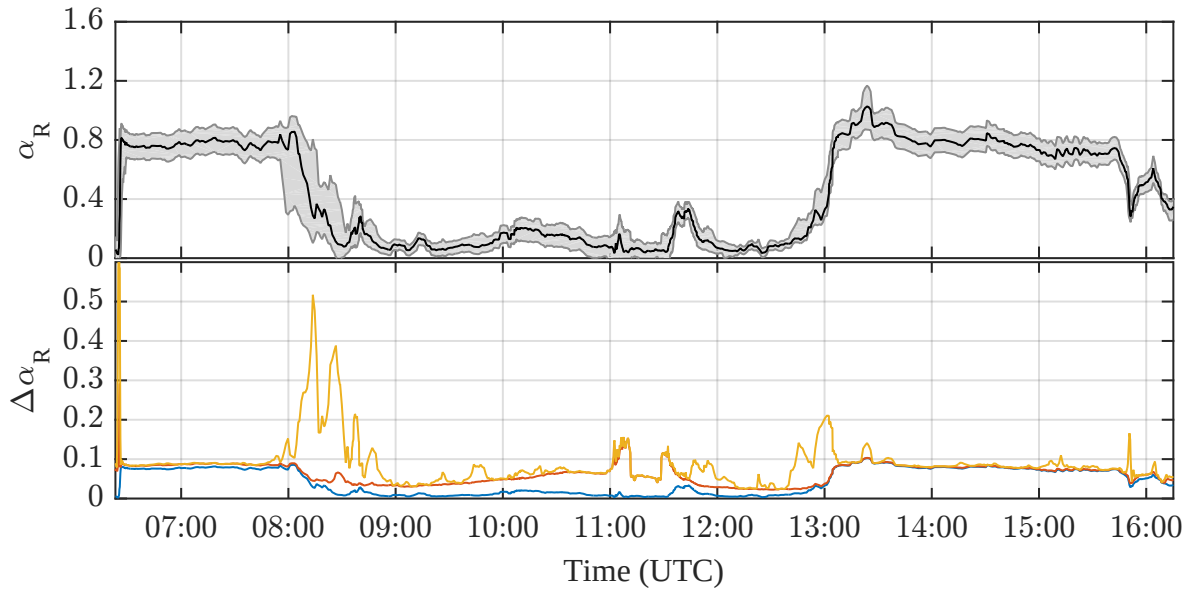

Figure 6.5: Random error contributions for science flight ANT. Top panel: α_R (black line) and its uncertainty $\Delta\alpha_R$ (grey shaded area) including all statistical components. Bottom panel: Individual $\Delta\alpha_R$ components added up. Blue: 10% uncertainty of α factors from Mie extinction influence (sect. 6.2.1). Red: Blue + uncertainty due to small scale variability (sect. 6.2.2). Yellow: Red + vertical sampling uncertainty (sect. 6.2.3).

The errors of the SCDs (terms 2 and 3) each consist of two contributions: The uncertainty of the retrieved $\mathrm{SCD_{Ref}}$ (sect. 5.5) and the uncertainty of the DOAS retrieval, which is the sum in quadrature of the DOAS fit error and the uncertainty of the trace gas reference cross section (sect. 5.2):

$$\left(\frac{\Delta S}{S} \right)^2 = \left(\frac{\Delta S_{\mathrm{Ref}}}{S_{\mathrm{Ref}}} \right)^2 + \sigma^2_{\mathrm{DOAS-Fit}} + \sigma^2_{\mathrm{cross-sect.}} \tag{6.13}$$

The last term in equation 6.9 is the uncertainty of the in-situ concentration of the scaling gas. In the case of O_3 scaling, it is given by the measurement uncertainty of the measurement device, such as the ozone monitor (sect. 4.2). The O_4 vertical profile scales with an error of 10^{-3} with air density (Thalman and Volkamer, 2013). The latter depends on p and T, which are known from the CTMs with an accuracy of $\approx 1\%$ (Figure A.9).

Table 6.1: Summary of random errors as discussed in section 6.3. The percentages in columns three and four refer to deviations of the parameter in the first column.

Parameter	Cause of the error	Typical value	Extreme value	Section
$\Delta\alpha_R$	RTM noise	3.5%	3.5%	5.3.2
	Mie scattering	10%	15%	6.2.1
	small scale variability	0 – 20%	100%	6.2.2
	vertical sampling	0 – 10%	60%	6.2.3
ΔSCD_R	DOAS fit error	5%	100%	5.2.2
	cross section	3%	6%	5.2.2
	SCD_{Ref}	5 – 10%	20%	5.5.3
$\Delta[X]$	O_3 measurement	<1%	1%	4.2
	O_4 calculation	1%	1%	6.1.2

The detection limits of trace gas mixing ratios retrieved by the scaling method are estimated by two times the random error at low trace gas concentrations. During science flight ANT, very low NO_2 mixing ratios are inferred inside the polar vortex. With an approximate random error of ± 5 ppt, the inferred detection limit for NO_2 is 10 ppt. The similarly derived detection limit for BrO is approximately 2 ppt.

6.4 Systematic errors

In order to assess the validity and accuracy of the retrieved mixing ratios, systematic errors of the retrieval method need to be examined. Two major sources for systematic biases are apparent: (a) Actual profile shapes deviate significantly from model predictions, and (b) unaccounted differences in radiative transfer (RT) appear for the BoxAMFs of target gas X and scaling gas P.

The impact of modified profile shapes is investigated in two ways: First, by adjusting the trace gas mixing ratio in the model curtain in the line of sight (i.e. around flight altitude) to the concentrations measured in-situ during flight (sect. 6.4.1), thus altering the profile shape. Second, by shifting the model-predicted profiles in such a way that mixing ratios of N_2O at flight altitude reproduce measured mixing ratios, yet still conserving the overall profile shape (sect. 6.4.2). In the scope of the present study, trace gas profiles are altered without re-calculating atmospheric chemistry. An alternate approach is the consideration of measured concentrations of dynamical tracers such as CH_4 in CTM calculations in order to distinguish between dynamical and chemical processes influencing profile shapes (Werner et al., 2016). However, this comes with a much greater effort, increasing with the amount of measurements that are evaluated, and was not carried out in the scope of the present thesis.

Differences in RT between target gas and scaling gas are investigated by considering strongly different profile shapes of the gases and the impact of low altitude cloud layers (sect. 6.4.3). Different wavelength ranges in the DOAS retrieval are compensated for by radiative transfer modelling, as

mentioned above in section 6.1.1. However, the wavelengths chosen from the respective DOAS-fit wavelength range may change the correction factor. This uncertainty is further investigated in an ongoing Diploma thesis in our research group (Dominique Loerks).

6.4.1 Changing [X] and [P] in the line of sight

Increasing or decreasing trace gas concentrations around flight altitude, i.e. in the altitude range directly sampled by the FOV (cf. sections 6.1 and 3.2.5), is equivalent to introducing a plume-like structure into the vertical trace gas profile. Such emission plumes can either come from sources like aircrafts, volcanoes or outflow of polluted air from convective clouds. The observation of plumes is however not within the scope of airborne limb measurements, primarily due to the poorer spatial resolution of our measurements. The typical spatial extent of aircraft emission plumes is ≈ 100 m in the vertical and $\approx 200-800$ m in the horizontal (Schumann et al., 1995). In contrast to that, the light recorded in limb viewing geometry samples a spatial area of $\sim$100 km $\times$ 20 km (Raecke, 2013) and an altitude range of $\sim$1.1 km (sect. 6.1). Therefore, the retrieved trace gas concentration represents an average of the sampled air mass, and not the concentration inside the plume itself. More readily accessible is the observation of spatial patterns of larger scales, such as the observation of elevated NO_2 mixing ratios over the eastern Mediterranean in air masses originating from the South Asian summer monsoon anticyclone presented by Aderhold (2016).

Changes to the profile shape at flight altitude are introduced in section 6.2.2. Equation 6.10 is applied to calculate the factor α^* using the relative enhancement of the trace gas concentration

$$x = \frac{[X]_{\text{measured}}}{[X]_{\text{modelled}}} - 1. \tag{6.14}$$

α is underestimated if the enhancement is not considered. This underestimation is plotted as a percentage in the right panel of Figure 6.4 (page 82) and is calculated from

$$1 - \frac{\alpha}{\alpha^*}. \tag{6.15}$$

As expected, α is largely underestimated. For example, if $\alpha = 0.3$ and the additional contribution in the observed altitude layer is 40% ($x = 0.4$), it follows that α is underestimated by 20% (Figure 6.4, right panel).

This conclusion is however only valid if either [X] or [P] are enhanced, but not if both gases are enhanced. For example in the monsoon outflow plume observed by Aderhold (2016), the scaling gas O_3 was increased in the plume simultaneously with the target gas NO_2. In the same way, if stratospheric air is sampled instead of tropospheric air, the mixing ratios of both O_3 and NO_2 increase substantially, both α factors increase and therefore α_R does not change as much.

The modification of modelled trace gas profiles are carried out with data from EMAC (Figure 6.6). Green dotted lines in panels d and e show α_R and [NO_2], respectively, calculated using eq. 6.10 and measured [O_3] (FAIRO) and [NO_2] (HALO mini-DOAS instrument). For the latter, the concentrations retrieved from HALO mini-DOAS instrument measurements using the scaling method with unmodified trace gas profiles is employed.

α_R is modified by about twice the random error for flight sections in the mid-latitude stratosphere (Figure 6.6: take off – 8:00 UTC and 13:30 – 15:30 UTC). Thus, adjusting the trace gas concentrations of $[X]$ and $[P]$ to measured concentrations can modify the retrieved trace gas concentrations, but the modified $[NO_2]_{O_3}$ rarely exceeds the random error of the unmodified $[NO_2]_{O_3}$.

6.4.2 Uncertainties arising from atmospheric dynamics

A major uncertainty in present CTM modelling is due to uncertainties in the diabatic heating rates, in particular in the tropical UT/LS (Wright and Fueglistaler, 2013). When integrated over longer time spans in the model, this can result in an altitude difference, or "vertical shift", between modelled and actual trace gas profiles by several hundred meters. Similar differences are observed during science flight ANT (Figure 6.6), but are thought to be due to planetary wave breaking (Rolf et al., 2015). A common method to monitor STE processes is the measurement of N_2O (nitrous oxide) concentrations (e.g. Hintsa et al., 1998; Fischer et al., 2000; Andrews et al., 2001). N_2O is emitted from the earth's surface by natural and anthropogenic processes and its lifetime in the atmosphere is $\approx$ 131 years, leading to almost constant mixing ratios throughout the troposphere (Seinfeld and Pandis, 2016). Main N_2O sinks are photodissociation and reaction with excited oxygen atoms $O(^1D)$, both occuring in the stratosphere and leading to the production of NO. These properties lead to a strong vertical concentration gradient in the UT/LS. Hence, the N_2O concentration can be used as a vertical coordinate, or "dynamical tracer", to estimate the ascent or descent of air masses in the UT/LS.

The investigation of uncertainties arising from atmospheric dynamics is carried out using CTMs EMAC (Figure 6.6) and CLaMS (Figure A.21). Comparing the predicted and measured $[N_2O]$ in each case (respective panel a), it is evident that small scale dynamic variabilites are much better covered by CLaMS, especially in polar vortex flight sections B and D. However, N_2O mixing ratios are constantly underestimated by CLaMS. Contrarily, EMAC estimates are realatively accurate in the ExTL (sections A and E), but disagree strongly with measurements in the polar vortex, where EMAC does not reproduce the descent of the air from higher altitudes (see below, section 7.2.1) and thus overestimates $[N_2O]$.

In order to estimate the retrieval error due to dynamics not covered by the CTMs, modelled trace gas concentration profiles of N_2O are shifted in such a way that they agree with the measurements at flight altitude (yellow line in panel a). This correction is based on finding the altitude nearest to flight altitude, where model predictions agree with the measurements (panel b). E.g. if 280 ppb nitrous oxide is measured at $h_{meas} = 12$ km altitude, but predicted at $h_{mod} = 14$ km altitude, then the modelled profile is shifted downwards by $\Delta h = 2$ km from 14 to 12 km, which is illustrated for a sample N_2O profile in panel c. The modelled profile shape (blue) is preserved by "stretching" the profile, i.e. decreasing the shift Δh linearly from $h_{mod} = 14$ km downwards to 0 km and upwards to 30 km, respectively. The resulting profile is shown in red, and h_{meas} and h_{mod} are shown as dashed and dotted lines, respectively. The time of the sample profile is marked in panels a and b by dashed lines.

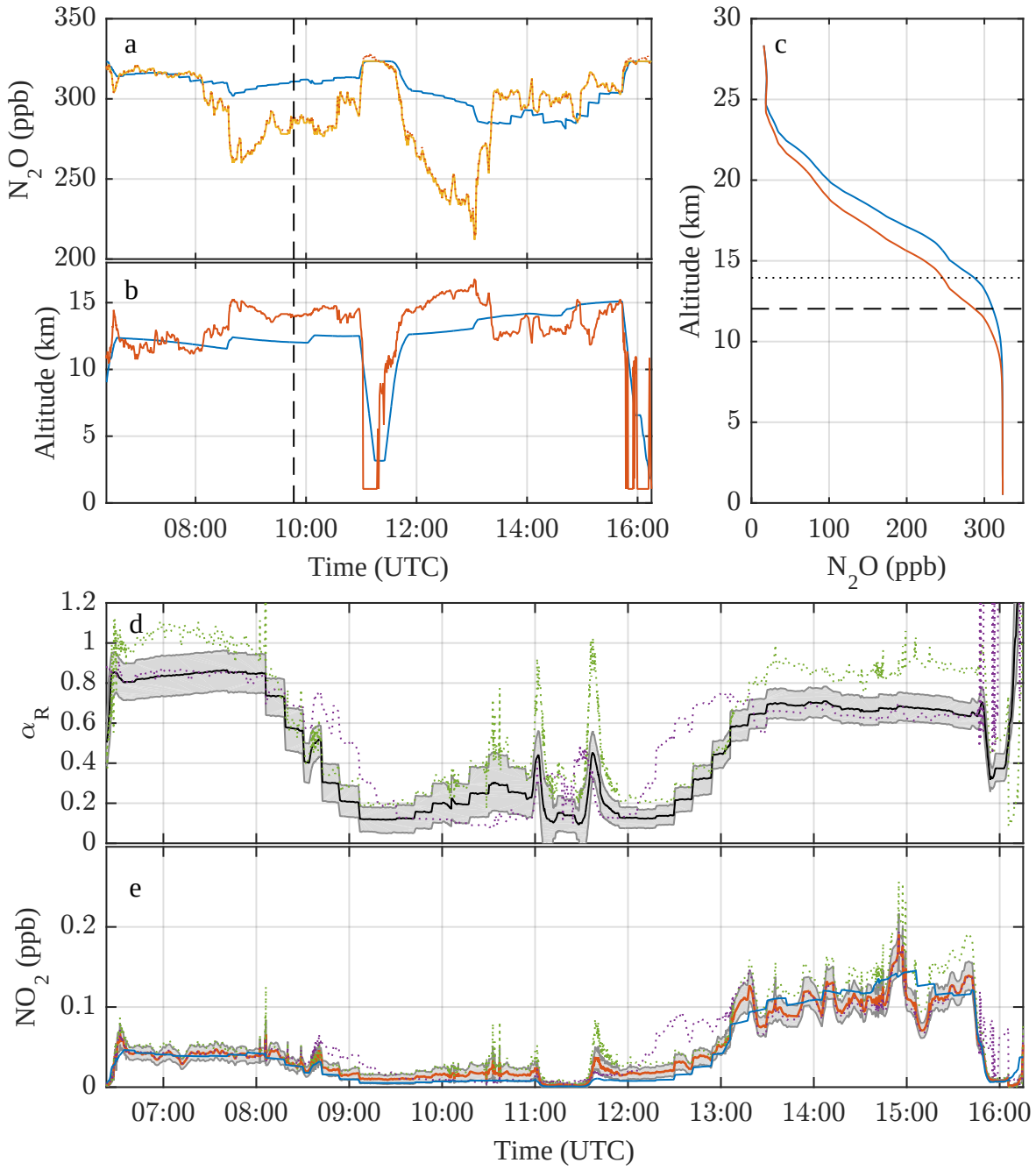

Figure 6.6: Examination of potential systematic errors for science flight ANT. Panel a: Nitrous oxide mixing ratio predicted by EMAC (blue), predicted by shifted EMAC profiles (yellow) and in-situ measured (red dots). Panel b: Aircraft GPS altitude (blue) and altitude at which the in-situ measured N_2O mixing ratios are found in the unmodified EMAC profiles (red). Panel c: Vertical profiles of N_2O at the time marked by black dashed lines in panels a and b. Unchanged profile in blue, shifted profile in red. The dashed line marks the measurement altitude, the dotted line marks the altitude of the respective N_2O mixing ratio in the unmodified EMAC profile. Panel d: α_R (black line) and $\Delta\alpha_R$ (grey shaded area). Additionally, α_R resulting from adjusted trace gas mixing ratios at flight altitude (green dots) and resulting from shifted profiles (violet dots) are shown. Panel e: Shown are NO_2 mixing ratios retrieved from unmodified profiles (orange line with grey shaded uncertainty) and from adjusted profiles at flight altitude (green dots) and shifted profiles (violet dots) as well as predicted by the EMAC model (blue line).

The predicted concentration profiles of NO_2 and O_3 are vertically shifted together with the N_2O profiles. In the case of EMAC predictions (Figure 6.6), the modified α_R (panel d, violet dots) and retrieved NO_2 mixing ratio (panel e, violet dots) are within the random error for most sections of the flight. Strong deviations occur during flight sections with strong disagreement between measured and predicted N_2O, i.e. 08:30 – 09:30 UTC and 12:00 – 13:00 UTC. Hence, vertical transport processes which are not covered by EMAC may change the profile shapes in such a way that systematic errors in the scaling method retrieval arise. However, since trace gases such as NO_2 and O_3 are chemically reactive, the altitude shift carried out here may not reflect the change in trace gas profile shape experienced by NO_2 and O_3. This is indicated by the fact that the modifications explained in the previous section (green dotted lines in Figure 6.6) do not give rise to large uncertainties in these flight sections, i.e. measured $[O_3]$ and $[NO_2]$ do not differ strongly from predictions at flight altitude.

CLaMS-based calculations (Figure A.21) show no strong deviations of α_R and $[NO_2]_{O_3}$ during flight sections B and D. Contrarily, α_R is lowered to almost zero for large parts of flight sections A and E. Although measured and modelled $[N_2O]$ do not disagree by large amounts (panel a), the concentration profiles are shifted upwards by 3 – 5 km (panel b). Such a strong change in the altitude profile shape of O_3 and NO_2 seems highly unlikely, especially in the ExTL.

The approach presented here assumes that differences between measured and predicted N_2O are only due to vertical misalignment of the modelled concentrations, and that NO_2 and O_3 profiles are similarly misaligned and do not change their mixing ratio at any altitude when the air descends or ascends. These oversimplifications imply that the retrieved errors are not realistic and probably strongly overestimated, but can be considered indications as to which atmospheric conditions could cause systematic errors for the scaling method. Overall, the retrieved deviations are within the random error, except where (a) strong vertical displacement is not covered by the EMAC model and (b) the vertical N_2O gradient in the ExTL predicted by CLaMS is so small that vertical displacement is unrealistically overestimated.

6.4.3 Influence of a low altitude cloud layer on α_R

Compact cloud layers at low altitudes are frequently occuring during HALO science missions, e.g. during science flight ANT. The influence of a low altitude cloud layer on α_R and retrieved $[NO_2]$ is investigated in the following by inspecting the results of O_3-scaled $[NO_2]$, hereafter denoted as $[NO_2]_{O_3}$, and O_4-scaled $[NO_2]$, hereafter denoted as $[NO_2]_{O_4}$. α_R and $[NO_2]$ for both methods are compared by switching a cloud layer on and off in the RTM. The clear sky scenario uses climatological background aerosol profiles from SAGEII/Calipso (sect. 5.5.3). In the cloud layer scenario, a surrogate cloud layer with optical density τ=20 is introduced at 4 – 8 km altitude in addition to the background aerosol profile. The altitude range of the cloud layer is derived from inspection of the HALO on-board camera recordings during the dive between 11:00 and 12:00 UTC. It is also supported by the GLORIA water vapour measurements (Rolf et al., 2015, Figure 4). The calculated parameters are shown for the clear sky scenario in Figure A.19 and for the cloud layer scenario in Figure A.20. The influence of the assumed cloud layer on the BoxAMFs can clearly be seen by com-

paring the respective panel c. Evidently, the cloud layer diminishes the sensitivity of high altitude measurements towards absorption near the ground, where $[O_4]$ is high. Hence, when the cloud layer is switched on α_{O_4} is increased approximately by a factor of 1.5, increasing the retrieved $[NO_2]_{O_4}$.

Figure 6.7 compares α_R, $[NO_2]_{O_3}$ and $[NO_2]_{O_4}$ for both the clear sky and the cloud layer case. Additionally, panel d in the Figure shows the 2-minute running mean of radiance (blue) and colour index (red) of spectra recorded by the nadir-pointing VIS telescope (VIS3) of the HALO mini-DOAS instrument, which can be used to infer cloud covered (high radiance and colour index) or clear sky (low radiance and colour index) conditions below the aircraft. Nadir-pointing camera images corresponding to the marked timestamps are shown in Figures A.22 and A.23 and correspond excellently with the VIS3 radiance measurements.

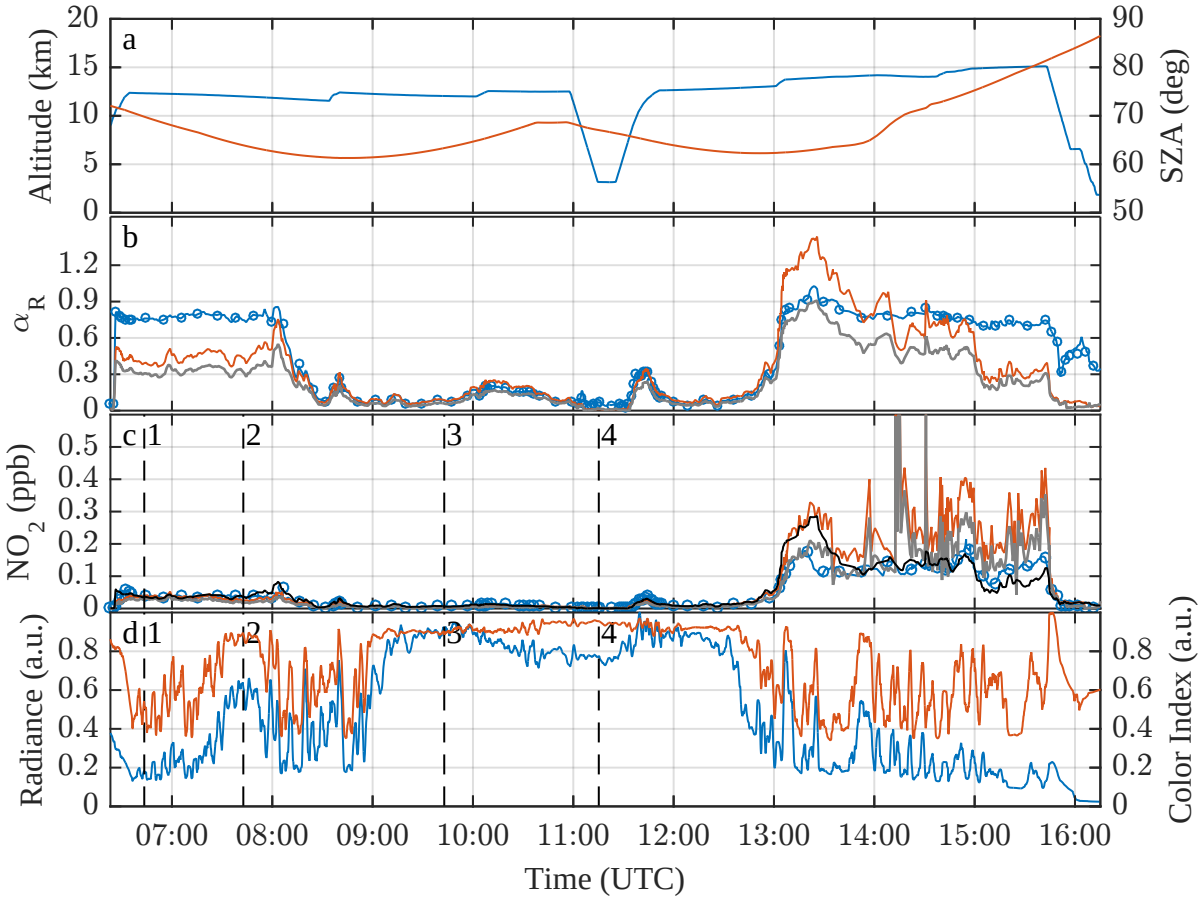

Figure 6.7: Comparison of O_3 and O_4 scaling calculations for science flight ANT. Panel a: Flight altitude (blue) and SZA (red). Panel b: α_R using O_3 (blue) and O_4 (red) as scaling gas, respectively. Calculations including the cloud layer (see text) are depicted for O_4 (grey line) and O_3 (blue circles) scaling. Panel c: $[NO_2]_{O_3}$ and $[NO_2]_{O_4}$ as in panel b together with CLaMS predicted $[NO_2]$ (black line). Panel d: Radiance (blue, 430 nm) and Colour Index (red, 600 nm / 430 nm) in relative units (scaled to the highest value), measured by the Nadir visible channel (VIS3) of the HALO mini-DOAS instrument . Nadir-pointing camera images corresponding to the marked timestamps are shown in Figure A.22.

The comparison of α_R for O_3 scaling (blue) and O_4 scaling (red) shows strongly different features for flight sections A (take off until 08:00 UTC), B (polar vortex, 08:00 - 13:00 UTC), and C (13:00 UTC until landing). In flight section A both α_R differ, but the retrieved $[NO_2]$ are similar. The timestamps

marked in flight section A show clear sky (timestamp 1) and cloudy (timestamp 2) conditions during the flight. The O_4-scaled α_R changes if the cloud layer is switched on in the model (grey line), but the impact on $[NO_2]_{O_4}$ is within the random error, since NO_2 mixing ratios are very low and near the detection limit. The O_3-scaled α_R is not influenced by the cloud layer. In flight section B, both α_R and $[NO_2]$ of both methods are close to or below the detection limit but agree within the random errors of the method. Flight section B shows clouds with underlying pack ice cover (timestamps 3 and 4). Since $[NO_2]$ is below the detection limit no firm conclusion on the validity of O_3 or O_4 scaling can be drawn from inspecting this flight section more closely.

Flight section C is the most interesting, and is shown with additional timestamps in Figure 6.8. The shape of α_R of the O_4 scaling method closely follows the predicted $[NO_2]$ at flight altitude, because α_{O_4} is almost constant for constant altitude. The inferred $[NO_2]_{O_4}$ strongly depends on the optical state of the atmosphere: In the case of clear sky conditions (prevailing from timestamp 5 to 7, and near timestamps 8, 11, and 14), the retrieved $[NO_2]_{O_4}$ (red line) closely follows the $[NO_2]$ predicted by the model (black line). Broken clouds below are detected by the nadir measurements at e.g. timestamps 6 and 10, showing little impact on $[NO_2]_{O_4}$. Limb measurements are not as sensitive to small scale variations of cloud cover, because they average over much larger areas than the FOV of the nadir pointing telescope. However, seemingly extended cloud cover (timestamps 7, 9, 12, 13 and 15) leads to increased $[NO_2]_{O_4}$ relative to $[NO_2]_{O_3}$ (blue line). Such cloud layers effectively prevent photons from lower parts of the atmosphere to be detected by UV/vis spectroscopy above. The measured O_4 SCD is thus decreased, which leads to an increased $[NO_2]_{O_4}$. If the surrogate cloud layer is switched on in the RTM, the agreement of $[NO_2]_{O_4}$ (grey line) and $[NO_2]_{O_4}$ (blue line and circles) is much better in some flight sections, e.g. 13:00 – 14:10 and 14:20 – 14:50 UTC. Flight sections where the disagreement between $[NO_2]_{O_4}$ and $[NO_2]_{O_3}$ is still large, e.g. between timestamps 9 and 10, may exhibit clouds at even higher altitudes than those introduced in the model. $[NO_2]_{O_4}$ is affected by a large and increasing uncertainty of SCD_R after 14:00 UTC due to decreasing O_4 SCDs (Figure A.19, panel e). $[NO_2]_{O_3}$ exhibits much smaller uncertainty at 70° – 85° SZA (Figure 6.8, panel a).

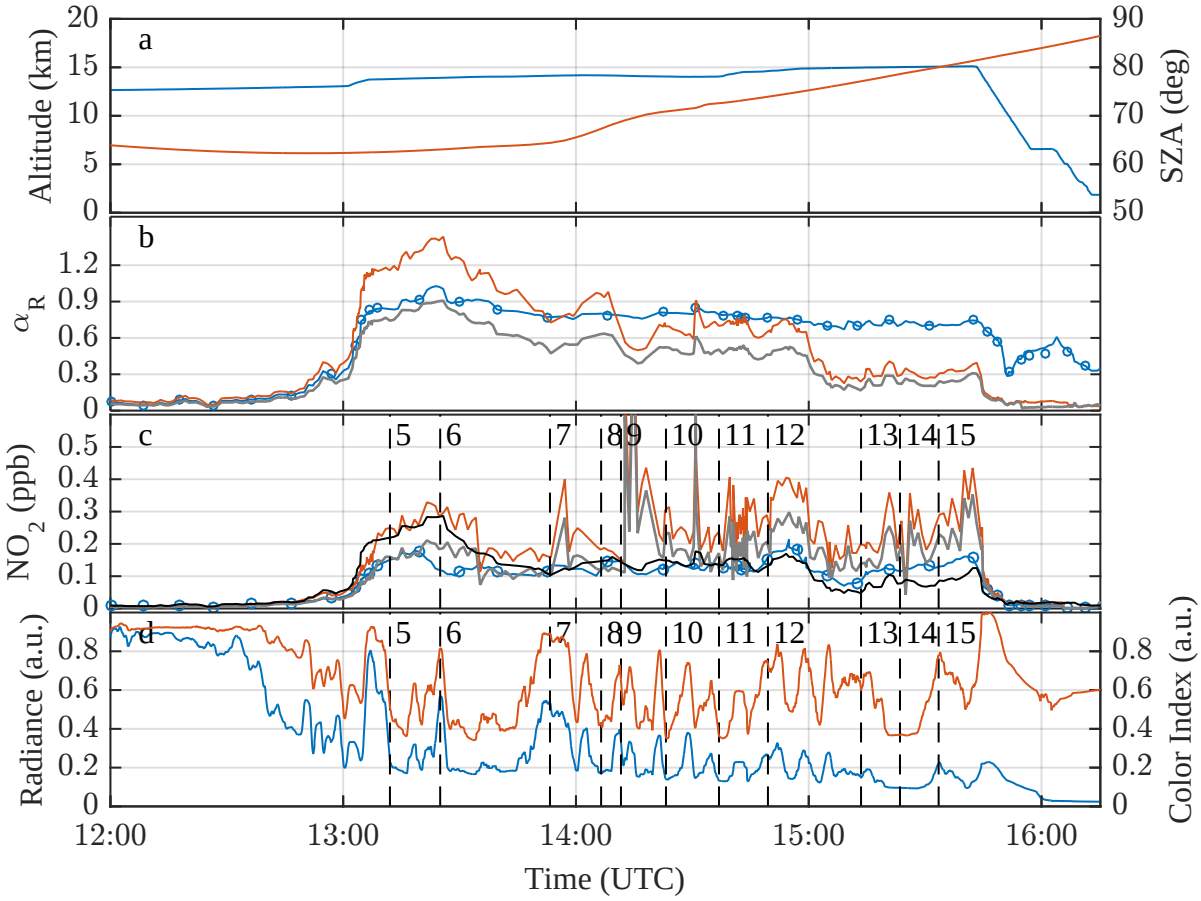

Figure 6.8: Comparison of O_3 and O_4 scaling calculations for science flight ANT. Panel a: Flight altitude (blue) and SZA (red). Panel b: α_R using O_3 (blue) and O_4 (red) as scaling gas, respectively. Calculations including the cloud layer (see text) are depicted for O_4 (grey line) and O_3 (blue circles) scaling. Panel c: $[NO_2]_{O_3}$ and $[NO_2]_{O_4}$ as in panel b together with CLaMS predicted $[NO_2]$ (black line). Panel d: Radiance (blue, 430 nm) and Colour Index (red, 600 nm / 430 nm) in relative units (scaled to the highest value), measured by the Nadir visible channel (VIS3) of the HALO mini-DOAS instrument . Nadir-pointing camera images corresponding to the marked timestamps are shown in figures A.22 and A.23.

Figure 6.9 shows the altitude profile of

$$\Delta[NO_2] = |[NO_2]^{clearsky} - [NO_2]^{cloudlayer}| \tag{6.16}$$

for both $[NO_2]_{O_4}$ (red) and $[NO_2]_{O_3}$ (blue) in absolute and relative units. Above the cloud layer, $\Delta[NO_2]_{O_3}$ is up to 10%, but mostly well below 5%. Contrarily, $\Delta[NO_2]_{O_4}$ is regularly between 20% and 40% at altitudes above 8 km, or more than 100 ppt in absolute units. Both methods exhibit large relative $\Delta[NO_2]$ in the altitude range of the cloud layer (4 – 8 km). Contrary to the higher altitudes mentioned above, the largest absolute $\Delta[NO_2]_{O_4}$ is approximately 20 ppt due to the very low absolute $[NO_2]$ of less than 40 ppt (Figure 6.7). $\Delta[NO_2]_{O_3}$ is within the random errors throughout the flight.

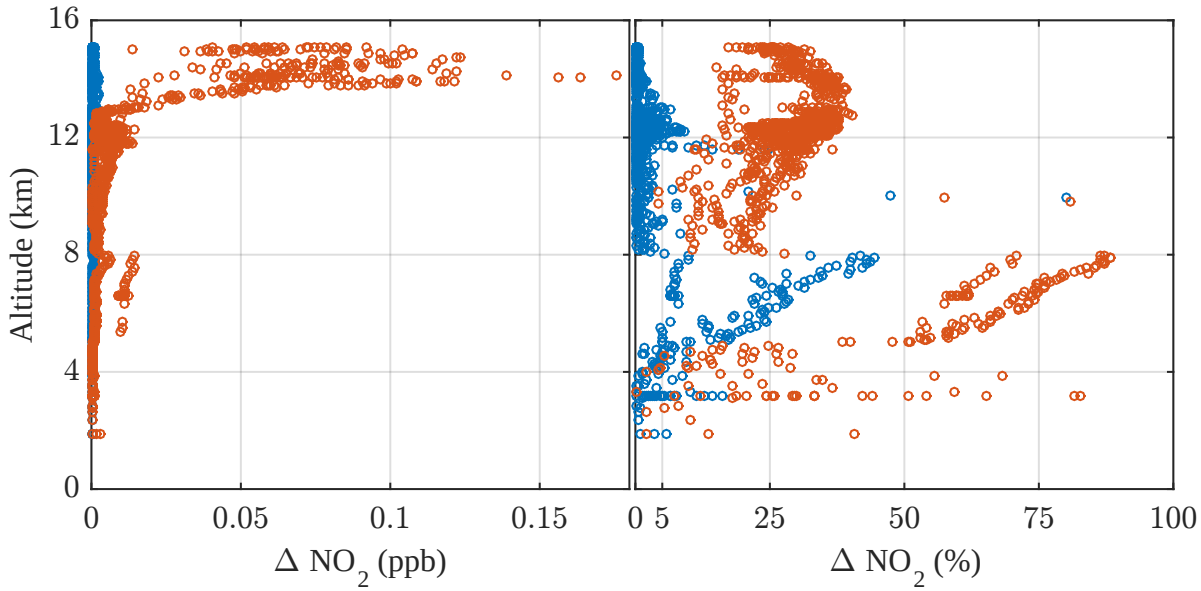

Figure 6.9: Altitude profiles of the absolute difference in inferred $[NO_2]_{O_4}$ (red) and $[NO_2]_{O_3}$ (blue) due to the inclusion of a surrogate cloud layer at 4 – 8 km altitude in the RTM in absolute (left panel) and relative (right panel) units.

Figure B.8 shows a comparison of $[NO_2]_{O_3}$ and $[NO_2]_{O_4}$ for science flight ML. A compact cloud layer prevails from take-off until 08:00 UTC (panel d). $[NO_2]_{O_4}$ is approximately two times larger than $[NO_2]_{O_3}$ and predicted $[NO_2]$ during this flight section, while the O_4 SCD is small (Figure B.6, panel e) and SZA > 60° (Figure B.8, panel a). Clear sky conditions dominate from 08:00 UTC until approximately 12:00 UTC, due to descending air of the stratospheric trough. $[NO_2]_{O_4}$ follows the predicted $[NO_2]$ closely. Scattered clouds return after 12:00 UTC, but do not influence $[NO_2]_{O_4}$ because of the low SZA ≈ 40°.

The retrieval of UT/LS $[NO_2]$ via O_3 scaling is a very robust approach. While the introduction of a cloud layer into the RTM does not change $[NO_2]_{O_3}$, $[NO_2]_{O_4}$ is strongly affected.

Chapter 7

Results and Discussion

The scaling method is applied to HALO mini-DOAS instrument measurements of NO_2 during all flights of the science mission TACTS/ESMVal (sect. 4.1) and to measurements of BrO during science flight ANT (sect. 4.1.2). At first, results obtained via CLaMS- and EMAC-based scaling retrievals are compared (sect. 7.1). Subsequently, science flight ANT including measurements of NO_2 and BrO is discussed in detail in section 7.2. Section 7.3 gives an overview of NO_x measurements during all science flights of the TACTS/ESMVal mission and compares measurements from flight ANT with those obtained during flight ML (sect. 4.1.1).

7.1 Comparison of CLaMS- and EMAC-based retrievals

In this section, $[BrO]_{O_3}$ and $[NO_2]_{O_3}$ are compared with respect to which CTM (sect. 5.4) is used for the RT calculations (sect. 5.3) to derive the α factors (sect. 6.1). The calculation of $[NO_2]_{O_3}$ using CLaMS is shown above in Figure 6.1 and the resulting concentration is denoted in this chapter as $[NO_2]_{O_3,\,CLaMS}$. The retrieval of NO_2 using EMAC is shown in Figure B.1 ($[NO_2]_{O_3,\,EMAC}$). Similarly, BrO is retrieved via O_3 scaling using CLaMS (Figure B.2) and EMAC (Figure B.3), and the retrieved concentrations are denoted as $[BrO]_{O_3,\,CLaMS}$ and $[BrO]_{O_3,\,EMAC}$, respectively.

Figure 7.1 shows the retrieved mixing ratios of BrO and NO_2 together with model predictions. The model-predicted concentrations are further on denoted as e.g. $[BrO]_{CL}$ and $[BrO]_{EM}$ for CLaMS- and EMAC-predictions, respectively. The following conclusions can be inferred from this comparison:

1. $[BrO]_{CL}$ and $[BrO]_{EM}$ (dashed lines in panel a) exhibit comparably large differences, especially inside the polar vortex (flight sections B and D) and in the troposphere (flight section C, compare also panel b in Figures B.2 and B.3).

2. CLaMS overestimates the subsidence in the polar vortex (see section 7.2.1) and misses tropospheric chemistry (sect. 5.4.1), i.e. tropospheric BrO sinks. Hence, it can be expected that $[BrO]_{CL}$ is overestimated compared to measured [BrO] in flight sections B and D. $[BrO]_{O_3,\,CLaMS}$

is generally underestimated at higher altitudes. The latter occurs because the overestimation of $[BrO]_{CL}$ in the troposphere leads to an underestimation of α_{BrO} at higher altitudes and thus decreases $[BrO]_{O_3,\,CLaMS}$ (eq. 6.5).

3. The retrieved mixing ratios $[BrO]_{O_3,\,ClaMS}$ and $[BrO]_{O_3,\,EMAC}$ agree within the random errors during flight sections A and E. Differences between $[BrO]_{O_3,\,ClaMS}$ and $[BrO]_{O_3,\,EMAC}$ in flight sections B and D are not only due to different BrO profiles, but because of differences in predicted $[O_3]$ at flight altitude. α_{O_3} is approximately 0.35 in the CLaMS-based retrieval compared to 0.25 in the EMAC-based retrieval (panel d in Figures B.2 and B.3). EMAC does not reproduce the polar vortex subsidence as well as CLaMS, but is better able to reproduce the general profile shapes of the trace gases (see following section). This could imply a more robust retrieval of $[BrO]_{O_3,\,EMAC}$ compared to $[BrO]_{O_3,\,CLaMS}$.

4. Retrieved $[BrO]_{O_3,\,CLaMS}$ and $[BrO]_{O_3,\,EMAC}$ agree within the random errors in flight sections A and E. The only exception is the last part of the flight after 15:00 UTC. Here, EMAC overestimates $[O_3]$ (Figure 7.2, panel b) and hence a larger α_{O_3} is calculated. Thus, $[BrO]_{O_3,\,EMAC}$ is probably underestimated (compare also panel a in Figures B.2 and B.3).

5. $[NO_2]_{O_3,\,EMAC}$ and $[NO_2]_{O_3,\,CLaMS}$ agree within the random errors for almost all flight sections. A remarkable exception is the edge of the polar vortex sampled at 13:00 – 13:30 UTC. A strong local maximum in NO_2 is predicted by CLaMS. But while it does not appear in the EMAC curtain, it is still retrieved from the measurements in $[NO_2]_{O_3,\,EMAC}$.

The trace gas profile retrieval in the troposphere (flight section C) is discussed in detail in section 7.2.2.

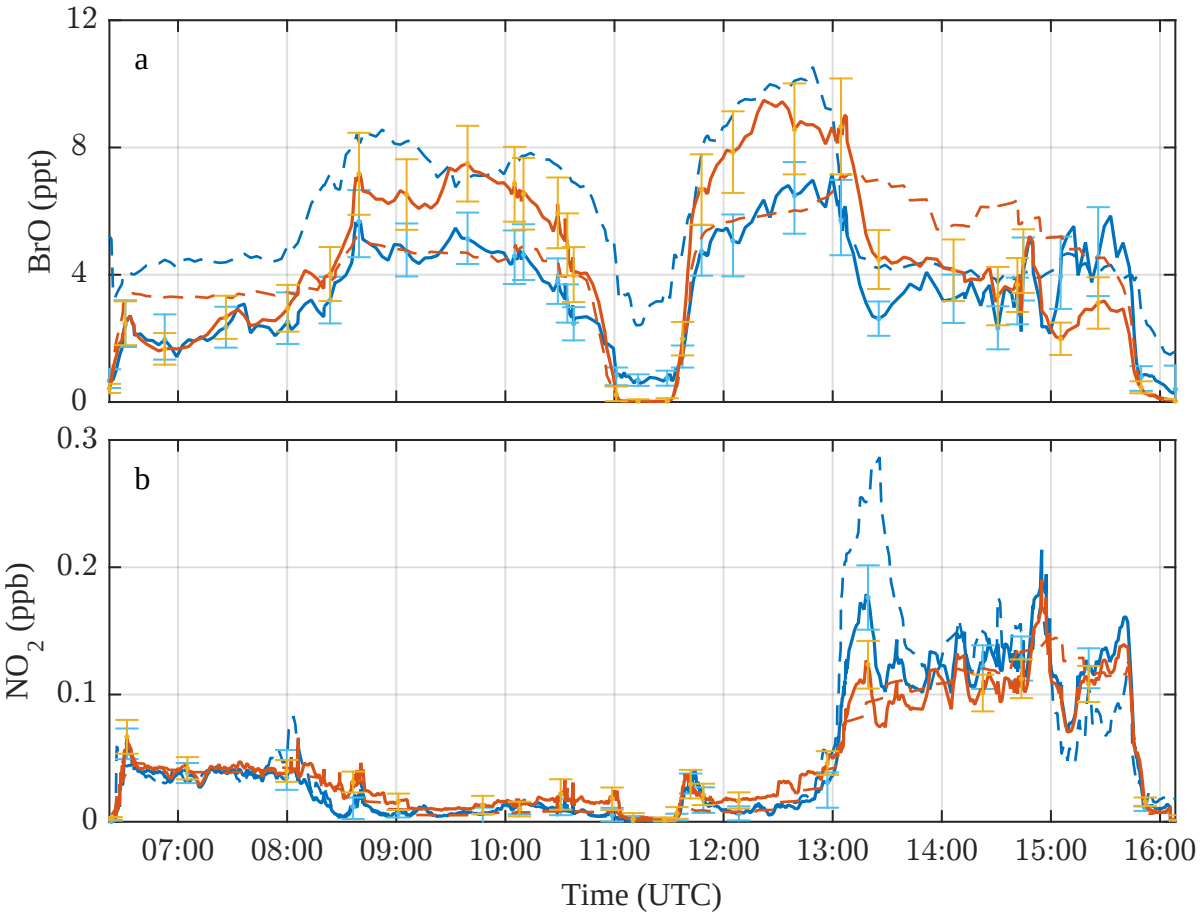

Figure 7.1: Mixing ratios of BrO (panel a) and NO_2 (panel b) retrieved via O_3 scaling for science flight ANT. Blue lines correspond to CLaMS-based RT calculations ($[BrO]_{O_3,\,CLaMS}$ and $[NO_2]_{O_3,\,CLaMS}$) and red lines correspond to EMAC-based RT calculations ($[BrO]_{O_3,\,EMAC}$ and $[NO_2]_{O_3,\,EMAC}$). Continuous lines show the retrieved mixing ratios, and error bars indicate the random error for a subset of the measurements. Broken lines represent model predicted $[BrO]_{CL}$, $[BrO]_{EM}$, $[NO_2]_{CL}$, and $[NO_2]_{EM}$.

7.2 Science flight ANT

Science flight ANT is introduced above in section 4.1.2, including a PV map (Figure 4.3) showing that a "blob" of high-PV air, i.e. air of stratospheric origin, was sampled during the flight. The dynamical features are analysed in more detail by Rolf et al. (2015). Figure 7.2 shows the trace gas measurements during this flight, which are discussed in the following.

7.2.1 UT/LS measurements

Panel b of Figure 7.2 shows methane (blue) and ozone (red) measurements, which are largely anticorrelated. Methane can be used as a transport tracer because it is reasonably well mixed in the troposphere (e.g. Kirschke et al., 2013) and its main sink is oxidation in the stratosphere, similar to N_2O (panel e, blue) (Bergamaschi et al., 2015). Tropospheric methane levels in the southern hemisphere (Cape Grim, Tasmania[1]) stood at 1778 ppb in September 2012 (panel b, black dashed line). Methane levels below 1600 ppb are observed in flight sections B and D, indicating stratospheric air descending from higher altitudes. Particularly old air with ages up to 4.5 years was sampled in flight section D in combination with strong dehydration (Rolf et al., 2015) and denitrification (Jurkat et al., 2016b). Panel b also shows predicted [CH_4] and [O_3] by EMAC (dotted lines) and CLaMS (dashed lines). CLaMS is much better able to reproduce the stratospheric loss of CH_4 and subsidence of high altitude stratospheric air in the polar vortex, which is already discussed in the context of systematic errors (section 6.4.2). However, the strength of stratospheric CH_4 loss and subsidence appears to be overestimated, since [CH_4] is underestimated while [O_3] is overestimated in flight sections B and D. EMAC does not cover the dynamical features as well, which is indicated by almost constant [CH_4] throughout the polar vortex.

The ExTL is sampled in flight sections A and E, with flight section A covering 11 – 12 km and E covering 13 – 15 km altitude, respectively. Ozone mixing ratios above 500 ppb are observed during flight section E before 15:00 UTC. Flight section A and the end of flight section E (after 15:00 UTC) show [O_3] < 500 ppb. The decreasing [O_3] and at the same time very high measurement altitude indicate that the tropopause height increased during the latter flight section (Figure 6.1, panel b).

Panel c shows measurements of HCl (blue) and BrO (red: $[BrO]_{O_3,EMAC}$, yellow: $[BrO]_{O_3,CLaMS}$, see section 7.1). As expected, BrO levels are enhanced in polar stratospheric air. Considering the EMAC-based retrieval, mixing ratios of 2-5 ppt BrO are measured in the extratropical LMS (flight sections A and E) and mixing ratios up to 7.5 ppt and 10 ppt are measured in the polar vortex during flight sections B and D, respectively. These concentrations are on the higher end of comparable BrO measurements in the same altitude range (12 – 13 km) reported in the literature (Harder et al., 1998; Dorf et al., 2006a; Hendrick et al., 2007; Werner et al., 2016). This high-bias could for example be caused by the subsidence of stratospheric air from higher altitudes discussed above.

[1] http://www.csiro.au/greenhouse-gases/

OClO is not detected by the HALO mini-DOAS instrument probably because of photodissociation due to low SZA < 70° at the time of the measurement (Figure 7.2, panel a). Jurkat et al. (2016b) show measurements of HCl, $ClONO_2$, and Cl_y, indicating the presence of up to 40% active chlorine of total Cl_y during flight sections B and D. Active chlorine could be present in the form of Cl, ClO, or $(ClO)_2$.

Panel d of Figure 7.2 shows NO_x measurements (NO (blue), $[NO_2]_{O_3,\,EMAC}$ (red), and $[NO_2]_{O_3,\,CLaMS}$ (yellow)). In polar vortex air (flight sections B and D), retrieved $[NO_2]$ is mostly between 5 and 20 ppt, i.e. near or below the detection limit of 10 ppt, similar to the in-situ measured NO. This small amount of NO_x thus limits the deactivation of active chlorine, i.e. the formation of $ClONO_2$, and thus prolongs ozone destruction in the polar winter vortex air (Douglass et al., 2014). For flight sections A and E, it is interesting to consider the Leighton ratio Φ in order to assess the atmospheric oxidation capacity. Φ is calculated using equation 2.1 with [NO] and $[O_3]$ averaged over the integration time for each spectral NO_2 measurement. The coefficient $k_{O3+NO}(T)$ is calculated from Sander et al. (2011) using in-situ ambient temperatures monitored by BAHAMAS. J_{NO_2} is approximated as a function of SZA derived from airborne actinic flux density measurements by Insa Lohse (pers. comm.). This approximation can be seen as a lower limit, since J_{NO_2} may increase by a factor of 1.5 – 2 above clouds or when the surface albedo is near 1, i.e. above snow covered land (Kelley et al., 1995; Heue et al., 2014). The Leighton ratio is approximately unity throughout flight sections A and E (black dotted line) but shows a trend towards larger Φ in the stratosphere. This trend is further discussed below in section 7.3.

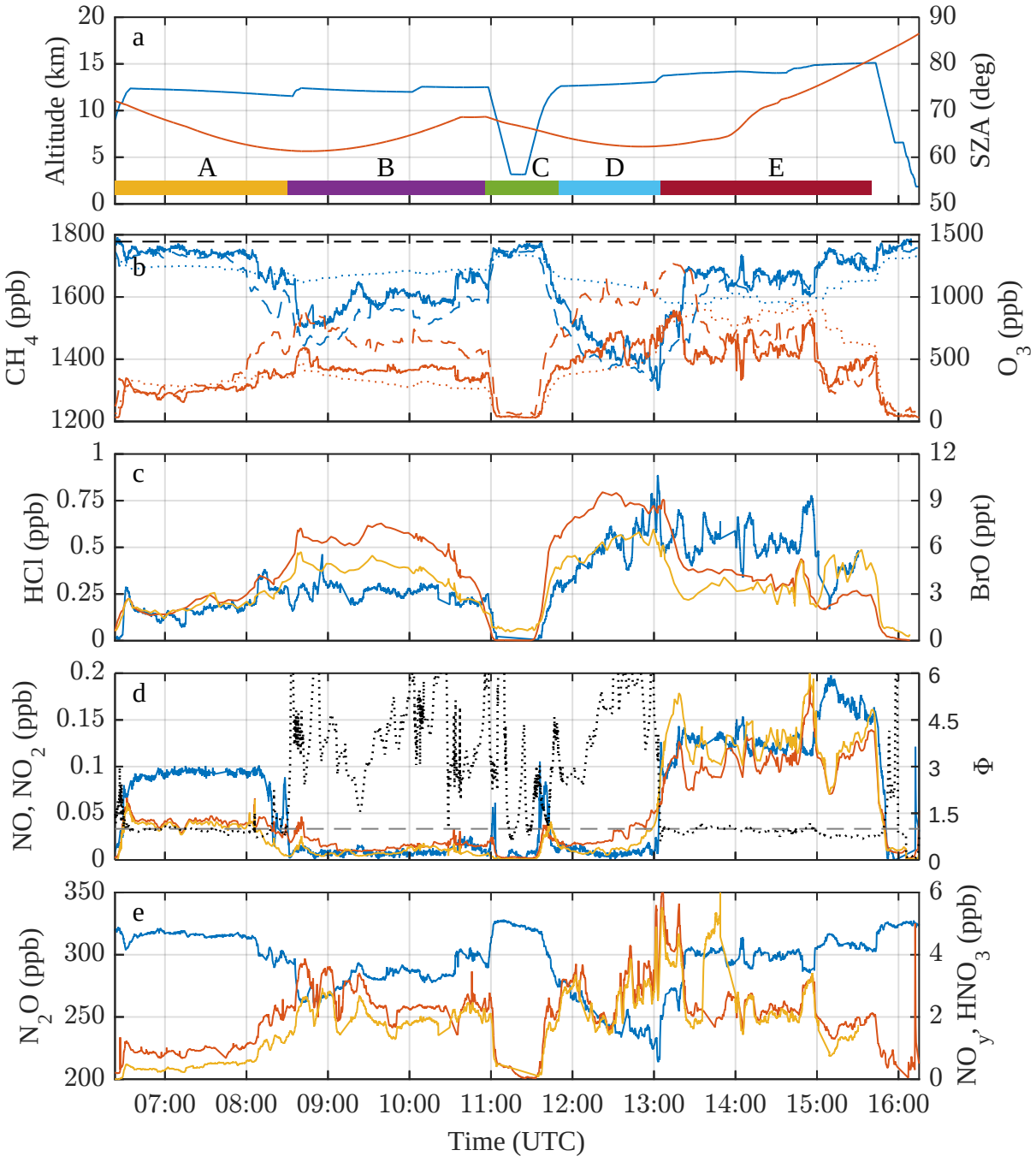

Figure 7.2: Time series of trace gases measured during science flight ANT. Panel a: Altitude (blue) and SZA (red). Coloured bars indicate the flight sections A – F introduced in section 4.1.2. Panel b: CH_4 (blue, TRIHOP) and O_3 (red, FAIRO). Panel c: HCl (blue, AIMS), $[BrO]_{O_3,\,EMAC}$ (red), and $[BrO]_{O_3,\,CLaMS}$ (yellow, both HALO mini-DOAS instrument). Panel d: NO (blue, AENEAS), $[NO_2]_{O_3,\,EMAC}$ (red), and $[NO_2]_{O_3,\,CLaMS}$ (yellow, both HALO mini-DOAS instrument). The Leighton ratio (black dotted line) calculated using $[NO_2]_{O_3,\,CLaMS}$ is compared to $\Phi = 1$ (grey dashed line), which indicates equilibrium between photolysis of NO_2 and oxidation of NO by O_3. Panel e: N_2O (blue, TRIHOP), NO_y (red, AENEAS), and HNO_3 (yellow, AIMS).

7.2.2 Measurements in the Antarctic troposphere

Trace gas concentration profiles measured during the dive (flight section C) are shown in Figure 7.3 for both descent (blue) and ascent (red). As mentioned earlier, CLaMS overestimates the stratospheric loss in CH_4 and/or the descent of high-altitude stratospheric air, indicated by the underestimation of $[CH_4]$ (panel g) compared to the measurements between 8 and 14 km altitude. CLaMS also underestimate HCl (panel f, HCl predictions were not provided by EMAC), which points either to a deficit in accounting for the Cl + CH_4 reaction (into HCl + CH_3), or that HCl is too rapidly reacting (together with $ClONO_2$) on stratospheric sulphuric acid water aerosols and/or PSC particles (Jaeglé et al., 1997).

One interesting aspect is the NO_x layer detected at altitudes of 9 – 13 km during descent and ascent (panels b and c). The largest [NO] of 60 – 80 ppt is measured at altitudes of 10 – 12 km, while the largest $[NO_2]$ of 30 – 40 ppt is measured at 11 – 13 km. The NO maximum is predicted by EMAC for descent and ascent, but in CLaMS the NO_2 maximum is only predicted for the ascent. The latter is shown in panel b of Figure 6.1, indicating in-mixing of tropospheric air from more NO_x rich latitudes. Rolf et al. (2015) also infer in-mixing of moister mid-latitude air into the polar vortex, albeit not at the same time during the flight, since the GLORIA instrument was switched off during the dive. $[NO_2]$ and [NO] are below their detection limits of 10 ppt and 7 ppt, respectively, throughout most of the troposphere, indicating very pristine air. Mixing ratios significantly above the detection limits are measured above 10 km and 9 km, respectively.

The amount and distribution of halogen oxides such as BrO (panel e) in the troposphere is a matter of current debate (e.g. Harder et al., 1998; Fitzenberger et al., 2000; Roozendael et al., 2002; Saiz-Lopez and von Glasow, 2012; Volkamer et al., 2015; Sherwen et al., 2016a,b) and is of significant scientific interest due to its potential influence on tropospheric ozone chemistry (von Glasow et al., 2004). The CTMs used in the present thesis, CLaMS and EMAC, predict strongly different tropospheric [BrO]. Below 9 km altitude CLaMS predicts 3 – 5 ppt, while EMAC predicts concentrations close to zero. This discrepancy is probably due to missing tropospheric sinks in the CLaMS model (sect. 5.4.1). Hence, the EMAC-predicted BrO profile is expected to be more accurate, in particular the gradient at 10 – 14 km altitude during the aircraft ascent. The retrieved $[BrO]_{O_3,\,EMAC}$ and $[Bro]_{O_3,\,CLaMS}$ are both below the detection limit of 2 ppt in the altitude range below 9.5 km, despite the differently predicted profile shapes. Mixing ratios above the detection limit of 2 ppt are detected in the altitude range above 9.5 km. The concentration increase with altitude is more pronounced in the case of $[BrO]_{O_3,\,EMAC}$, because the lower $[BrO]_{EM}$ in the troposphere implies higher calculated α_{BrO} at altitudes above, compared with the CLaMS-based RT calculations. Additionally, the $[O_3]_{EM}$ is lower than $[O_3]_{CL}$ (panel a), reducing α_{O_3}. Overall, the BrO concentrations inferred using EMAC-based RT calculations seem more reliable because (a) CLaMS appears to overestimate BrO concentrations in the troposphere, and (b) the EMAC-predicted profile shape of O_3, which is used as scaling gas, reproduces in-situ measurements much better. Interestingly, $[BrO]_{O_3,\,EMAC}$ is below 3 ppt during the descent even in the altitude range of 12 – 14 km, but mixing ratios near 10 ppt are measured during the ascent at the same altitudes. This may be caused by the lower tropopause height during the ascent compared to the descent (Rolf et al., 2015, Figure 2).

Elevated BrO concentrations were observed in the polar spring troposphere via satellite (Platt and Wagner, 1998; Roscoe et al., 2014) and aircraft (McElroy et al., 1999; Salawitch et al., 2010), including between 60° and 70° S (Schönhardt et al., 2012). Most plumes of enhanced BrO may be of tropospheric origin (Theys et al., 2011). Up to 41 ppt BrO have been measured in the polar boundary layer (Pöhler et al., 2010), causing so-called ozone depletion events (e.g. Evans et al., 2003; Platt and Hönninger, 2003). Several measurements of tropospheric BrO profiles under background conditions have also been reported in recent years. Among them, Fitzenberger et al. (2000) derive tropospheric BrO profiles above Kiruna (Sweden) from balloon measurements and conclude that tropospheric BrO amounting to 0.4 – 2.3 ppt eventually was present, assuming a uniform distribution within the troposphere. Prados-Roman et al. (2011) use airborne DOAS measurements based in Spitzbergen to derive a BrO mixing ratio profile in Arctic spring with 15 ppt in the PBL, 1.5 ppt in FT, and up to 6 ppt at 10 km in the LMS. Tropical profiles have been retrieved by e.g. Dorf et al. (2008), who infer [BrO] < 1 ppt throughout the troposphere, and Volkamer et al. (2015), who show BrO DOAS measurements aboard the NSF GV aircraft over the tropical Pacific. They derive BrO profiles with 0 – 1 ppt below 6 km altitude, approximately 2 ppt at 10 km and 3 ppt at 12 – 13 km altitude. The measurements derived in the present thesis are compatible with these previously inferred background profiles and do not show elevated BrO concentrations in the Antarctic spring in September 2012. Even when using RT calculations based on CLaMS, which predicts 3 ppt BrO in the troposphere, the retrieved mixing ratios below 9.5 km altitude are 1.5 to 2 ppt BrO, i.e. below or near the detection limit of 2 ppt. Hence, no BrO could be detected below 9.5 km altitude.

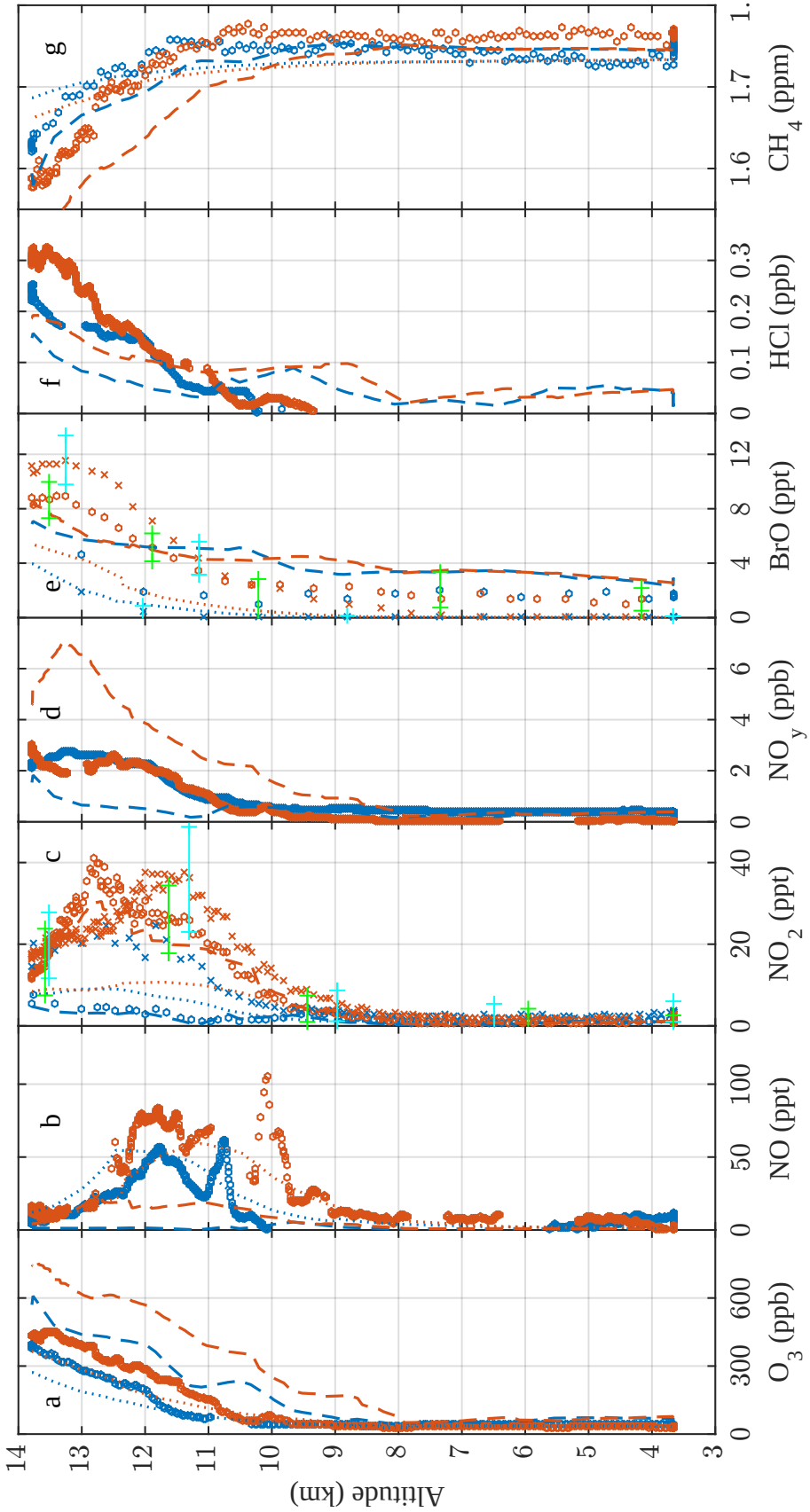

Figure 7.3: Altitude profiles of trace gases measured between 10:56 – 11:53 UTC during science flight ANT. The descent (65° S, 21° E) is indicated in blue and the ascent (61° S, 20° E) is indicated in red. Measurements are shown as symbols, and model predictions are shown as lines (dotted lines: EMAC, dashed lines: CLaMS). In the case of NO_2 (panel c) and BrO (panel e), circles indicate $[X]_{O_3,\,\mathrm{CLaMS}}$ (green error bars) and crosses indicate $[X]_{O_3,\,\mathrm{EMAC}}$ (cyan error bars). Panel a: O_3 (FAIRO). Panel b: NO_2 (AENEAS). Panel c: NO_2 (HALO mini-DOAS instrument). Panel d: NO_y (AENEAS). Panel e: BrO (HALO mini-DOAS instrument). Panel f: HCl (AIMS). Panel g: CH_4 (TRIHOP).

7.3 NO_x measurements during TACTS/ESMVal

HALO mini-DOAS instrument NO_2 measurements are evaluated for all flights of the science mission TACTS/ESMVal using the scaling method with predicted trace gas profiles provided by the CLaMS model. The derived [NO_2] is shown together with in-situ measurements of O_3, NO, NO_y, CH_4, and CO in Figure 7.6. Several distinct regimes can be identified:

1. Mid-latitude stratospheric air (40°– 80°N, 30°– 50°S, above 12 km) is identified by [O_3] > 300 ppb, elevated [NO_y] and [NO_2] as well as strongly diminished [CH_4] and [CO].
2. Processed polar winter vortex air (south of 50°S, above 12 km altitude) is indicated by very low [NO_x] as well as reduced [CH_4] and [Co] compared with the mid-latitude stratosphere.
3. Pristine polar tropospheric air (south of 50°S, below 12 km altitude) exhibits very low O_3, NO_x, and NO_y.
4. Polluted air at high altitudes in the tropics may either be influence by biomass burning (elevated NO_x and CO) or thunderstorms (elevated NO_x but low CO).
5. Aircraft emissions increase NO_x pollution particularly in the flight corridor above the mid-latitude North Atlantic.
6. Increased background concentrations of CO, CH_4, and NO_x are encountered in the European boundary layer.
7. Air influenced by aged biomass burning emissions is identified by high organic nitrate (e.g. PAN) concentrations.

Exemplarily, the nature of the stratosphere-troposphere transition in different atmospheric regimes is investigated by comparison of transport tracer and NO_x measurements gathered during science flights ANT and ML. The Leighton ratio (eq. 2.1) is calculated for both flights (Figures 7.2 and B.10) as explained above. It is further on denoted as Φ_{ANT} and Φ_{ML}, respectively. Figure 7.4 shows the Leighton ratio as a function of altitude and [N_2O]. N_2O is chosen as a vertical coordinate instead of CH_4, since the science flights ANT and ML took place in opposite hemispheres and tropospheric [CH_4] exhibits an offset of approximately 70 ppb between the northern and southern hemispheres.

Φ_{ML} shows two distinct clusters, namely (a) a "stratospheric" cluster around $\Phi_{ML} \approx 1$ and [N_2O] = 310 ppb, and (b) a "tropospheric" cluster around $\Phi_{ML} \approx 0.5$ and [N_2O] = 325 ppb. Almost all measurements are confined to these clusters. Additionally, some connecting lines are visible, presumably due to mixing of stratospheric and tropospheric air masses (Müller et al., 2016). Φ_{ANT} shows a similar gradient with N_2O. Additionally, many measurements scatter with a maximum of $\Phi_{ANT} = 6$. It is again noted that Φ is derived from an approximation of J_{NO_2} seen as a lower limit. Therefore, Leighton ratios below unity may occur because J_{NO_2} is underestimated. Hence, during both science flights the NO_x budget appears to be near $\Phi = 1$ where significant amounts of NO_x are detected. The

majority of measurements exhibits an apparent gradient from $\Phi \approx 0.5...1$ at $[N_2O]$ = 325 ppb towards $\Phi \approx 1...2$ at $[N_2O]$ = 300 ppb, with no significant discrepancy between Φ_{ANT} and Φ_{ML}, i.e. air masses of southern hemispheric and northern hemispheric origin. Leighton ratios $\Phi > 1$ indicate that peroxy radicals (HO_x), halogen monoxides such as BrO, nitrate radicals (NO_3), or other species oxidise NO to NO_2 in excess of the reaction between NO and O_3. Hence it is concluded that additional oxidants begin to significantly influence the oxidation capacity in the UT/LS region at altitudes above $[N_2O]$ = 310 ppb in the air masses sampled during research flights ANT and ML.

Figure 7.5 shows that measurements with very large Φ_{ANT} predominantly occur under very low NO_x conditions, i.e. in the polar stratosphere and troposphere. However, it has to be noted that these Leighton ratios are derived from NO and NO_2 measurements near the detection limit of 7 and 10 ppt, respectively, and therefore are uncertain. Nevertheless, comparable findings for low-NO_x conditions have been obtained from other measurements, for example at a small-town site close to the Atlantic Ocean in Durham, New Hempshire, USA (Griffin et al., 2007, Figure 7) and from ship measurements in the remote South Atlantic Ocean (Hosaynali Beygi et al., 2011, Figure 4). They argue that a yet unidentified oxidant is needed in order to explain high Leighton ratios under unpolluted low-NO_x conditions. These in-situ measurements are based on photolytic conversion of NO_2 to NO in a UV-LED irradiated reaction cell and subsequent chemiluminescent detection of NO. Reed et al. (2016) contend that thermal decomposition of PAN within such instrument's photolysis cell may give a partial explanation for anomalously high NO_2 in low-NO_x regimes. This kind of interference does not apply to the DOAS measurements presented here. Overall, the measurements are uncertain, but appear to support previous findings of high Leighton ratios under low-NO_x conditions, while excluding the kind of interferences that in-situ measurements may be subject to.

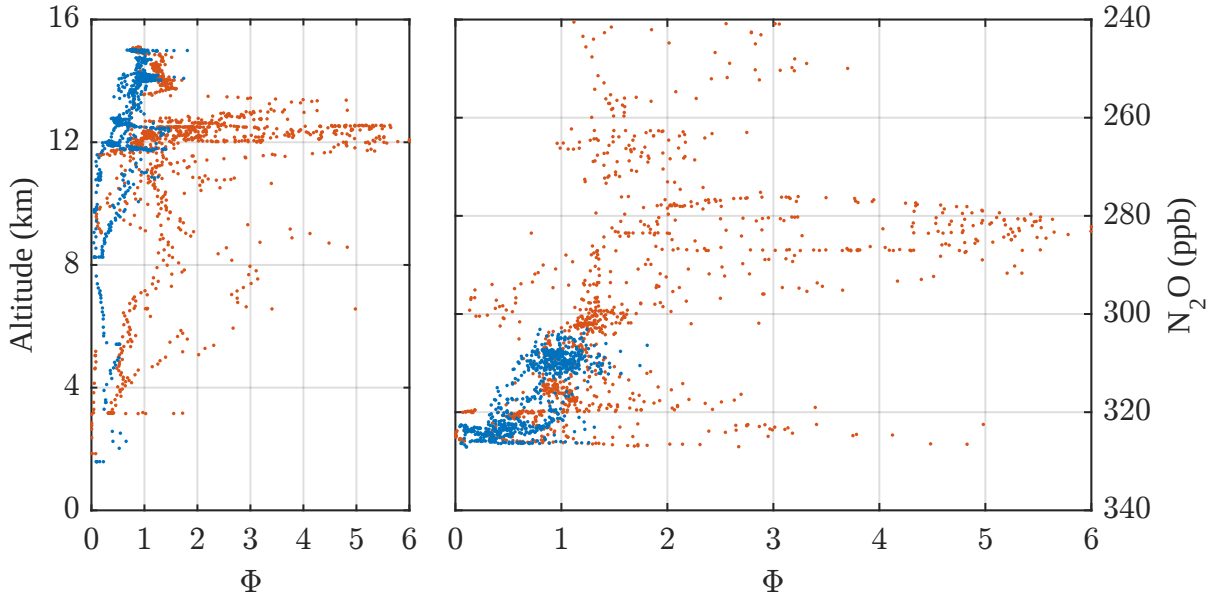

Figure 7.4: Measurement inferred Leighton ratio Φ as a function of flight altitude (left panel) and in-situ measured (TRIHOP) N_2O mixing ratio (right panel). Blue symbols indicate Φ_{ML}, red symbols indicate Φ_{ANT}.

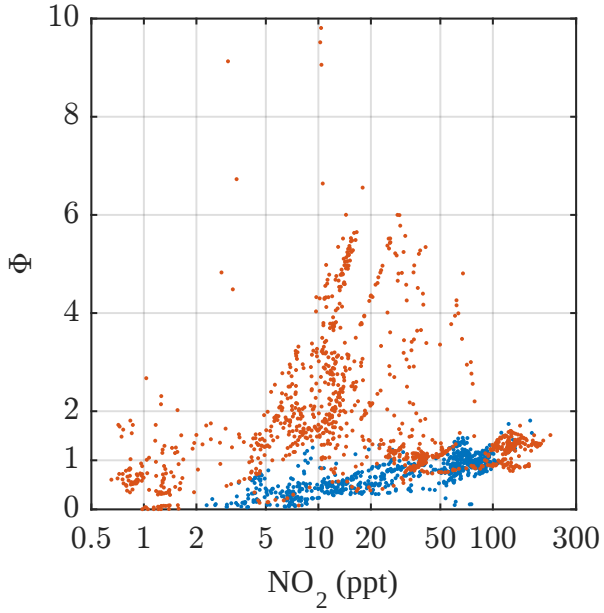

Figure 7.5: Measurement inferred Leighton ratio Φ_{ML} (blue) and Φ_{ANT} (red) as a function of derived $[NO_2]_{O_3,\,CLaMS}$.

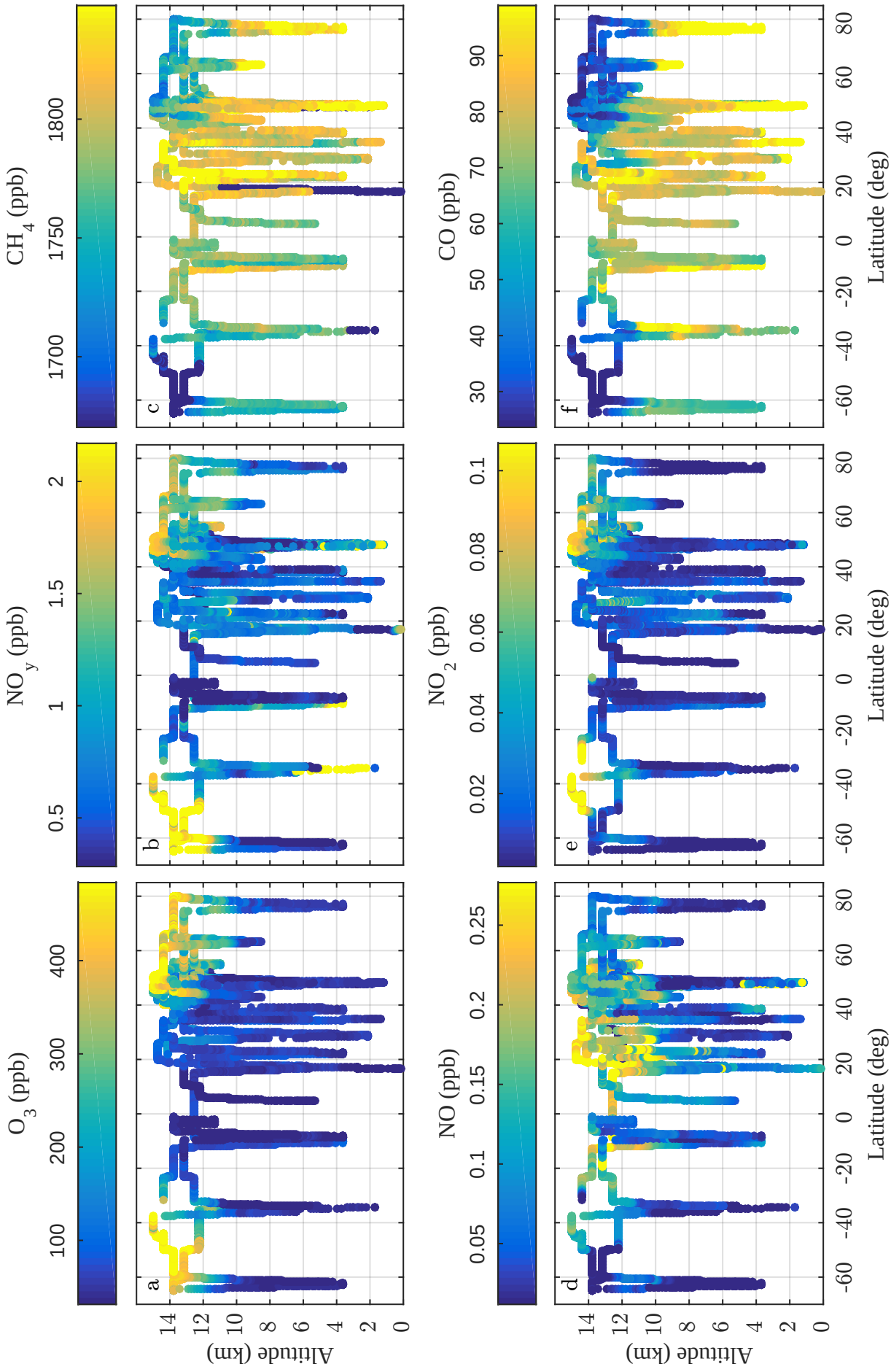

Figure 7.6: Overview of all measurements during the TACTS/ESMVal mission. In-situ measurements are interpolated on the measurement times of the HALO mini-DOAS instrument NO_2 measurements. Panel a: O_3 (FAIRO). Panel b: NO_y (AENEAS). Panel c: CH_4 (TRIHOP). Panel d: NO (AENEAS). Panel e: NO_2 (HALO mini-DOAS instrument). Panel f: CO (TRIHOP).

Chapter 8

Conclusion and Outlook

The present thesis describes (a) the major features of the novel HALO mini-DOAS instrument (chapter 3) which was developed by the author within his diploma and PhD theses, (b) introduces and tests a novel retrieval technique to quantify the concentrations of the targeted gases from airborne limb measured slant column densities at all sky conditions (chapter 6), and (c) reports on some first atmospheric measurements using the novel instrument and the retrieval method (chapter 7).

The following sections summarise the characterisation of the scaling method applied to HALO mini-DOAS instrument trace gas measurements (sect. 8.1), highlight the sample measurements analysed in the previous chapter (section 8.2) and give an outlook on scientific objectives which can be tackled by evaluating data already obtained from various science missions (sect. 8.3).

8.1 Characteristics and applicability of the scaling method

Seven science missions were carried out with the HALO mini-DOAS instrument to date, comprising more than 80 research flights (chapter 4). Most of the data collected during the science missions is at present at a preliminary stage of processing. The largest obstacle with regards to evaluating the spectra recorded in UV/vis limb spectroscopy lies in the limitations of the traditional retrieval method of inversion by optimal estimation (OEI). OEI strongly depends on a priori knowledge of the atmospheric state, i.e. the aerosol- and cloud-profile, which is not known under most conditions. Accordingly, a novel scaling method (chapter 6) has been developed in recent years by our research group (Raecke, 2013; Großmann, 2014; Knecht, 2015; Werner, 2015; Werner et al., 2016; Stutz et al., 2016; Aderhold, 2016; Knapp, 2016, and the present thesis). The novel scaling method promises that UV/vis limb spectroscopy measurements can be processed for all skies, which greatly extends the usefulness of such meaurements. The scaling method makes use of a simultaneously in-situ measured (O_3) or calculated scaling gas (O_4), the ratio of the slant column amount of the target gas and the scaling gas, and a correction term determined by RT modelling which accounts for the ratio in the detectibility of the target and scaling gas.

The present thesis shows the adaptation of the scaling method for HALO mini-DOAS instrument measurements and thoroughly investigates its random and systematic errors for tropospheric and lower stratospheric measurements for the first time. The random errors are further on used as a measure of retrieval uncertainty and the systematic errors point to potential weaknesses or potential biases of the scaling method.

Sections 6.2 and 6.3 show an extensive analysis of the random error of the scaling method. Generally, the uncertainty of the Fraunhofer reference SCD_{Ref} and the uncertainty of α_R are among the major contributors to the random error (Table 6.1). Depending on the measurement conditions, the vertical sampling uncertainty can dominate the error budget during flight sections with strong vertical concentration gradients of the involved scaling and target gas (Figure 6.5). For low SCDs the DOAS fit error may dominate the error budget (Figure A.19, panel e). Overall, the random error is of the order of 10 – 20 % for most measurement conditions (Figure 7.1).

Potential systematic errors of the scaling method are investigated for science flight ANT in section 6.4. It is shown that strong concentration gradients in the vicinity of the measurement and a misprediction of their vertical alignment by the employed CTMs may cause a systematic bias in the target gas concentration. The confidence in the relative profile shapes of the involved trace gases can be increased by comparing model predictions with independent measurements of the scaling gas and/or dynamical tracers. The accuracy of the scaling method can be further validated in science missions where independent validation measurements of the target gas are available (sect. 8.3).

Further, the influence of low altitude cloud cover, which is frequently encountered during research missions, on O_3 and O_4 scaling is investigated in section 6.4.3. It is shown that, while both methods may provide comparable results under clear sky conditions, extended cloud layers strongly influence O_4 scaling when applied to stratospheric trace gases at high altitudes (see also Figure 7 in Stutz et al. (2016)). The inspection of nadir radiances and camera images indicates that the influence of low level clouds on O_4 scaling increases with their areal coverage and compactness and at higher SZAs. The deviations of $[NO_2]_{O_4}$ from predicted NO_2 can in part be compensated by introducing a surrogate cloud layer into the RTM. This is assumed to occur due to the backscattering of light from atmospheric layers at lower altitudes (Oikarinen, 2002), where most O_4 absorption occurs (Greenblatt et al., 1990; Pfeilsticker et al., 1997b, 2001). Contrarily, $[NO_2]_{O_3}$ is independent of the presence of clouds below the aircraft altitude.

From the comparison of O_3 and O_4 scaling it is argued that a scaling gas P with a profile shape similar to the target gas X significantly reduces the sensitivity towards changing radiative properties of the atmosphere (Figure 6.2). RT simulations presented by Knecht (2015) indicate that this is required in order for the scaling gas to adequately represent changes in light path distributions.

The detection limits and measurement uncertainties of targeted trace gases are assessed with respect to the instrument performance under laboratory conditions (Table 3.6), the spectral retrieval applied to field measurements (Table 5.3) and the scaling method (sect. 6.3). Detection limits of 10 ppt NO_2 and 2 ppt BrO are estimated for the research flights investigated in the present thesis.

Overall, the present thesis shows the applicability of the scaling method to HALO mini-DOAS instrument measurements of NO_2 and BrO at altitudes between 3.5 and 15 km. The results obtained by O_3 scaling are practically unperturbed by the presence and properties of cloud cover. However, the scaling method depends on the a priori assumed relative profile shape of the scaling and target gas. Hence, it is suggested that comparing measured profile shapes of the scaling gas and dynamical tracers such as CH_4 and N_2O with model predictions is essential in assessing the validity of the applied relative profile shapes.

8.2 Sample measurements

The mixing ratios of NO_2 (for all flights of science mission TACTS/ESMVal) and BrO (for science flight ANT) are retrieved by O_3 scaling and compared with model predictions and complementary measurements by other instruments.

Several distinct atmospheric regimes encountered during the TACTS/ESMVal science mission are identified using measurements of O_3, NO, NO_2, NO_y, CH_4, and CO. The Leighton ratio is derived for (a) science flight ANT from Cape Town into the Antarctic polar vortex and (b) science flight ML above the mid-latitude Atlantic and Europe. The measurement derived Leighton ratios increase from $\Phi < 1$ at $[N_2O] > 310$ ppb to $\Phi > 1$ at $[N_2O] < 310$ ppb in the UT/LS during both science flights. It is further shown that while Leighton ratios are close to unity if several hundred ppt NO_2 are present, there is a relatively large scatter towards larger Leighton ratios if $[NO_2] < 100$ ppt (Figure 7.5). Hence, oxidants other than O_3 may dominate oxidation of NO under these conditions. This finding supports similar evidence at low-NO_x conditions obtained from other measurement sites, and it has been argued that a yet-unknown oxidant may be responsible for the additional oxidation (Hosaynali Beygi et al., 2011). However, the results need further consolidation due to their proximity to the detection limits of NO and NO_2 measurements of 7 and 10 ppt, respectively.

No elevated levels of BrO could be detected at 65° S between 3.5 and 9.5 km altitude during the dive on September 13, 2012. BrO concentrations were below the detection limit of 2 ppt for the altitude range below 9.5 km and increased to 4 ppt at 11 km, 8 ppt at 12.2 km and 11 ppt at 13 – 14 km altitude. This altitude profile and inferred BrO mixing ratios of 7.5 – 11 ppt at altitudes of 12 – 14 km in the Antarctic polar vortex are in agreement with previous airborne BrO measurements in the Arctic troposphere and lower stratosphere (e.g. Dorf et al., 2008), but do not support enhanced tropospheric BrO concentrations inferred from satellite measurements for Antarctic spring (Schönhardt et al., 2012).

8.3 Ongoing studies and further scientific objectives

Currently, the HALO mini-DOAS instrument is modified in order to improve temperature stability and operability. Further science missions are planned with HALO starting in 2017. At the same time, the following scientific questions and methodical investigations remain to be tackled with respect to the already collected data:

1. The NO_2 measurements presented in chapter 7 are currently used together with in-situ measurements during science flight ANT to assess the denitrification in the Antarctic polar vortex (Jurkat et al., 2016b). The measurements indicate denitrification of up to 4 ppb at potential temperatures down to 360 K and renitrification below. Denitrification can increase ozone depletion in the polar stratosphere because it inhibits the deactivation of ozone-depleting substances.

2. The Arctic polar winter atmosphere was sampled during science mission Polstracc in winter 2015/16. In the scope of a diploma thesis in our research group, measurements of BrO and OClO by the HALO mini-DOAS instrument during Polstracc are employed to test the ClO + BrO reaction chain and help quantify the total inorganic and organic bromine budget (Werner et al., 2016). Knowledge of the latter is essential for better assessing the future of the global ozone layer (WMO, 2014).

3. The scaling method can be validated by comparison of HALO mini-DOAS instrument NO_2 measurements (Aderhold, 2016) with independently obtained laser-induced fluorescense measurements of NO_2 by the HORUS and Air-LIF instruments during the OMO science mission.

4. NO_2 measurements from all science missions carried out so far can be combined to study the distribution and transport of NO_x and the impact of various sources such as lightning, aircraft emissions, biomass burning, and uplift of boundary layer pollution by convective cloud systems on the NO_x budget of the FT and UT/LS. Of particular interest are, for example, Asian boundary layer pollution lifted to higher altitudes by the Asian summer monsoon circulation, which was sampled during science mission TACTS/ESMVal (Vogel et al., 2014) and OMO (Aderhold, 2016).

5. Raecke (2013) retrieved H_2O using the scaling method for DOAS limb measurements aboard the NASA Global Hawk. This can be adapted for the HALO mini-DOAS instrument measurements and validated against in-situ measured H_2O. Very precise H_2O measurement devices were deployed on HALO science missions (Zöger et al., 1999; Buchholz et al., 2014), which enable the validation of retrieval results. Water vapour (H_2O) is itself a potent greenhouse gas (Stocker et al., 2013) and a precursor of HO_x, which plays a major roll in atmospheric oxidation processes (Stone et al., 2012; Jaeglé et al., 2001). Additionally, knowledge of ambient relative humidity is necessary for the correction of measurements by some in-situ instrumentation aboard the aircraft. In-situ H_2O measurements failed during parts of the OMO mission and thus relative humidity provided from DOAS measurements could be used to fill in the gaps.

6. The Acridicon science mission (Wendisch et al., 2016) surveyed deep convective clouds above the Amazon basin, which are known to transport boundary layer pollution into the FT and TTL. One of the scientific objectives of the mission was to study vertical transport and mixing of trace gases from below cloud base to cloud anvils. HALO mini-DOAS instrument measurements of CH_2O, NO_2, and potentially $C_2H_2O_2$ and HONO during these science flights can give further insight into the properties of the transported air masses. They will also complement previous measurements of tropical trace gas profiles such as over Borneo (Grossmann et al., 2013; Sala et al., 2014) and the tropical eastern Pacific (Werner et al., 2016).

7. Wolf et al. (2016) compare cirrus cloud optical thickness retrievals from HALO mini-DOAS instrument measurements to those obtained from the radiance-calibrated HALO-SR instrument using an approach similar to Nakajima and King (1990). They derive comparable cloud optical thicknesses and conclude from simulations that limb measurements are generally better suited to retrieve properties of optically thin clouds. Currently, a PhD student of our research group (Lisa Scalone) is developing a novel retrieval algorithm for cloud optical thickness and particle size using near-IR spectra of cirrus clouds obtained by the NASA Global Hawk mini-DOAS instrument. A similar approach can be used on HALO mini-DOAS instrument spectra, in particular for measurements during the ML-Cirrus science mission (Voigt et al., 2016). Since during other missions, such as Acridicon and Narval (Klepp et al., 2014), mixed-phase and water clouds were dominant, the novel cloud algorithm can be tested to infer liquid water content (LWC) and ice water content (IWC) of these mixed phase clouds.

Bibliography

Oliver-Alex Aderhold. Auswertung flugzeuggetragener DOAS-Messungen mit der Skalierungsmethode: Fallbeispiel anhand von NO_2 in Luftmassen des südasiatischen Monsuns. Master thesis, Institut für Umweltphysik, Universität Heidelberg, Heidelberg, Germany, 2016.

S.R. Aliwell, M. Van Roozendael, P.V. Johnston, A. Richter, T. Wagner, D.W. Arlander, J.P. Burrows, D.J. Fish, R.L. Jones, K.K. Tørnkvist, et al. Analysis for BrO in zenith-sky spectra: An intercomparison exercise for analysis improvement. *Journal of Geophysical Research: Atmospheres*, 107 (D14), 2002. doi: 10.1029/2001JD000329. URL http://dx.doi.org/10.1029/2001JD000329.

A. E. Andrews, K. A. Boering, B. C. Daube, S. C. Wofsy, M. Loewenstein, H. Jost, J. R. Podolske, C. R. Webster, R. L. Herman, D. C. Scott, G. J. Flesch, E. J. Moyer, J. W. Elkins, G. S. Dutton, D. F. Hurst, F. L. Moore, E. A. Ray, P. A. Romashkin, and S. E. Strahan. Mean ages of stratospheric air derived from in situ observations of CO_2, CH_4, and N_2O. *Journal of Geophysical Research: Atmospheres*, 106(D23):32295–32314, 2001. doi: 10.1029/2001JD000465. URL http://dx.doi.org/10.1029/2001JD000465.

J. Aschmann and B.-M. Sinnhuber. Contribution of very short-lived substances to stratospheric bromine loading: uncertainties and constraints. *Atmospheric Chemistry and Physics*, 13(3):1203–1219, 2013. doi: 10.5194/acp-13-1203-2013. URL http://www.atmos-chem-phys.net/13/1203/2013/.

J. Aschmann, B.-M. Sinnhuber, E. L. Atlas, and S. M. Schauffler. Modeling the transport of very short-lived substances into the tropical upper troposphere and lower stratosphere. *Atmospheric Chemistry and Physics*, 9(23):9237–9247, 2009. doi: 10.5194/acp-9-9237-2009. URL http://www.atmos-chem-phys.net/9/9237/2009/.

J. Aschmann, B.-M. Sinnhuber, M. P. Chipperfield, and R. Hossaini. Impact of deep convection and dehydration on bromine loading in the upper troposphere and lower stratosphere. *Atmospheric Chemistry and Physics*, 11(6):2671–2687, 2011. doi: 10.5194/acp-11-2671-2011. URL http://www.atmos-chem-phys.net/11/2671/2011/.

S. Baidar, H. Oetjen, S. Coburn, B. Dix, I. Ortega, R. Sinreich, and R. Volkamer. The CU Airborne MAX-DOAS instrument: Vertical profiling of aerosol extinction and trace gases. *Atmospheric Measurement Techniques*, 6(3):719–739, 2013. doi: 10.5194/amt-6-719-2013. URL http://www.atmos-meas-tech.net/6/719/2013/.

W.T. Ball, J.D. Haigh, E.V. Rozanov, A. Kuchar, T. Sukhodolov, F. Tummon, A.V. Shapiro, and W. Schmutz. High solar cycle spectral variations inconsistent with stratospheric ozone observations. *Nature Geoscience*, 9(3):206–209, 2016.

Steffen Beirle, K. Folkert Boersma, Ulrich Platt, Mark G. Lawrence, and Thomas Wagner. Megacity Emissions and Lifetimes of Nitrogen Oxides Probed from Space. *Science*, 333(6050):1737–1739, 2011. ISSN 0036-8075. doi: 10.1126/science.1207824. URL http://science.sciencemag.org/content/333/6050/1737.

Niklas Berg, Johan Mellqvist, J.P. Jalkanen, and J. Balzani. Ship emissions of SO_2 and NO_2: DOAS measurements from airborne platforms. *Atmospheric Measurement Techniques*, 5(5):1085–1098, 2012. doi: 10.5194/amt-5-1085-2012. URL http://www.atmos-meas-tech.net/5/1085/2012/.

P. Bergamaschi, M. Corazza, U. Karstens, M. Athanassiadou, R. L. Thompson, I. Pison, A. J. Manning, P. Bousquet, A. Segers, A. T. Vermeulen, G. Janssens-Maenhout, M. Schmidt, M. Ramonet, F. Meinhardt, T. Aalto, L. Haszpra, J. Moncrieff, M. E. Popa, D. Lowry, M. Steinbacher, A. Jordan, S. O'Doherty, S. Piacentino, and E. Dlugokencky. Top-down estimates of European CH_4 and N_2O emissions based on four different inverse models. *Atmospheric Chemistry and Physics*, 15(2):715–736, 2015. doi: 10.5194/acp-15-715-2015. URL http://www.atmos-chem-phys.net/15/715/2015/.

T. Birner and H. Bönisch. Residual circulation trajectories and transit times into the extratropical lowermost stratosphere. *Atmospheric Chemistry and Physics*, 11(2):817–827, 2011. doi: 10.5194/acp-11-817-2011. URL http://www.atmos-chem-phys.net/11/817/2011/.

K. Bogumil, J. Orphal, T. Homann, S. Voigt, P. Spietz, O.C. Fleischmann, A. Vogel, M. Hartmann, H. Kromminga, H. Bovensmann, et al. Measurements of molecular absorption spectra with the SCIAMACHY pre-flight model: instrument characterization and reference data for atmospheric remote-sensing in the 230–2380 nm region. *Journal of Photochemistry and Photobiology A: Chemistry*, 157(2):167–184, 2003.

Mark J. Bollinger, Robert E. Sievers, David W. Fahey, and Frederick C. Fehsenfeld. Conversion of nitrogen dioxide, nitric acid, and n-propyl nitrate to nitric oxide by a gold-catalyzed reduction with carbon monoxide. *Analytical Chemistry*, 55(12):1980–1986, 1983.

H. Bönisch, A. Engel, Th. Birner, P. Hoor, D. W. Tarasick, and E. A. Ray. On the structural changes in the Brewer-Dobson circulation after 2000. *Atmospheric Chemistry and Physics*, 11(8):3937–3948, 2011. doi: 10.5194/acp-11-3937-2011. URL http://www.atmos-chem-phys.net/11/3937/2011/.

Jannik Bounin. Investigation of the temperature dependent characteristics of the HALO miniDOAS spectrometer and improvement of the spectral imaging properties. Bachelor thesis, Institut für Umweltphysik, Universität Heidelberg, Heidelberg, Germany, 2015.

J. Bradshaw, D. Davis, G. Grodzinsky, S. Smyth, R. Newell, S. Sandholm, and S. Liu. Observed distributions of nitrogen oxides in the remote free troposphere from the nasa global tropospheric experiment programs. *Reviews of Geophysics*, 38(1):61–116, 2000. doi: 10.1029/1999RG900015. URL http://dx.doi.org/10.1029/1999RG900015.

Ronald Brandtjen, T. Klüpfel, D. Perner, and B. M. Knudsen. Airborne measurements during the European Arctic Stratospheric Ozone Experiment: Observation of OClO. *Geophysical Research Letters*, 21(13):1363–1366, 1994. doi: 10.1029/93GL01868. URL http://dx.doi.org/10.1029/93GL01868.

Guy P. Brasseur and Susan Solomon. *Aeronomy of the middle atmosphere: Chemistry and physics of the stratosphere and mesosphere*, volume 32. Springer Science & Business Media, 2006.

S. Brinckmann, A. Engel, H. Bönisch, B. Quack, and E. Atlas. Short-lived brominated hydrocarbons – observations in the source regions and the tropical tropopause layer. *Atmospheric Chemistry and Physics*, 12(3):1213–1228, 2012. doi: 10.5194/acp-12-1213-2012. URL http://www.atmos-chem-phys.net/12/1213/2012/.

M. Bruns, S.A. Buehler, J.P. Burrows, A. Richter, A. Rozanov, P. Wang, K.P. Heue, U. Platt, I. Pundt, and T. Wagner. NO_2 Profile retrieval using airborne multi axis UV-visible skylight absorption measurements over central Europe. *Atmospheric Chemistry and Physics*, 6(10):3049–3058, 2006. doi: 10.5194/acp-6-3049-2006. URL http://www.atmos-chem-phys.net/6/3049/2006/.

Marco Bruns, Stefan A. Buehler, John P. Burrows, Klaus-Peter Heue, Ulrich Platt, Irene Pundt, Andreas Richter, Alexej Rozanov, Thomas Wagner, and Ping Wang. Retrieval of profile information from airborne multiaxis UV-visible skylight absorption measurements. *Applied optics*, 43(22): 4415–4426, 2004.

H. Bösch, C. Camy-Peyret, M. P. Chipperfield, R. Fitzenberger, H. Harder, U. Platt, and K. Pfeilsticker. Upper limits of stratospheric IO and OIO inferred from center-to-limb-darkening-corrected balloon-borne solar occultation visible spectra: Implications for total gaseous iodine and stratospheric ozone. *Journal of Geophysical Research: Atmospheres*, 108(D15):n/a, 2003. doi: 10.1029/2002JD003078. URL http://dx.doi.org/10.1029/2002JD003078. 4455.

B. Buchholz, N. Böse, and V Ebert. Absolute validation of a diode laser hygrometer via intercomparison with the German national primary water vapor standard. *Applied Physics B*, 116(4):883–899, 2014.

Markus Bussemer. Der Ring-Effekt: Ursachen und Einfluß auf die spektroskopische Messung stratosphärischer Spurenstoffe. Diploma thesis, Institut für Umweltphysik, Universität Heidelberg, Heidelberg, Germany, 1993.

A. Butz, H. Bösch, C. Camy-Peyret, M. Dorf, A. Engel, S. Payan, and K. Pfeilsticker. Observational constraints on the kinetics of the ClO-BrO and ClO-ClO ozone loss cycles in the Arctic winter stratosphere. *Geophysical Research Letters*, 34(5):n/a, 2007. doi: 10.1029/2006GL028718. URL http://dx.doi.org/10.1029/2006GL028718. L05801.

A. Butz, H. Bösch, C. Camy-Peyret, M. P. Chipperfield, M. Dorf, S. Kreycy, L. Kritten, C. Prados-Román, J. Schwärzle, and K. Pfeilsticker. Constraints on inorganic gaseous iodine in the tropical upper troposphere and stratosphere inferred from balloon-borne solar occultation observations. *Atmospheric Chemistry and Physics*, 9(18):7229–7242, 2009. doi: 10.5194/acp-9-7229-2009. URL http://www.atmos-chem-phys.net/9/7229/2009/.

T. Canty, E. D. Rivière, R. J. Salawitch, G. Berthet, J.-B. Renard, K. Pfeilsticker, M. Dorf, A. Butz, H. Bösch, R. M. Stimpfle, D. M. Wilmouth, E. C. Richard, D. W. Fahey, P. J. Popp, M. R. Schoeberl, L. R. Lait, and T. P. Bui. Nighttime OClO in the winter Arctic vortex. *Journal of Geophysical Research: Atmospheres*, 110(D1):n/a, 2005. doi: 10.1029/2004JD005035. URL http://dx.doi.org/10.1029/2004JD005035. D01301.

L.J. Carpenter, K.C. Clemitshaw, R.A. Burgess, S.A. Penkett, J.N. Cape, and G.G. Mcfadyen. Investigation and evaluation of the NO_x/O_3 photochemical steady state. *Atmospheric Environment*, 32 (19):3353 – 3365, 1998. ISSN 1352-2310. doi: http://dx.doi.org/10.1016/S1352-2310(97)00416-0. URL http://www.sciencedirect.com/science/article/pii/S1352231097004160.

K. Chance and J. Orphal. Revised ultraviolet absorption cross sections of H_2O for the HITRAN database. *Journal of Quantitative Spectroscopy and Radiative Transfer*, 112(9):1509–1510, 2011.

Kelly Chance, Thomas P. Kurosu, and Christopher E. Sioris. Undersampling correction for array detector-based satellite spectrometers. *Appl. Opt.*, 44(7):1296–1304, Mar 2005. doi: 10.1364/AO.44.001296. URL http://ao.osa.org/abstract.cfm?URI=ao-44-7-1296.

Kelly V. Chance and Robert J.D. Spurr. Ring effect studies: Rayleigh scattering, including molecular parameters for rotational Raman scattering, and the Fraunhofer spectrum. *Applied Optics*, 36(21): 5224–5230, 1997.

Dilip M. Chate, Sachin D. Ghude, Gurfan Beig, Anoop S. Mahajan, Chinmay Jena, Reka Srinivas, Anita Dahiya, and Nandini Kumar. Deviations from the O_3–NO–NO_2 photo-stationary state in Delhi, India. *Atmospheric Environment*, 96:353 – 358, 2014. ISSN 1352-2310. doi: http://dx.doi.org/10.1016/j.atmosenv.2014.07.054. URL http://www.sciencedirect.com/science/article/pii/S1352231014005846.

Dexian Chen, L. Gregory Huey, David J. Tanner, Ross J. Salawitch, Daniel C. Anderson, Pamela A. Wales, Laura L. Pan, Elliot L. Atlas, Rebecca S. Hornbrook, Eric C. Apel, Nicola J. Blake, Teresa L. Campos, Valeria Donets, Frank M. Flocke, Samuel R. Hall, Thomas F. Hanisco, Alan J. Hills, Shawn B. Honomichl, Jørgen B. Jensen, Lisa Kaser, Denise D. Montzka, Julie M. Nicely, J. Michael Reeves, Daniel D. Riemer, Sue M. Schauffler, Kirk Ullmann, Andrew J. Weinheimer, and Glenn M. Wolfe. Airborne measurements of BrO and the sum of HOBr and Br_2 over the Tropical West Pacific from 1 to 15 km during the CONvective TRansport of Active Species in the Tropics (CONTRAST) experiment. *Journal of Geophysical Research: Atmospheres*, page n/a, 2016. doi: 10.1002/2016JD025561. URL http://dx.doi.org/10.1002/2016JD025561. 2016JD025561.

S. Choi, J. Joiner, Y. Choi, B. N. Duncan, A. Vasilkov, N. Krotkov, and E. Bucsela. First estimates of global free-tropospheric NO_2 abundances derived using a cloud-slicing technique applied to

satellite observations from the Aura Ozone Monitoring Instrument (OMI). *Atmospheric Chemistry and Physics*, 14(19):10565–10588, 2014. doi: 10.5194/acp-14-10565-2014. URL http://www.atmos-chem-phys.net/14/10565/2014/.

J. Curtius, M. Scheinert, and M. Wendisch. Atmospheric and Earth System Research with the Research Aircraft HALO, Priority Program 1294 of the German Research Foundation (DFG SPP 1294). Renewal proposal, Universität Leipzig, Leipziger Institut für Meteorologie (LIM), 2012.

D. D. Davis, G. Chen, W. Chameides, J. Bradshaw, S. Sandholm, M. Rodgers, J. Schendal, S. Madronich, G. Sachse, G. Gregory, B. Anderson, J. Barrick, M. Shipham, J. Collins, L. Wade, and D. Blake. A photostationary state analysis of the NO_2-NO system based on airborne observations from the subtropical/tropical North and South Atlantic. *Journal of Geophysical Research: Atmospheres*, 98(D12):23501–23523, 1993. doi: 10.1029/93JD02412. URL http://dx.doi.org/10.1029/93JD02412.

Sean Davis, Dennis Hlavka, Eric Jensen, Karen Rosenlof, Qiong Yang, Sebastian Schmidt, Stephan Borrmann, Wiebke Frey, Paul Lawson, Holger Voemel, and T. P. Bui. In situ and lidar observations of tropopause subvisible cirrus clouds during TC4. *Journal of Geophysical Research: Atmospheres*, 115(D10):n/a, 2010. doi: 10.1029/2009JD013093. URL http://dx.doi.org/10.1029/2009JD013093. D00J17.

R. De Beek, M. Vountas, V.V. Rozanov, A. Richter, and J.P. Burrows. The Ring effect in the cloudy atmosphere. *Geophysical research letters*, 28(4):721–724, 2001.

I. De Smedt, T. Stavrakou, F. Hendrick, T. Danckaert, T. Vlemmix, G. Pinardi, N. Theys, C. Lerot, C. Gielen, C. Vigouroux, C. Hermans, C. Fayt, P. Veefkind, J.-F. Müller, and M. Van Roozendael. Diurnal, seasonal and long-term variations of global formaldehyde columns inferred from combined OMI and GOME-2 observations. *Atmospheric Chemistry and Physics*, 15(21):12519–12545, 2015. doi: 10.5194/acp-15-12519-2015. URL http://www.atmos-chem-phys.net/15/12519/2015/.

D. P. Dee, S. M. Uppala, A. J. Simmons, P. Berrisford, P. Poli, S. Kobayashi, U. Andrae, M. A. Balmaseda, G. Balsamo, P. Bauer, P. Bechtold, A. C. M. Beljaars, L. van de Berg, J. Bidlot, N. Bormann, C. Delsol, R. Dragani, M. Fuentes, A. J. Geer, L. Haimberger, S. B. Healy, H. Hersbach, E. V. Hólm, L. Isaksen, P. Kållberg, M. Köhler, M. Matricardi, A. P. McNally, B. M. Monge-Sanz, J.-J. Morcrette, B.-K. Park, C. Peubey, P. de Rosnay, C. Tavolato, J.-N. Thépaut, and F. Vitart. The ERA-Interim reanalysis: configuration and performance of the data assimilation system. *Quarterly Journal of the Royal Meteorological Society*, 137(656):553–597, 2011. ISSN 1477-870X. doi: 10.1002/qj.828. URL http://dx.doi.org/10.1002/qj.828.

T. Deutschmann. Atmospheric radiative transfer modelling with Monte Carlo methods. Diploma thesis, Institut für Umweltphysik, Universität Heidelberg, Heidelberg, Germany, 2008.

T. Deutschmann, S. Beirle, et al. The Monte Carlo atmospheric radiative transfer model McArtim: Introduction and validation of Jacobians and 3D features. *Journal of Quantitative Spectroscopy and Radiative Transfer*, 2011. ISSN 0022-4073.

Tim Deutschmann. On Modeling Elastic and Inelastic Polarized Radiation Transport in the Earth Atmosphere with Monte Carlo Methods. PhD thesis, Institut für Umweltphysik, Universität Heidelberg, Heidelberg, Germany, 2014.

B. Dix, C.A.M. Brenninkmeijer, U. Frieß, T. Wagner, and U. Platt. Airborne multi-axis DOAS measurements of atmospheric trace gases on CARIBIC long-distance flights. *Atmospheric Measurement Techniques*, 2(2):639–652, 2009. doi: 10.5194/amt-2-639-2009. URL http://www.atmos-meas-tech.net/2/639/2009/.

Barbara Dix, Sunil Baidar, James F. Bresch, Samuel R. Hall, K. Sebastian Schmidt, Siyuan Wang, and Rainer Volkamer. Detection of iodine monoxide in the tropical free troposphere. *Proceedings of the National Academy of Sciences*, 110(6):2035–2040, 2013. doi: 10.1073/pnas.1212386110. URL http://www.pnas.org/content/110/6/2035.abstract.

M. Dorf, H. Bösch, A. Butz, C. Camy-Peyret, M. P. Chipperfield, A. Engel, F. Goutail, K. Grunow, F. Hendrick, S. Hrechanyy, B. Naujokat, J.-P. Pommereau, M. Van Roozendael, C. Sioris, F. Stroh, F. Weidner, and K. Pfeilsticker. Balloon-borne stratospheric BrO measurements: comparison with Envisat/SCIAMACHY BrO limb profiles. *Atmospheric Chemistry and Physics*, 6(9):2483–2501, 2006a. doi: 10.5194/acp-6-2483-2006. URL http://www.atmos-chem-phys.net/6/2483/2006/.

M. Dorf, J. H. Butler, A. Butz, C. Camy-Peyret, M. P. Chipperfield, L. Kritten, S. A. Montzka, B. Simmes, F. Weidner, and K. Pfeilsticker. Long-term observations of stratospheric bromine reveal slow down in growth. *Geophysical Research Letters*, 33(24):n/a, 2006b. doi: 10.1029/2006GL027714. URL http://dx.doi.org/10.1029/2006GL027714.

M. Dorf, A. Butz, C. Camy-Peyret, M. P. Chipperfield, L. Kritten, and K. Pfeilsticker. Bromine in the tropical troposphere and stratosphere as derived from balloon-borne BrO observations. *Atmospheric Chemistry and Physics*, 8(23):7265–7271, 2008. doi: 10.5194/acp-8-7265-2008. URL http://www.atmos-chem-phys.net/8/7265/2008/.

Anne R. Douglass, Paul A. Newman, and Susan Solomon. The antarctic ozone hole: An update. *Physics Today*, 67(7):42–48, 2014.

John W. Drummond, Andreas Volz, and Dieter H. Ehhalt. An optimized chemiluminescence detector for tropospheric NO measurements. *Journal of Atmospheric Chemistry*, 2(3):287–306, 1985. ISSN 1573-0662. doi: 10.1007/BF00051078. URL http://dx.doi.org/10.1007/BF00051078.

C. Dyroff, D. Fütterer, and A. Zahn. Compact diode-laser spectrometer ISOWAT for highly sensitive airborne measurements of water-isotope ratios. *Applied Physics B*, 98(2):537–548, 2010. ISSN 1432-0649. doi: 10.1007/s00340-009-3775-6. URL http://dx.doi.org/10.1007/s00340-009-3775-6.

A. Engel, H. Bönisch, D. Brunner, H. Fischer, H. Franke, G. Günther, C. Gurk, M. Hegglin, P. Hoor, R. Königstedt, M. Krebsbach, R. Maser, U. Parchatka, T. Peter, D. Schell, C. Schiller,

U. Schmidt, N. Spelten, T. Szabo, U. Weers, H. Wernli, T. Wetter, and V. Wirth. Highly resolved observations of trace gases in the lowermost stratosphere and upper troposphere from the Spurt project: an overview. *Atmospheric Chemistry and Physics*, 6(2):283–301, 2006. doi: 10.5194/acp-6-283-2006. URL http://www.atmos-chem-phys.net/6/283/2006/.

F. Erle, K. Pfeilsticker, and U. Platt. On the influence of tropospheric clouds on zenith-scattered-light measurements of stratospheric species. *Geophysical research letters*, 22(20):2725–2728, 1995.

M. J. Evans, D. J. Jacob, E. Atlas, C. A. Cantrell, F. Eisele, F. Flocke, A. Fried, R. L. Mauldin, B. A. Ridley, B. Wert, R. Talbot, D. Blake, B. Heikes, J. Snow, J. Walega, A. J. Weinheimer, and J. Dibb. Coupled evolution of BrO_x-ClO_x-HO_x-NO_x chemistry during bromine-catalyzed ozone depletion events in the arctic boundary layer. *Journal of Geophysical Research: Atmospheres*, 108(D4):n/a, 2003. doi: 10.1029/2002JD002732. URL http://dx.doi.org/10.1029/2002JD002732. 8368.

D.W. Fahey, C.S. Eubank, G. Hübler, and F.C. Fehsenfeld. Evaluation of a catalytic reduction technique for the measurement of total reactive odd-nitrogen NO_y in the atmosphere. *Journal of Atmospheric Chemistry*, 3(4):435–468, 1985.

F. Ferlemann, N. Bauer, R. Fitzenberger, H. Harder, H. Osterkamp, D. Perner, U. Platt, M. Schneider, P. Vradelis, and K. Pfeilsticker. Differential optical absorption spectroscopy instrument for stratospheric balloonborne trace-gas studies. *Applied Optics*, 39(15):2377–2386, 2000. ISSN 1539-4522.

BJ Finlayson-Pitts and JN Pitts. Chemistry of the upper and lower atmosphere: Theory, experiments and applications. *Academic, US*, 2000.

E. V. Fischer, D. J. Jacob, R. M. Yantosca, M. P. Sulprizio, D. B. Millet, J. Mao, F. Paulot, H. B. Singh, A. Roiger, L. Ries, R. W. Talbot, K. Dzepina, and S. Pandey Deolal. Atmospheric peroxyacetyl nitrate (PAN): a global budget and source attribution. *Atmospheric Chemistry and Physics*, 14(5): 2679–2698, 2014. doi: 10.5194/acp-14-2679-2014. URL http://www.atmos-chem-phys.net/14/2679/2014/.

H. Fischer, F. G. Wienhold, P. Hoor, O. Bujok, C. Schiller, P. Siegmund, M. Ambaum, H. A. Scheeren, and J. Lelieveld. Tracer correlations in the northern high latitude lowermost stratosphere: Influence of cross-tropopause mass exchange. *Geophysical Research Letters*, 27(1):97–100, 2000. doi: 10.1029/1999GL010879. URL http://dx.doi.org/10.1029/1999GL010879.

DJ Fish and RL Jones. Rotational Raman scattering and the ring effect in zenith-sky spectra. *Geophysical Research Letters*, 22(7):811–814, 1995.

R. Fitzenberger, H. Bösch, C. Camy-Peyret, M. P. Chipperfield, H. Harder, U. Platt, B. M. Sinnhuber, T. Wagner, and K. Pfeilsticker. First profile measurements of tropospheric BrO. *Geophysical Research Letters*, 27(18):2921–2924, 2000. doi: 10.1029/2000GL011531. URL http://dx.doi.org/10.1029/2000GL011531.

Oliver C. Fleischmann, Matthias Hartmann, John P. Burrows, and Johannes Orphal. New ultraviolet absorption cross-sections of BrO at atmospheric temperatures measured by time-windowing

Fourier transform spectroscopy. *Journal of Photochemistry and Photobiology A: Chemistry*, 168 (1):117–132, 2004.

K. Frieler, M. Rex, R. J. Salawitch, T. Canty, M. Streibel, R. M. Stimpfle, K. Pfeilsticker, M. Dorf, D. K. Weisenstein, and S. Godin-Beekmann. Toward a better quantitative understanding of polar stratospheric ozone loss. *Geophysical Research Letters*, 33(10):n/a, 2006. doi: 10.1029/2005GL025466. URL http://dx.doi.org/10.1029/2005GL025466. L10812.

G. J. Frost, A. Fried, Y.-N. Lee, B. Wert, B. Henry, J. R. Drummond, M. J. Evans, F. C. Fehsenfeld, P. D. Goldan, J. S. Holloway, G. Hübler, R. Jakoubek, B. T. Jobson, K. Knapp, W. C. Kuster, J. Roberts, J. Rudolph, T. B. Ryerson, A. Stohl, C. Stroud, D. T. Sueper, M. Trainer, and J. Williams. Comparisons of box model calculations and measurements of formaldehyde from the 1997 North Atlantic Regional Experiment. *Journal of Geophysical Research: Atmospheres*, 107(D8):n/a, 2002. doi: 10.1029/2001JD000896. URL http://dx.doi.org/10.1029/2001JD000896.

Tzung-May Fu, Daniel J. Jacob, Folkard Wittrock, John P. Burrows, Mihalis Vrekoussis, and Daven K. Henze. Global budgets of atmospheric glyoxal and methylglyoxal, and implications for formation of secondary organic aerosols. *Journal of Geophysical Research: Atmospheres*, 113(D15):n/a, 2008. doi: 10.1029/2007JD009505. URL http://dx.doi.org/10.1029/2007JD009505. D15303.

S. Fueglistaler, A. E. Dessler, T. J. Dunkerton, I. Folkins, Q. Fu, and P. W. Mote. Tropical tropopause layer. *Reviews of Geophysics*, 47(1):1944–9208, 2009. doi: 10.1029/2008RG000267. URL http://dx.doi.org/10.1029/2008RG000267. RG1004.

S. General, D. Pöhler, H. Sihler, N. Bobrowski, U. Frieß, J. Zielcke, M. Horbanski, PB Shepson, BH Stirm, WR Simpson, et al. The Heidelberg Airborne Imaging DOAS Instrument (HAIDI)–a novel imaging DOAS device for 2-D and 3-D imaging of trace gases and aerosols. *Atmospheric Measurement Techniques*, 7(10):3459–3485, 2014. doi: 10.5194/amt-7-3459-2014. URL http://www.atmos-meas-tech.net/7/3459/2014/.

K. Gerilowski, A. Tretner, T. Krings, M. Buchwitz, P. P. Bertagnolio, F. Belemezov, J. Erzinger, J. P. Burrows, and H. Bovensmann. MAMAP – a new spectrometer system for column-averaged methane and carbon dioxide observations from aircraft: instrument description and performance analysis. *Atmospheric Measurement Techniques*, 4(2):215–243, 2011. doi: 10.5194/amt-4-215-2011. URL http://www.atmos-meas-tech.net/4/215/2011/.

A. Gettelman, P. Hoor, L. L. Pan, W. J. Randel, M. I. Hegglin, and T. Birner. The extratropical upper troposphere and lower stratosphere. *Reviews of Geophysics*, 49(3):1944–9208, 2011. doi: 10.1029/2011RG000355. URL http://dx.doi.org/10.1029/2011RG000355. RG3003.

Andrew Gettelman, Piers M. de F. Forster, Masatomo Fujiwara, Qiang Fu, Holger Vömel, Laila K. Gohar, Celeste Johanson, and Marie Ammerman. Radiation balance of the tropical tropopause layer. *Journal of Geophysical Research: Atmospheres*, 109(D7), 2004.

M. Gil-Ojeda, M. Navarro-Comas, L. Gómez-Martín, J. A. Adame, A. Saiz-Lopez, C. A. Cuevas, Y. González, O. Puentedura, E. Cuevas, J.-F. Lamarque, D. Kinninson, and S. Tilmes. NO_2 seasonal evolution in the north subtropical free troposphere. *Atmospheric Chemistry and Physics*, 15(18): 10567–10579, 2015. doi: 10.5194/acp-15-10567-2015. URL http://www.atmos-chem-phys.net/15/10567/2015/.

N. Glatthor, C. E. Blom, T. von Clarmann, H. Fischer, T. Gulde, C. Piesch, F. Erle, K. Pfeilsticker, M. P. Chipperfield, A. M. Lee, and J. A. Pyle. Airborne remote sensing of no2 in the arctic winter of 1994–1995 and comparison with a three-dimensional chemical transport model. *Journal of Geophysical Research: Atmospheres*, 103(D11):13315–13326, 1998. doi: 10.1029/98JD00521. URL http://dx.doi.org/10.1029/98JD00521.

L. Gomez, M. Navarro-Comas, O. Puentedura, Y. Gonzalez, E. Cuevas, and M. Gil-Ojeda. Long-path averaged mixing ratios of O_3 and NO_2 in the free troposphere from mountain MAX-DOAS. *Atmospheric Measurement Techniques*, 7(10):3373–3386, 2014. doi: 10.5194/amt-7-3373-2014. URL http://www.atmos-meas-tech.net/7/3373/2014/.

Richard M. Goody and Yuk Ling Yung. *Atmospheric radiation: theoretical basis*. Oxford University Press, 1995.

Victor Gorshelev, Anna Serdyuchenko, Mark Weber, W. Chehade, and J.P. Burrows. High spectral resolution ozone absorption cross-sections – Part 1: Measurements, data analysis and comparison with previous measurements around 293 K. *Atmospheric Measurement Techniques*, 7(2):609–624, 2014. doi: 10.5194/amt-7-609-2014. URL http://www.atmos-meas-tech.net/7/609/2014/.

JF Grainger and J Ring. Anomalous Fraunhofer line profiles. *Nature*, 193:762, 1962.

L. E. Gratz, J. L. Ambrose, D. A. Jaffe, V. Shah, L. Jaeglé, J. Stutz, J. Festa, M. Spolaor, C. Tsai, N. E. Selin, S. Song, X. Zhou, A. J. Weinheimer, D. J. Knapp, D. D. Montzka, F. M. Flocke, T. L. Campos, E. Apel, R. Hornbrook, N. J. Blake, S. Hall, G. S. Tyndall, M. Reeves, D. Stechman, and M. Stell. Oxidation of mercury by bromine in the subtropical pacific free troposphere. *Geophysical Research Letters*, 42(23):10,494–10,502, 2015. doi: 10.1002/2015GL066645. URL http://dx.doi.org/10.1002/2015GL066645. 2015GL066645.

Gary D. Greenblatt, John J. Orlando, James B. Burkholder, and A.R. Ravishankara. Absorption measurements of oxygen between 330 and 1140 nm. *Journal of Geophysical Research: Atmospheres*, 95(D11):18577–18582, 1990. doi: 10.1029/JD095iD11p18577. URL http://dx.doi.org/10.1029/JD095iD11p18577.

Robert J. Griffin, Pieter J. Beckman, Robert W. Talbot, Barkley C. Sive, and Ruth K. Varner. Deviations from ozone photostationary state during the International Consortium for Atmospheric Research on Transport and Transformation 2004 campaign: Use of measurements and photochemical modeling to assess potential causes. *Journal of Geophysical Research: Atmospheres*, 112(D10): n/a, 2007. doi: 10.1029/2006JD007604. URL http://dx.doi.org/10.1029/2006JD007604. D10S07.

Katja Großmann. Aircraft-borne DOAS limb observations of UV/visible absorbing trace gas species over Borneo: Implications for the photochemistry of iodine, volatile organic oxide degradation, and lightning-produced radicals. PhD thesis, Institut für Umweltphysik, Universität Heidelberg, Heidelberg, Germany, 2014.

J.-U. Grooß, I. Engel, S. Borrmann, W. Frey, G. Günther, C. R. Hoyle, R. Kivi, B. P. Luo, S. Molleker, T. Peter, M. C. Pitts, H. Schlager, G. Stiller, H. Vömel, K. A. Walker, and R. Müller. Nitric acid trihydrate nucleation and denitrification in the Arctic stratosphere. *Atmospheric Chemistry and Physics*, 14(2):1055–1073, 2014. doi: 10.5194/acp-14-1055-2014. URL http://www.atmos-chem-phys.net/14/1055/2014/.

K. Grossmann, M. Dorf, M. Kenntner, V. Catoire, H. Schlager, F. Hendrick, I. DeSmedt, Y. Huan, and K Pfeilsticker. DOAS observations over Borneo during the SHIVA aircraft campaign. *Malaysian Journal of Science*, 32((SCS Sp Issue)):259 – 266, 2013.

H. Harder, C. Camy-Peyret, F. Ferlemann, R. Fitzenberger, T. Hawat, H. Osterkamp, M. Schneider, D. Perner, U. Platt, P. Vradelis, and K. Pfeilsticker. Stratospheric BrO profiles measured at different latitudes and seasons: Atmospheric observations. *Geophysical Research Letters*, 25(20):3843–3846, 1998. doi: 10.1029/1998GL900026. URL http://dx.doi.org/10.1029/1998GL900026.

Martin Hausmann, Uwe Brandenburger, Theo Brauers, and Hans-Peter Dorn. Simple Monte Carlo methods to estimate the spectra evaluation error in differential-optical-absorption spectroscopy. *Appl. Opt.*, 38(3):462–475, Jan 1999. doi: 10.1364/AO.38.000462. URL http://ao.osa.org/abstract.cfm?URI=ao-38-3-462.

M. I. Hegglin, D. Brunner, T. Peter, P. Hoor, H. Fischer, J. Staehelin, M. Krebsbach, C. Schiller, U. Parchatka, and U. Weers. Measurements of NO, NO_y, N_2O, and O_3 during SPURT: implications for transport and chemistry in the lowermost stratosphere. *Atmospheric Chemistry and Physics*, 6 (5):1331–1350, 2006. doi: 10.5194/acp-6-1331-2006. URL http://www.atmos-chem-phys.net/6/1331/2006/.

F. Hendrick, M. Van Roozendael, M. P. Chipperfield, M. Dorf, F. Goutail, X. Yang, C. Fayt, C. Hermans, K. Pfeilsticker, J.-P. Pommereau, J. A. Pyle, N. Theys, and M. De Mazière. Retrieval of stratospheric and tropospheric BrO profiles and columns using ground-based zenith-sky DOAS observations at Harestua 60N. *Atmospheric Chemistry and Physics*, 7(18):4869–4885, 2007. doi: 10.5194/acp-7-4869-2007. URL http://www.atmos-chem-phys.net/7/4869/2007/.

K.-P. Heue, T. Wagner, S. P. Broccardo, D. Walter, S. J. Piketh, K. E. Ross, S. Beirle, and U. Platt. Direct observation of two dimensional trace gas distributions with an airborne Imaging DOAS instrument. *Atmospheric Chemistry and Physics*, 8(22):6707–6717, 2008. doi: 10.5194/acp-8-6707-2008. URL http://www.atmos-chem-phys.net/8/6707/2008/.

K.-P. Heue, H. Riede, D. Walter, C.A.M. Brenninkmeijer, T. Wagner, U. Frieß, U. Platt, A. Zahn, G. Stratmann, and H. Ziereis. CARIBIC DOAS observations of nitrous acid and formaldehyde in a large convective cloud. *Atmospheric Chemistry and Physics*, 14(13):6621–6642, 2014. doi: 10.5194/acp-14-6621-2014. URL http://www.atmos-chem-phys.net/14/6621/2014/.

E. J. Hintsa, K. A. Boering, E. M. Weinstock, J. G. Anderson, B. L. Gary, L. Pfister, B. C. Daube, S. C. Wofsy, M. Loewenstein, J. R. Podolske, J. J. Margitan, and T. P. Bui. Troposphere-to-stratosphere transport in the lowermost stratosphere from measurements of H_2O, CO_2, N_2O and O_3. *Geophysical Research Letters*, 25(14):2655–2658, 1998. doi: 10.1029/98GL01797. URL http://dx.doi.org/10.1029/98GL01797.

Tilman Hüneke. Aufbau und Charakterisierung eines sechsfach-miniDOAS-Spektrographen für das Forschungsflugzeug DLR-HALO. Diploma thesis, Institut für Umweltphysik, Universität Heidelberg, Heidelberg, Germany, 2011.

James R. Holton, Peter H. Haynes, Michael E. McIntyre, Anne R. Douglass, Richard B. Rood, and Leonhard Pfister. Stratosphere-troposphere exchange. *Reviews of geophysics*, 33(4):403–439, 1995.

Z. Hosaynali Beygi, H. Fischer, H. D. Harder, M. Martinez, R. Sander, J. Williams, D. M. Brookes, P. S. Monks, and J. Lelieveld. Oxidation photochemistry in the Southern Atlantic boundary layer: unexpected deviations of photochemical steady state. *Atmospheric Chemistry and Physics*, 11(16): 8497–8513, 2011. doi: 10.5194/acp-11-8497-2011. URL http://www.atmos-chem-phys.net/11/8497/2011/.

R. Hossaini, MP Chipperfield, SA Montzka, A. Rap, S. Dhomse, and W. Feng. Efficiency of short-lived halogens at influencing climate through depletion of stratospheric ozone. *Nature Geoscience*, 8(3):186–190, 2015. doi: 10.1038/ngeo2363.

R. Hossaini, P. K. Patra, A. A. Leeson, G. Krysztofiak, N. L. Abraham, S. J. Andrews, A. T. Archibald, J. Aschmann, E. L. Atlas, D. A. Belikov, H. Bönisch, L. J. Carpenter, S. Dhomse, M. Dorf, A. Engel, W. Feng, S. Fuhlbrügge, P. T. Griffiths, N. R. P. Harris, R. Hommel, T. Keber, K. Krüger, S. T. Lennartz, S. Maksyutov, H. Mantle, G. P. Mills, B. Miller, S. A. Montzka, F. Moore, M. A. Navarro, D. E. Oram, K. Pfeilsticker, J. A. Pyle, B. Quack, A. D. Robinson, E. Saikawa, A. Saiz-Lopez, S. Sala, B.-M. Sinnhuber, S. Taguchi, S. Tegtmeier, R. T. Lidster, C. Wilson, and F. Ziska. A multi-model intercomparison of halogenated very short-lived substances (TransCom-VSLS): linking oceanic emissions and tropospheric transport for a reconciled estimate of the stratospheric source gas injection of bromine. *Atmospheric Chemistry and Physics*, 16(14):9163–9187, 2016. doi: 10.5194/acp-16-9163-2016. URL http://www.atmos-chem-phys.net/16/9163/2016/.

H. Huntrieser, C. Feigl, H. Schlager, F. Schröder, C. Gerbig, P. van Velthoven, F. Flatøy, C. Théry, A. Petzold, H. Höller, and U. Schumann. Airborne measurements of NO_x, tracer species, and small particles during the European Lightning Nitrogen Oxides Experiment. *Journal of Geophysical Research: Atmospheres*, 107(D11):n/a, 2002. doi: 10.1029/2000JD000209. URL http://dx.doi.org/10.1029/2000JD000209.

H. Huntrieser, J. Heland, H. Schlager, C. Forster, A. Stohl, H. Aufmhoff, F. Arnold, H. E. Scheel, M. Campana, S. Gilge, R. Eixmann, and O. Cooper. Intercontinental air pollution transport from North America to Europe: Experimental evidence from airborne measurements and surface observations. *Journal of Geophysical Research: Atmospheres*, 110(D1):n/a, 2005. doi: 10.1029/2004JD005045. URL http://dx.doi.org/10.1029/2004JD005045. D01305.

L. Jaeglé, C. R. Webster, R. D. May, D. C. Scott, R. M. Stimpfle, D. W. Kohn, P. O. Wennberg, T. F. Hanisco, R. C. Cohen, M. H. Proffitt, K. K. Kelly, J. Elkins, D. Baumgardner, J. E. Dye, J. C. Wilson, R. F. Pueschel, K. R. Chan, R. J. Salawitch, A. F. Tuck, S. J. Hovde, and Y. L. Yung. Evolution and stoichiometry of heterogeneous processing in the Antarctic stratosphere. *Journal of Geophysical Research: Atmospheres*, 102(D11):13235–13253, 1997. doi: 10.1029/97JD00935. URL http://dx.doi.org/10.1029/97JD00935.

Lyatt Jaeglé, Daniel J. Jacob, William H. Brune, and Paul O. Wennberg. Chemistry of HO_x radicals in the upper troposphere. *Atmospheric Environment*, 35(3):469 – 489, 2001. ISSN 1352-2310. doi: http://dx.doi.org/10.1016/S1352-2310(00)00376-9. URL http://www.sciencedirect.com/science/article/pii/S1352231000003769.

Patrick Jöckel, Astrid Kerkweg, Andrea Pozzer, Rolf Sander, Holger Tost, Hella Riede, Andreas Baumgaertner, Sergey Gromov, and Bastian Kern. Development cycle 2 of the modular earth submodel system (MESSy2). *Geoscientific Model Development*, 3:717–752, 2010.

P.V. Johnston. Studies on the I_0-effect. Unpublished manuscript, 1996.

J. Joiner and P. K. Bhartia. The determination of cloud pressures from rotational Raman scattering in satellite backscatter ultraviolet measurements. *Journal of Geophysical Research: Atmospheres*, 100(D11):23019–23026, 1995. doi: 10.1029/95JD02675. URL http://dx.doi.org/10.1029/95JD02675.

T. Jurkat, C. Voigt, S. Kaufmann, A. Zahn, M. Sprenger, P. Hoor, H. Bozem, S. Müller, A. Dörnbrack, H. Schlager, H. Bönisch, and A. Engel. A quantitative analysis of stratospheric HCl, HNO_3, and O_3 in the tropopause region near the subtropical jet. *Geophysical Research Letters*, 41(9):3315–3321, 2014. doi: 10.1002/2013GL059159. URL http://dx.doi.org/10.1002/2013GL059159.

T. Jurkat, S. Kaufmann, C. Voigt, D. Schäuble, P. Jeßberger, and H. Ziereis. The airborne mass spectrometer AIMS – Part 2: Measurements of trace gases with stratospheric or tropospheric origin in the UTLS. *Atmospheric Measurement Techniques*, 9(4):1907–1923, 2016a. doi: 10.5194/amt-9-1907-2016. URL http://www.atmos-meas-tech.net/9/1907/2016/.

T. Jurkat, C. Voigt, S. Kaufmann, J.-U. Grooß, H. Ziereis, P. Hoor, H. Bozem, A. Engel, T. Keber, H. Bönisch, T. Hüneke, A. Dörnbrack, K. Walker, K. Pfeilsticker, and H. Schlager. Depletion of chlorine and nitrogen oxide reservoir species in the lower Antarctic polar vortex measured from aircraft. *Geophysical Research Letters*, in preparation, 2016b.

Marilena Kampa and Elias Castanas. Human health effects of air pollution. *Environmental Pollution*, 151(2):362 – 367, 2008. ISSN 0269-7491. doi: http://dx.doi.org/10.1016/j.envpol.2007.06.012. URL http://www.sciencedirect.com/science/article/pii/S0269749107002849. Proceedings of the 4th International Workshop on Biomonitoring of Atmospheric Pollution (With Emphasis on Trace Elements).

G.W. Kattawar, Andrew T. Young, and Terry J. Humphreys. Inelastic scattering in planetary atmospheres. I. The Ring effect, without aerosols. *The Astrophysical Journal*, 243:1049–1057, 1981.

M. Kaufmann, J. Blank, T. Guggenmoser, J. Ungermann, A. Engel, M. Ern, F. Friedl-Vallon, D. Gerber, J. U. Grooß, G. Guenther, M. Höpfner, A. Kleinert, E. Kretschmer, Th. Latzko, G. Maucher, T. Neubert, H. Nordmeyer, H. Oelhaf, F. Olschewski, J. Orphal, P. Preusse, H. Schlager, H. Schneider, D. Schuettemeyer, F. Stroh, O. Suminska-Ebersoldt, B. Vogel, C. M. Volk, W. Woiwode, and M. Riese. Retrieval of three-dimensional small-scale structures in upper-tropospheric/lower-stratospheric composition as measured by GLORIA. *Atmospheric Measurement Techniques*, 8(1): 81–95, 2015. doi: 10.5194/amt-8-81-2015. URL http://www.atmos-meas-tech.net/8/81/2015/.

S. Kaufmann, C. Voigt, T. Jurkat, T. Thornberry, D. W. Fahey, R.-S. Gao, R. Schlage, D. Schäuble, and M. Zöger. The airborne mass spectrometer AIMS – Part 1: AIMS-H_2O for UTLS water vapor measurements. *Atmospheric Measurement Techniques*, 9(3):939–953, 2016. doi: 10.5194/amt-9-939-2016. URL http://www.atmos-meas-tech.net/9/939/2016/.

Paul Kelley, Russell R. Dickerson, Winston T. Luke, and Gregory L. Kok. Rate of NO_2 photolysis from the surface to 7.6 km altitude in clear-sky and clouds. *Geophysical Research Letters*, 22(19): 2621–2624, 1995. doi: 10.1029/95GL02563. URL http://dx.doi.org/10.1029/95GL02563.

Mareike Kenntner. A novel Limb and Nadir DOAS Optical Spectrometer for the German research aircraft HALO - Feasibility and Validation. Diploma thesis, Institut für Umweltphysik, Universität Heidelberg, Heidelberg, Germany, 2013.

Sven Kühl, Janis Pukite, T. Deutschmann, Ulrich Platt, and Thomas Wagner. SCIAMACHY limb measurements of NO_2, BrO and OClO. Retrieval of vertical profiles: Algorithm, first results, sensitivity and comparison studies. *Advances in Space Research*, 42(10):1747 – 1764, 2008. ISSN 0273-1177. doi: http://dx.doi.org/10.1016/j.asr.2007.10.022. URL http://www.sciencedirect.com/science/article/pii/S027311770701040X.

Stefanie Kirschke, Philippe Bousquet, Philippe Ciais, Marielle Saunois, Josep G. Canadell, Edward J. Dlugokencky, Peter Bergamaschi, Daniel Bergmann, Donald R. Blake, Lori Bruhwiler, et al. Three decades of global methane sources and sinks. *Nature Geoscience*, 6(10):813–823, 2013.

Christian Klepp, Felix Ament, Stephan Bakan, Lutz Hirsch, and Bjorn Stevens. The NARVAL Campaign Report, 2014.

Marvin Knapp. Optische und Elektronische Charakterisierung des HALO mini-DOAS Instruments sowie eine Analyse der Unsicherheit in der Blickrichtung für die Skalierungsmethode. Bachelor thesis, Institut für Umweltphysik, Universität Heidelberg, Heidelberg, Germany, 2016.

Matthias Knecht. Simulation of radiative field modification due to tropical clouds. Master thesis, Institut für Umweltphysik, Universität Heidelberg, Heidelberg, Germany, 2015.

Monika Krautstrunk and Andreas Giez. The transition from FALCON to HALO era airborne atmospheric research. In *Atmospheric Physics*, pages 609–624. Springer, 2012.

S. Kreycy, C. Camy-Peyret, MP Chipperfield, M. Dorf, W. Feng, R. Hossaini, L. Kritten, B. Werner, and K Pfeilsticker. Atmospheric test of the J($BrONO_2$)/k(BrO+NO_2) ratio: implications for total

stratospheric Br_y and bromine-mediated ozone loss. *Atmospheric Chemistry and Physics*, 13(13): 6263–6274, 2013. doi: 10.5194/acp-13-6263-2013. URL http://www.atmos-chem-phys.net/13/6263/2013/.

L. Kritten, A. Butz, M. Dorf, T. Deutschmann, S. Kühl, C. Prados-Roman, J. Puķīte, A. Rozanov, R. Schofield, and K. Pfeilsticker. Time dependent profile retrieval of UV/vis absorbing radicals from balloon-borne limb measurements – a case study on NO_2 and O_3. *Atmospheric Measurement Techniques*, 3(4):933–946, 2010. doi: 10.5194/amt-3-933-2010. URL http://www.atmos-meas-tech.net/3/933/2010/.

L. Kritten, A. Butz, M. P. Chipperfield, M. Dorf, S. Dhomse, R. Hossaini, H. Oelhaf, C. Prados-Roman, G. Wetzel, and K. Pfeilsticker. Constraining the N_2O_5 UV absorption cross section from spectroscopic trace gas measurements in the tropical mid-stratosphere. *Atmospheric Chemistry and Physics*, 14(18):9555–9566, 2014. doi: 10.5194/acp-14-9555-2014. URL http://www.atmos-chem-phys.net/14/9555/2014/.

H. Kromminga, J. Orphal, P. Spietz, S. Voigt, and J.P. Burrows. New measurements of OClO absorption cross-sections in the 325–435 nm region and their temperature dependence between 213 and 293 K. *Journal of Photochemistry and Photobiology A: Chemistry*, 157(2):149–160, 2003.

J. Lampel, U. Frieß, and U. Platt. The impact of vibrational Raman scattering of air on DOAS measurements of atmospheric trace gases. *Atmospheric Measurement Techniques*, 8(9):3767–3787, 2015. doi: 10.5194/amt-8-3767-2015. URL http://www.atmos-meas-tech.net/8/3767/2015/.

A.O. Langford, Robyn Schofield, J.S. Daniel, R.W. Portmann, M.L. Melamed, H.L. Miller, E.G. Dutton, and S. Solomon. On the variability of the Ring effect in the near ultraviolet: understanding the role of aerosols and multiple scattering. *Atmospheric Chemistry and Physics*, 7(3):575–586, 2007. doi: 10.5194/acp-7-575-2007. URL http://www.atmos-chem-phys.net/7/575/2007/.

J. C. Laube, A. Engel, H. Bönisch, T. Möbius, D. R. Worton, W. T. Sturges, K. Grunow, and U. Schmidt. Contribution of very short-lived organic substances to stratospheric chlorine and bromine in the tropics – a case study. *Atmospheric Chemistry and Physics*, 8(23):7325–7334, 2008. doi: 10.5194/acp-8-7325-2008. URL http://www.atmos-chem-phys.net/8/7325/2008/.

Philip A. Leighton. *Photochemistry of Air Pollution*. Academic Press, 1961.

J. Lelieveld, T.M. Butler, J.N. Crowley, T.J. Dillon, H. Fischer, L. Ganzeveld, H. Harder, MG Lawrence, M. Martinez, D. Taraborrelli, et al. Atmospheric oxidation capacity sustained by a tropical forest. *Nature*, 452(7188):737–740, 2008.

K. Levenberg. A Method for the Solution of Certain Non-Linear problems in Least Squares. *Q. Appl. Math.*, 2:164–168, 1944.

J. G. Levine, P. Braesicke, N. R. P. Harris, and J. A. Pyle. Seasonal and inter-annual variations in troposphere-to-stratosphere transport from the tropical tropopause layer. *Atmospheric*

Chemistry and Physics, 8(13):3689 – 3703, 2008. doi: 10.5194/acp-8-3689-2008. URL http://www.atmos-chem-phys.net/8/3689/2008/.

Gilbert N Lewis. The magnetism of oxygen and the molecule O_4. *Journal of the American Chemical Society*, 46(9):2027–2032, 1924.

Xin Li, Franz Rohrer, Andreas Hofzumahaus, Theo Brauers, Rolf Häseler, Birger Bohn, Sebastian Broch, Hendrik Fuchs, Sebastian Gomm, Frank Holland, Julia Jäger, Jennifer Kaiser, Frank N. Keutsch, Insa Lohse, Keding Lu, Ralf Tillmann, Robert Wegener, Glenn M. Wolfe, Thomas F. Mentel, Astrid Kiendler-Scharr, and Andreas Wahner. Missing gas-phase source of HONO inferred from zeppelin measurements in the troposphere. *Science*, 344(6181):292–296, 2014. ISSN 0036-8075. doi: 10.1126/science.1248999. URL http://science.sciencemag.org/content/344/6181/292.

Q. Liang, E. Atlas, D. Blake, M. Dorf, K. Pfeilsticker, and S. Schauffler. Convective transport of very short lived bromocarbons to the stratosphere. *Atmospheric Chemistry and Physics*, 14(11):5781–5792, 2014. doi: 10.5194/acp-14-5781-2014. URL http://www.atmos-chem-phys.net/14/5781/2014/.

Anoop S. Mahajan, Cristina Prados-Roman, Timothy D. Hay, Johannes Lampel, Denis Pöhler, Katja Großmann, Jens Tschritter, Udo Frieß, Ulrich Platt, Paul Johnston, Karin Kreher, Folkard Wittrock, John P. Burrows, John M.C. Plane, and Alfonso Saiz-Lopez. Glyoxal observations in the global marine boundary layer. *Journal of Geophysical Research: Atmospheres*, 119(10):6160–6169, 2014. doi: 10.1002/2013JD021388. URL http://dx.doi.org/10.1002/2013JD021388. 2013JD021388.

L.C. Marquard, T. Wagner, and U. Platt. Improved air mass factor concepts for scattered radiation differential optical absorption spectroscopy of atmospheric species. *Journal of geophysical research*, 105:1315–1327, 2000.

D. W. Marquardt. An algorithm for the least-squares estimation of nonlinear parameters. *J. Appl. Math.*, 11:431–441, 1963. doi: 10.1137/0111030.

Alexander Marshak and Anthony Davis. *3D radiative transfer in cloudy atmospheres*. Springer Science & Business Media, 2005.

C.T. McElroy, C.A. McLinden, and J.C. McConnell. Evidence for bromine monoxide in the free troposphere during the Arctic polar sunrise. *Nature*, 397(6717):338–341, 1999.

Megan Louise Melamed, S. Solomon, John S. Daniel, Andrew O. Langford, Robert W. Portmann, TB Ryerson, DK Nicks Jr, and SA McKeen. Measuring reactive nitrogen emissions from point sources using visible spectroscopy from aircraft. *Journal of Environmental Monitoring*, 5(1):29–34, 2003.

A. Merlaud, M. Van Roozendael, N. Theys, C. Fayt, C. Hermans, Boris Quennehen, A. Schwarzenboeck, Gérard Ancellet, Matthieu Pommier, Jacques Pelon, et al. Airborne DOAS measurements in

Arctic: vertical distributions of aerosol extinction coefficient and NO_2 concentration. *Atmospheric Chemistry & Physics Discussions*, 11(5), 2011.

A. Merlaud, M. Van Roozendael, J. van Gent, C. Fayt, J. Maes, X. Toledo-Fuentes, O. Ronveaux, and M. De Mazière. DOAS measurements of NO_2 from an ultralight aircraft during the Earth Challenge expedition. *Atmospheric Measurement Techniques*, 5(8):2057–2068, 2012. doi: 10.5194/amt-5-2057-2012. URL http://www.atmos-meas-tech.net/5/2057/2012/.

S. Müller, P. Hoor, H. Bozem, E. Gute, B. Vogel, A. Zahn, H. Bönisch, T. Keber, M. Krämer, C. Rolf, M. Riese, H. Schlager, and A. Engel. Impact of the Asian monsoon on the extratropical lower stratosphere: trace gas observations during TACTS over Europe 2012. *Atmospheric Chemistry and Physics*, 16(16):10573–10589, 2016. doi: 10.5194/acp-16-10573-2016. URL http://www.atmos-chem-phys.net/16/10573/2016/.

Teruyuki Nakajima and Michael D. King. Determination of the optical thickness and effective particle radius of clouds from reflected solar radiation measurements. Part I: Theory. *Journal of the Atmospheric Sciences*, 47(15):1878–1893, 1990. doi: 10.1175/1520-0469(1990)047<1878:DOTOTA>2.0.CO;2. URL http://dx.doi.org/10.1175/1520-0469(1990)047<1878:DOTOTA>2.0.CO;2.

J. A. Neuman, M. Trainer, S. S. Brown, K.-E. Min, J. B. Nowak, D. D. Parrish, J. Peischl, I. B. Pollack, J. M. Roberts, T. B. Ryerson, and P. R. Veres. HONO emission and production determined from airborne measurements over the Southeast U.S. *Journal of Geophysical Research: Atmospheres*, 121(15):9237–9250, 2016. doi: 10.1002/2016JD025197. URL http://dx.doi.org/10.1002/2016JD025197. 2016JD025197.

Julie M. Nicely, Daniel C. Anderson, Timothy P. Canty, Ross J. Salawitch, Glenn M. Wolfe, Eric C. Apel, Steve R. Arnold, Elliot L. Atlas, Nicola J. Blake, James F. Bresch, Teresa L. Campos, Russell R. Dickerson, Bryan Duncan, Louisa K. Emmons, Mathew J. Evans, Rafael P. Fernandez, Johannes Flemming, Samuel R. Hall, Thomas F. Hanisco, Shawn B. Honomichl, Rebecca S. Hornbrook, Vincent Huijnen, Lisa Kaser, Douglas E. Kinnison, Jean-Francois Lamarque, Jingqiu Mao, Sarah A. Monks, Denise D. Montzka, Laura L. Pan, Daniel D. Riemer, Alfonso Saiz-Lopez, Stephen D. Steenrod, Meghan H. Stell, Simone Tilmes, Solene Turquety, Kirk Ullmann, and Andrew J. Weinheimer. An observationally constrained evaluation of the oxidative capacity in the tropical western Pacific troposphere. *Journal of Geophysical Research: Atmospheres*, 121(12):7461–7488, 2016. doi: 10.1002/2016JD025067. URL http://dx.doi.org/10.1002/2016JD025067. 2016JD025067.

J. F. Noxon. Nitrogen dioxide in the stratosphere and troposphere measured by ground-based absorption spectroscopy. *Science*, 189(4202):547 – 549, 1975. doi: 10.1126/science.189.4202.547.

J. F. Noxon, E. C. Whipple, and R. S. Hyde. Stratospheric NO_2: 1. Observational method and behavior at mid-latitude. *Journal of Geophysical Research: Oceans*, 84(C8):5047–5065, 1979. doi: 10.1029/JC084iC08p05047. URL http://dx.doi.org/10.1029/JC084iC08p05047.

Liisa Oikarinen. Effect of surface albedo variations on UV-visible limb-scattering measurements of the atmosphere. *Journal of Geophysical Research: Atmospheres*, 107(D19):n/a, 2002. doi: 10.1029/2001JD001492. URL http://dx.doi.org/10.1029/2001JD001492. 4404.

Clara Orbe, Darryn W. Waugh, and Paul A. Newman. Air-mass origin in the tropical lower stratosphere: The influence of Asian boundary layer air. *Geophysical Research Letters*, 42(10):4240–4248, 2015. doi: 10.1002/2015GL063937. URL http://dx.doi.org/10.1002/2015GL063937. 2015GL063937.

Lesley E. Ott, Kenneth E. Pickering, Georgiy L. Stenchikov, Heidi Huntrieser, and Ulrich Schumann. Effects of lightning NO_x production during the 21 July European Lightning Nitrogen Oxides Project storm studied with a three-dimensional cloud-scale chemical transport model. *Journal of Geophysical Research: Atmospheres*, 112(D5):n/a, 2007. doi: 10.1029/2006JD007365. URL http://dx.doi.org/10.1029/2006JD007365. D05307.

Lori M. Perliski and Susan Solomon. On the evaluation of air mass factors for atmospheric near-ultraviolet and visible absorption spectroscopy. *Journal of Geophysical Research: Atmospheres*, 98(D6):10363–10374, 1993. doi: 10.1029/93JD00465. URL http://dx.doi.org/10.1029/93JD00465.

D. Perner and U. Platt. Absorption of light in the atmosphere by collision pairs of oxygen $(O_2)_2$. *Geophysical Research Letters*, 7(12):1053–1056, 1980. doi: 10.1029/GL007i012p01053. URL http://dx.doi.org/10.1029/GL007i012p01053.

K. Pfeilsticker and U. Platt. Airborne measurements during the Arctic Stratospheric Experiment: Observation of O_3 and NO_2. *Geophysical Research Letters*, 21(13):1375–1378, 1994. doi: 10.1029/93GL01870. URL http://dx.doi.org/10.1029/93GL01870.

K. Pfeilsticker, C.E. Blom, R. Brandtjen, H. Fischer, N. Glatthor, W. Renger, J. Sessler, and M. Wirth. Aircraft-borne detection of stratospheric column amounts of O_3, NO_2, OClO, $ClNO_3$, HNO_3, and aerosols around the arctic vortex (79° N to 39° N) during spring 1993. *Journal of Geophysical Research: Atmospheres*, 102(D9):10801–10814, 1997a. doi: 10.1029/96JD03124. URL http://dx.doi.org/10.1029/96JD03124.

K. Pfeilsticker, F. Erle, O. Funk, L. Marquard, T. Wagner, and U. Platt. Optical path modifications due to tropospheric clouds: Implications for zenith sky measurements of stratospheric gases. *Journal of Geophysical Research: Atmospheres*, 103(D19):25323–25335, 1998a. doi: 10.1029/98JD01803. URL http://dx.doi.org/10.1029/98JD01803.

K. Pfeilsticker, F. Erle, O. Funk, H. Veitel, and U. Platt. First geometrical pathlengths probability density function derivation of the skylight from spectroscopically highly resolving oxygen A-band observations: 1. Measurement technique, atmospheric observations and model calculations. *Journal of Geophysical Research: Atmospheres*, 103(D10):11483–11504, 1998b. doi: 10.1029/98JD00725. URL http://dx.doi.org/10.1029/98JD00725.

K. Pfeilsticker, W. T. Sturges, H. Bösch, C. Camy-Peyret, M. P. Chipperfield, A. Engel, R. Fitzenberger, M. Müller, S. Payan, and B.-M. Sinnhuber. Lower stratospheric organic and inorganic bromine budget for the Arctic winter 1998/99. *Geophysical Research Letters*, 27(20):3305–3308, 2000. doi: 10.1029/2000GL011650. URL http://dx.doi.org/10.1029/2000GL011650.

K. Pfeilsticker, H. Bösch, C. Camy-Peyret, R. Fitzenberger, H. Harder, and H. Osterkamp. First atmospheric profile measurements of UV/visible O_4 absorption band intensities: Implications for the spectroscopy, and the formation enthalpy of the O_2-O_2 dimer. *Geophysical Research Letters*, 28(24):4595–4598, 2001. doi: 10.1029/2001GL013734. URL http://dx.doi.org/10.1029/2001GL013734.

Klaus Pfeilsticker, Frank Erle, and Ulrich Platt. Absorption of solar radiation by atmospheric o4. *Journal of the atmospheric sciences*, 54(7):933–939, 1997b.

Klaus Pfeilsticker, F. Erle, and U. Platt. Observation of the stratospheric NO_2 latitudinal distribution in the northern winter hemisphere. *Journal of atmospheric chemistry*, 32(1):101–120, 1999.

Denis Pöhler, Leif Vogel, Udo Frieß, and Ulrich Platt. Observation of halogen species in the Amundsen Gulf, Arctic, by active long-path differential optical absorption spectroscopy. *Proceedings of the National Academy of Sciences*, 107(15):6582–6587, 2010. doi: 10.1073/pnas.0912231107. URL http://www.pnas.org/content/107/15/6582.abstract.

Arthur Pierson and Jack Goldstein. Stray light in spectrometers: causes and cures. *Lasers & Optronics*, 8(9):67–72, 1989.

U. Platt and G. Hönninger. The role of halogen species in the troposphere. *Chemosphere*, 52 (2):325 – 338, 2003. ISSN 0045-6535. doi: http://dx.doi.org/10.1016/S0045-6535(03)00216-9. URL http://www.sciencedirect.com/science/article/pii/S0045653503002169. Naturally Produced Organohalogens.

U. Platt and J. Stutz. *Differential Optical Absorption Spectroscopy: Principles and Applications*. Springer Verlag, 2008. ISBN 3540211934.

U. Platt and T. Wagner. Satellite mapping of enhanced BrO concentrations in the troposphere. *Nature*, 395(6701):486–490, 1998.

U. Platt, D. Perner, and H. W. Pätz. Simultaneous measurement of atmospheric CH_2O, O_3 and NO_2 by differential optical absorption. *Journal of Geophysical Research: Oceans*, 84(C10): 6329–6335, 1979. doi: 10.1029/JC084iC10p06329. URL http://dx.doi.org/10.1029/JC084iC10p06329.

U. Platt, L. Marquard, T. Wagner, and D. Perner. Corrections for zenith scattered light DOAS. *Geophysical research letters*, 24(14):1759–1762, 1997.

C. Prados-Roman, A. Butz, T. Deutschmann, M. Dorf, L. Kritten, A. Minikin, U. Platt, H. Schlager, H. Sihler, N. Theys, M. Van Roozendael, T. Wagner, and K. Pfeilsticker. Airborne DOAS limb measurements of tropospheric trace gas profiles: case studies on the profile retrieval of O_4 and BrO.

Atmospheric Measurement Techniques, 4(6):1241–1260, 2011. doi: 10.5194/amt-4-1241-2011. URL http://www.atmos-meas-tech.net/4/1241/2011/.

John K. Pribram and Claude M Penchina. Stray light in Czerny-Turner and Ebert spectrometers. *Applied optics*, 7(10):2005–2014, 1968.

J. Puķīte and T. Wagner. Quantification and parametrization of non-linearity effects by higher-order sensitivity terms in scattered light differential optical absorption spectroscopy. *Atmospheric Measurement Techniques*, 9(5):2147–2177, 2016. doi: 10.5194/amt-9-2147-2016. URL http://www.atmos-meas-tech.net/9/2147/2016/.

J. Puķīte, S. Kühl, T. Deutschmann, U. Platt, and T. Wagner. Extending differential optical absorption spectroscopy for limb measurements in the UV. *Atmospheric Measurement Techniques*, 3(3):631–653, 2010. doi: 10.5194/amt-3-631-2010. URL http://www.atmos-meas-tech.net/3/631/2010/.

Rasmus Raecke. Charakterisierung des Heidelberger mini-DOAS-Spektrographen auf dem Forschungsflugzeug DLR-HALO. Bachelor thesis, Institut für Umweltphysik, Universität Heidelberg, Heidelberg, Germany, 2010.

Rasmus Raecke. Atmospheric Spectroscopy of Trace Gases and Water Vapor in the Tropical Tropopause Layer from the NASA Global Hawk. Master thesis, Institut für Umweltphysik, Universität Heidelberg, Heidelberg, Germany, 2013.

William J. Randel, Dian J. Seidel, and Laura L. Pan. Observational characteristics of double tropopauses. *Journal of Geophysical Research: Atmospheres*, 112(D7):n/a, 2007. doi: 10.1029/2006JD007904. URL http://dx.doi.org/10.1029/2006JD007904. D07309.

W.J. Randel, J.C. Gille, A.E. Roche, J.B. Kumer, J.L. Mergenthaler, J.W. Waters, E.F. Fishbein, and W.A. Lahoz. Stratospheric transport from the tropics to middle latitudes by planetary-wave mixing. *Nature*, 365(6446):533–535, 1993.

C. Reed, M. J. Evans, P. Di Carlo, J. D. Lee, and L. J. Carpenter. Interferences in photolytic no_2 measurements: explanation for an apparent missing oxidant? *Atmospheric Chemistry and Physics*, 16 (7):4707–4724, 2016. doi: 10.5194/acp-16-4707-2016. URL http://www.atmos-chem-phys.net/16/4707/2016/.

Marcel Reichert. Messung und Charakterisierung von Nahinfrarot-Spektren mit dem Instrument HALO mini-DOAS und Vergleich mit Strahlungstransportsimulationen unter Berücksichtigung von Flüssigwasser und Eis. Diploma thesis, Institut für Umweltphysik, Universität Heidelberg, Heidelberg, Germany, 2014.

M. Riese, G. L. Manney, J. Oberheide, X. Tie, R. Spang, and V. Küll. Stratospheric transport by planetary wave mixing as observed during CRISTA-2. *Journal of Geophysical Research: Atmospheres*, 107(D23):n/a, 2002. doi: 10.1029/2001JD000629. URL http://dx.doi.org/10.1029/2001JD000629. 8179.

M. Riese, F. Ploeger, A. Rap, B. Vogel, P. Konopka, M. Dameris, and P. Forster. Impact of uncertainties in atmospheric mixing on simulated UTLS composition and related radiative effects. *Journal of Geophysical Research: Atmospheres*, 117(D16):n/a, 2012. doi: 10.1029/2012JD017751. URL http://dx.doi.org/10.1029/2012JD017751. D16305.

M. Riese, H. Oelhaf, P. Preusse, J. Blank, M. Ern, F. Friedl-Vallon, H. Fischer, T. Guggenmoser, M. Höpfner, P. Hoor, M. Kaufmann, J. Orphal, F. Plöger, R. Spang, O. Suminska-Ebersoldt, J. Ungermann, B. Vogel, and W. Woiwode. Gimballed limb observer for radiance imaging of the atmosphere (GLORIA) scientific objectives. *Atmospheric Measurement Techniques*, 7(7):1915–1928, 2014. doi: 10.5194/amt-7-1915-2014. URL http://www.atmos-meas-tech.net/7/1915/2014/.

C.D. Rodgers. *Inverse Methods for Atmospheric Sounding: Theory and Practice*. World Scientific, 2000.

E. Roeckner, R. Brokopf, M. Esch, M. Giorgetta, S. Hagemann, L. Kornblueh, E. Manzini, U. Schlese, and U. Schulzweida. Sensitivity of Simulated Climate to Horizontal and Vertical Resolution in the ECHAM5 Atmosphere Model. *Journal of Climate*, 19(16):3771–3791, 2006. doi: 10.1175/JCLI3824.1. URL http://dx.doi.org/10.1175/JCLI3824.1.

W. Roedel and T. Wagner. *Physik unserer Umwelt: Die Atmosphäre.* Springer, Berlin, Heidelberg, 2011.

Franz Rohrer and Harald Berresheim. Strong correlation between levels of tropospheric hydroxyl radicals and solar ultraviolet radiation. *Nature*, 442(7099):184–187, 2006.

C. Rolf, A. Afchine, H. Bozem, B. Buchholz, V. Ebert, T. Guggenmoser, P. Hoor, P. Konopka, E. Kretschmer, S. Müller, H. Schlager, N. Spelten, O. Sumińska-Ebersoldt, J. Ungermann, A. Zahn, and M. Krämer. Transport of Antarctic stratospheric strongly dehydrated air into the troposphere observed during the HALO-ESMVal campaign 2012. *Atmospheric Chemistry and Physics*, 15(16):9143–9158, 2015. doi: 10.5194/acp-15-9143-2015. URL http://www.atmos-chem-phys.net/15/9143/2015/.

M. Van Roozendael, T. Wagner, A. Richter, I. Pundt, D.W. Arlander, J.P. Burrows, M. Chipperfield, C. Fayt, P.V. Johnston, J.-C. Lambert, K. Kreher, K. Pfeilsticker, U. Platt, J.-P. Pommereau, B.-M. Sinnhuber, K.K. Tørnkvist, and F. Wittrock. Intercomparison of BrO measurements from ERS-2 GOME, ground-based and balloon platforms. *Advances in Space Research*, 29(11):1661 – 1666, 2002. ISSN 0273-1177. doi: http://dx.doi.org/10.1016/S0273-1177(02)00098-4. URL http://www.sciencedirect.com/science/article/pii/S0273117702000984.

H. K. Roscoe, D. J. Fish, and R. L. Jones. Interpolation errors in UV-visible spectroscopy for stratospheric sensing: implications for sensitivity, spectral resolution, and spectral range. *Appl. Opt.*, 35(3):427–432, Jan 1996. doi: 10.1364/AO.35.000427. URL http://ao.osa.org/abstract.cfm?URI=ao-35-3-427.

H.K. Roscoe, N. Brough, A.E. Jones, F. Wittrock, A. Richter, M. Van Roozendael, and F. Hendrick. Characterisation of vertical BrO distribution during events of enhanced tropospheric BrO in Antarctica, from combined remote and in-situ measurements. *Journal of Quantitative Spectroscopy and Radiative Transfer*, 138:70 – 81, 2014. ISSN 0022-4073. doi: http://dx.doi.org/10.1016/j.jqsrt.2014.01.026. URL http://www.sciencedirect.com/science/article/pii/S0022407314000454.

Laurence S. Rothman, Iouli E. Gordon, Alain Barbe, D. Chris Benner, Peter F. Bernath, Manfred Birk, Vincent Boudon, Linda R. Brown, Alain Campargue, J.-P. Champion, et al. The HITRAN 2008 molecular spectroscopic database. *Journal of Quantitative Spectroscopy and Radiative Transfer*, 110(9):533–572, 2009.

V.V. Rozanov and A.V. Rozanov. Differential optical absorption spectroscopy (DOAS) and air mass factor concept for a multiply scattering vertically inhomogeneous medium: theoretical consideration. *Atmospheric Measurement Techniques*, 3(3):751–780, 2010. doi: 10.5194/amt-3-751-2010. URL http://www.atmos-meas-tech.net/3/751/2010/.

A. Saiz-Lopez, S. Baidar, C. A. Cuevas, T. K. Koenig, R. P. Fernandez, B. Dix, D. E. Kinnison, J.-F. Lamarque, X. Rodriguez-Lloveras, T. L. Campos, and R. Volkamer. Injection of iodine to the stratosphere. *Geophysical Research Letters*, 42(16):6852–6859, 2015. doi: 10.1002/2015GL064796. URL http://dx.doi.org/10.1002/2015GL064796. 2015GL064796.

Alfonso Saiz-Lopez and Roland von Glasow. Reactive halogen chemistry in the troposphere. *Chemical Society Reviews*, 41(19):6448–6472, 2012.

S. Sala, H. Bönisch, T. Keber, D. E. Oram, G. Mills, and A. Engel. Deriving an atmospheric budget of total organic bromine using airborne in situ measurements from the western Pacific area during SHIVA. *Atmospheric Chemistry and Physics*, 14(13):6903–6923, 2014. doi: 10.5194/acp-14-6903-2014. URL http://www.atmos-chem-phys.net/14/6903/2014/.

R. J. Salawitch, T. Canty, T. Kurosu, K. Chance, Q. Liang, A. da Silva, S. Pawson, J. E. Nielsen, J. M. Rodriguez, P. K. Bhartia, X. Liu, L. G. Huey, J. Liao, R. E. Stickel, D. J. Tanner, J. E. Dibb, W. R. Simpson, D. Donohoue, A. Weinheimer, F. Flocke, D. Knapp, D. Montzka, J. A. Neuman, J. B. Nowak, T. B. Ryerson, S. Oltmans, D. R. Blake, E. L. Atlas, D. E. Kinnison, S. Tilmes, L. L. Pan, F. Hendrick, M. Van Roozendael, K. Kreher, P. V. Johnston, R. S. Gao, B. Johnson, T. P. Bui, G. Chen, R. B. Pierce, J. H. Crawford, and D. J. Jacob. A new interpretation of total column BrO during Arctic spring. *Geophysical Research Letters*, 37(21):n/a, 2010. doi: 10.1029/2010GL043798. URL http://dx.doi.org/10.1029/2010GL043798. L21805.

S. Sander, R. R. Friedl, J.R. Barkern, D.M. Golden, M.J. Kurylo, P.H. Wine, J.P.D. Abbat, J.B. Burkholder, C.E. Moortgaret, R.E. Huie, and R. E. Orkin. Chemical kinetics and photochemical data for use in atmospheric studies. *Technical Report, NASA/JPL Publication*, 17(10-06), 2011.

Craig J. Sansonetti, Marc L. Salit, and Joseph Reader. Wavelengths of spectral lines in mercury pencil lamps. *Applied optics*, 35(1):74–77, 1996.

C.L. Schiller, H. Bozem, C. Gurk, U. Parchatka, R. Königstedt, G.W. Harris, J. Lelieveld, and H. Fischer. Applications of quantum cascade lasers for sensitive trace gas measurements of CO, CH_4, N_2O and HCHO. *Applied Physics B*, 92(3):419–430, 2008. ISSN 1432-0649. doi: 10.1007/s00340-008-3125-0. URL http://dx.doi.org/10.1007/s00340-008-3125-0.

Cornelius Schiller, Andreas Wahner, Ulrich Platt, Hans-Peter Dorn, Jörg Callies, and Dieter H. Ehhalt. Near UV atmospheric absorption measurements of column abundances during Airborne Arctic Stratospheric Expedition, January – February 1989: 2. OClO observations. *Geophysical Research Letters*, 17(4):501–504, 1990. doi: 10.1029/GL017i004p00501. URL http://dx.doi.org/10.1029/GL017i004p00501.

J. A. Schmidt, D. J. Jacob, H. M. Horowitz, L. Hu, T. Sherwen, M. J. Evans, Q. Liang, R. M. Suleiman, D. E. Oram, M. Le Breton, C. J. Percival, S. Wang, B. Dix, and R. Volkamer. Modeling the observed tropospheric BrO background: Importance of multiphase chemistry and implications for ozone, OH, and mercury. *Journal of Geophysical Research: Atmospheres*, 121(19):11,819–11,835, 2016. doi: 10.1002/2015JD024229. URL http://dx.doi.org/10.1002/2015JD024229. 2015JD024229.

Steffen Schnierle. Vermessung der Spaltfunktion eines Acton SP-500i. Bachelor thesis, Institut für Umweltphysik, Universität Heidelberg, Heidelberg, Germany, 2014.

A. Schönhardt, M. Begoin, A. Richter, F. Wittrock, L. Kaleschke, J. C. Gómez Martín, and J. P. Burrows. Simultaneous satellite observations of IO and BrO over Antarctica. *Atmospheric Chemistry and Physics*, 12(14):6565–6580, 2012. doi: 10.5194/acp-12-6565-2012. URL http://www.atmos-chem-phys.net/12/6565/2012/.

A. Schönhardt, P. Altube, K. Gerilowski, S. Krautwurst, J. Hartmann, AC Meier, A. Richter, and J.P. Burrows. A wide field-of-view imaging DOAS instrument for two-dimensional trace gas mapping from aircraft. *Atmospheric Measurement Techniques*, 8(12):5113–5131, 2015. doi: 10.5194/amt-8-5113-2015. URL http://www.atmos-meas-tech.net/8/5113/2015/.

S. F. Schreier, A. Richter, F. Wittrock, and J. P. Burrows. Estimates of free-tropospheric NO_2 and HCHO mixing ratios derived from high-altitude mountain MAX-DOAS observations at midlatitudes and in the tropics. *Atmospheric Chemistry and Physics*, 16(5):2803–2817, 2016. doi: 10.5194/acp-16-2803-2016. URL http://www.atmos-chem-phys.net/16/2803/2016/.

Isabella Schulte. Electronic characterisation of the airborne HALO mini-DOAS instrument and recording and simulation of reference spectra. Bachelor thesis, Institut für Umweltphysik, Universität Heidelberg, Heidelberg, Germany, 2013.

U. Schumann, P. Konopka, R. Baumann, R. Busen, T. Gerz, H. Schlager, P. Schulte, and H. Volkert. Estimate of diffusion parameters of aircraft exhaust plumes near the tropopause from nitric oxide and turbulence measurements. *Journal of Geophysical Research: Atmospheres*, 100(D7):14147–14162, 1995. doi: 10.1029/95JD01277. URL http://dx.doi.org/10.1029/95JD01277.

Ulrich Schumann and Heidi Huntrieser. The global lightning-induced nitrogen oxides source. *Atmospheric Chemistry and Physics*, 7(14):3823–3907, 2007. doi: 10.5194/acp-7-3823-2007. URL http://www.atmos-chem-phys.net/7/3823/2007/.

John H. Seinfeld and Spyros N. Pandis. *Atmospheric chemistry and physics: from air pollution to climate change*. John Wiley & Sons, 2016.

A. Serdyuchenko, V. Gorshelev, M. Weber, W. Chehade, and J.P. Burrows. High spectral resolution ozone absorption cross-sections – Part 2: Temperature dependence. *Atmospheric Measurement Techniques*, 7(2):625–636, 2014. doi: 10.5194/amt-7-625-2014. URL http://www.atmos-meas-tech.net/7/625/2014/.

T. Sherwen, M. J. Evans, L. J. Carpenter, J. A. Schmidt, and L. J. Mickely. Halogen chemistry reduces tropospheric o_3 radiative forcing. *Atmospheric Chemistry and Physics Discussions*, 2016: 1–18, 2016a. doi: 10.5194/acp-2016-688. URL http://www.atmos-chem-phys-discuss.net/acp-2016-688/.

T. Sherwen, J. A. Schmidt, M. J. Evans, L. J. Carpenter, K. Großmann, S. D. Eastham, D. J. Jacob, B. Dix, T. K. Koenig, R. Sinreich, I. Ortega, R. Volkamer, A. Saiz-Lopez, C. Prados-Roman, A. S. Mahajan, and C. Ordóñez. Global impacts of tropospheric halogens (Cl, Br, I) on oxidants and composition in GEOS-Chem. *Atmospheric Chemistry and Physics*, 16(18):12239–12271, 2016b. doi: 10.5194/acp-16-12239-2016. URL http://www.atmos-chem-phys.net/16/12239/2016/.

B.-M. Sinnhuber, A. Rozanov, N. Sheode, O. T. Afe, A. Richter, M. Sinnhuber, F. Wittrock, J. P. Burrows, G. P. Stiller, T. von Clarmann, and A. Linden. Global observations of stratospheric bromine monoxide from SCIAMACHY. *Geophysical Research Letters*, 32(20):n/a–n/a, 2005. doi: 10.1029/2005GL023839. URL http://dx.doi.org/10.1029/2005GL023839. L20810.

R. Sinreich, R. Volkamer, F. Filsinger, U. Frieß, C. Kern, U. Platt, O. Sebastián, and T. Wagner. MAX-DOAS detection of glyoxal during ICARTT 2004. *Atmospheric Chemistry and Physics*, 7 (5):1293–1303, 2007. doi: 10.5194/acp-7-1293-2007. URL http://www.atmos-chem-phys.net/7/1293/2007/.

Christopher E. Sioris and Wayne F.J. Evans. Filling in of Fraunhofer and gas-absorption lines in sky spectra as caused by rotational Raman scattering. *Applied optics*, 38(12):2706–2713, 1999.

Susan Solomon. Stratospheric ozone depletion: A review of concepts and history. *Reviews of Geophysics*, 37(3):275–316, 1999. doi: 10.1029/1999RG900008. URL http://dx.doi.org/10.1029/1999RG900008.

Susan Solomon, Arthur L. Schmeltekopf, and Ryan W. Sanders. On the interpretation of zenith sky absorption measurements. *Journal of Geophysical Research: Atmospheres*, 92(D7): 8311–8319, 1987. doi: 10.1029/JD092iD07p08311. URL http://dx.doi.org/10.1029/JD092iD07p08311.

Susan Solomon, Rolando R. Garcia, and A. R. Ravishankara. On the role of iodine in ozone depletion. *Journal of Geophysical Research: Atmospheres*, 99(D10):20491–20499, 1994. doi: 10.1029/94JD02028. URL http://dx.doi.org/10.1029/94JD02028.

Susan Solomon, Karen H. Rosenlof, Robert W. Portmann, John S. Daniel, Sean M. Davis, Todd J. Sanford, and Gian-Kasper Plattner. Contributions of Stratospheric Water Vapor to Decadal Changes in the Rate of Global Warming. *Science*, 327(5970):1219–1223, 2010. ISSN 0036-8075. doi: 10.1126/science.1182488. URL http://science.sciencemag.org/content/327/5970/1219.

R. Spang, K. Arndt, A. Dudhia, M. Höpfner, L. Hoffmann, J. Hurley, R. G. Grainger, S. Griessbach, C. Poulsen, J. J. Remedios, M. Riese, H. Sembhi, R. Siddans, A. Waterfall, and C. Zehner. Fast cloud parameter retrievals of MIPAS/Envisat. *Atmospheric Chemistry and Physics*, 12(15):7135–7164, 2012. doi: 10.5194/acp-12-7135-2012. URL http://www.atmos-chem-phys.net/12/7135/2012/.

M. Speidel, R. Nau, F. Arnold, H. Schlager, and A. Stohl. Sulfur dioxide measurements in the lower, middle and upper troposphere: Deployment of an aircraft-based chemical ionization mass spectrometer with permanent in-flight calibration. *Atmospheric Environment*, 41(11):2427 – 2437, 2007. ISSN 1352-2310. doi: http://dx.doi.org/10.1016/j.atmosenv.2006.07.047. URL http://www.sciencedirect.com/science/article/pii/S1352231006008041.

T. Stavrakou, J.-F. Müller, I. De Smedt, M. Van Roozendael, G. R. van der Werf, L. Giglio, and A. Guenther. Global emissions of non-methane hydrocarbons deduced from sciamachy formaldehyde columns through 2003–2006. *Atmospheric Chemistry and Physics*, 9(11):3663–3679, 2009. doi: 10.5194/acp-9-3663-2009. URL http://www.atmos-chem-phys.net/9/3663/2009/.

T.F. Stocker, D. Qin, G.K. Plattner, M. Tignor, S.K. Allen, J. Boschung, A. Nauels, Y. Xia, B. Bex, and B.M. Midgley. IPCC, 2013. Climate change: the physical science basis. Contribution of working group I. to the fifth assessment report of the intergovernmental panel on climate change, 2013.

Daniel Stone, Lisa K. Whalley, and Dwayne E Heard. Tropospheric OH and HO_2 radicals: field measurements and model comparisons. *Chemical Society Reviews*, 41(19):6348–6404, 2012.

G. Stratmann, H. Ziereis, P. Stock, C.A.M. Brenninkmeijer, A. Zahn, A. Rauthe-Schöch, P.V. Velthoven, H. Schlager, and A. Volz-Thomas. NO and NO_y in the upper troposphere: Nine years of CARIBIC measurements onboard a passenger aircraft. *Atmospheric Environment*, 133:93 – 111, 2016. ISSN 1352-2310. doi: http://dx.doi.org/10.1016/j.atmosenv.2016.02.035. URL http://www.sciencedirect.com/science/article/pii/S1352231016301480.

J. Stutz, E.S. Kim, U. Platt, P. Bruno, C. Perrino, and A. Febo. UV-visible absorption cross sections of nitrous acid. *Journal of Geophysical Research: Atmospheres*, 105(D11):14585–14592, 2000. doi: 10.1029/2000JD900003. URL http://dx.doi.org/10.1029/2000JD900003.

J. Stutz, B. Werner, M. Spolaor, L. Scalone, J. Festa, C. Tsai, R. Cheung, S. F. Colosimo, U. Tricoli, R. Raecke, Ru-Shan Gao, E. J. Hintsa, J. W. Elkins, F. L. Moore, R. Hossaini, W. Feng, M. P. Chipperfield, B. Daube, J. Pittman, S. Wofsy, and K. Pfeilsticker. A new differential optical absorption

spectroscopy instrument to study atmospheric chemistry from an high-altitude unmanned aircraft. *Atmospheric Measurement Techniques Discussions*, (submitted), 2016.

Jochen Stutz and Ulrich Platt. Numerical analysis and estimation of the statistical error of differential optical absorption spectroscopy measurements with least-squares methods. *Appl. Opt.*, 35(30): 6041–6053, Oct 1996. doi: 10.1364/AO.35.006041. URL http://ao.osa.org/abstract.cfm?URI=ao-35-30-6041.

Ryan Thalman and Rainer Volkamer. Temperature dependent absorption cross-sections of o_2–o_2 collision pairs between 340 and 630 nm and at atmospherically relevant pressure. *Physical Chemistry Chemical Physics*, 15(37):15371–15381, 2013.

N. Theys, M. Van Roozendael, F. Hendrick, X. Yang, I. De Smedt, A. Richter, M. Begoin, Q. Errera, P. V. Johnston, K. Kreher, and M. De Mazière. Global observations of tropospheric BrO columns using GOME-2 satellite data. *Atmospheric Chemistry and Physics*, 11(4):1791–1811, 2011. doi: 10.5194/acp-11-1791-2011. URL http://www.atmos-chem-phys.net/11/1791/2011/.

J. Ungermann, J. Blank, M. Dick, A. Ebersoldt, F. Friedl-Vallon, A. Giez, T. Guggenmoser, M. Höpfner, T. Jurkat, M. Kaufmann, S. Kaufmann, A. Kleinert, M. Krämer, T. Latzko, H. Oelhaf, F. Olchewski, P. Preusse, C. Rolf, J. Schillings, O. Suminska-Ebersoldt, V. Tan, N. Thomas, C. Voigt, A. Zahn, M. Zöger, and M. Riese. Level 2 processing for the imaging Fourier transform spectrometer GLORIA: derivation and validation of temperature and trace gas volume mixing ratios from calibrated dynamics mode spectra. *Atmospheric Measurement Techniques*, 8(6): 2473–2489, 2015. doi: 10.5194/amt-8-2473-2015. URL http://www.atmos-meas-tech.net/8/2473/2015/.

Guus J. M. Velders, Claire Granier, Robert W. Portmann, Klaus Pfeilsticker, Mark Wenig, Thomas Wagner, Ulrich Platt, Andreas Richter, and John P. Burrows. Global tropospheric NO_2 column distributions: Comparing three-dimensional model calculations with GOME measurements. *Journal of Geophysical Research: Atmospheres*, 106(D12):12643–12660, 2001. doi: 10.1029/2000JD900762. URL http://dx.doi.org/10.1029/2000JD900762.

B. Vogel, L. L. Pan, P. Konopka, G. Günther, R. Müller, W. Hall, T. Campos, I. Pollack, A. Weinheimer, J. Wei, E. L. Atlas, and K. P. Bowman. Transport pathways and signatures of mixing in the extratropical tropopause region derived from Lagrangian model simulations. *Journal of Geophysical Research: Atmospheres*, 116(D5):n/a, 2011. doi: 10.1029/2010JD014876. URL http://dx.doi.org/10.1029/2010JD014876. D05306.

B. Vogel, G. Günther, R. Müller, J.-U. Grooß, P. Hoor, M. Krämer, S. Müller, A. Zahn, and M. Riese. Fast transport from Southeast Asia boundary layer sources to northern Europe: rapid uplift in typhoons and eastward eddy shedding of the Asian monsoon anticyclone. *Atmospheric Chemistry and Physics*, 14(23):12745–12762, 2014. doi: 10.5194/acp-14-12745-2014. URL http://www.atmos-chem-phys.net/14/12745/2014/.

B. Vogel, G. Günther, R. Müller, J.-U. Grooß, and M. Riese. Impact of different Asian source regions on the composition of the Asian monsoon anticyclone and of the extratropical lowermost stratosphere. *Atmospheric Chemistry and Physics*, 15(23):13699–13716, 2015. doi: 10.5194/acp-15-13699-2015. URL http://www.atmos-chem-phys.net/15/13699/2015/.

L. Vogel, H. Sihler, J. Lampel, T. Wagner, and U. Platt. Retrieval interval mapping: a tool to visualize the impact of the spectral retrieval range on differential optical absorption spectroscopy evaluations. *Atmospheric Measurement Techniques*, 6(2):275–299, 2013. doi: 10.5194/amt-6-275-2013. URL http://www.atmos-meas-tech.net/6/275/2013/.

Christiane Voigt, Ulrich Schumann, Andreas Minikin, Ahmed Abdelmonem, Armin Afchine, Stephan Borrmann, Maxi Boettcher, Bernhard Buchholz, Luca Bugliaro, Anja Costa, Joachim Curtius, Maximilian Dollner, Andreas Dörnbrack, Volker Dreiling, Volker Ebert, Andre Ehrlich, Andreas Fix, Linda Forster, Fabian Frank, Daniel Fütterer, Andreas Giez, Kaspar Graf, Jens-Uwe Grooß, Silke Groß, Katharina Heimerl, Bernd Heinold, Tilman Hüneke, Emma Järvinen, Tina Jurkat, Stefan Kaufmann, Mareike Kenntner, Marcus Klingebiel, Thomas Klimach, Rebecca Kohl, Martina Krämer, Trismono Candra Krisna, Anna Luebke, Bernhard Mayer, Stephan Mertes, Sergej Molleker, Andreas Petzold, Klaus Pfeilsticker, Max Port, Markus Rapp, Philipp Reutter, Christian Rolf, Diana Rose, Daniel Sauer, Andreas Schäfler, Romy Schlage, Martin Schnaiter, Johannes Schneider, Nicole Spelten, Peter Spichtinger, Paul Stock, Adrian Walser, Ralf Weigel, Bernadett Weinzierl, Manfred Wendisch, Frank Werner, Heini Wernli, Martin Wirth, Andreas Zahn, Helmut Ziereis, and Martin Zöger. ML-CIRRUS - The airborne experiment on natural cirrus and contrail cirrus with the high-altitude long-range research aircraft HALO. *Bulletin of the American Meteorological Society*, 0(0):null, 2016. doi: 10.1175/BAMS-D-15-00213.1. URL http://dx.doi.org/10.1175/BAMS-D-15-00213.1.

R. Volkamer, S. Baidar, T. L. Campos, S. Coburn, J. P. DiGangi, B. Dix, E. W. Eloranta, T. K. Koenig, B. Morley, I. Ortega, B. R. Pierce, M. Reeves, R. Sinreich, S. Wang, M. A. Zondlo, and P. A. Romashkin. Aircraft measurements of BrO, IO, glyoxal, NO_2, H_2O, O_2–O_2 and aerosol extinction profiles in the tropics: comparison with aircraft-/ship-based in situ and lidar measurements. *Atmospheric Measurement Techniques*, 8(5):2121–2148, 2015. doi: 10.5194/amt-8-2121-2015. URL http://www.atmos-meas-tech.net/8/2121/2015/.

Rainer Volkamer, Luisa T. Molina, Mario J. Molina, Terry Shirley, and William H. Brune. DOAS measurement of glyoxal as an indicator for fast VOC chemistry in urban air. *Geophysical Research Letters*, 32(8):n/a, 2005. doi: 10.1029/2005GL022616. URL http://dx.doi.org/10.1029/2005GL022616. L08806.

R. von Glasow, R. von Kuhlmann, M. G. Lawrence, U. Platt, and P. J. Crutzen. Impact of reactive bromine chemistry in the troposphere. *Atmospheric Chemistry and Physics*, 4(11/12):2481–2497, 2004. doi: 10.5194/acp-4-2481-2004. URL http://www.atmos-chem-phys.net/4/2481/2004/.

M. Vountas, V.V. Rozanov, and J.P. Burrows. Ring effect: Impact of rotational Raman scattering

on radiative transfer in Earth's atmosphere. *Journal of Quantitative Spectroscopy and Radiative Transfer*, 60(6):943–961, 1998.

M. Vrekoussis, F. Wittrock, A. Richter, and J. P. Burrows. Temporal and spatial variability of glyoxal as observed from space. *Atmospheric Chemistry and Physics*, 9(13):4485–4504, 2009. doi: 10.5194/acp-9-4485-2009. URL http://www.atmos-chem-phys.net/9/4485/2009/.

T. Wagner, F. Erle, L. Marquard, C. Otten, K. Pfeilsticker, T. Senne, J. Stutz, and U. Platt. Cloudy sky optical paths as derived from differential optical absorption spectroscopy observations. *Journal of Geophysical Research: Atmospheres*, 103(D19):25307–25321, 1998. doi: 10.1029/98JD01021. URL http://dx.doi.org/10.1029/98JD01021.

T. Wagner, M. Bruns, J.P. Burrows, S. Fietkau, F. Finocchi, K.P. Heue, G. Hönninger, U. Platt, I. Pundt, A. Richter, et al. The AMAXDOAS instrument and its application for SCIAMACHY validation. *EUROPEAN SPACE AGENCY-PUBLICATIONS-ESA SP*, 471:331–336, 2001a.

T. Wagner, K. Chance, U. Frieß, M. Gil, F. Goutail, G. Hönninger, P. Johnston, K. Karlsen-Tørnkvist, I. Kostadinov, H. Leser, et al. Correction of the Ring effect and I_0-effect for DOAS observations of scattered sunlight. In *1st DOAS Workshop, Heidelberg, Germany*, pages 13–14, 2001b.

T. Wagner, S. Beirle, and T. Deutschmann. Three-dimensional simulation of the Ring effect in observations of scattered sun light using Monte Carlo radiative transfer models. *Atmospheric Measurement Techniques*, 2(1):113–124, 2009a. doi: 10.5194/amt-2-113-2009. URL http://www.atmos-meas-tech.net/2/113/2009/.

T. Wagner, T. Deutschmann, and U. Platt. Determination of aerosol properties from MAX-DOAS observations of the Ring effect. *Atmospheric Measurement Techniques*, 2(2):495–512, 2009b. doi: 10.5194/amt-2-495-2009. URL http://www.atmos-meas-tech.net/2/495/2009/.

T. Wagner, A. Apituley, S. Beirle, S. Dörner, U. Friess, J. Remmers, and R. Shaiganfar. Cloud detection and classification based on MAX-DOAS observations. *Atmospheric Measurement Techniques*, 7(5):1289–1320, 2014. doi: 10.5194/amt-7-1289-2014. URL http://www.atmos-meas-tech.net/7/1289/2014/.

Andreas Wahner, Jörg Callies, Hans-Peter Dorn, Ulrich Platt, and Cornelius Schiller. Near UV atmospheric absorption measurements of column abundances during Airborne Arctic Stratospheric Expedition, January – February 1989: 1. Technique and NO_2 observations. *Geophysical Research Letters*, 17(4):497–500, 1990a. doi: 10.1029/GL017i004p00497. URL http://dx.doi.org/10.1029/GL017i004p00497.

Andreas Wahner, Jörg Callies, Hans-Peter Dorn, Ulrich Platt, and Cornelius Schiller. Near UV atmospheric absorption measurements of column abundances during Airborne Arctic Stratospheric Expedition, January – February 1989: 3. BrO observations. *Geophysical Research Letters*, 17(4):517–520, 1990b. doi: 10.1029/GL017i004p00517. URL http://dx.doi.org/10.1029/GL017i004p00517.

John M. Wallace and Peter V Hobbs. *Atmospheric science: an introductory survey*, volume 92. Academic press, 2006.

P. Wang, A. Richter, M. Bruns, V.V. Rozanov, J.P. Burrows, K.-P. Heue, T. Wagner, I. Pundt, and U. Platt. Measurements of tropospheric NO_2 with an airborne multi-axis DOAS instrument. *Atmospheric Chemistry and Physics*, 5(2):337–343, 2005. doi: 10.5194/acp-5-337-2005. URL http://www.atmos-chem-phys.net/5/337/2005/.

P. Wang, A. Richter, M. Bruns, J.P. Burrows, R. Scheele, W. Junkermann, K-P Heue, T. Wagner, U. Platt, and I Pundt. Airborne multi-axis DOAS measurements of tropospheric SO_2 plumes in the Po-valley, Italy. *Atmospheric Chemistry and Physics*, 6(2):329–338, 2006. doi: 10.5194/acp-6-329-2006. URL http://www.atmos-chem-phys.net/6/329/2006/.

F. Weidner, H. Bösch, H. Bovensmann, J.P. Burrows, A. Butz, C. Camy-Peyret, M. Dorf, K. Gerilowski, W. Gurlit, U. Platt, et al. Balloon-borne limb profiling of UV/vis skylight radiances, O_3, NO_2, and BrO: technical set-up and validation of the method. *Atmospheric Chemistry and Physics*, 5(5):1409–1422, 2005. doi: 10.5194/acp-5-1409-2005. URL http://www.atmos-chem-phys.net/5/1409/2005/.

Jannis Weimar. Detection characteristics of VIS spectrometers of the airborne HALO mini-DOAS instrument and their influence on the retrieval of trace gas abundances. Bachelor thesis, Institut für Umweltphysik, Universität Heidelberg, Heidelberg, Germany, 2014.

Manfred Wendisch and Jean-Louis Brenguier. *Airborne measurements for environmental research: methods and instruments*. John Wiley & Sons, 2013.

Manfred Wendisch and Ping Yang. *Theory of atmospheric radiative transfer*. John Wiley & Sons, 2012.

Manfred Wendisch, Peter Pilewskie, John Pommier, Steve Howard, Ping Yang, Andrew J. Heymsfield, Carl G. Schmitt, Darrel Baumgardner, and Bernhard Mayer. Impact of cirrus crystal shape on solar spectral irradiance: A case study for subtropical cirrus. *Journal of Geophysical Research: Atmospheres*, 110(D3):n/a, 2005. doi: 10.1029/2004JD005294. URL http://dx.doi.org/10.1029/2004JD005294. D03202.

Manfred Wendisch, Ping Yang, and Peter Pilewskie. Effects of ice crystal habit on thermal infrared radiative properties and forcing of cirrus. *Journal of Geophysical Research: Atmospheres*, 112(D8): n/a, 2007. doi: 10.1029/2006JD007899. URL http://dx.doi.org/10.1029/2006JD007899. D08201.

Manfred Wendisch, Ulrich Pöschl, Meinrat O. Andreae, Luiz A. T. Machado, Rachel Albrecht, Hans Schlager, Daniel Rosenfeld, Scot T. Martin, Ahmed Abdelmonem, Armin Afchine, Alessandro Araùjo, Paulo Artaxo, Heinfried Aufmhoff, Henrique M. J. Barbosa, Stephan Borrmann, Ramon Braga, Bernhard Buchholz, Micael Amore Cecchini, Anja Costa, Joachim Curtius, Maximilian Dollner, Marcel Dorf, Volker Dreiling, Volker Ebert, André Ehrlich, Florian Ewald,

Gilberto Fisch, Andreas Fix, Fabian Frank, Daniel Fütterer, Christopher Heckl, Fabian Heidelberg, Tilman Hüneke, Evelyn Jäkel, Emma Järvinen, Tina Jurkat, Sandra Kanter, Udo Kästner, Mareike Kenntner, Jürgen Kesselmeier, Thomas Klimach, Matthias Knecht, Rebecca Kohl, Tobias Kölling, Martina Krämer, Mira Krüger, Trismono Candra Krisna, Jost V. Lavric, Karla Longo, Christoph Mahnke, Antonio O. Manzi, Bernhard Mayer, Stephan Mertes, Andreas Minikin, Sergej Molleker, Steffen Münch, Björn Nillius, Klaus Pfeilsticker, Christopher Pöhlker, Anke Roiger, Diana Rose, Dagmar Rosenow, Daniel Sauer, Martin Schnaiter, Johannes Schneider, Christiane Schulz, Rodrigo A. F. de Souza, Antonio Spanu, Paul Stock, Daniel Vila, Christiane Voigt, Adrian Walser, David Walter, Ralf Weigel, Bernadett Weinzierl, Frank Werner, Marcia A. Yamasoe, Helmut Ziereis, Tobias Zinner, and Martin Zöger. The ACRIDICON-CHUVA campaign: Studying tropical deep convective clouds and precipitation over Amazonia using the new German research aircraft HALO. *Bulletin of the American Meteorological Society*, 0(0):null, 2016. doi: 10.1175/BAMS-D-14-00255.1. URL http://dx.doi.org/10.1175/BAMS-D-14-00255.1.

P. O. Wennberg, T. F. Hanisco, L. Jaeglé, D. J. Jacob, E. J. Hintsa, E. J. Lanzendorf, J. G. Anderson, R.-S. Gao, E. R. Keim, S. G. Donnelly, L. A. Del Negro, D. W. Fahey, S. A. McKeen, R. J. Salawitch, C. R. Webster, R. D. May, R. L. Herman, M. H. Proffitt, J. J. Margitan, E. L. Atlas, S. M. Schauffler, F. Flocke, C. T. McElroy, and T. P. Bui. Hydrogen radicals, nitrogen radicals, and the production of o_3 in the upper troposphere. *Science*, 279(5347):49–53, 1998. ISSN 0036-8075. doi: 10.1126/science.279.5347.49. URL http://science.sciencemag.org/content/279/5347/49.

B. Werner, J. Stutz, M. Spolaor, L. Scalone, R. Raecke, J. Festa, F. Colosimo, R. Cheung, C. Tsai, R. Hossaini, M. P. Chipperfield, G. S. Taverna, W. Feng, J. W. Elkins, D. W. Fahey, R.-S. Gao, E. J. Hintsa, T. D. Thornberry, F. L. Moore, M. A. Navarro, E. Atlas, B. Daube, J. Pittman, S. Wofsy, and K. Pfeilsticker. Probing the subtropical lowermost stratosphere, tropical upper troposphere, and tropopause layer for inorganic bromine. *Atmospheric Chemistry and Physics Discussions*, 2016: 1–43, 2016. doi: 10.5194/acp-2016-656. URL http://www.atmos-chem-phys-discuss.net/acp-2016-656/.

Bodo Werner. Spectroscopic UV/vis limb measurements from aboard the NASA Global Hawk: Implications for the photochemistry and budget of bromine in the tropical tropopause layer. PhD thesis, Institut für Umweltphysik, Universität Heidelberg, Heidelberg, Germany, 2015.

Folkard Wittrock, Andreas Richter, Hilke Oetjen, John P. Burrows, Maria Kanakidou, Stelios Myriokefalitakis, Rainer Volkamer, Steffen Beirle, Ulrich Platt, and Thomas Wagner. Simultaneous global observations of glyoxal and formaldehyde from space. *Geophysical Research Letters*, 33(16):n/a, 2006. doi: 10.1029/2006GL026310. URL http://dx.doi.org/10.1029/2006GL026310. L16804.

WMO. Scientific Assessment of Ozone Depletion: 2014. Global ozone research and monitoring project-report no. 55, World Meteorological Organization, 2014.

K. Wolf, A. Ehrlich, T. Hüneke, K. Pfeilsticker, F. Werner, M. Wirth, and M. Wendisch. Potential of

remote sensing of cirrus optical thickness by airborne spectral radiance measurements in limb and nadir geometry. *Atmospheric Measurement Techniques*, in preparation, 2016.

J. S. Wright and S. Fueglistaler. Large differences in reanalyses of diabatic heating in the tropical upper troposphere and lower stratosphere. *Atmospheric Chemistry and Physics*, 13(18):9565–9576, 2013. doi: 10.5194/acp-13-9565-2013. URL http://www.atmos-chem-phys.net/13/9565/2013/.

Chunxiang Ye, Xianliang Zhou, Dennis Pu, James Stutz Jochen, Festa, Max Spolaor, Catalina Tsai, Christopher Cantrell, Roy L. Mauldin, Teresa Campos, Andrew Weinheimer, Rebecca S. Hornbrook, Eric C. Apel, Alex Guenther, Lisa Kaser, Bin Yuan, Thomas Karl, Julie Haggerty, Samuel Hall, Kirk Ullmann, James N. Smith, John Ortega, and Christoph Knote. Rapid cycling of reactive nitrogen in the marine boundary layer. *Nature*, 532:489–491, 2016. doi: doi:10.1038/nature17195.

A. Zahn, J. Weppner, H. Widmann, K. Schlote-Holubek, B. Burger, T. Kühner, and H. Franke. A fast and precise chemiluminescence ozone detector for eddy flux and airborne application. *Atmospheric Measurement Techniques*, 5(2):363–375, 2012. doi: 10.5194/amt-5-363-2012. URL http://www.atmos-meas-tech.net/5/363/2012/.

M. Zöger, A. Afchine, N. Eicke, M.-T. Gerhards, E. Klein, D. S. McKenna, U. Mörschel, U. Schmidt, V. Tan, F. Tuitjer, T. Woyke, and C. Schiller. Fast in situ stratospheric hygrometers: A new family of balloon-borne and airborne Lyman alpha photofragment fluorescence hygrometers. *Journal of Geophysical Research: Atmospheres*, 104(D1):1807–1816, 1999. doi: 10.1029/1998JD100025. URL http://dx.doi.org/10.1029/1998JD100025.

Ying Zhang, Andreas Macke, and Frank Albers. Effect of crystal size spectrum and crystal shape on stratiform cirrus radiative forcing. *Atmospheric Research*, 52(1–2):59 – 75, 1999. ISSN 0169-8095. doi: http://dx.doi.org/10.1016/S0169-8095(99)00026-5. URL http://www.sciencedirect.com/science/article/pii/S0169809599000265.

Helmut Ziereis, H. Schlager, P. Schulte, P.F.J. van Velthoven, and F. Slemr. Distributions of NO, NO_x, and NO_y in the upper troposphere and lower stratosphere between 28 and 61 N during POLINAT 2. *Journal of Geophysical Research: Atmospheres*, 105(D3):3653–3664, 2000.

List of Abbreviations

AMF	Air Mass Factor
AOD	Aerosol optical depth
BAMF, BoxAMF	Box-Air Mass Factor
CTM	Chemical transport model
DC	Dark current
DOAS	Differential optical absorption spectroscopy
(d)SCD	(Differential) slant column density
EA	Elevation angle
ExTL	Extratropical tropopause layer
FOV	Field of view
FT	Free troposphere
HALO	High altitude, long range research aircraft
LMS	lowermost stratosphere
ML	Mid-latitude
NIR, near-IR	Near-infrared
OD	Optical depth
ODE	Ozone depletion event
OEI	Inversion by optimal estimation
PBL	Planetary boundary layer
RRS	Rotational Raman scattering
RTM / RTE	Radiative transfer model / equation
SCD	Slant column density
SCD_{Ref}	Fraunhofere reference slant column density
SOA	Secondary organic aerosol
STE	Stratosphere-troposphere exchange
SZA	Solar zenith angle
TTL	Tropical tropopause layer
UDP	User Datagram Protocol
UT/LS	Upper troposphere / lower stratosphere
UV/vis	Ultra-violet / visible
VOC	Volatile organic compounds
VRS	Vibrational Raman scattering
VSLS	Very short-lived substances

List of Figures

List of Tables

Appendix A

Instrument and methods

A.1 Instrument

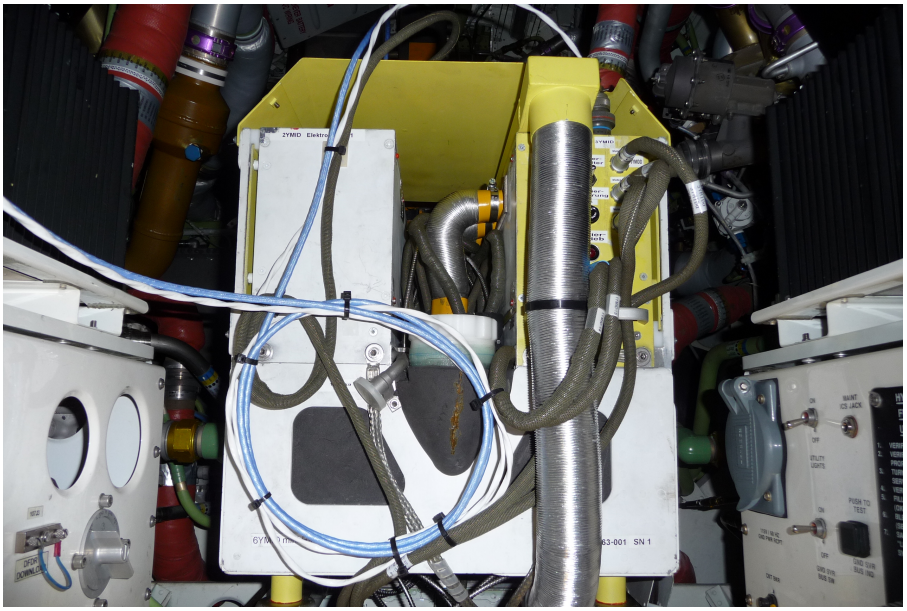

Figure A.1: Fully assembled HALO mini-DOAS instrument rack mounted at the specified position in the HALO boiler room in August, 2014.

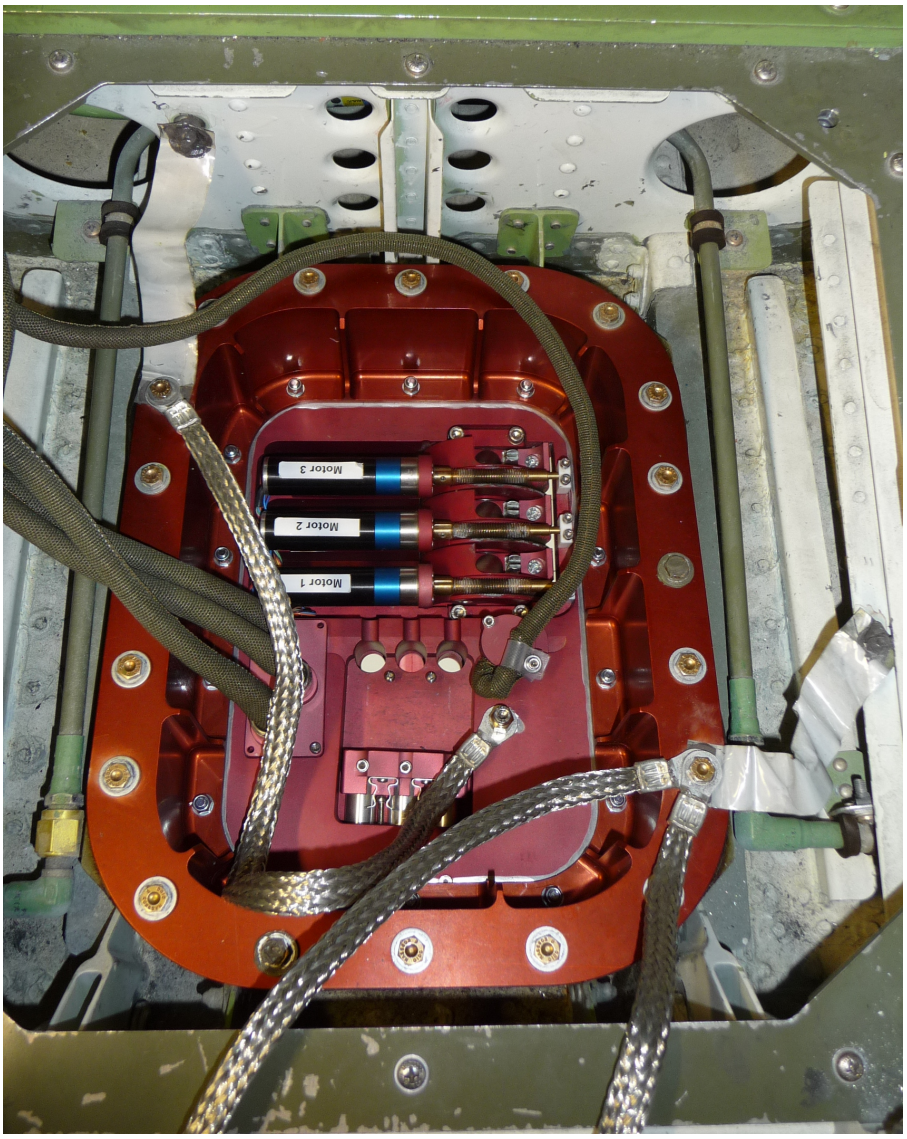

Figure A.2: Aperture plate mounted to the aircraft fuselage in the boiler room in July, 2012.

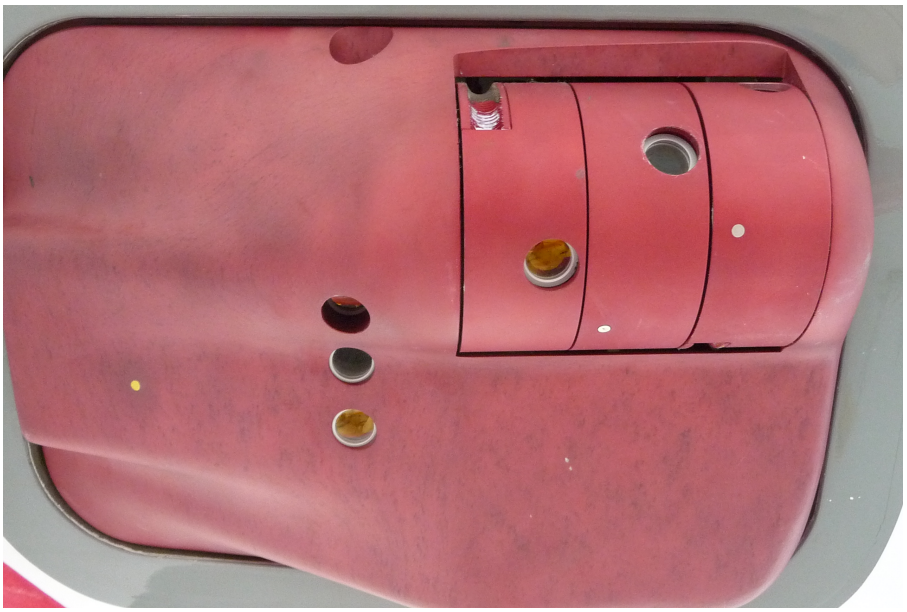

Figure A.3: Nadir (center left) and limb (top right) telescopes assembled in the aperture plate in July, 2012.

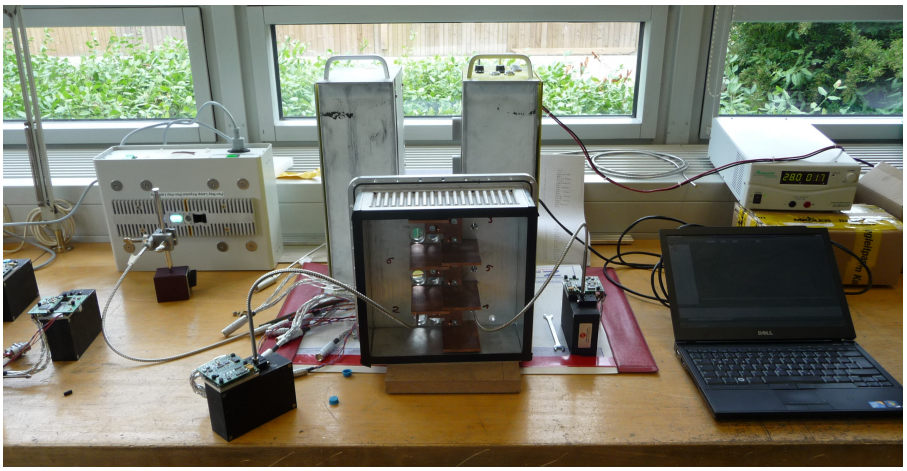

Figure A.4: Assembly of the spectrometer unit. Calibration gas lamp (Hg) on the left, spectrometer housing with opened bottom in the center, PC and electricity supply on the right. The fibre bundles are fixed to the spectrometer entrance slits while simultaneously controlling the slit function in order to optimise the imaging for each spectrometer.

A.2 Software

Measurement script / configuration file example

```
[General]
LogFile=1 ;Switch logfile on or off
LogIntervall=1000 ;Set logfile interval in ms
BasePath=/C/Spectra/
Location=OP
Campaign=POL
Description="POLSTRACC"
Author=Dominique_Alex
DOAS-IP=192.168.1.202
DOAS-Port=20520
OperatorIP=192.168.1.195
OperatorPort=20521
InfoPort=20000 ;Info-Port of BAHAMAS
Hdlen=16 ;Header-Length of BAHAMAS-Data
Sender=1 ;Switch instrument status data on/off
DummyScans=2 ;Set number of dummyscans after each change of exposure time
ScanningHeightMin=5000 ;Set minimum aircraft altitude [m] for scanning operation

[Spectrometer_Switch] ;Switch readout of spectra on or off
UV1=1
UV2=1
VIS3=1
```

```
VIS4=1
NIR5=1
NIR6=1

[Spectrometer_ID] ;set up device id for each spectrometer
UV1=0
UV2=1
VIS3=2
VIS4=3
NIR5=4
NIR6=5

[Saturation] ;Set target saturation for recorded spectra in %
UV1=70
UV2=70
VIS3=70
VIS4=70
NIR5=70
NIR6=70
Tolerance=20

[Cooling] ;Switch peltier-elements on or off
UV1=0
UV2=0
VIS3=0
VIS4=0
NIR5=0
NIR6=0
Target_Temperature=10 ;Set target temperature in C
Tolerance=0,5 ;Set temperature tolerance in C
Interval=1 ;Set correction interval in s

[Motors] ;Switch Motors on or off and set target angles
Motor1=1
Motor2=1
Motor3=1
QDS_Correction=1 ;Switch angle correction by BAHAMAS-data on or off
Tolerance=0,4 ;Set tolerance for 'motor is in position'
TimeForHomingSequence=30 ;Set maximum time for homing sequence in s
Offset1=-1,09 ;Angle Offset
Offset2=-0,26
Offset3=-0,54
```

```
ScanDefault=0 ;Switch scanning default on/off

[Angles_UV]
NumberOfAngles=8
Angle1=0 ;Set numbers of angles
Angle2=0.5
Angle3=1
Angle4=2.5
Angle5=6
Angle6=15
Angle7=-1
Angle8=-0.5

[Angles_VIS]
NumberOfAngles=8
Angle1=0 ;Set numbers of angles
Angle2=0.5
Angle3=1
Angle4=2.5
Angle5=6
Angle6=15
Angle7=-1
Angle8=-0.5

[Angles_NIR]
NumberOfAngles=5
Angle1=0 ;Set numbers of angles
Angle2=2.5
Angle3=5
Angle4=10
Angle5=15

[Integration_Times] ;Set integration times (in seconds!) for each angle / each spectrum
UV1=60
UV2_M1=60
VIS3=60
VIS4_M2=60
NIR5=1
NIR6_M3=1

[NumOfScans] ;Set number of scans for each spectrum
UV1=100
```

```
UV2_M1=100
VIS3=100
VIS4_M2=100
NIR5=1
NIR6_M3=1
ZeroDegFactor=1
```

Table A.1: Explanations of selected commands in the measurement script.

Category	Parameter	Explanation
General	InfoPort	Port at which the address to read out the XML-file can be received from the BAHAMAS system.
	DOAS-IP, DOAS-Port	IP address and port number of the measurement instrument computer which runs the script
	OperatorIP, OperatorPort	IP and port number of the operator computer which runs the DOAS-Operator software
	DummyScans	Determines how many readouts of the spectrometer electronic are discarded after a change of exposure time.
	ScanningHeightMin	If the aircraft is below this altitude, scanning will be automatically switched off.
Spectrom. ID	UV1 ... NIR6	The driver will identify each readout electronic board with a specific instrument ID. If the readout electronic boards are switched or the wiring between boards and spectrometers is changed, the ID under which a certain spectrometer is accessed can change.
Saturation	UV1 ... NIR6	The exposure time will be kept constant, if the saturation (maximum intensity) is between [Saturation - Tolerance] and [Saturation + Tolerance].
Motors	Tolerance	When the motor is moving to the next elevation angle in scannig mode, the recording of spectra of the corresponding spectrometer is started when this criteria is fulfilled.
	Offset	See section 3.2.6.
	ScanDefault	Determines if scanning should be switched on or off, if the aircraft is at sufficiently high and constant altitude and no command from the operator is given.
Angles UV/VIS/ NIR	Angle1 ... n	Defines the set of elevation angles. When not in scanning mode, the motors will move to the EA given as Angle1.
Integration Times	UV1 ... NIR6	Gives the maximum integration time for each spectrometer. Set to 1 for NIR, so that each exposure is saved as a spectrum.
NumOf Scans	UV1 ... NIR6	Gives the maximum number of exposures for each spectrum.
	ZeroDegFactor	The factor by which the above numbers are multiplied when the elevation angle is 0°.

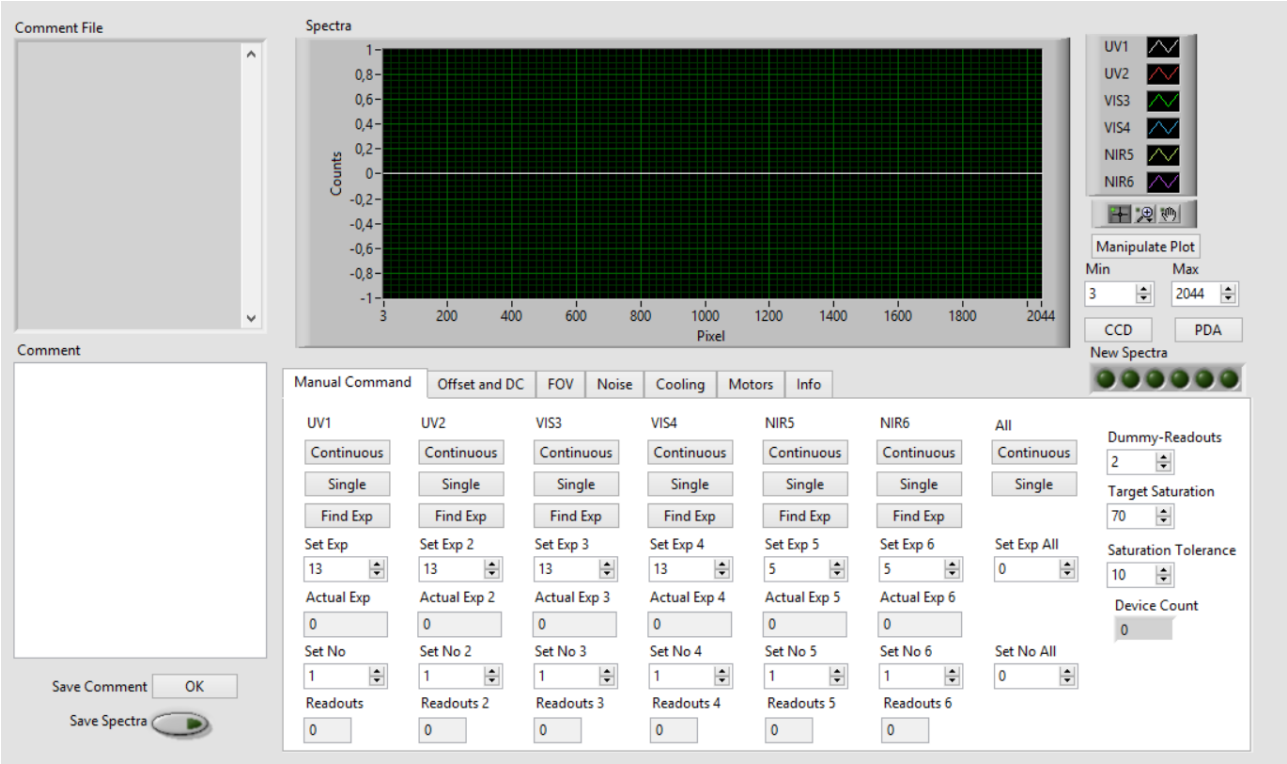

Figure A.5: Screenshot of the Calibration software user interface.

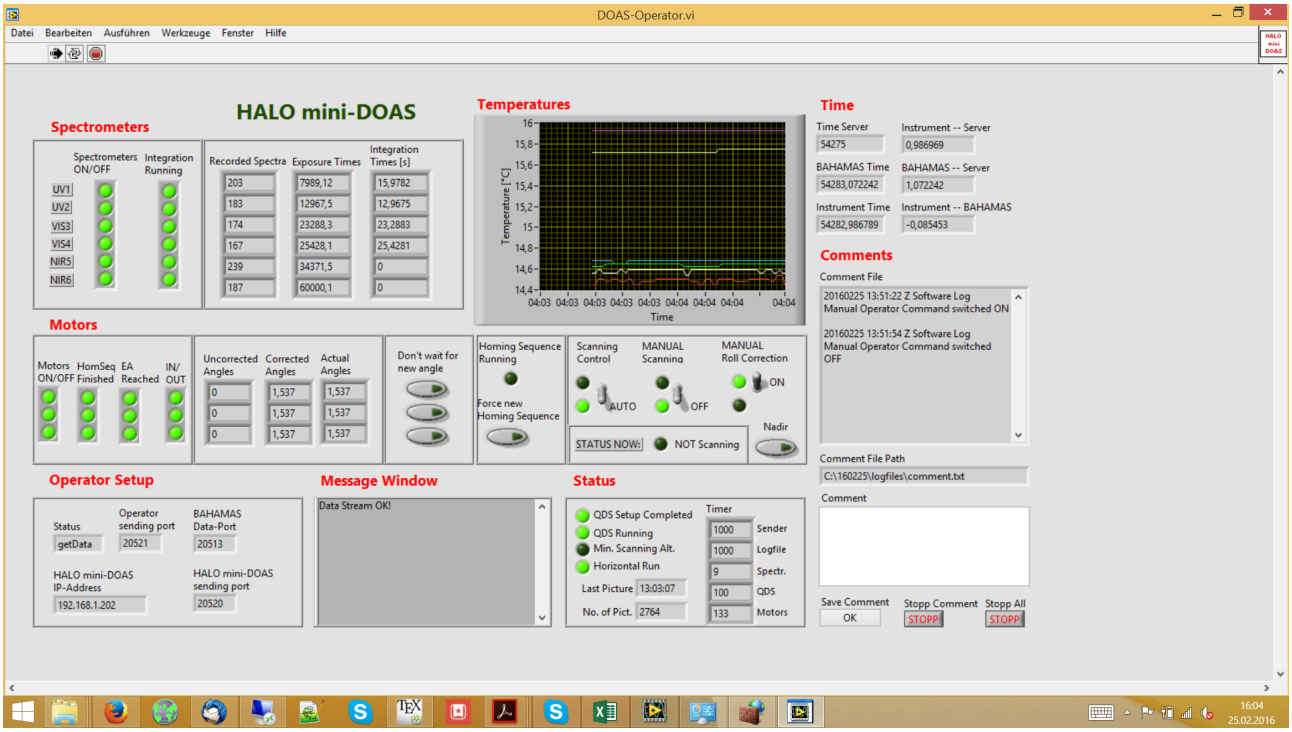

Figure A.6: Screenshot of the operator interface during operation.

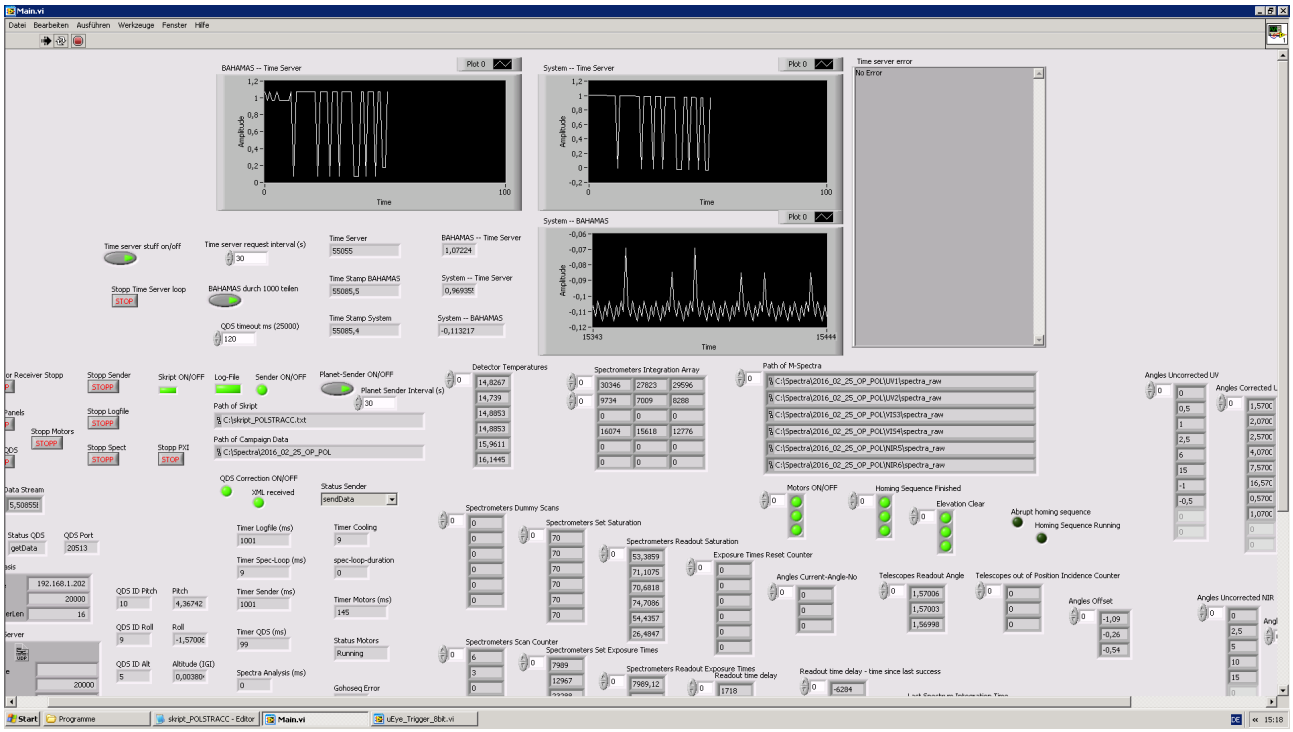

Figure A.7: Screenshot of the measurement software user interface during operation.

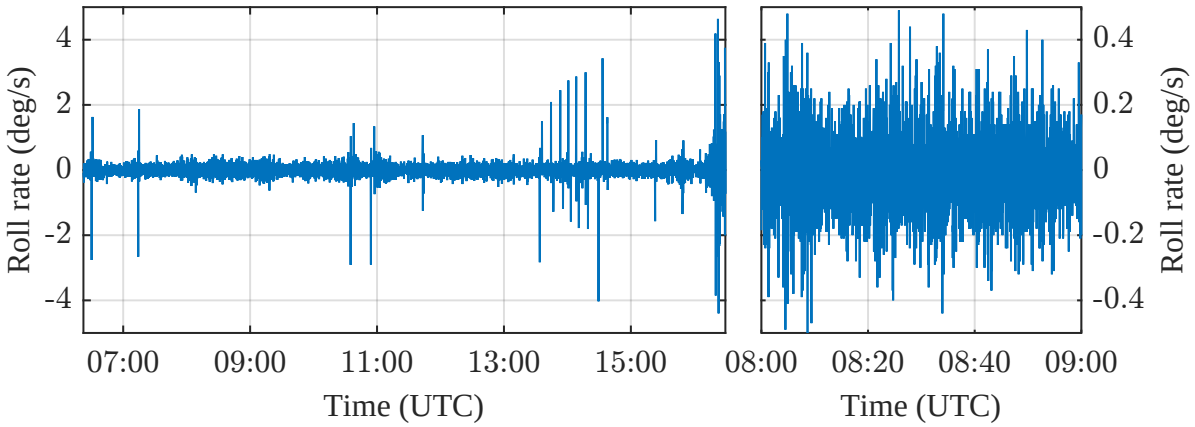

Figure A.8: Roll rate recorded by the BAHAMAS system during science flight ANT (left panel). Subsection of the flight from 8:00 to 9:00 UTC (right panel, note the changed scale).

A.3 Additional methods

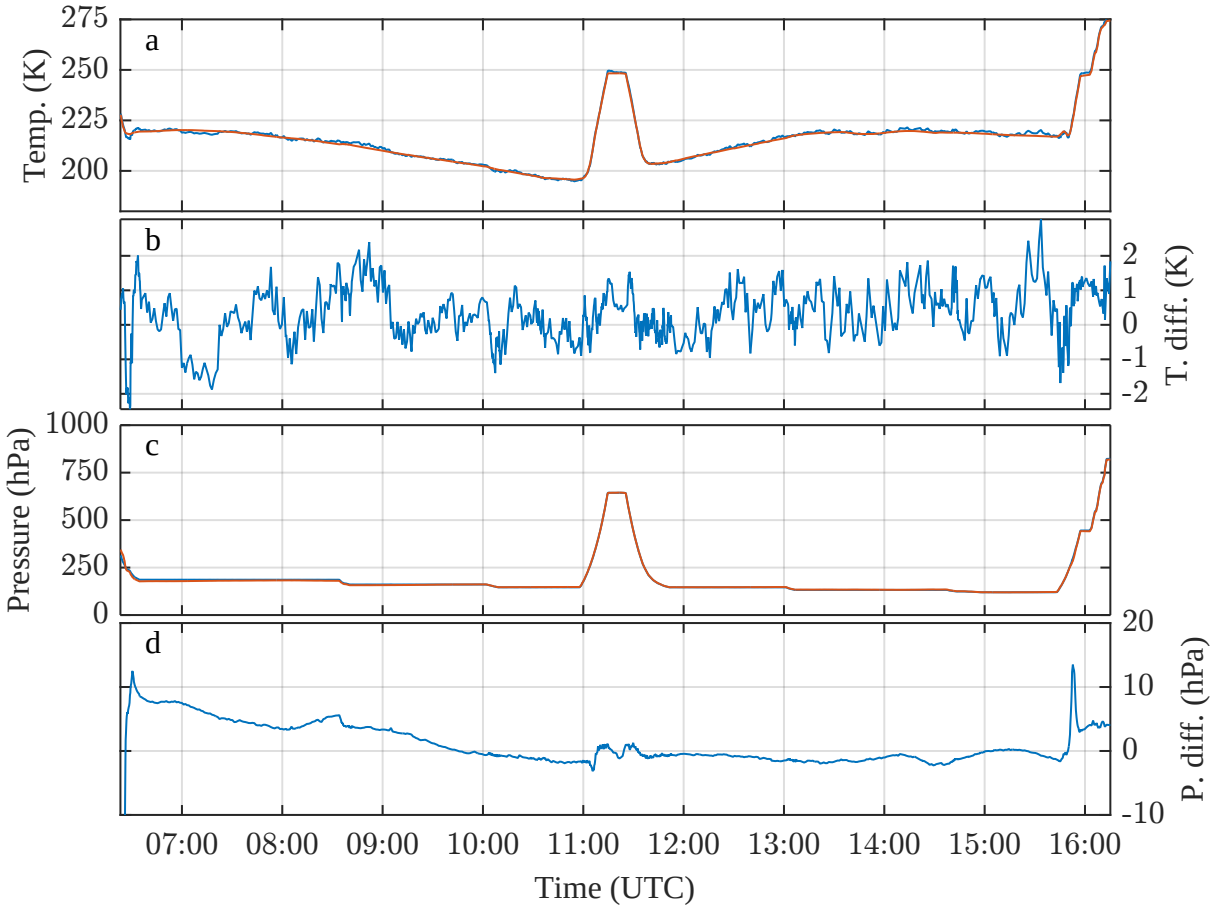

Figure A.9: Temperature and pressure during science flight ANT. Panel a: Temperature measured (blue) and modelled (red) and their difference (panel b). Panel c: Pressure measured (blue) and modelled (red) and their difference (panel d). In-situ measurements carried out by the BAHAMAS system (ZITAT), model data from CTM CLAMS.

A.3.1 OEI Flight section 1

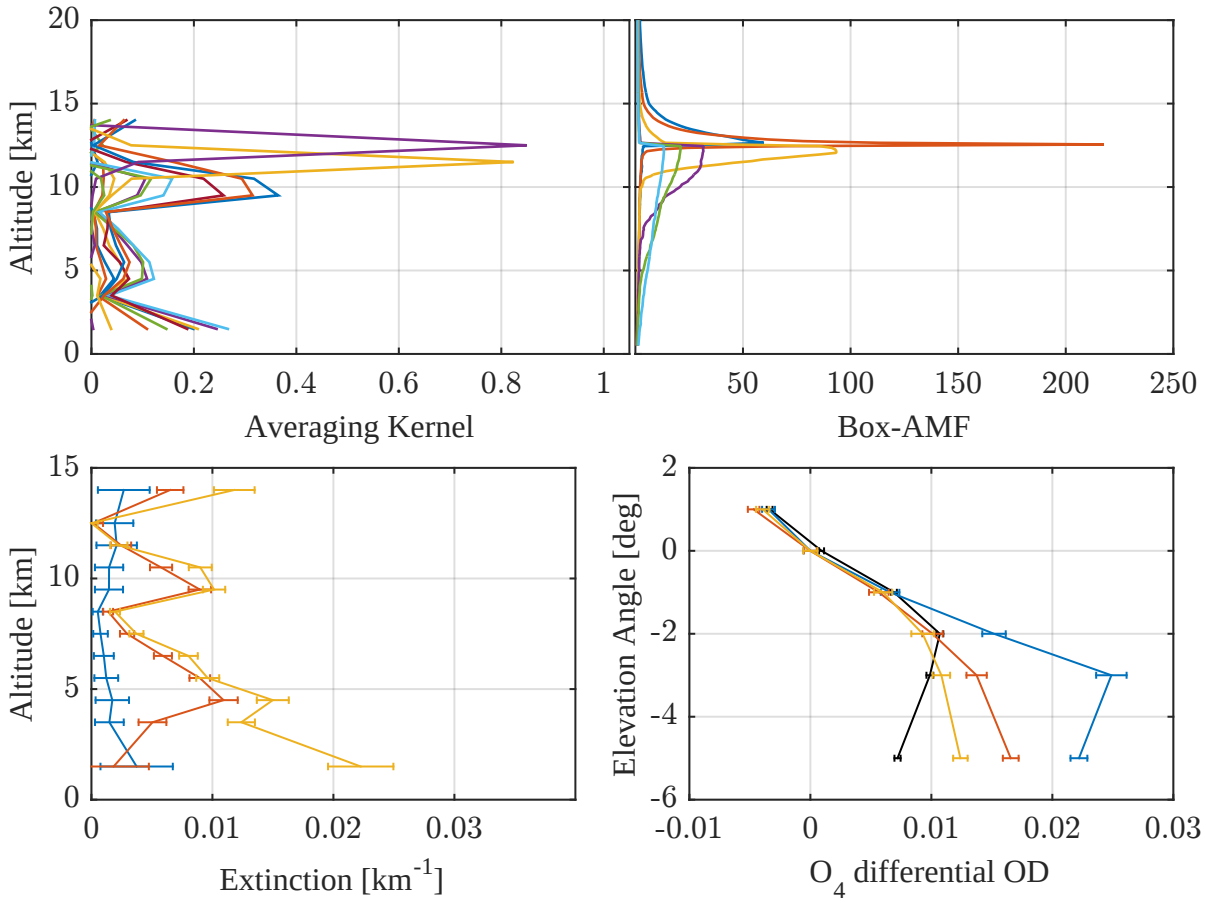

Figure A.10: Optimal estimation inversion (OEI) for flight section 1 based on O_4 optical densities. Top left: The trace of the averaging kernel (AK) matrix is 2.91. Top right: The Box-AMF show the very long light paths at flight altitude and the comparably very short light paths (and correspondingly low sensitivity) below 7 km altitude. Bottom left: A retrieval grid with 7 elements was chosen. Shown are the a priori profile (blue) as well as the first (red), and second (yellow) iteration. Bottom right: Comparison of the O_4 ODs with respect to the OD at 0°EA. Shown are the measurements (black), a priori (blue) as well as the first (red), and second (yellow) iteration.

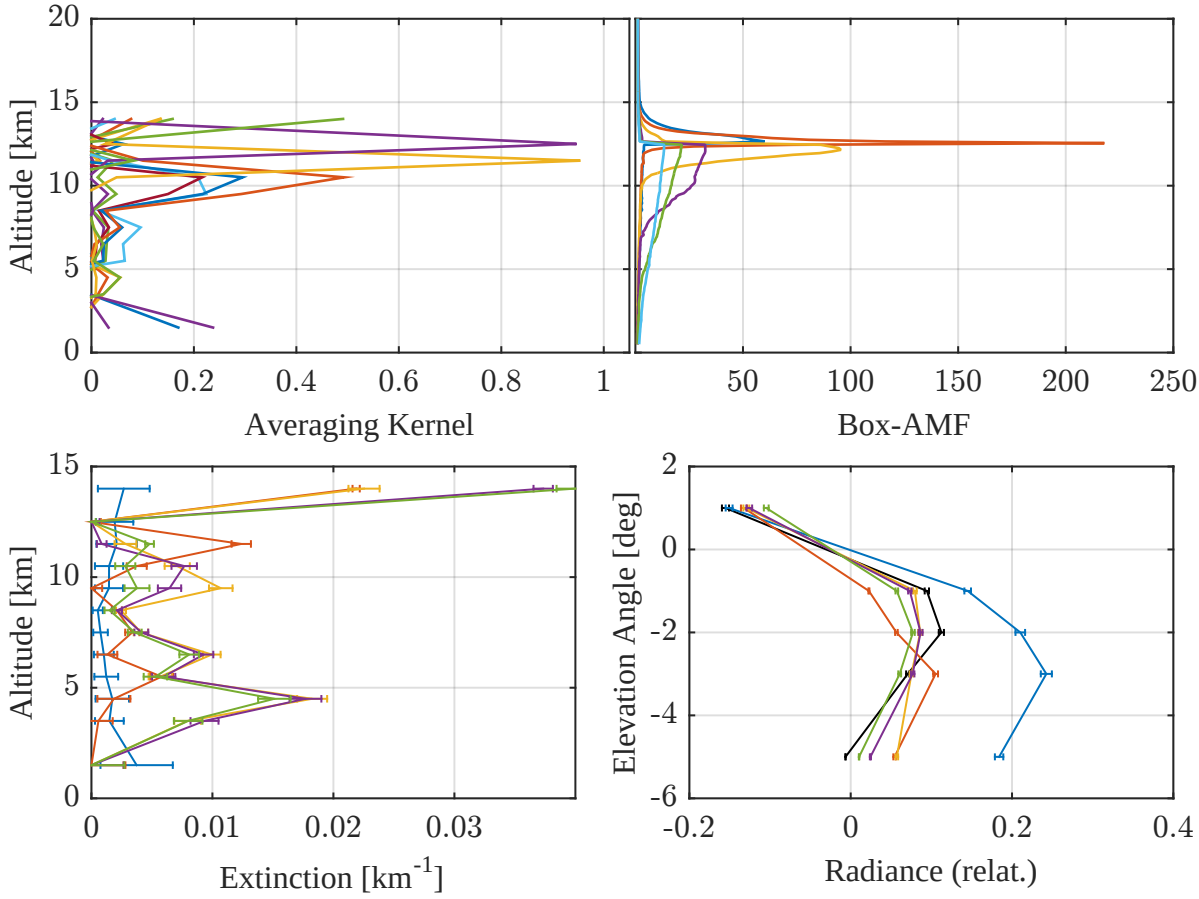

Figure A.11: OEI for flight section 1 based on relative radiances. Top left: The trace of the AK matrix is 3.5. Top right: Box-AMFs. Bottom left: Shown are the a priori profile (blue) as well as the first (red), second (yellow), third (violet), and fourth (green) iteration. Bottom right: Comparison of the logarithm of the radiances, normed to 0°EA. Shown are the measurements (black), a priori (blue) as well as the first (red), second (yellow), third (violet), and fourth (green) iteration.

(a) Cockpit view around the time of the section 1 reference spectrum.

(b) Nadir view around the time of the section 1 reference spectrum.

Figure A.12: Pictures of the meteorological conditions during flight section 1, recorded by the HALO aircraft built-in camera system. Although the cloud presence was variable, the picture gives a good impression of average conditions.

A.3.2 OEI Flight section 2

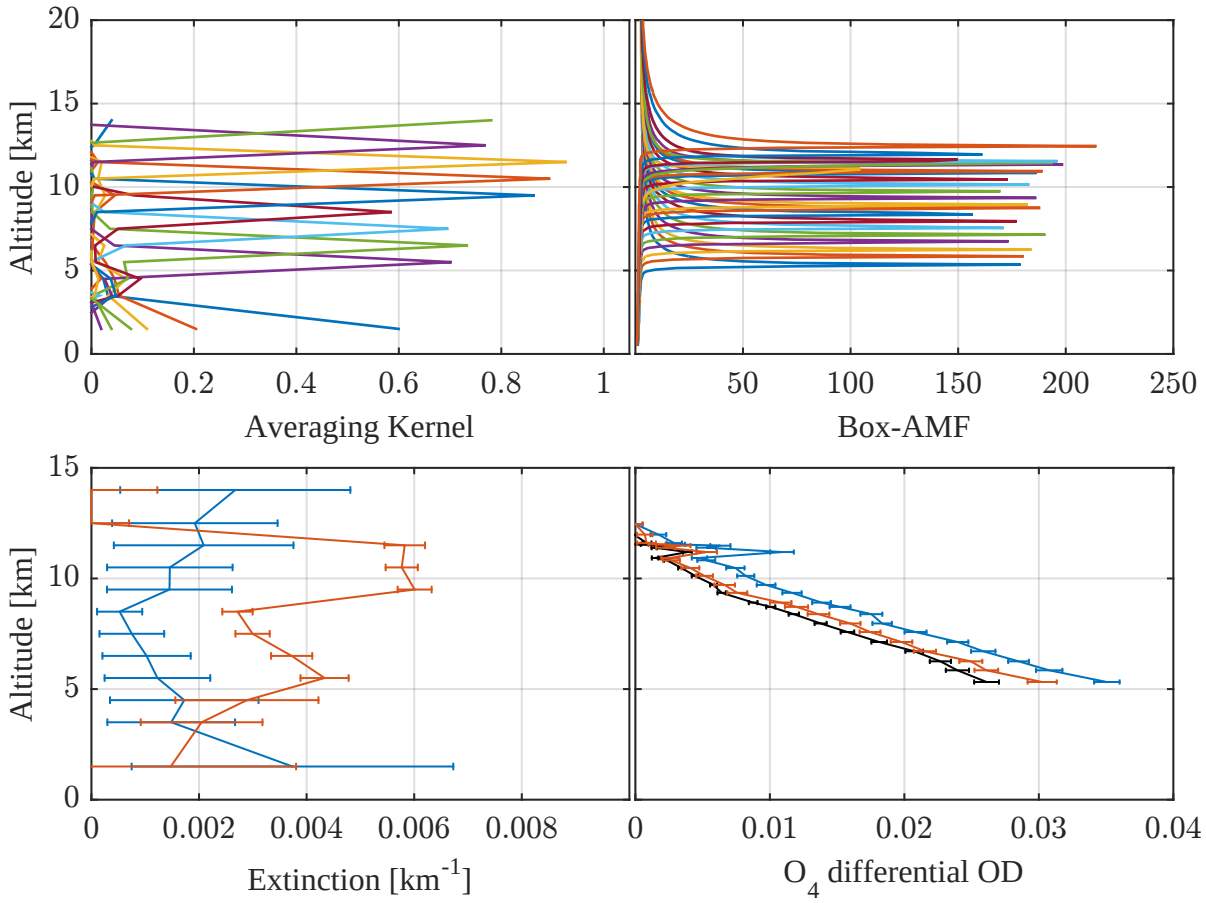

Figure A.13: OEI based on O_4 ODs for flight section 2. Top left: The trace of the AK matrix is 7.68. Top right: The Box-AMFs show a high sensitivity between 5 and 12 km altitude. Bottom left: A retrieval grid with 12 elements was chosen. Shown are the a priori profile (blue) as well as the first (red) iteration. Bottom right: Comparison of the O_4 ODs with respect to the OD at the highest altitude. Shown are the measurements (black), a priori (blue) as well as the first (red) iteration.

(a) Cockpit view around the time of the section 2 reference spectrum.

(b) Nadir view around the time of the section 2 reference spectrum.

Figure A.14: Pictures of the meteorological conditions during flight section 2, recorded by the HALO aircraft built-in camera system.

A.3.3 OEI Flight section 3

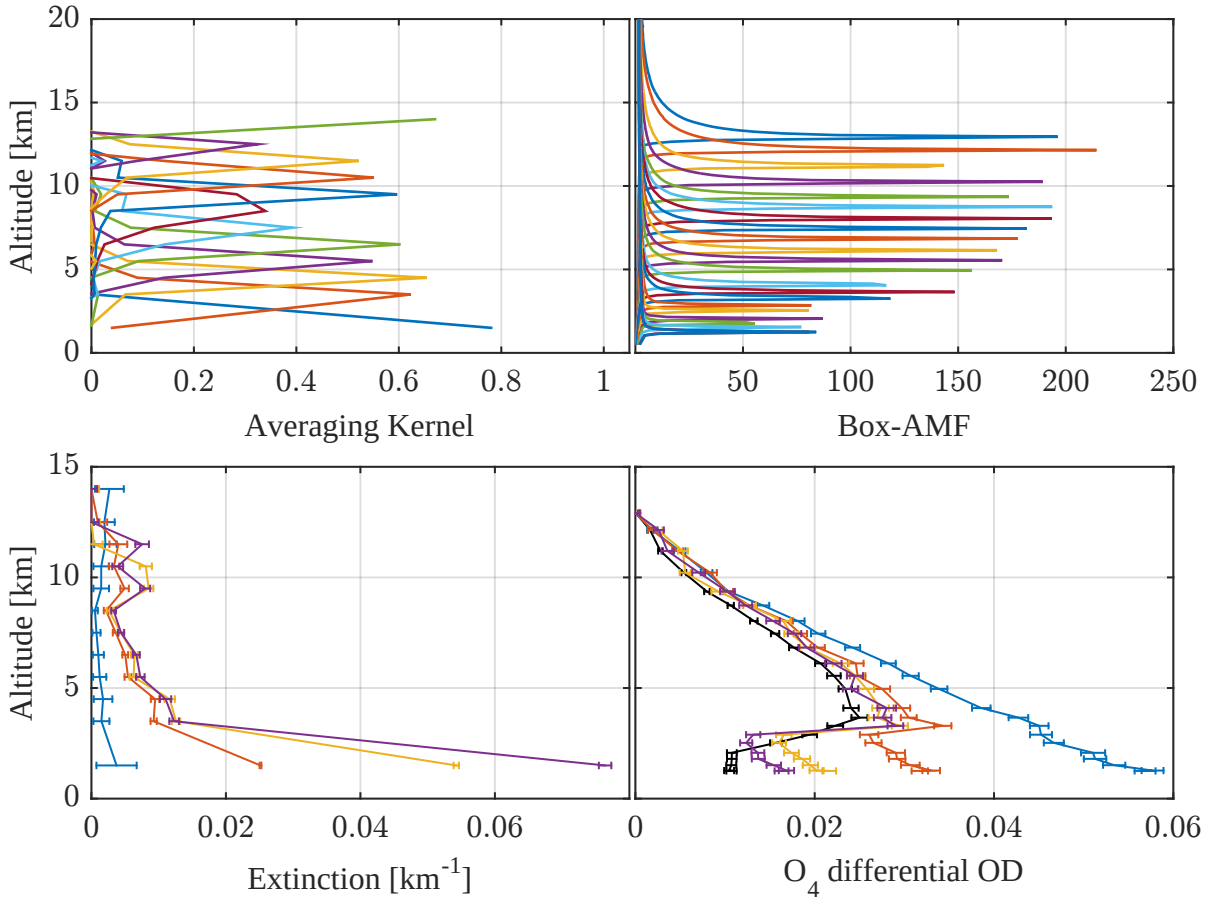

Figure A.15: OEI based on O_4 ODs for flight section 3. Top left: The trace of the AK matrix is 6.61. Top right: The Box-AMFs show a high sensitivity between 1 and 13 km altitude. Bottom left: A retrieval grid with 12 elements was chosen. Shown are the a priori profile (blue) as well as the first (red), second (yellow), and third (violet) iteration. Bottom right: Comparison of the O_4 ODs with respect to the OD at the highest altitude. Shown are the measurements (black), a priori (blue) as well as the first (red), second (yellow), and third (violet) iteration.

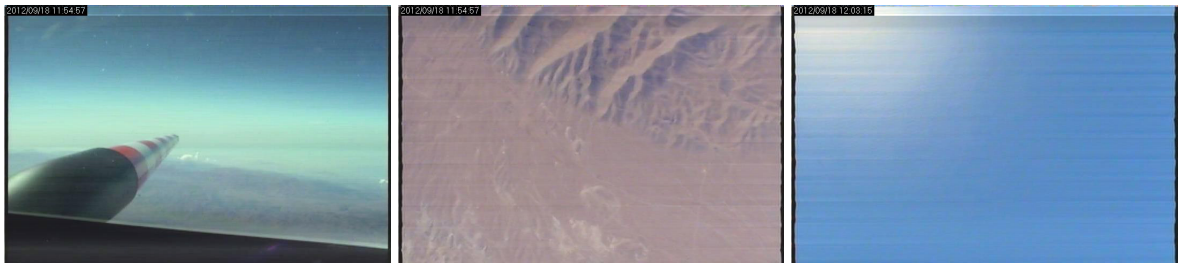

(a) Cockpit view around the time of the section 3 reference spectrum.

(b) Nadir view around the time of the section 3 reference spectrum.

(c) Nadir view shortly after the section 3 reference spectrum.

Figure A.16: Pictures of the meteorological conditions during flight section 3, recorded by the HALO aircraft built-in camera system.

A.4 Scaling method

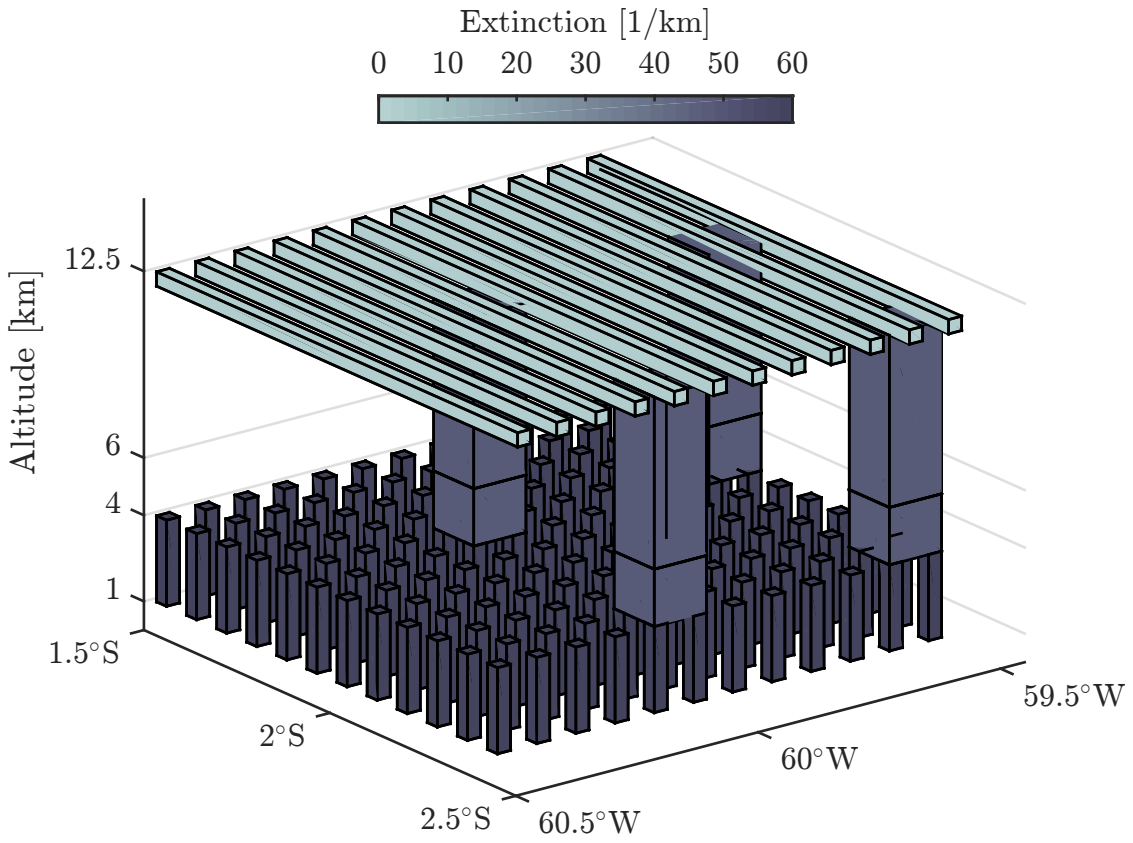

Figure A.17: Cloud pattern for RTM simulations presented in Figure 6.3. Adopted from Knecht (2015).

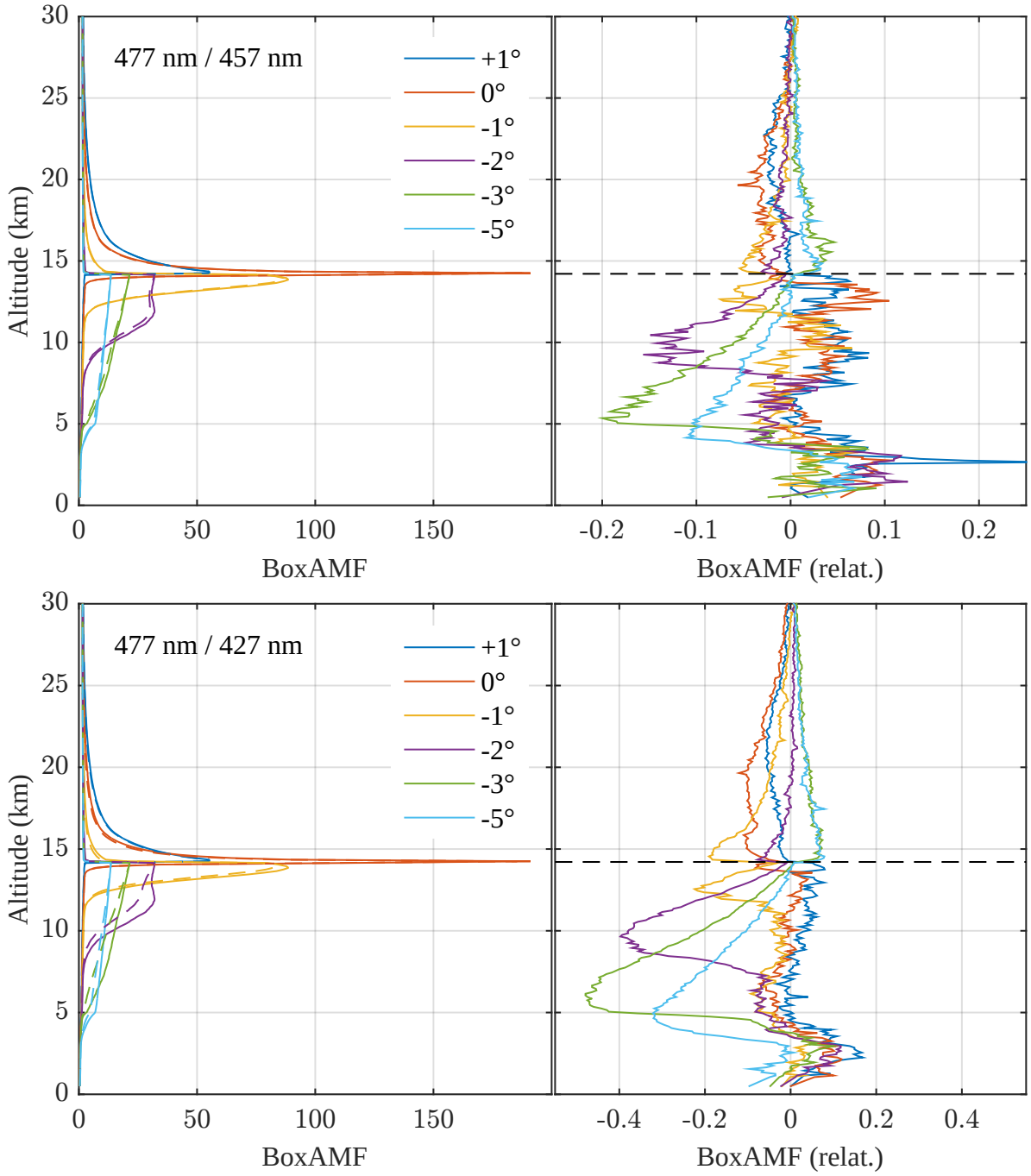

Figure A.18: BoxAMFs simulated with McArtim for a typical set of elevation angles for a measurement at 14.21 km altitude and 50° SZA. Top panels: 477 nm (lines) and 457 nm (broken lines). Bottom panels: 477 nm (lines) and 427 nm (broken lines). Left panels: BoxAMFs. Right panels: BoxAMFs at lower wavelengths (457 nm / 427 nm) relative to the BoxAMFs at 477 nm. Black broken lines indicate the aircraft altitude.

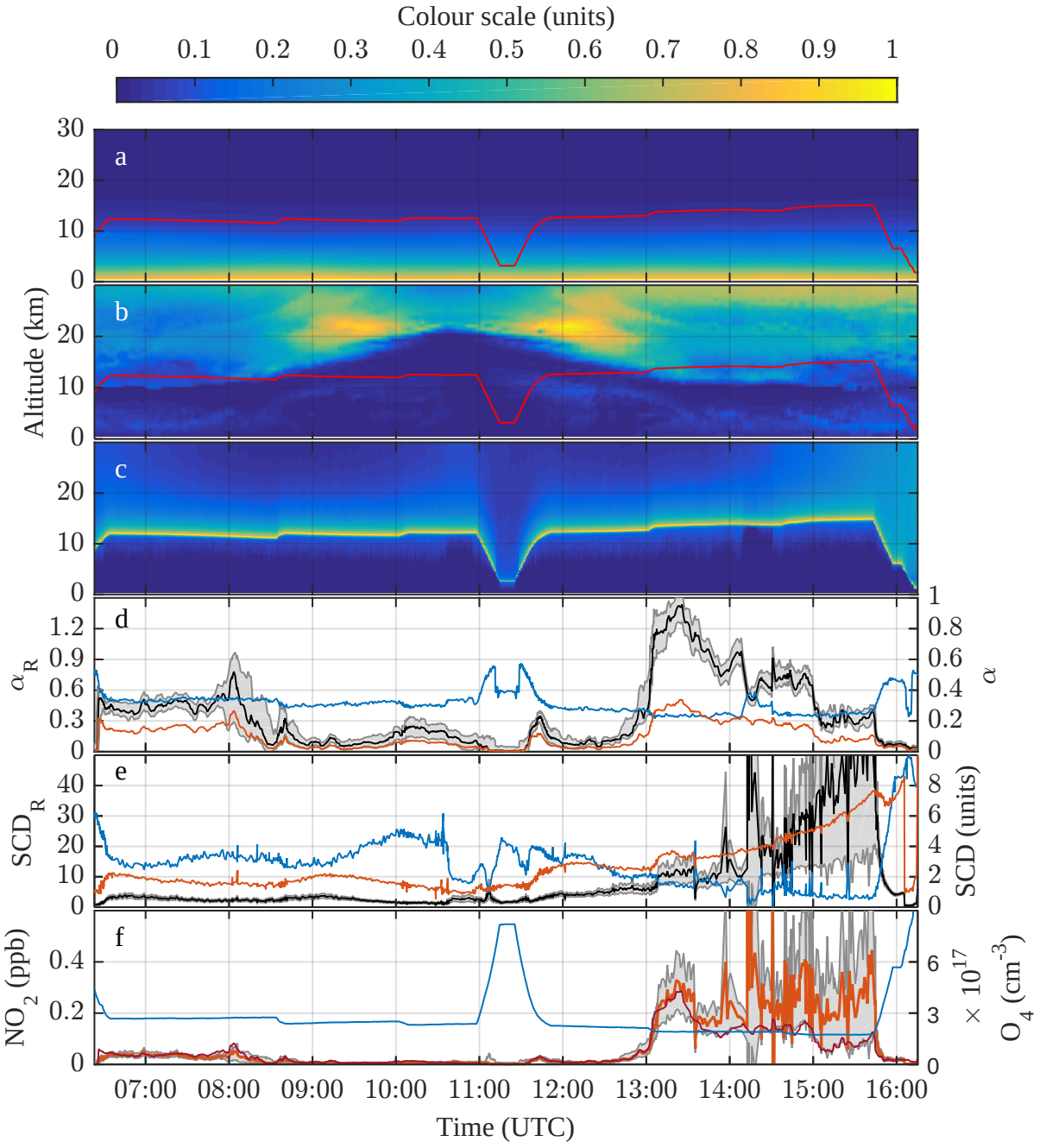

Figure A.19: Illustration of NO_2 mixing ratio retrieval with O_4 scaling for science flight ANT. Panel a: Curtain of O_4 "concentration" (colour scale $\times$ $3.0 \cdot 10^{37}$ molec.^{2}cm^{-6}) calculated from CLaMS temperature and pressure, and aircraft altitude (red line). Panel b: CLaMS curtain of NO_2 concentrations (colour scale $\times$ $2.9 \cdot 10^9$ cm^{-3}) and flight altitude (red line). Panel c: Box-AMFs calculated by the RTM McArtim (colour scale $\times \log(217)$). Panel d: α factors for O_4 (blue) and NO_2 (red) as well as α_R (black line) with its uncertainty range (grey shaded area). Panel e: SCDs from DOAS evaluation of the recorded spectra for O_4 (blue) and NO_2 (red) as well as their ratio (black line) with its uncertainty range (grey shaded area). SCDs are normalised to the maximum value recorded. Panel f: Retrieved NO_2 mixing ratio (red line) with its uncertainty range (grey shaded area) and in-situ measured O_4 "mixing ratio" (blue line). The dark red line denotes the NO_2 mixing ratio predicted by the CLaMS model.

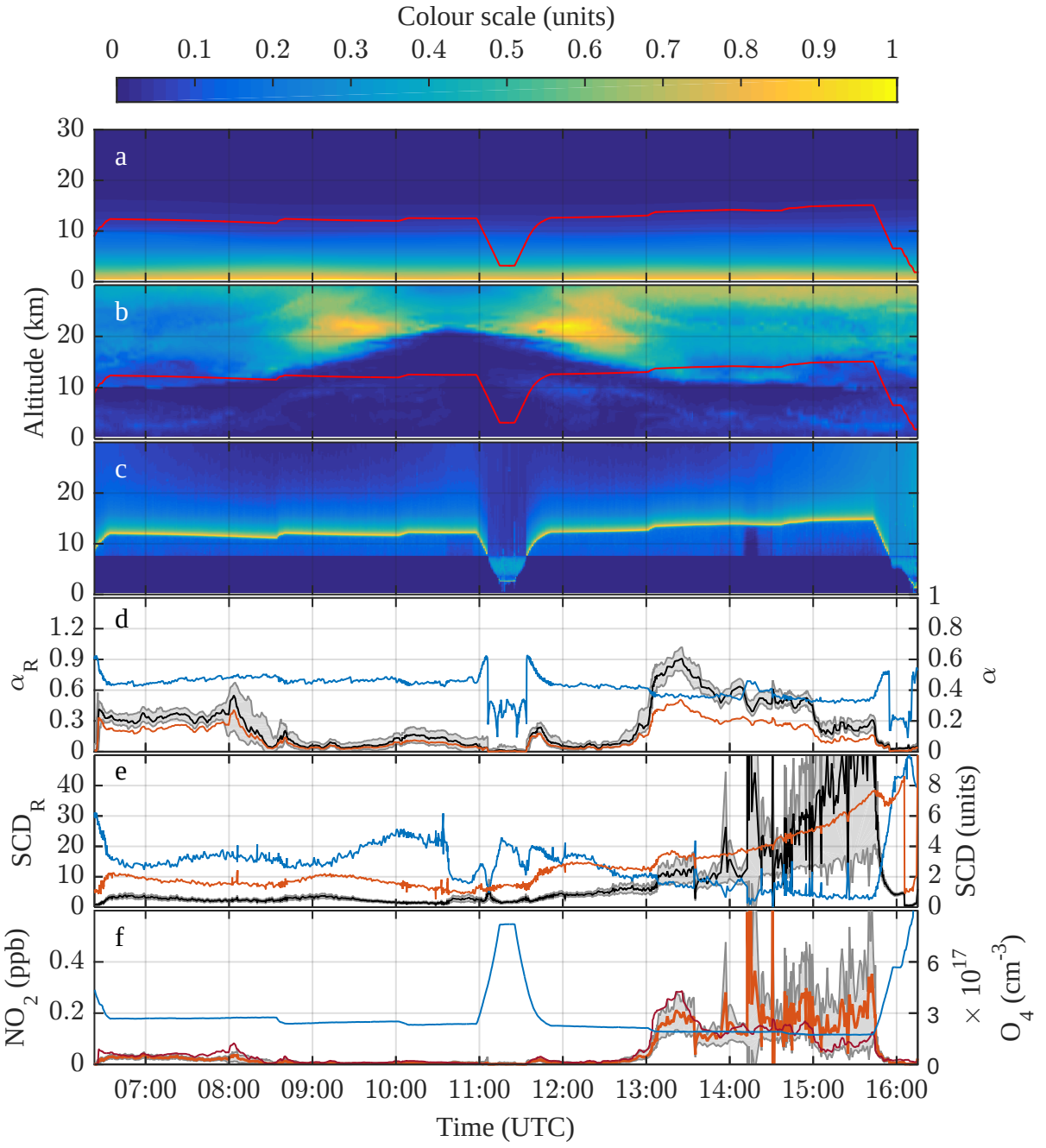

Figure A.20: Illustration of NO_2 mixing ratio retrieval with O_4 scaling for science flight ANT with an assumed cloud layer at 4 – 8 km altitude. Panel a: Curtain of O_4 "concentration" (colour scale $\times\ 3.0 \cdot 10^{37}$ molec.^{2}cm^{-6}) calculated from CLaMS temperature and pressure, and aircraft altitude (red line). Panel b: CLaMS curtain of NO_2 concentrations (colour scale $\times\ 2.9 \cdot 10^9$ cm^{-3}) and flight altitude (red line). Panel c: Box-AMFs calculated by the RTM McArtim (colour scale $\times \log(260)$). Panel d: α factors for O_4 (blue) and NO_2 (red) as well as α_R (black line) with its uncertainty range (grey shaded area). Panel e: SCDs from DOAS evaluation of the recorded spectra for O_4 (blue) and NO_2 (red) as well as their ratio (black line) with its uncertainty range (grey shaded area). SCDs are normalised to the maximum value recorded. Panel f: Retrieved NO_2 mixing ratio (red line) with its uncertainty range (grey shaded area) and in-situ measured O_4 "mixing ratio" (blue line). The dark red line denotes the NO_2 mixing ratio predicted by the CLaMS model.

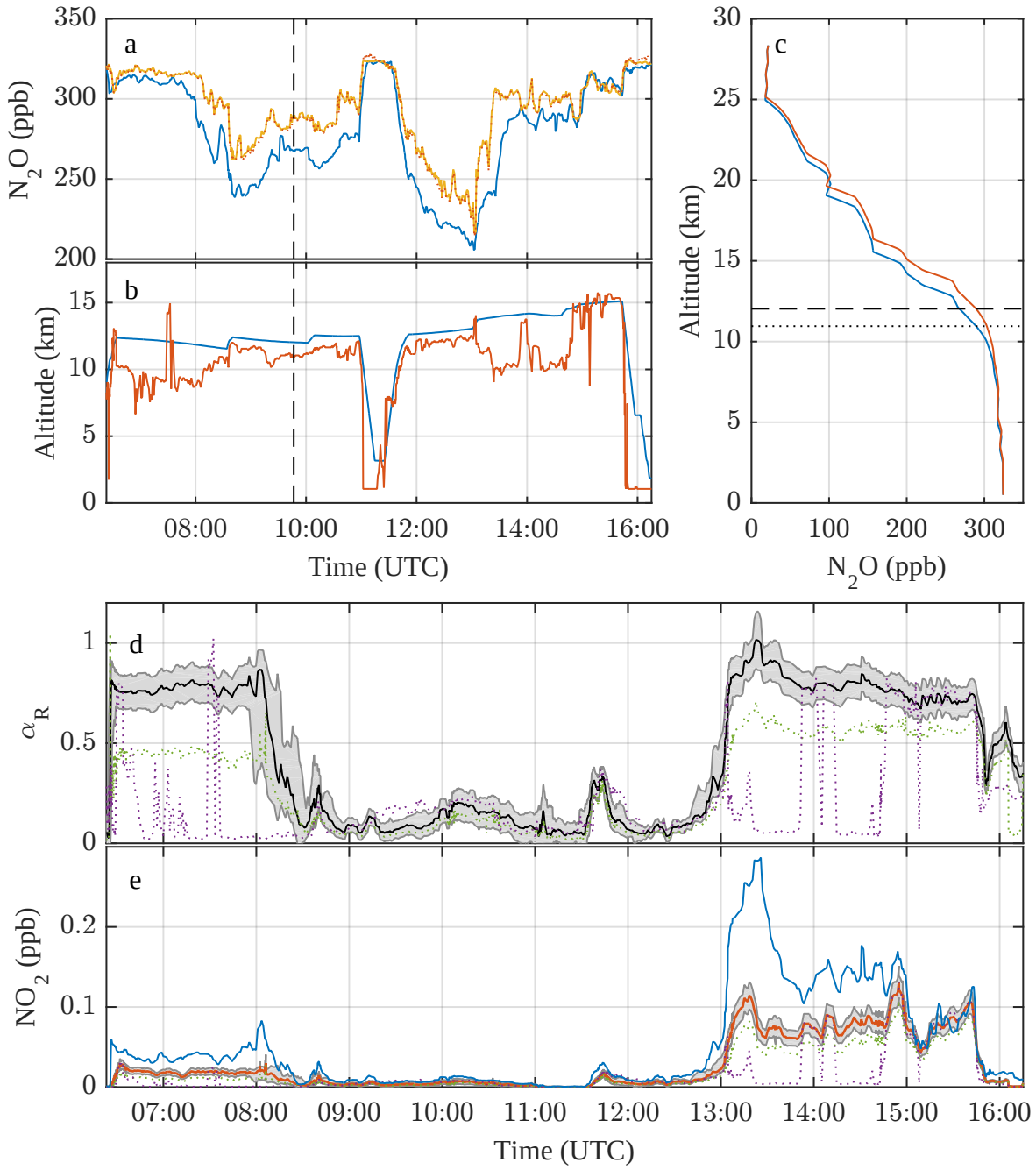

Figure A.21: Examination of potential systematic errors for science flight ANT by comparing CLaMS-modelled and measured N_2O. Panel a: Nitrous oxide mixing ratio predicted by CLaMS (blue), predicted by shifted CLaMS profiles (yellow) and in-situ measured (red dots). Panel b: Aircraft GPS altitude (blue) and altitude at which the in-situ measured N_2O mixing ratios are found in the unmodified CLaMS profiles (red). Panel c: Vertical profiles of N_2O at the time marked by black dashed lines in panels a and b. Unchanged profile in blue, shifted profile in red. The dashed line marks the measurement altitude, the dotted line marks the altitude of the respective N_2O mixing ratio in the unmodified CLaMS profile. Panel d: α_R (black line) and $\Delta\alpha_R$ (grey shaded area). Additionally, α_R resulting from adjusted trace gas mixing ratios at flight altitude (green dots) and resulting from shifted profiles (violet dots) are shown. Panel e: Shown are NO_2 mixing ratios retrieved from unmodified profiles (orange line with grey shaded uncertainty) and from adjusted profiles at flight altitude (green dots) and shifted profiles (violet dots) as well as predicted by the CLaMS model (blue line).

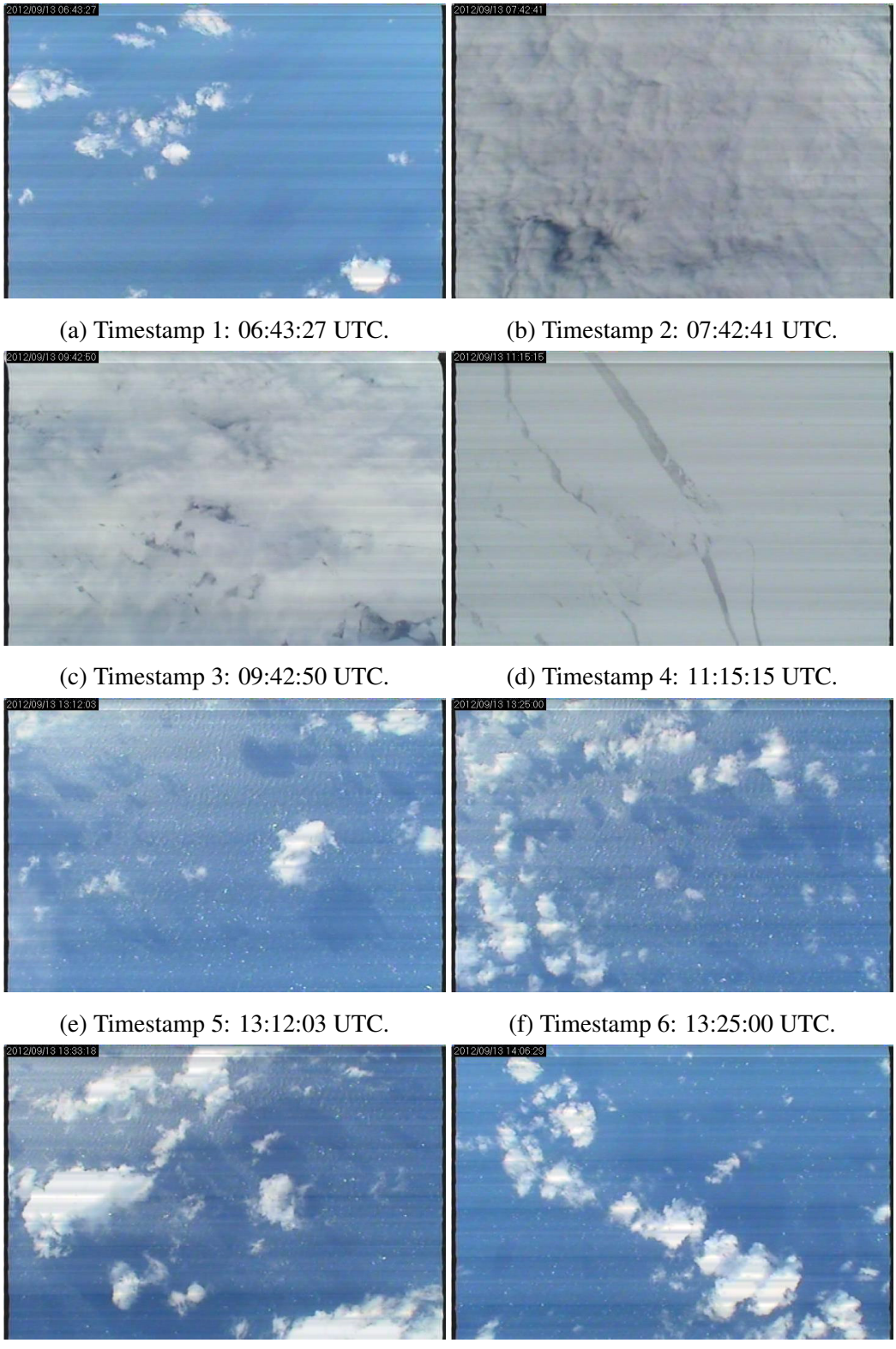

(a) Timestamp 1: 06:43:27 UTC. (b) Timestamp 2: 07:42:41 UTC.

(c) Timestamp 3: 09:42:50 UTC. (d) Timestamp 4: 11:15:15 UTC.

(e) Timestamp 5: 13:12:03 UTC. (f) Timestamp 6: 13:25:00 UTC.

(g) Timestamp 7: 13:53:18 UTC. (h) Timestamp 8: 14:06:29 UTC.

Figure A.22: Images recorded by the nadir-pointing camera aboard the HALO aircraft during science flight ANT. The timestamps refer to Figures 6.7 and 6.8.

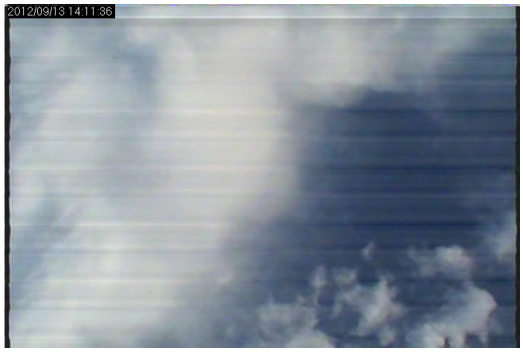

(a) Timestamp 9: 14:11:36 UTC.

(b) Timestamp 10: 14:23:12 UTC.

(c) Timestamp 11: 14:36:52 UTC.

(d) Timestamp 12: 14:49:29 UTC.

(e) Timestamp 13: 15:13:29 UTC.

(f) Timestamp 14: 15:23:31 UTC.

(g) Timestamp 15: 15:33:29 UTC.

Figure A.23: Images recorded by the nadir-pointing camera aboard the HALO aircraft during science flight ANT, continued. The timestamps refer to Figure 6.8.

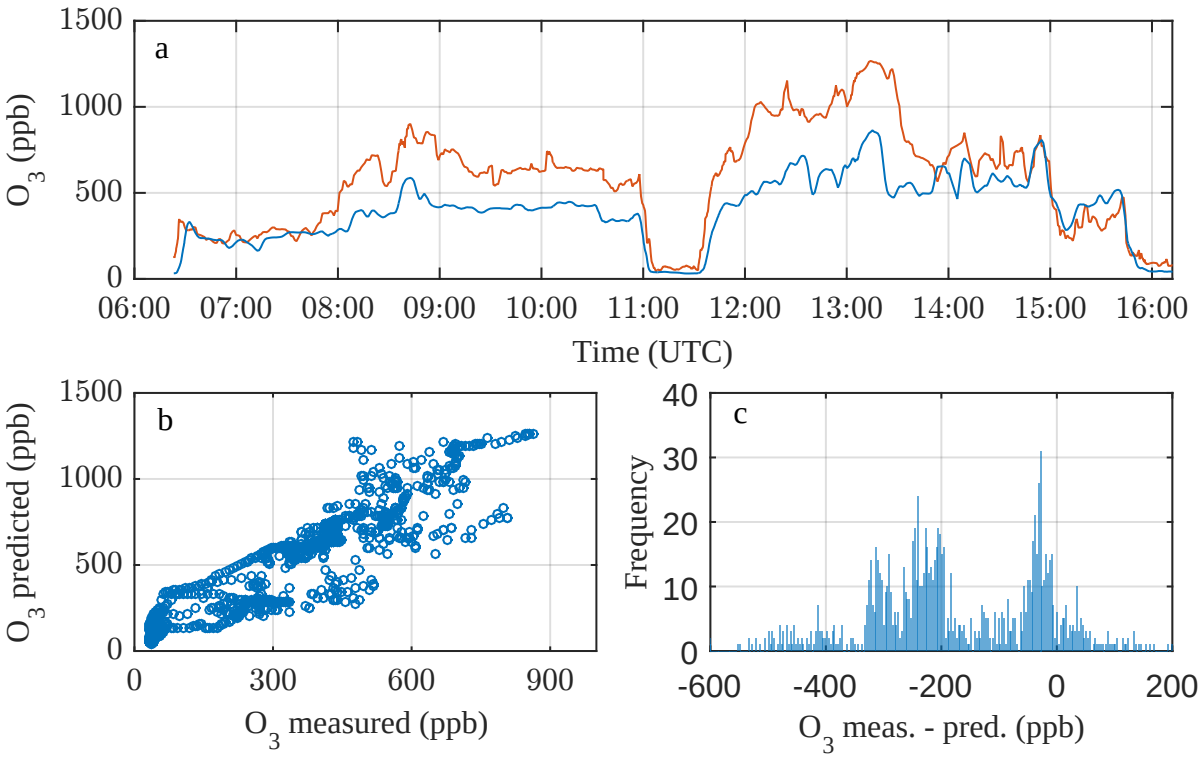

Figure A.24: O_3 in situ measurement (FAIRO) and CLaMS model output at flight altitude for science flight ANT.

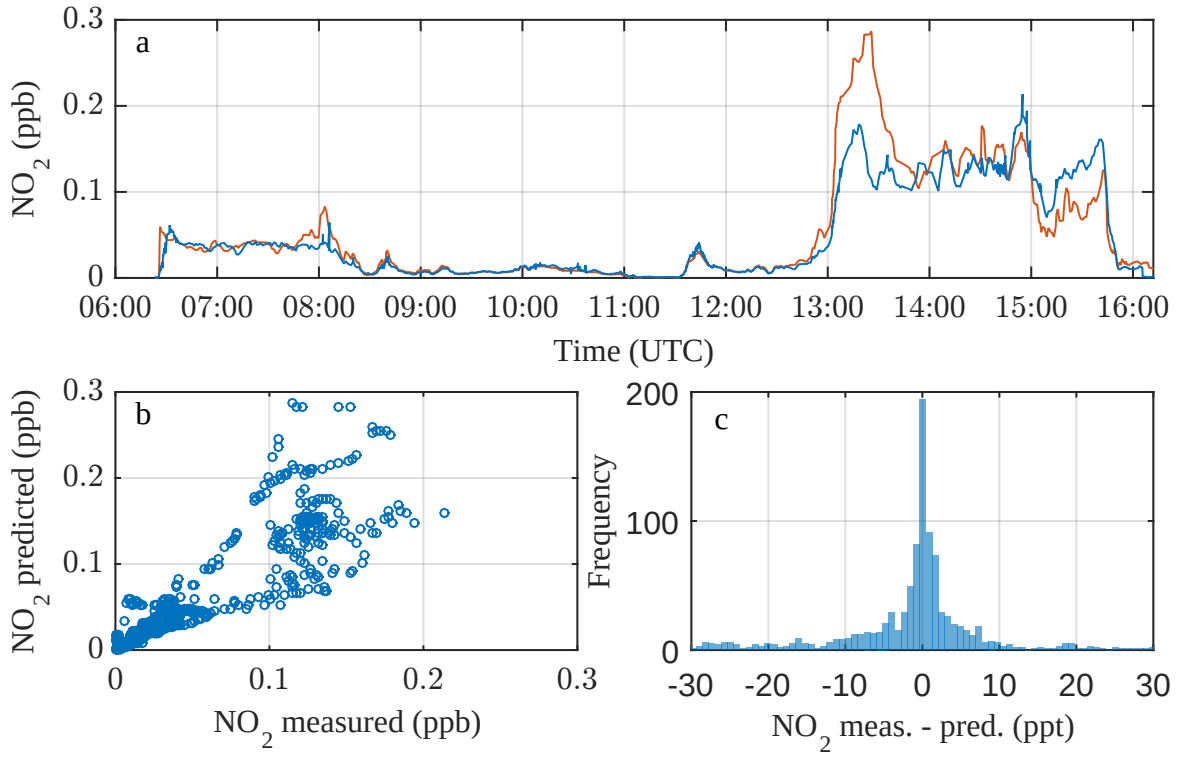

Figure A.25: NO_2 retrieved from DOAS measurements and CLaMS model output at flight altitude for science flight ANT.

Appendix B

Additional analysis

B.1 Additional science flight ANT retrievals

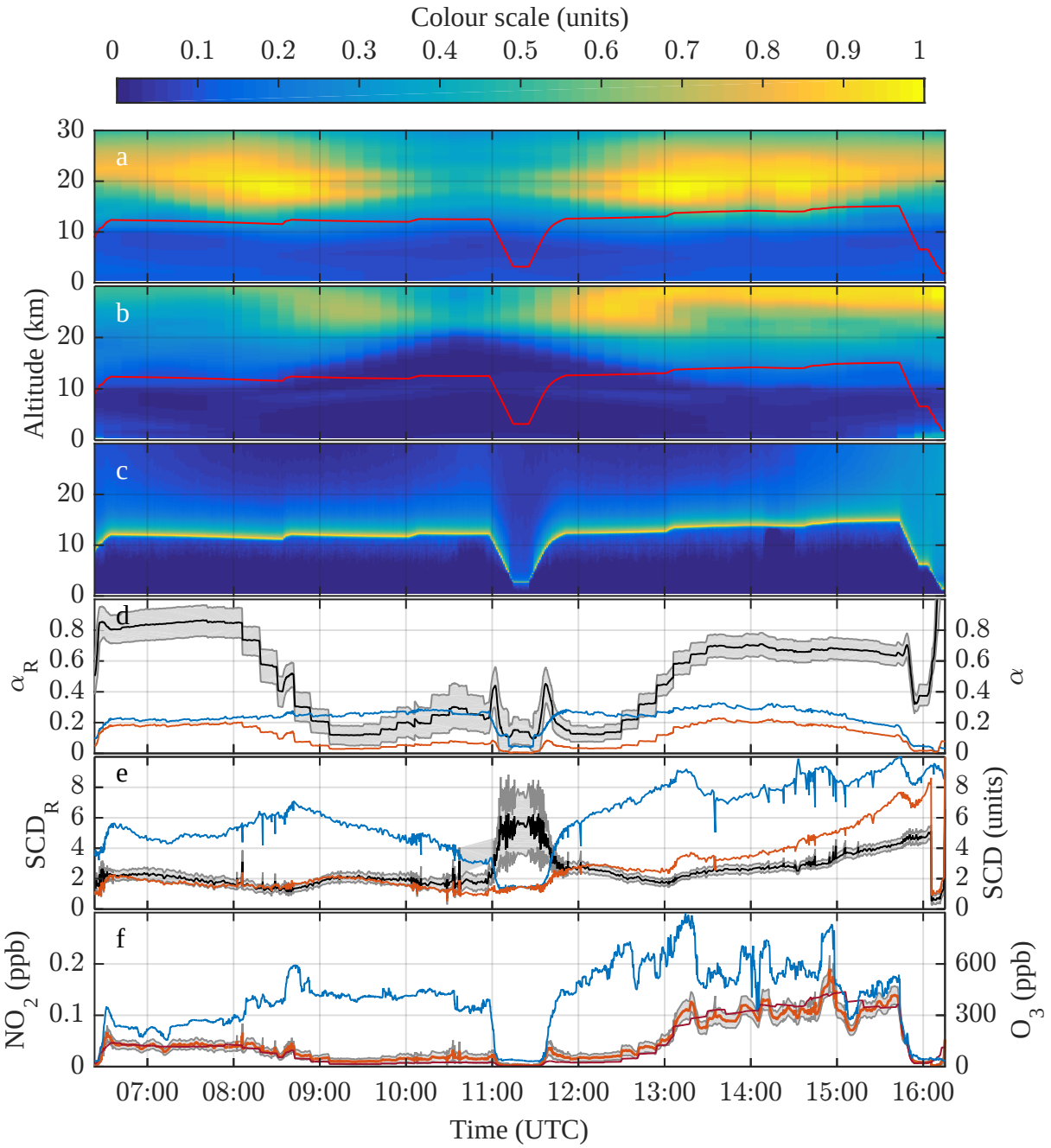

Figure B.1: Illustration of NO_2 mixing ratio retrieval for science flight ANT via O_3 scaling. Panel a: EMAC curtain of O_3 concentration (colour scale $\times$ $7.9 \cdot 10^{12}$ cm^{-3}) and aircraft altitude (red line). Panel b: EMAC curtain of NO_2 concentrations (colour scale $\times$ $2.9 \cdot 10^{9}$ cm^{-3}) and flight altitude (red line). Panel c: Box-AMFs calculated by the RTM McArtim (colour scale $\times \log(217)$). Panel d: α factors for O_3 (blue) and NO_2 (red) as well as α_R (black line) with its uncertainty range (grey shaded area). Panel e: SCDs from DOAS evaluation of the recorded spectra for O_3 (blue) and NO_2 (red) as well as their ratio (black line) with its uncertainty range (grey shaded area). SCDs are normalised to the maximum value recorded. Panel f: Retrieved NO_2 mixing ratio (red line) with its uncertainty range (grey shaded area) and in-situ measured O_3 (blue line), which was used as scaling gas. The dark red line denotes the NO_2 mixing ratio predicted by the EMAC model.

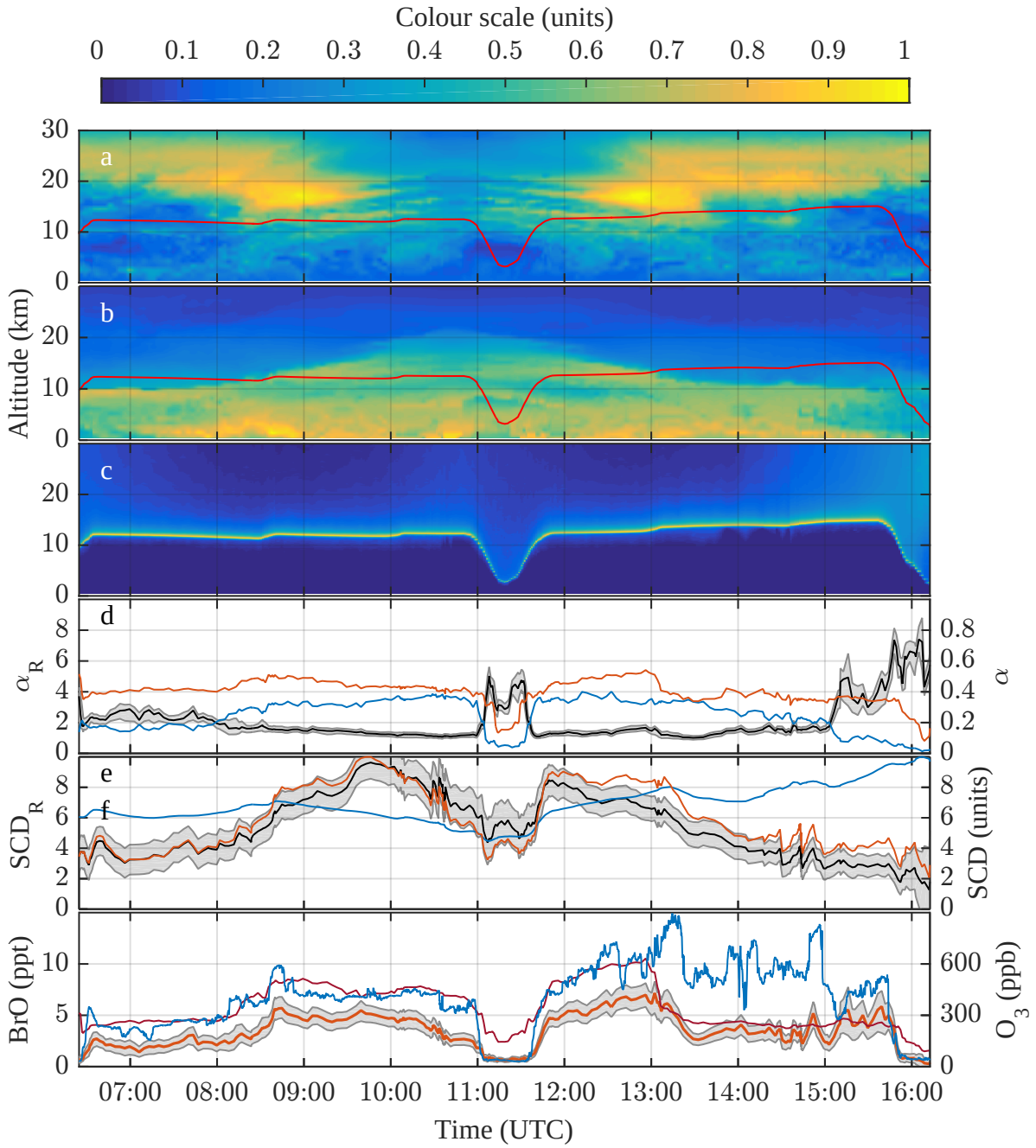

Figure B.2: Illustration of BrO mixing ratio retrieval for science flight ANT via O_3 scaling. Panel a: CLaMS curtain of O_3 concentration (colour scale $\times$ $7.9 \cdot 10^{12}$ cm^{-3}) and aircraft altitude (red line). Panel b: CLaMS curtain of BrO concentrations (colour scale $\times$ $2.9 \cdot 10^{9}$ cm^{-3}) and flight altitude (red line). Panel c: Box-AMFs calculated by the RTM McArtim (colour scale $\times \log(217)$). Panel d: α factors for O_3 (blue) and BrO (red) as well as α_R (black line) with its uncertainty range (grey shaded area). Panel e: SCDs from DOAS evaluation of the recorded spectra for O_3 (blue) and BrO (red) as well as their ratio (black line) with its uncertainty range (grey shaded area). SCDs are normalised to the maximum value recorded. Panel f: Retrieved BrO mixing ratio (red line) with its uncertainty range (grey shaded area) and in-situ measured O_3 (blue line), which was used as scaling gas. The dark red line denotes the BrO mixing ratio predicted by the CLaMS model.

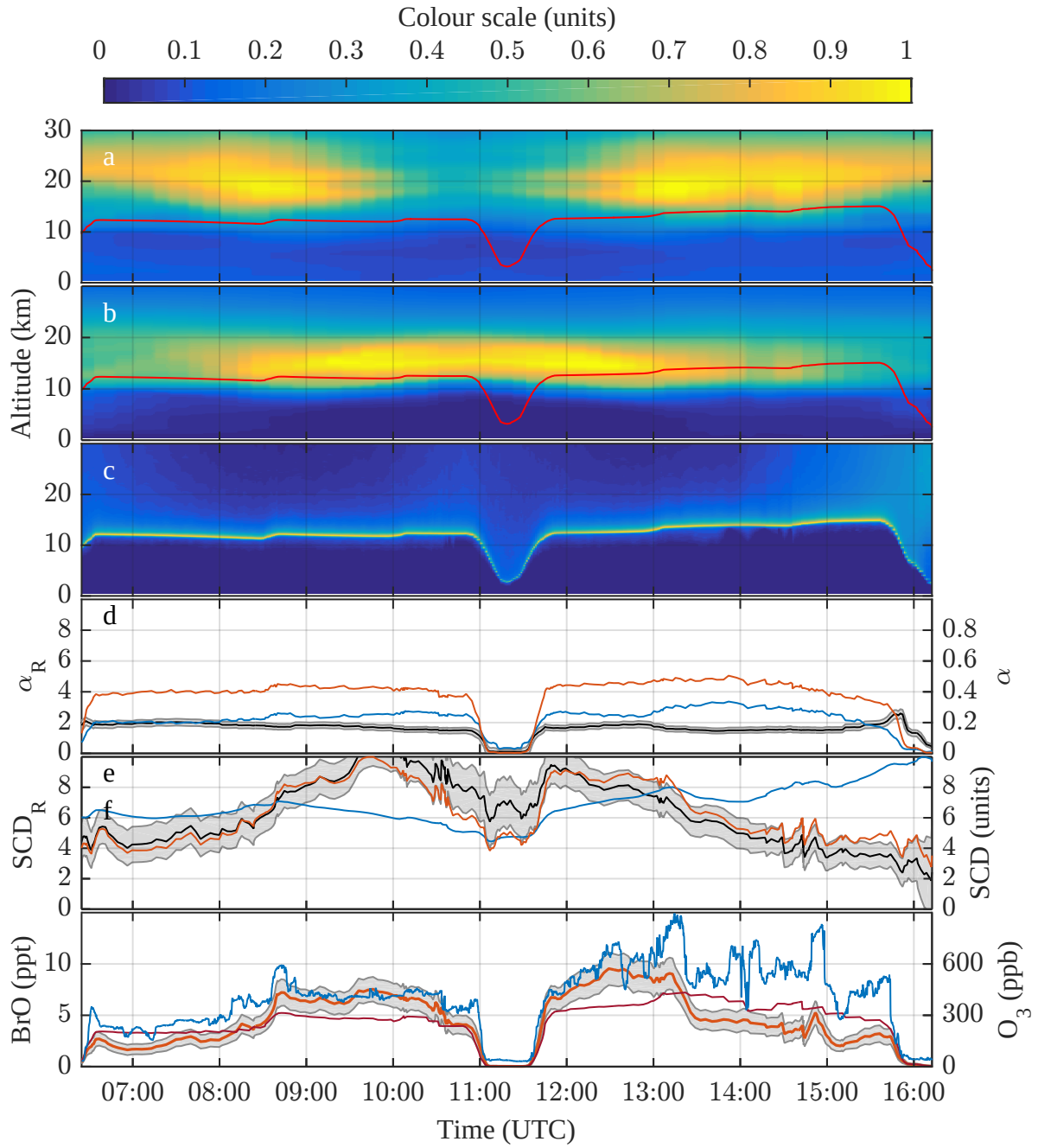

Figure B.3: Illustration of BrO mixing ratio retrieval for science flight ANT via O_3 scaling. Panel a: EMAC curtain of O_3 concentration (colour scale $\times$ $7.9 \cdot 10^{12}$ cm^{-3}) and aircraft altitude (red line). Panel b: EMAC curtain of BrO concentrations (colour scale $\times$ $2.9 \cdot 10^{9}$ cm^{-3}) and flight altitude (red line). Panel c: Box-AMFs calculated by the RTM McArtim (colour scale $\times \log(217)$). Panel d: α factors for O_3 (blue) and BrO (red) as well as α_R (black line) with its uncertainty range (grey shaded area). Panel e: SCDs from DOAS evaluation of the recorded spectra for O_3 (blue) and BrO (red) as well as their ratio (black line) with its uncertainty range (grey shaded area). SCDs are normalised to the maximum value recorded. Panel f: Retrieved BrO mixing ratio (red line) with its uncertainty range (grey shaded area) and in-situ measured O_3 (blue line), which was used as scaling gas. The dark red line denotes the BrO mixing ratio predicted by the EMAC model.

B.2 Science flight ML analysis

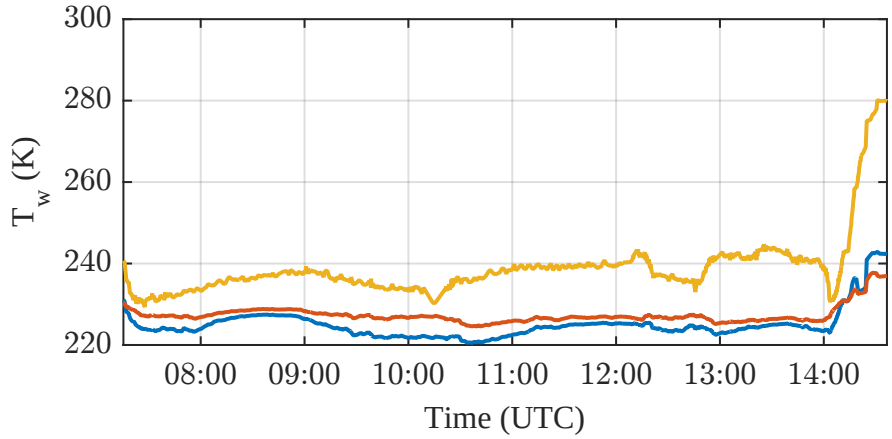

Figure B.4: Weighted mean temperature T_w for the absorption of O_3 (blue), NO_2 (red), and O_4 (yellow) during science flight ML. T_w is calculated by multiplying the BoxAMFs (sect. 5.3.2) with the trace gas profiles provided by the chemical transport model (sect. 5.4) to retrieve so-called Contribution profiles (sect. 6.1), i.e. a measure for the amount of trace gas absorption at a certain altitude. Using the altitude temperature profiles provided by the CTM, the weighted mean temperature T_w of the observed trace gas absorption is retrieved.

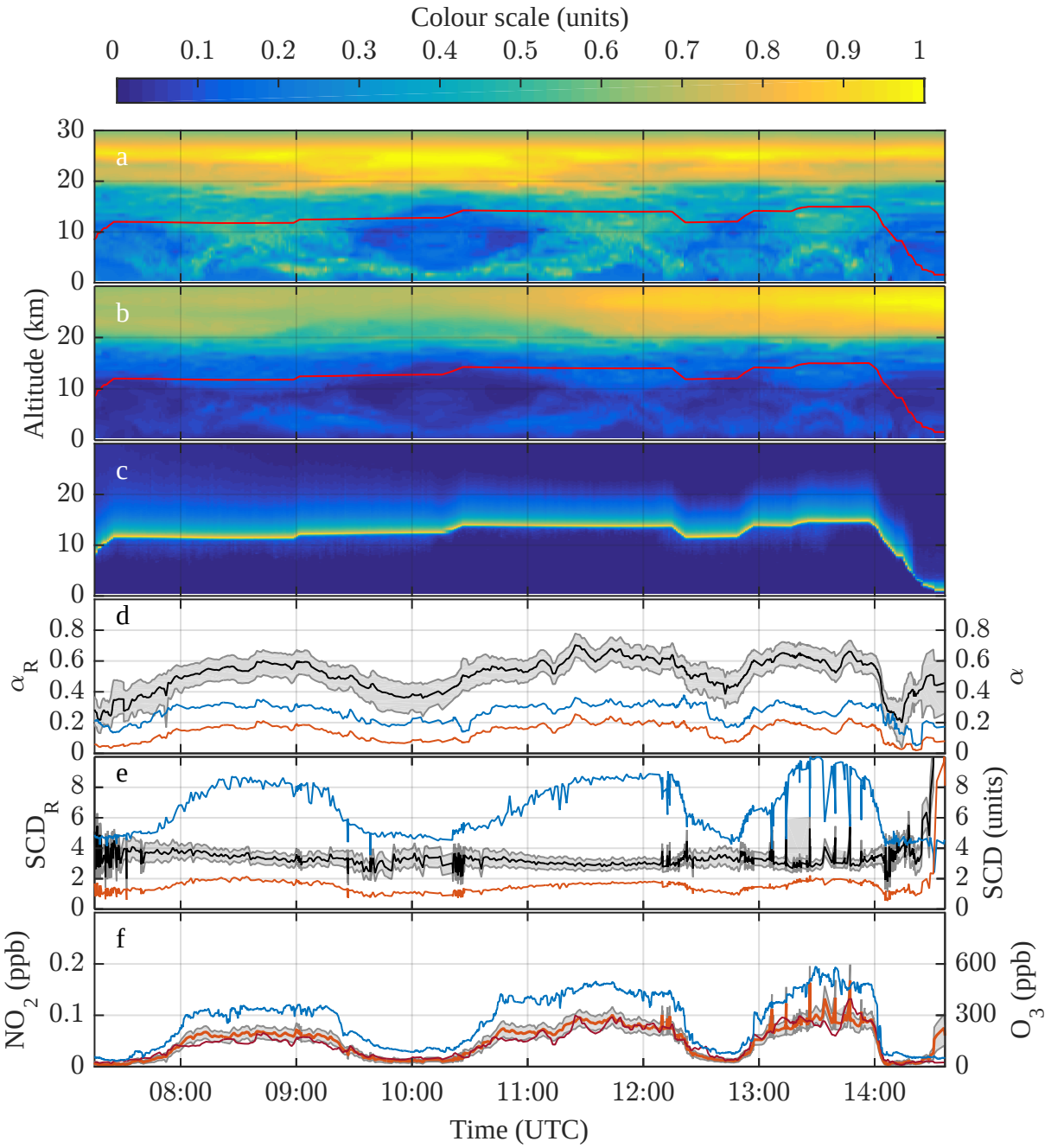

Figure B.5: Illustration of NO_2 mixing ratio retrieval for science flight ML. Panel a: CLaMS curtain of O_3 concentration (colour scale $\times\ 5.0 \cdot 10^{12}$ cm^{-3}) and aircraft altitude (red line). Panel b: CLaMS curtain of NO_2 concentration (colour scale $\times\ 2.3 \cdot 10^{9}$ cm^{-3}) and flight altitude (red line). Panel c: Box-AMFs calculated by the RTM McArtim (colour scale $\times \log(214)$). Panel d: α factors of O_3 (blue) and NO_2 (red) as well as α_R (black line) with its uncertainty range (grey shaded area). Panel e: SCDs from DOAS evaluation of the recorded spectra for O_3 (blue) and NO_2 (red) as well as their ratio (black line) with its uncertainty range (grey shaded area). SCDs are normalised to the maximum value recorded. Panel f: Retrieved NO_2 mixing ratio (red line) with its uncertainty range (grey shaded area) and in-situ measured O_3 (blue line), which was used as scaling gas.

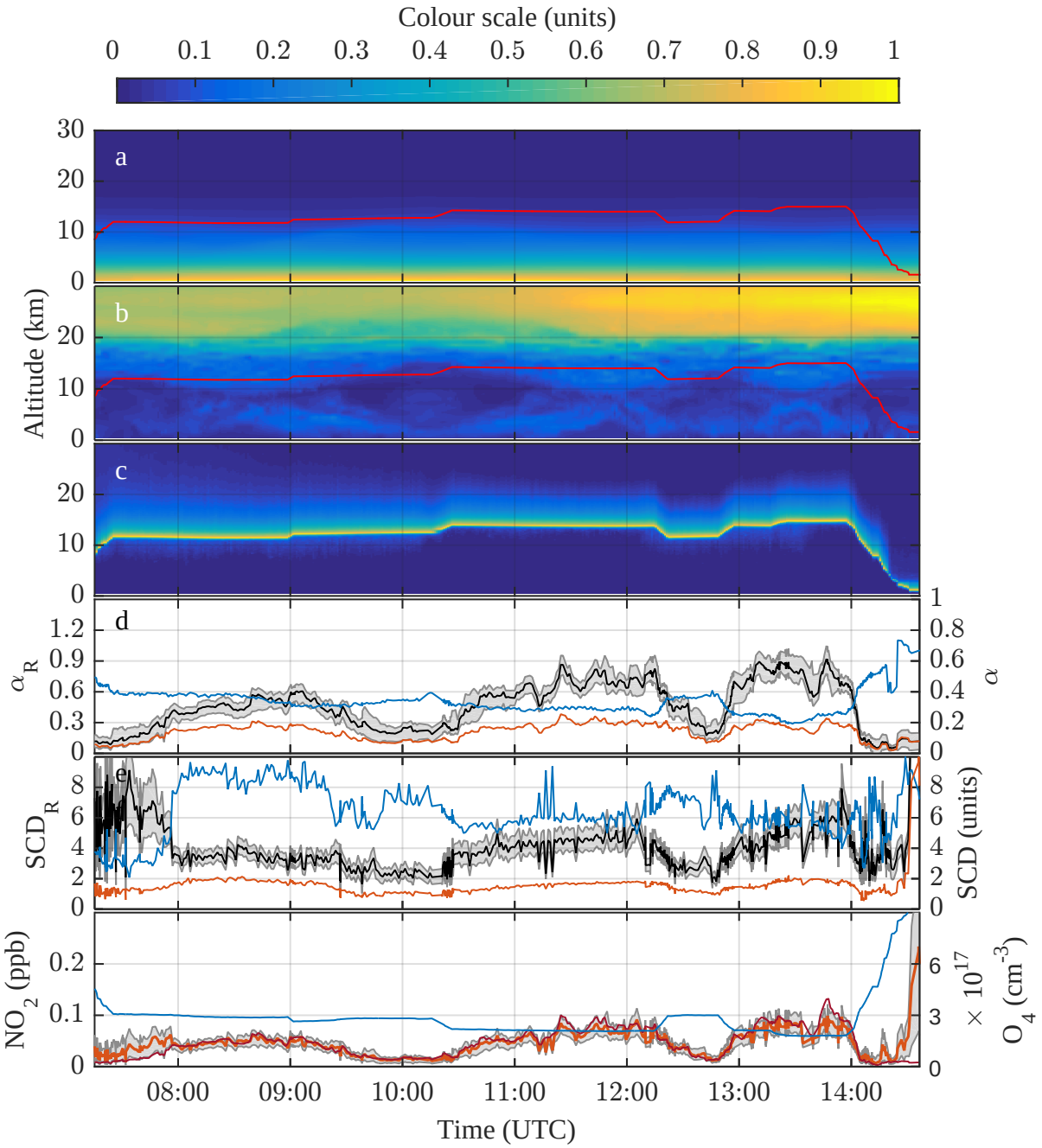

Figure B.6: Illustration of NO_2 mixing ratio retrieval for science flight ML. Panel a: CLaMS curtain of O_4 "concentration" (colour scale $\times$ $2.7 \cdot 10^{37}$ molec.^{2}cm^{-6}) and aircraft altitude (red line). Panel b: CLaMS curtain of NO_2 concentration (colour scale $\times$ $2.3 \cdot 10^9$ cm^{-3}) and flight altitude (red line). Panel c: Box-AMFs calculated by the RTM McArtim (colour scale $\times \log(214)$). Panel d: α factors of O_4 (blue) and NO_2 (red) as well as α_R (black line) with its uncertainty range (grey shaded area). Panel e: SCDs from DOAS evaluation of the recorded spectra for O_4 (blue) and NO_2 (red) as well as their ratio (black line) with its uncertainty range (grey shaded area). SCDs are normalised to the maximum value recorded. Panel f: Retrieved NO_2 mixing ratio (red line) with its uncertainty range (grey shaded area) and O_4 "mixing ratio" (blue line) derived from in-situ pressure and temperature measurements.

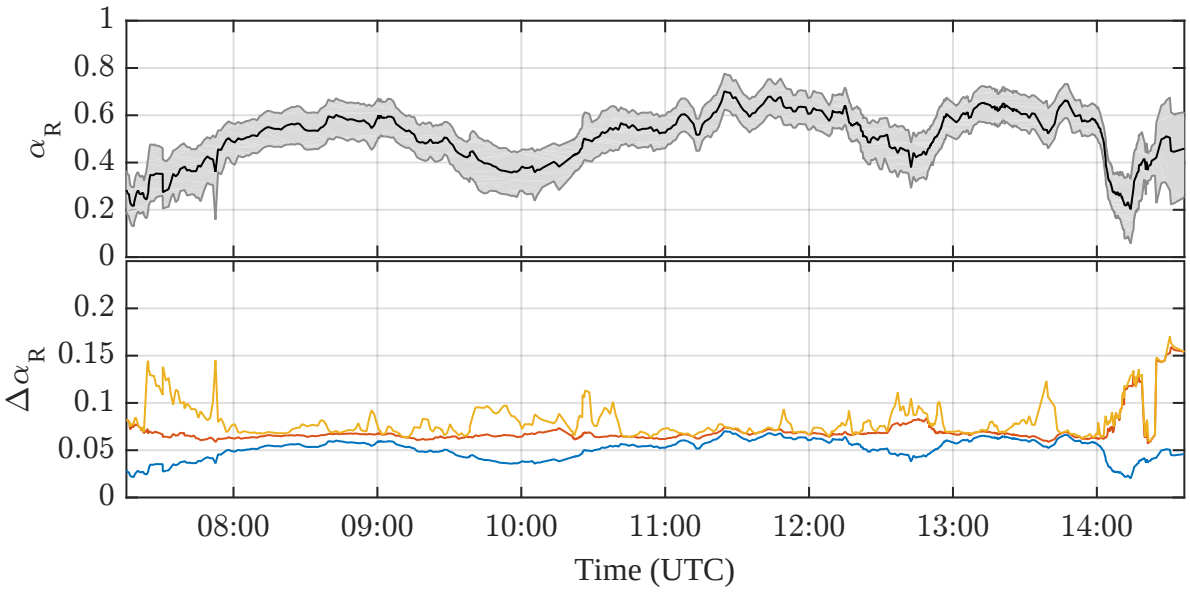

Figure B.7: α_R and its uncertainties for science flight ML. Top panel: α_R (black line) and its uncertainty $\Delta\alpha_R$ (grey shaded area) including all statistical components. Bottom panel: Individual $\Delta\alpha_R$ components added up. Blue: 10% uncertainty of α factors from Mie extinction influence (sect. 6.2.1). Red: Blue + uncertainty due to small scale variability (sect. 6.2.2). Yellow: Red + vertical sampling uncertainty (sect. 6.2.3).

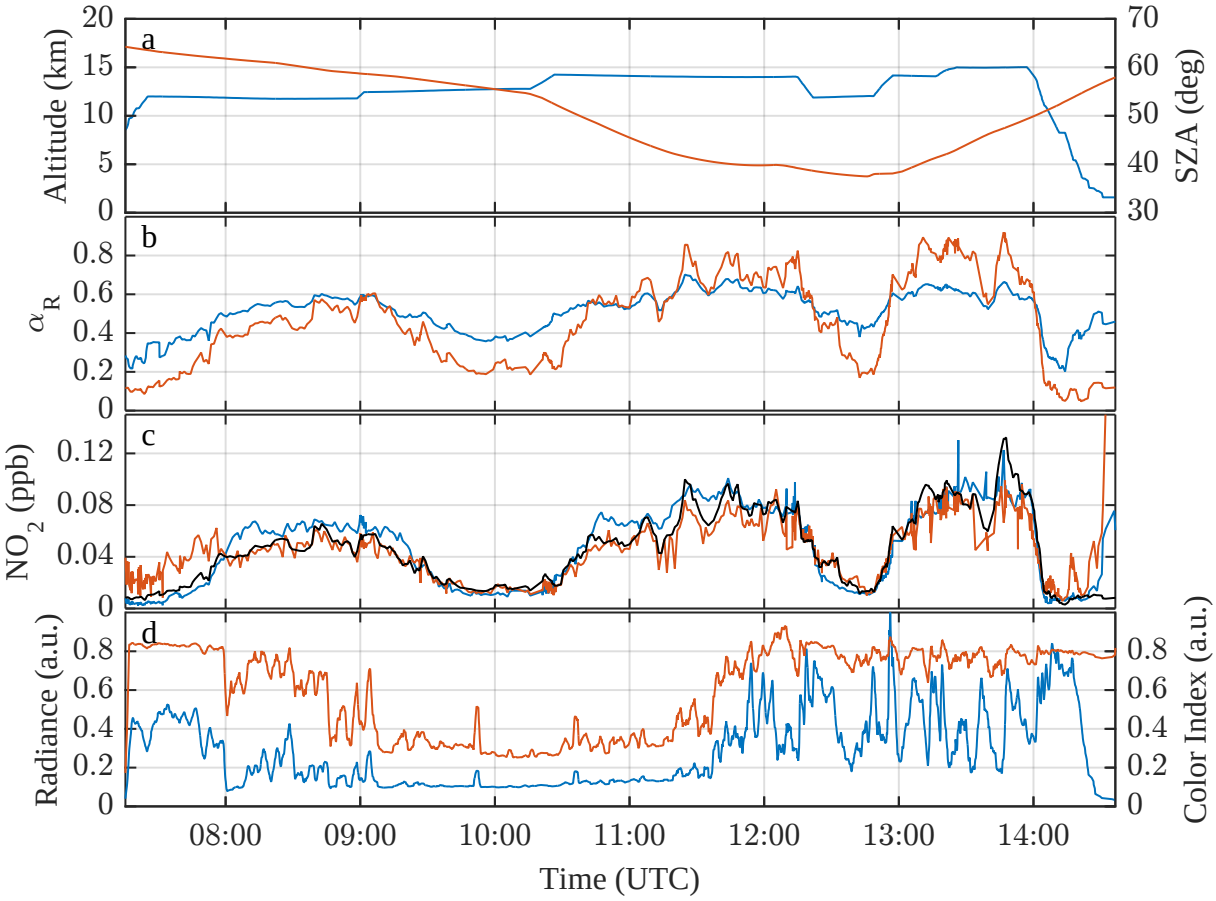

Figure B.8: Comparison of O_3- and O_4-scaling for science flight ML. Panel a: Flight altitude (blue) and SZA (red). Panel b: α_R using O_3 (blue) and O_4 (red) as scaling gas, respectively. Dotted lines show calculations assuming a continuous cloud layer at 4-8 km altitude in the model. Panel c: Retrieved NO_2 mixing ratios using O_3 (blue) and O_4 (red) as scaling gas, respectively. Dotted lines calculated using α_R with assumed cloud layer (as in panel b). The NO_2 mixing ratios predicted by the CTM CLAMs are shown as a black line. Panel d: Radiance at 430 nm and Colour Index (600 nm / 430 nm) in relative units (scaled to the highest value), measured by the Nadir visible channel (VIS3) of the HALO mini-DOAS instrument .

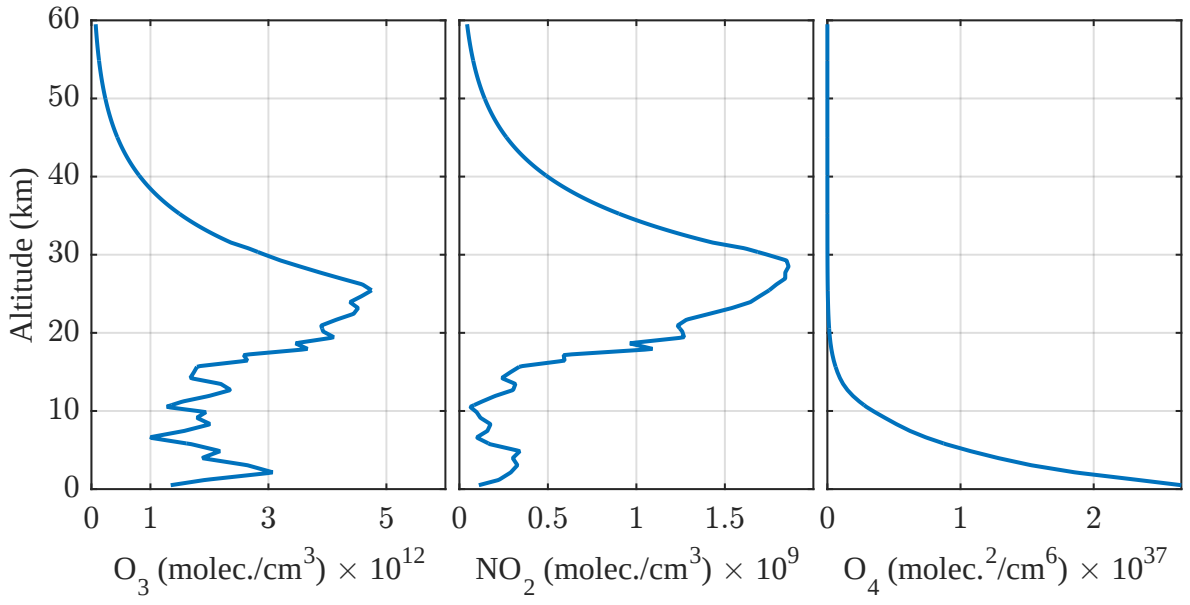

Figure B.9: Concentration profiles for trace gases O_3, NO_2, and O_4 over the mid-latitude North Atlantic as predicted by CLaMS for science flight ML at 08:12 UTC, 49° N, 1° E.

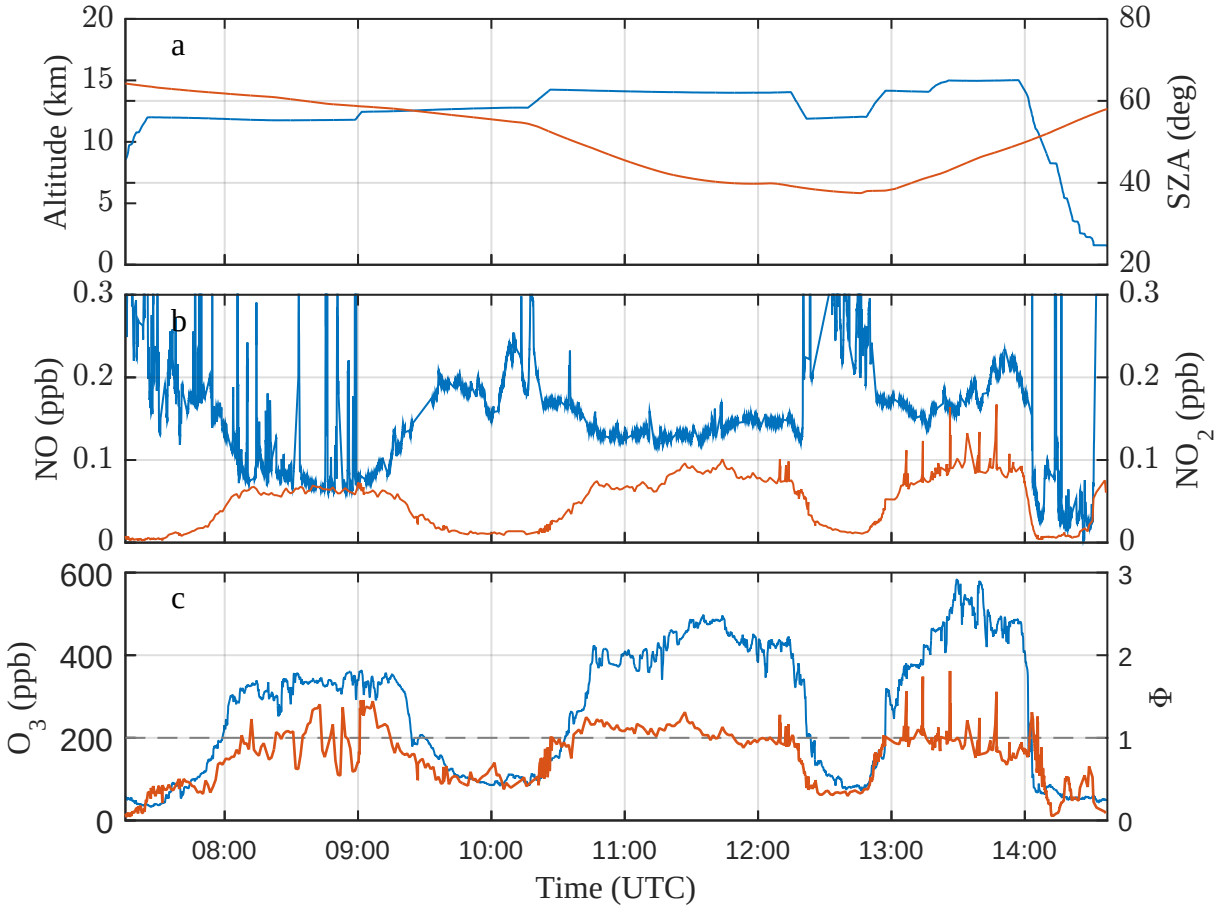

Figure B.10: NO_x and Leighton ratio Φ during science flight ML. Panel a: Flight altitude (blue) and SZA (red). Panel b: NO in-situ measurements (blue, AENEAS) and [[]$_N$O2][O3,CLaMS] (red, HALO mini-DOAS instrument). Panel c: O_3 (blue, FAIRO) and Leighton ratio Φ (red).

Appendix C

Acknowledgements

I want to express my gratitude to the many people who supported me during the course of the thesis:

- My most sincere gratitude to Klaus Pfeilsticker, who opened this opportunity for me and the other students involved. I am incredibly thankful for his scientific advice and the many discussions on topics far and wide.
- I thank Prof. Dr. Thomas Wagner who agreed to serve as a referee on this thesis.
- I am grateful for proof-reading to Zoe Davis, Eric Gentry, Dominique Loerks, and Lindsey Walter.
- I want to express my great admiration and thanks to all students involved in the project over the years. It would not have been possible to get this far without their hard work. Their enthusiasm, ideas, support and character were a constant supply of joy and encouragement: Oliver-Alex Aderhold, Jannik Bounin, Eric Gentry, Mareike Kenntner, Marvin Knapp, Matthias Knecht, Dominique Loerks, Rasmus Raecke, Marcel Reichert, Isabella Schulte, and Jannis Weimar.
- The atmosphere in the research group has been full of support and trust, fruitful discussions and at times a lot of fun. I am very grateful to Tina Buchmann, Tim Deutschmann, Katja Großmann, Sabrina Ludmann, Lisa Scalone, Ugo Tricoli, Bodo Werner and all the students mentioned above for their friendship and help. I would also like to include the "extended family", Hannah Fobbe and Alina Muschko.
- I am particularly thankful to Johanna Kerch (who provided me with a cozy home during the final phase) and Helene Hoffmann (who lead me to Heidelberg in the first place) for their support and enduring friendship.
- I would like to express my gratitude to all those at DLR who have made the various science missions possible: Katrin Witte, Martina Hierle, Andrea Hausold and Frank Probst for their organisational talent and seemingly endless work-hours, Robert Uebelacker and Sebastian Burwitz for their support during various certification processes, Thomas "Thommy" Lederer for

his friendly help making it all possible on airports around the world, Volker Dreiling for his support with BAHAMAS, and Annemarie Wunderl and her family who provided us with a friendly, flexible and always reliable home near Oberpfaffenhofen.

- I express my gratitude to all colleagues who helped this thesis come to life by providing their simulations (Jens-Uwe Grooß, Sigrun Matthes), their measurements (Tina Jurkat, Andreas Zahn, Helmut Ziereis, and many others) and their advice.

- Additional thanks go to the Manfred Wendisch group from Leipzig (Andre Ehrlich, Clemens Fricke, Evi Jäkel, Insa Lohse, Frank Werner) as well as Bernhard Buchholz and Layal Safadi, who were always great collegues for advice as well as leisure time during science missions.

- I am grateful to the IUP workshop, in particular Ralph Pfeifer and Sebastian Gehrig, for their ideas, advice, and hard work on improving the HALO mini-DOAS instrument throughout the years. I would also like to thank Karl-Heinz Schmidt for his support (sometimes on short notice) and advice on the instrument electronics.

- Last but not least, nothing would be possible without the trust, support, and encouragement by Katja, Hendrikje, Saskia, and Andreas. I admire you and I feel incredibly lucky.